Design and Feasibility Studies for a High Energy Neutrino Detector

Janice Reid B.Sc. (Hons)

Thesis submitted for the degree of

Doctor of Philosophy

in

The University of Adelaide

(Faculty of Science)

November 1995

Statement

This thesis contains neither material which has been accepted for the award of any other degree or diploma in any university or other tertiary institution, nor, to the best of the author's knowledge and belief, material previously published or written by any other person, except where due reference is made in the text.

The author consents to this copy of the thesis, when deposited in the University Library, being made available for loan and photocopying.

Signed:

J. L. Reid

November 1995

Abstract

In this thesis, the design of a high energy neutrino detector intended to observe astrophysical point sources, is developed. In the first two chapters an introduction to the field of neutrino astrophysics is presented along with a review of neutrino astronomy, including a description of proposed and existing neutrino detectors.

Chapter 3 describes the selection of a suitable site for the proposed detector. Factors which are considered are the physical properties of the site and the optical properties of the water in the site with respect to the transmission of Cerenkov light. This involves a detailed analysis of the attenuation length of the water using a spectrometer and also a specifically built transmissometer.

In chapter 4 the design of a detector, to be located in the Blue Lake, is optimised using Monte Carlo techniques to simulate the detector response to relativistic muons. The design is optimised with respect to the rate of signal events registered, the signal to noise ratio and the angular resolution.

The final chapter describes *in situ* measurements taken using a custom built device to track individual muons and record the emitted Cerenkov light. This device is used to assess the feasibility of detecting muons in the Blue Lake via the resulting Cerenkov light and also to investigate the level of background light in the lake and the effect of this light on the detection of Cerenkov signals.

Acknowledgments

I would like to thank my supervisor, Dr.Roger Clay, for providing inspiration and encouragement throughout my candidature. His enthusiasm and scientific experience were greatly appreciated. I would also like to thank my unofficial supervisor, Dr.Bruce Dawson, whose guidance and scientific input were invaluable.

Thanks are due to Neville Wild for his expert advice on the technical aspects of this project, and in particular for providing most of the electronics used in the test devices. I would like to thank Gary Hill for his collaboration on this project and for many discussions on the problems encountered. Thanks also to Dr.Leon Mitchell for his generous assistance.

I am indebted to everyone who assisted on the field trips:- the staff at E&WS at Mount Gambier, Gary Hill, Bruce Dawson, Roger Clay, Rishi Meyhandan, Leon Mitchell, Jon Baxter and Bradley Gould. I am grateful to Andrew Telfer at E&WS, Adelaide, who provided considerable information on the Blue Lake. I would also like to thank the mechanical workshop staff at Adelaide University and Flinders University for constructing the test devices.

I would like to thank my fellow members of the High Energy Astrophysics Group for their suggestions and assistance. In particular, thanks are due to Andrew Smith for his expertise in retrieving data from dead lap-top computers. Thanks to Shane for his support and for proof-reading this thesis.

I would like to acknowledge the Overseas Commonwealth and Fellowship Plan, the University of Adelaide and the British Federation of University Women for their financial assistance.

Contents

Chapter 1

Introduction

1.1 Motivation for Building a High Energy Neutrino Detector

Observational astronomy is based on detecting the electromagnetic radiation, or particles in the form of cosmic rays, emitted from astrophysical sources. In the case of electromagnetic radiation, photons are electrically neutral with long lifetimes and hence can travel for large distances undeflected by electric and magnetic fields. A major limitation in photon-based astronomy is that electromagnetic radiation is absorbed and scattered by matter and hence the intensity is often significantly reduced due to interactions within the source itself and with interstellar matter. Photons produced in energetic reactions in the centre of stars are virtually all absorbed in the source and hence conventional astronomy can provide little information on processes occurring in such regions of dense matter. Except at the highest energies Cosmic rays consist mainly of charged particles which are deflected by magnetic fields and hence retain no information about the direction of the source.

Neutrinos, on the other hand are uncharged, probably massless particles which interact extremely weakly with matter. They are produced in the highest energy reactions and travel undeflected and unattenuated for large distances. For this reason, high energy neutrino astronomy is potentially a technique for observing energetic interactions occurring in regions which are inaccessible using existing telescopes.

High energy neutrinos are products of the same energetic processes which produce very high energy gamma-rays. Hence, astrophysical sources of high energy gamma-rays are also expected to be high energy neutrino sources. Observations by the Compton Gamma-Ray Observatory (CGRO) of significant fluxes of 100MeV to 10GeV gamma-rays emitted from over a dozen active galaxies (Fichtel 1994), and the detection of intense TeV gamma-rays from the giant elliptical galaxy Markarian 421 (Punch et al. 1992, Weekes 1992), indicate that these sources are expected to be significant emitters of high energy neutrinos. Intergalactic space is relatively opaque to TeV gamma-rays because of absorption by infra-red starlight acccording to the interaction $\gamma\gamma \rightarrow e^{+} + e^{-}$ (Stecker, De Jager and Salamon 1992). High energy gamma-rays will therefore be detected only from relatively close sources such as Markarian 421 at 124Mpc. As high energy neutrinos experience no such absorption, the neutrino flux from a source is expected to be greater than the gamma-ray flux. Also, distant objects which are invisible in the TeV gamma-ray region may still be strong emitters of high energy neutrinos.

A significant number of astrophysical sources such as active galactic nuclei, binary systems and supernova remnants, are expected to be high energy neutrino sources and detection of these neutrinos would provide information on the energetic processes occuring and the composition and structure of these sources. No extra-terrestrial high energy neutrinos ($E >$ 1GeV) have been observed to date. However, low energy neutrinos have been detected from the sun and from the supernova SN1987a. Using current neutrino flux calculations it is believed that existing detectors do not have sufficient collecting area to observe high energy neutrino point sources and a new generation of large area detectors is being developed specifically with this aim.

1.2 Neutrino Physics

Neutrinos are uncharged leptons which are believed to be massless. There are three families of neutrinos; the electron, muon and tau neutrinos and their respective antiparticles. Neutrinos are products of the decay of hadrons according to the following schemes:-

$$\begin{aligned}
\pi^{+/-} &\rightarrow \mu^{+/-} + \nu_\mu(\overline{\nu_\mu}) \\
\mu^{+/-} &\rightarrow e^{+/-} + \nu_e(\overline{\nu_e}) + \overline{\nu_\mu}(\nu_\mu) \\
\kappa^{+/-} &\rightarrow \mu^{+/-} + \nu_\mu\overline{(\nu_\mu)} \\
\kappa^0 &\rightarrow \mu^{+/-} + \nu_\mu(\overline{\nu_\mu}) + \pi^{-/+}
\end{aligned} \tag{1.1}$$

In order for a neutrino to be detected, it must first interact with matter. The neutrino interacts exclusively via the charged current interaction. The charged current interaction involves the exchange of a virtual charged W particle whereas the neutral current interaction is mediated via a virtual Z^0 particle. The cross-section for the charged current interaction is extremely small:- approximately $10^{-35}\mathrm{cm}^2$ for a neutrino of energy 1 TeV. For a reaction with this value of cross-section, the Earth's diameter represents about 10^{-2} of an interaction length. Hence most neutrinos pass straight through the Earth. However, if the neutrino flux is large enough, then a small but measurable proportion will interact with nuclei in the Earth producing secondary particles according to the following equations:-

$$\begin{aligned}
\nu_\mu + \text{nucleus} &\rightarrow \mu + X + \ldots \\
\nu_e + \text{nucleus} &\rightarrow e + Y + \ldots \\
\nu_\tau + \text{nucleus} &\rightarrow \tau + Z + \ldots
\end{aligned} \tag{1.2}$$

High energy neutrino astronomy is based on detecting muon-neutrinos by observing the secondary muons produced in interactions with nuclei in the Earth. This interaction is significant for high energy neutrino astronomy for several reasons:-

1. Muons have relatively large pathlengths and hence can be detected at significant distances from their production sites, thereby greatly increasing the effective volume of the detector. The ranges of relativistic muons and electrons are shown in figure 1.1 from which it can be seen that, at energies greater than a few GeV, muons travel significantly greater distances than electrons.

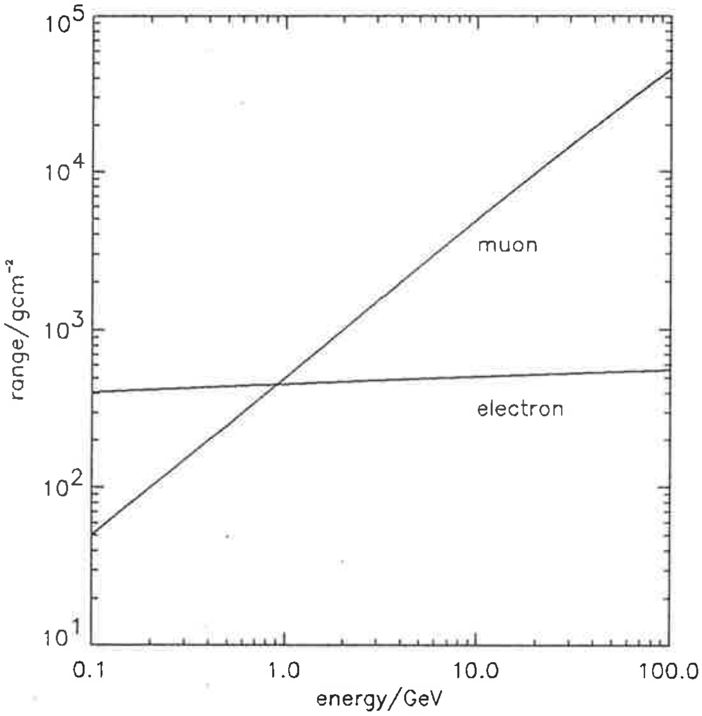

Figure 1.1: Range of electrons and muons as a function of energy

2. In order to relate detected secondary muons to neutrino point sources, the scattering angle between the parent neutrino and the resulting muon must be very small. The mean scattering angle, θ_s, as a function of neutrino energy, E_ν, is given by equation 1.3 (Berezinsky et al. 1990) and this function is shown in figure 1.2.

$$\theta_s = 2.6^\circ \sqrt{\frac{100\,GeV}{E_\nu}} \tag{1.3}$$

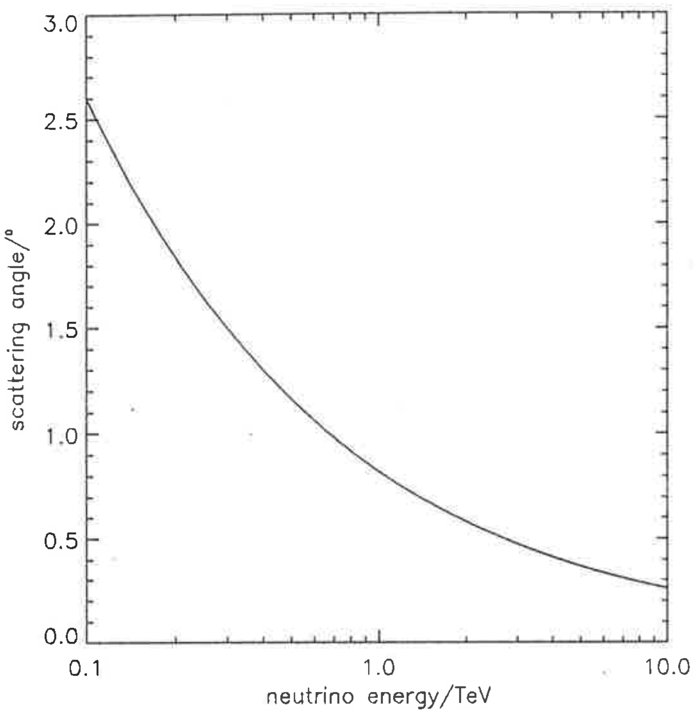

Figure 1.2: Mean scattering angle as a function of muon energy

From this figure it can be seen that for neutrino energies greater than about 1TeV the scattering angle is less than 1°. Hence high energy muons resulting from neutrinos of energy greater than about 1TeV will preserve the direction of the parent neutrino to within about 1°. The angle between the parent neutrino and resulting muon sets a limit on the angular resolution which can be achieved by a high energy neutrino detector.

1.3 Astrophysical Sources of Neutrinos

High energy neutrinos are produced when energetic protons or photons collide with matter producing pions and kaons which subsequently decay producing neutrinos as shown in figure 1.3. The first stage of neutrino production in an astrophysical source is thus the production of high energy protons and/or photons. These energetic particles then interact with a target material producing pions and kaons.

A typical neutrino source is thought to consist of a central compact object which acts as an accelerator e.g. pulsar, neutron star, black hole; and a surrounding target material such as an accretion disc, companion star, radio cocoon or 3K cosmic photons. Sources of high energy cosmic rays and gamma-rays are also expected to be sources of high energy neutrinos as neutrinos, cosmic rays and gamma-rays are all products of the decay of hadrons. Such sources must satisfy the criteria that protons are accelerated efficiently to high energies and that there is sufficient target material surrounding these protons to stop a significant proportion of them. Several types of astrophysical objects which are expected to satisfy these conditions are described in the following sections.

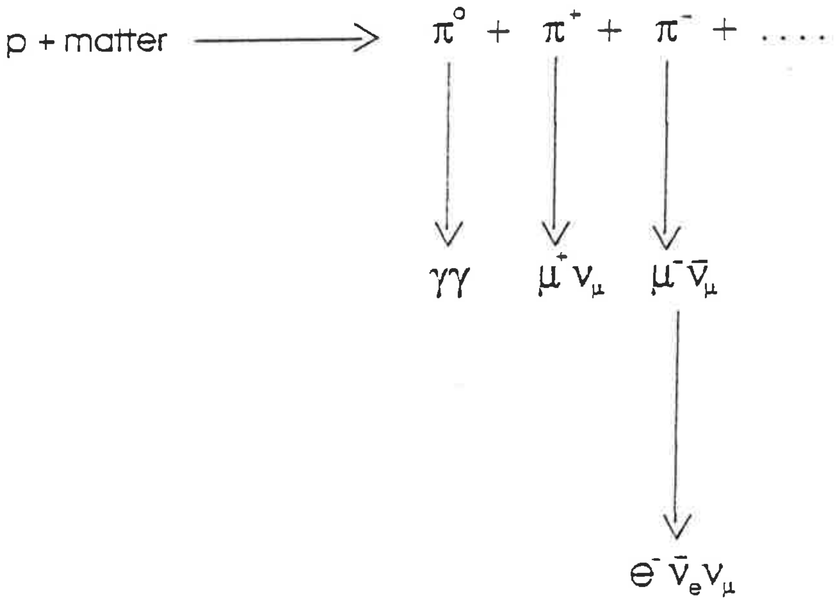

Figure 1.3: Schematic representation of neutrino production in an astrophysical source

1.3.1 Active Galactic Nuclei

The idea that active galactic nuclei may be sources of high energy neutrinos was first developed in the late 1970s (Berezinsky 1977, Silberberg and Shapiro 1979). An active galactic nucleus refers to the central region of any galaxy which exhibits energetic behaviour and encompasses a range of sources such as Seyfert galaxies, radio galaxies, quasars, blazars and BL Lacertae objects. Active galactic nuclei are the most luminous astrophysical objects and current theories predict they are the production sites of high energy particles. This prediction is supported by the fact that most of the GeV gamma-ray sources detected by CGRO are strong emitters at radio wavelengths. These radio emissions are believed to be due to synchrotron radiation from high energy electrons indicating that a mechanism for accelerating charged particles to very high energies is present.

The generally accepted model of AGNs is that of an accretion flow onto a central supermassive black hole which results in the shock acceleration of protons to high energies. This accretion model of neutrino production in AGNs is shown schematically in figure 1.4.

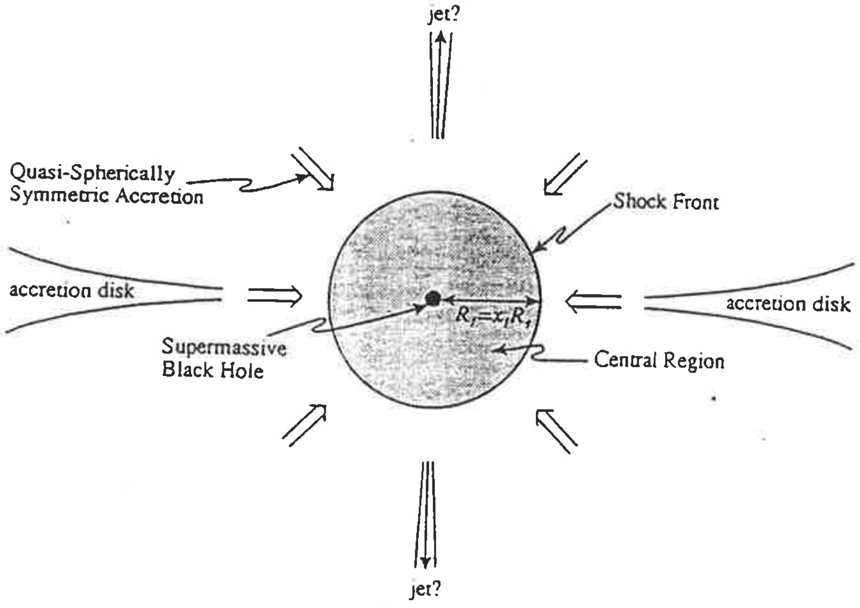

Figure 1.4: Schematic representation of accretion model of AGNs (from Szabo 1992). R_1 =shock radius, R_s =Schwarzchild radius of the black hole. At large radii, matter accretes via an accretion disc. As matter approaches the black hole, the accretion becomes quasi spherically symmetric. A shock forms at radius R_1. The volume contained by the shock is assumed to correspond to the central region of the AGN.

The high photon luminosity in the central region provides a suitable target for the accelerated protons resulting in the production of pions which subsequently decay to high energy neutrinos and gamma-rays. The neutrino flux is dependent on several parameters such as the magnetic field at the acceleration site which determines the location of the shock, and the spectrum of the target material which determines the probability of proton-photon interactions. Hence, the observation of neutrinos from AGNs could potentially yield information on the composition of AGNs and the acceleration processes occuring therein.

Several AGN models have been developed recently and the expected flux of neutrinos from individual AGNs has been calculated by several authors (Stecker et al. 1991, Protheroe and Stanev 1992, Sikora and Begelman 1992, Biermann 1992, Szabo and Protheroe 1994, Stecker and Salamon 1995, Battersby, Drolias and Quenby 1995). The predicted neutrino fluxes from individual AGNs are too low to be detected by the new generation of detectors, requiring a detector area of the order of $1km^2$ for a significant observation (Battersby, Drolias and Quenby 1995). Attention has since focussed on detecting the diffuse neutrino flux from AGNs.

The diffuse AGN neutrino flux is calculated by integrating the flux from all single AGNs. The integration must take into account the density of AGNs as a function of time, the evolution of AGN luminosity with time, the red-shift of the radiation produced and the evolution of the geometry of the universe. A detailed description of the method of calculating the diffuse neutrino flux is presented in Szabo (1992). The diffuse muon-neutrino flux as predicted by several authors is shown in figure 1.5.

Recent results from the Frejus detector (Fr~~ejus Collaboration, to be published~~ (Rhode 1995)) have set an upper limit on the upward neutrino flux of $7 \times 10^{-13}\mathrm{cm}^{-2}\mathrm{s}^{-1}\mathrm{sr}^{-1}\mathrm{GeV}^{-1}$ at a neutrino energy of 2.6GeV. This result rules out some of the predicted fluxes shown in figure 1.5, in particular the results of Szabo and Protheroe (1994) and Battersby, Drolias and Quenby (1995) for inclined shocks. However, the remaining predicted fluxes are expected to be detectable by the new generation of detectors. For example, the flux predicted by Stecker (1995) would result in an upward event rate of the order of 100 events per year at energies greater than 10^5GeV, in neutrino detectors such as DUMAND II, AMANDA and NESTOR (see chapter 2 for a detailed description of these detectors).

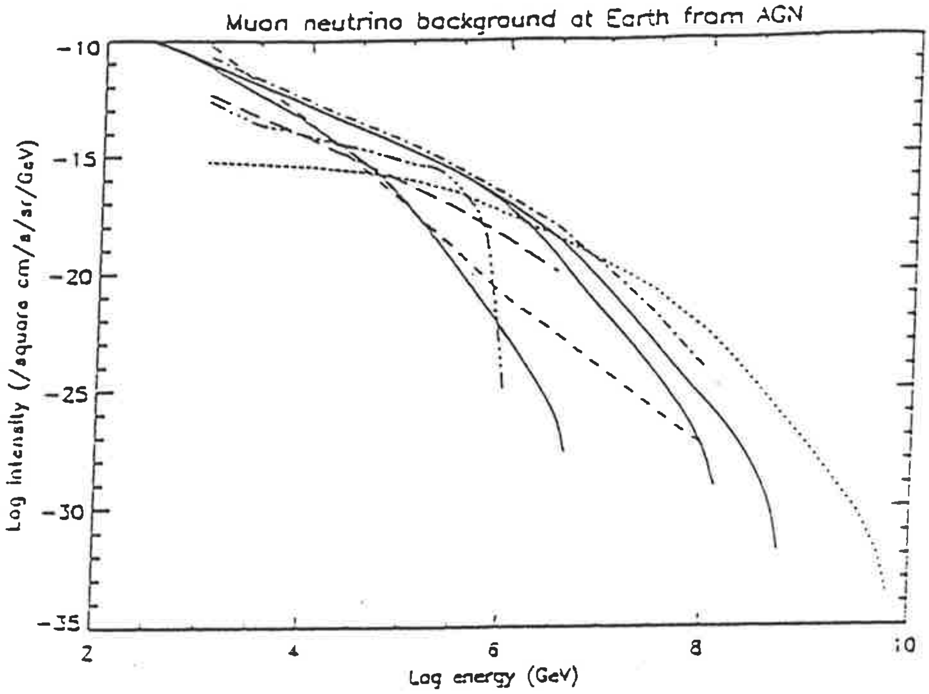

Figure 1.5: Theoretical predictions of diffuse neutrino flux from AGNs (from Battersby, Drolias and Quenby 1995). Solid lines - Battersby, Drolias and Quenby, 1995, (in order of decreasing energy:- inclined shocks, inclined shocks to x=10 [where x=shock radius/Schwarzchild radius], parallel shocks); dotted line - Stecker and Salamon, 1995; dot-dash - Szabo and Protheroe, 1994; long dashes - Biermann, 1992; dot-dot-dot-dash - Sikora and Begelmann, 1992; dashes - atmospheric background.

1.3.2 X-Ray Binaries

Interest in X-ray binary systems as sources of high energy neutrinos was initiated mainly by the apparent detection of ultra-high energy gamma-rays from Cygnus X-3 by the Kiel detector and the Haverah Park detector in the early 1980s (Samorski and Stamm 1983, Lloyd-Evans et al. 1983). Ultra-high energy gamma-ray detection was subsequently claimed for other X-ray binary systems, i.e. Vela X-1, LMC X-4 and Her X-1 (Baltrusaitis 1985, Protheroe and Clay 1985, Protheroe 1984, Raubenheimer

1987), and the observed fluxes indicated that neutrino fluxes should also be detectable from these sources. Following the apparent UHE gamma-ray detection from Cygnus X-3 in 1983, a number of UHE air shower experiments were designed to observe this flux with a higher statistical significance. However, no steady source of UHE radiation has since been observed with convincing significance. Recent results from the CASA-MIA detector have placed upper limits on the continuous gamma-ray emission from Cygnus X-3 (Borione et al. 1995). These flux limits are shown in figure 1.6 along with the flux limits set by other air shower experiments and the results claimed using the Kiel detector and Haverah Park detector in the 1980s. These results clearly shows that this source is not currently emitting high energy gamma-rays at the level apparently observed in the 1980s. A similar result was also obtained for Her X-1. This suggests that either Cygnus X-3 switched off as a high energy gamma-ray emitter at the end of the 1980s or that the gamma-ray flux observations claimed by Samorski and Stamm and Lloyd-Evans were statistical fluctuations. The probability that these results were due to random fluctuations was re-evaluated by Yodh (1992) and is of the order of 0.1 to 0.05%.

In this thesis, Cygnus X-3 has been used as an example of a high energy neutrino point source in order to calculate the predicted rate of high energy neutrinos detected by the proposed detector. As an indication of the expected neutrino flux from such a source, the predicted neutrino flux from Cygnus X-3 has been calculated based on the apparent gamma-ray flux measurements by Samorski and Stamm (1983) and Lloyd-Evans (1983). This calculation is presented in section 1.4.1 although it should be noted that the assumed high energy gamma-ray flux from th~~u~~is source certainly cannot be continuous.

X-ray binaries consist of a compact object, such as a neutron star or black hole, and a companion star. The energy source for the acceleration of particles depends on the nature of the central object. For a black hole the accretion flow from the surrounding material onto the black hole may result in shock acceleration. Neutron stars, however, have strong surface magnetic fields and spin very rapidly causing

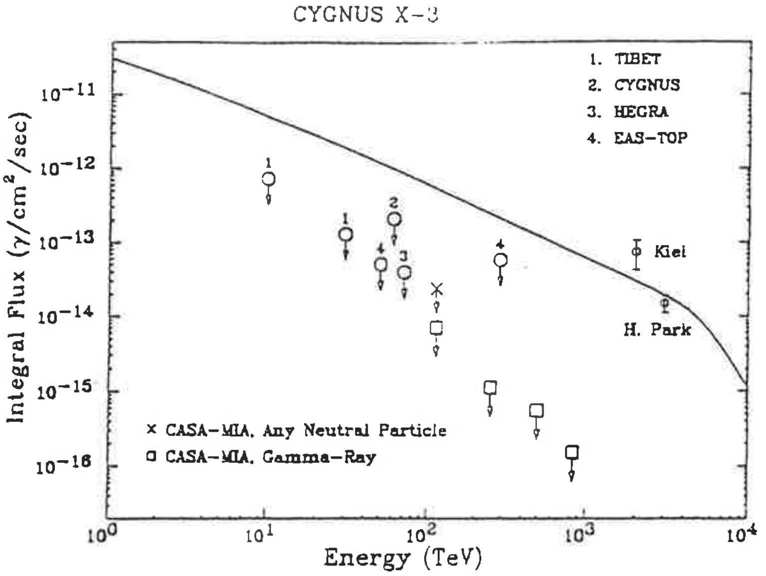

Figure 1.6: Flux limits on continuous gamma-ray emission from Cygnus X-3. Flux limits are presented for the CASA-MIA detector and other air shower experiments (Aglietta 1993, Alexandreas 1993, Amenomori 1993, Merck 1993). Also shown are claimed detections in the 1980s by the Kiel and Haverah Park experiments. The solid line is from the model of Hillas (1994) (from Borione et al. 1995)

charged particles to be accelerated through a combination of accretion flow and magnetic dipole radiation. The target material can be gas nuclei in the outer layers of the companion star, the accretion flow from the companion star onto the compact object, or stellar winds.

Several possible configurations for binary systems have been suggested based on the observed variations of X-ray flux with phase and the main models are shown in figure 1.7.

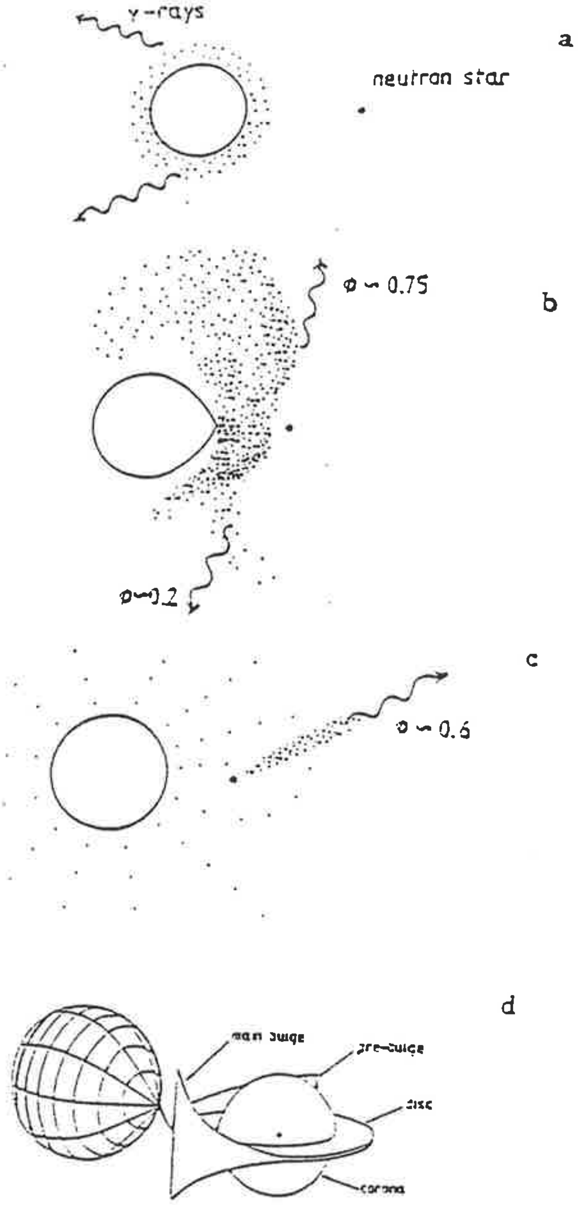

Figure 1.7: Binary system models (from Stanev 1990)

Model 'a' was proposed by Vestrand and Eichler (1982) to explain the observed X-rays from Cygnus X-3. The neutron star is assumed to be a strong emitter of X-rays which are periodically obscured from the Earth when the companion star eclipses the neutron star. According to this model, high energy neutrinos and gamma-rays would reach Earth when the accretion material lies between the neutron star and Earth, while both fluxes would be eclipsed when the companion star lies between the Earth and the neutron star. At high energies the gamma-ray absorption cross-section is independent of energy and hence the high energy gamma-ray flux should follow the source spectrum and be observed at phases of ±0.25. The neutrino cross-section is energy dependent and the predicted neutrino light curves at different neutrino energies, for Cygnus X-3, are shown in figure 1.8.

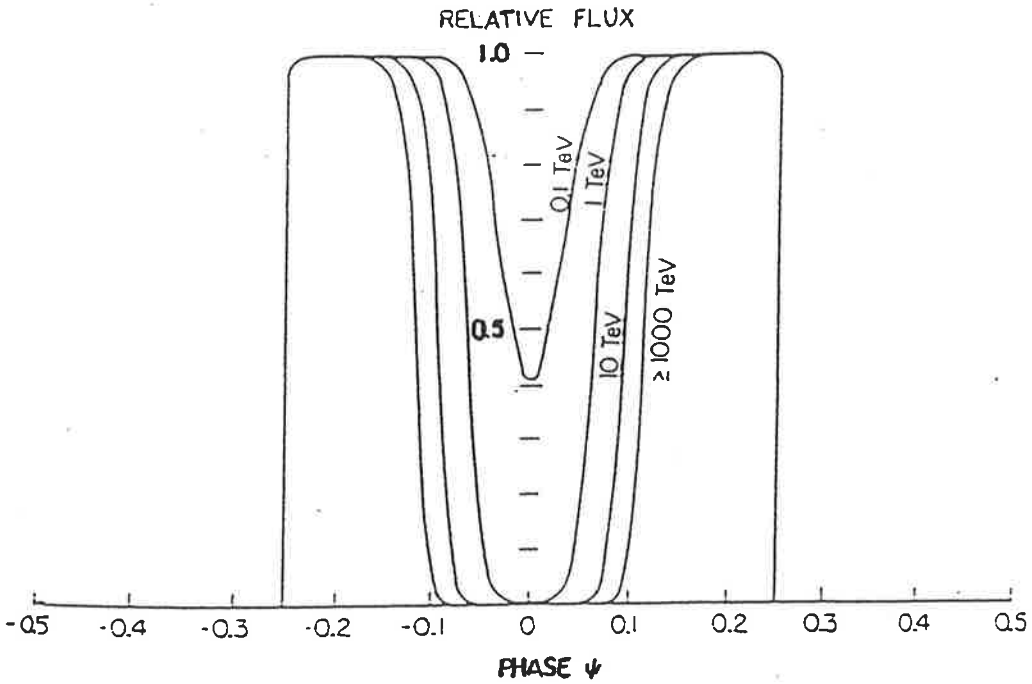

Figure 1.8: Predicted neutrino light curves for Cygnus X-3 (from Kolb, Turner and Walker 1985)

Apparent observations of the high energy gamma-ray flux from binary systems indicate that this model is too simplistic. Very high energy gamma-rays are claimed to have been observed from Her X-1 at all phases, even during the X-ray eclipse, while gamma-ray emission from Cygnus X-3 has apparently been detected at a range of phases and never in the symmetrical pattern implied by the light curves in figure 1.8. Models 'b' and 'c', suggested by Hillas (1984), assume that the accretion material forms into clouds due to gravitational forces. Neutrinos are formed when high energy protons interact with the accretion wake or tail streaming behind the neutron star. Model 'd' was proposed by White and Holt (1982). In this model the accretion disc forms with bulges on the rim which obscure the X-ray and infra-red emissions and provide targets for the production of high energy gamma-rays and neutrinos.

1.3.3 Supernova Remnants

A supernova is the explosive disruption of a star. A huge amount of energy is released in this process:- up to 10^{46}J, and the visible light produced during the first few minutes is comparable to the total light emitted by an entire galaxy. This visible light represents less than 1% of the total energy radiated with the majority of the energy being carried away by neutrinos. Kinetic energy is manifested by fragments of the original star which are ejected from the explosion site at high velocity and then form the supernova remnant. Supernova remnants can remain visible for up to 10^5 years and are some of the brightest astrophysical sources in the radio, X-ray and gamma-ray regions.

Supernovae are classified into two main types based on the optical spectral properties exhibited close to maximum light production. The spectra from type I supernovae show no evidence of hydrogen which indicates that the hydrogen envelope of the progenitor star is lost before the explosion occurs. Current models for type I supernovae are the deflagration of accreting carbon and oxygen white dwarfs (type Ia) and the explosion of Wolf-Rayet and helium stars (types Ib and Ic). A detailed description of type I supernovae is presented in Wheeler and Harkness (1990).

Type II supernovae result from short-lived stars, usually found in the spiral arms of spiral galaxies, which undergo gravitational collapse leaving behind a neutron star, black hole or pulsar in the centre of an expanding supernova remnant. The production of high energy neutrinos is expected in type II supernovae as a result of the central power source accelerating charged particles to high energies which then interact with the expanding supernova shell to form charged pions. A comprehensive description of the processes involved in a type II supernova explosion can be found in Woosley and Weaver (1986) and Koshiba (1992).

Type II supernovae occur in massive stars (8-40 times the mass of the sun) which are comparatively short-lived due to their high luminosity and high rate of energy release. When all the elements in such a star have been burnt to form an iron core, the gravitational force exceeds the outward thermal pressure and the core starts to collapse. When the core density starts to exceed the nuclear density, the repulsive component of the strong nuclear force halts the collapse. At this point about half of the core stops while the other half collapses in at supersonic speed and rebounds off the inner compressed core, resulting in a shock wave. If the shock has enough energy it exits the core which is now becoming a neutron star. If no other processes occur the shock will have lost all its kinetic energy by the time it reaches the outer layers of the core. Some explosion mechanism must therefore occur which sustains the shock. One generally accepted model is that the binding energy released when the neutron-rich compressed core forms a neutron star is radiated away in the form of electron neutrinos. If a small percentage of this energy is deposited at the edge of the core an explosion can occur which would eject the outer layers of the star. At this stage neutrino and anti-neutrino pairs of all three flavours are thermally generated, although the mean energy of neutrinos produced in the first stages of the explosion is significantly lower than the proposed threshold energies of high energy neutrino detectors. The mean energies of electrons, anti-electrons and muon neutrinos in the first half second of a supernova explosion are shown in figure 1.9.

The shock wave then moves through the rest of the star taking about 1 minute to exit the helium shell and 2 hours to one day to pass through the hydrogen envelope. As the shock wave exits the source, the star surface is heated to very high

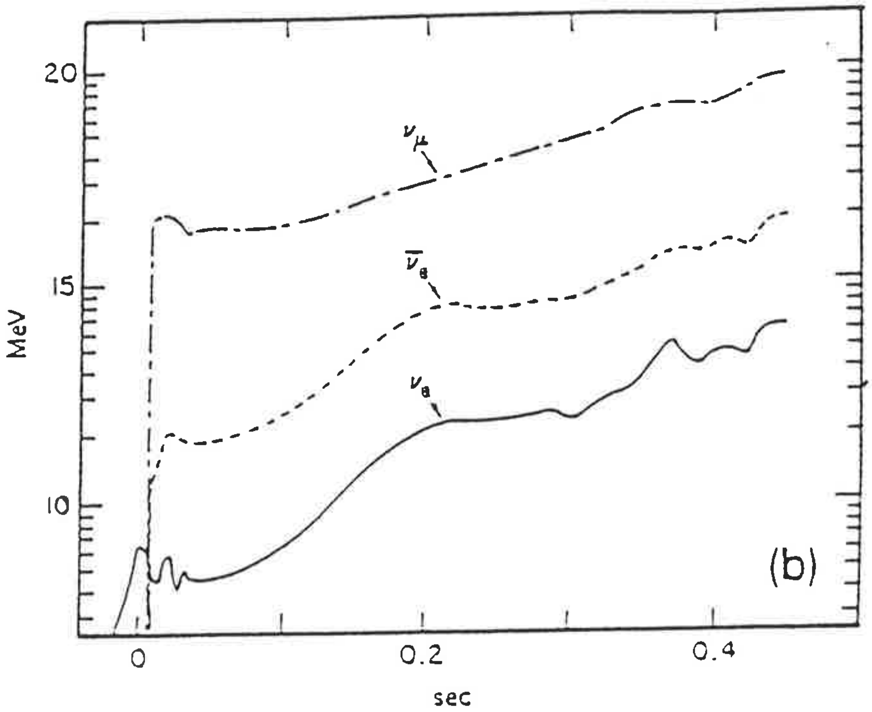

Figure 1.9: Mean neutrino energies at the start of a supernova explosion (from Koshiba 1992)

temperatures and the supernova becomes optically visible. The system then consisits of a central neutron star surrounded by an expanding remnant providing conditions suitable for the production of high energy muon-neutrinos.

Current theories on the mechanisms involved in a supernova explosion were supported by the observation of low energy electron-neutrinos from SN1987a (Bionta et al. 1987, Hirata et al. 1987). This burst of neutrinos corresponds well with the model of the gravitational collapse of the iron core of a large star to form a neutron star, while photographs of the supernova region taken before the explosion have identified the progenitor star as having a mass 20 times the mass of the sun. This is within the mass range required for gravitational collapse.

High energy neutrinos are expected to be produced as a result of accelerated particles interacting with the expanding supernova shell. The resulting high energy neutrino induced upward muon flux from a supernova depends on several factors such as the source luminosity, the distance to the supernova and the assumed power law spectrum of the accelerated protons. This flux has been calculated by Gaisser and Stanev (1987) for a supernova at the same distance from Earth as SN1987a (50kpc) and is given by equation 1.4.

$$N_\mu = \frac{L_{cr}}{(10^{36} J/s)} \tag{1.4}$$

where L_{cr} = cosmic ray luminosity

N_μ = muon rate /100m^2/week

Consider a high energy neutrino detector of area 10^4m^2 observing a supernova at a distance of 50kpc. If the cosmic ray luminosity is greater than a few times 10^{33}J/s then a TeV neutrino signal of tens of events per year would be observed for the first few years after the explosion. SN1987a is not expected to be observed in the high energy neutrino region as an upper limit on the total pulsar luminosity of this source has been set at a few times 10^{31} J/s (Pennypacker et al. 1989). However, SN1987a is quite a distant source being located in the Large Magellenic Cloud. A supernova of this order of luminosity occurring within our galaxy may be detectable but the expected rate of such supernova explosions is only about 1 every 30 years.

1.4 Expected Fluxes of Neutrinos

We expect the detectable neutrino signal from sources to be small due to the extremely low value of the charged current cross-section. Hence, in assessing the minimum size of detector required to observe high energy neutrinos it is important to know the expected flux from possible neutrino sources. There are two approaches to calculating the neutrino flux. The first uses the fact that gamma-rays and neutrinos are produced as a result of the same high energy processes and hence the neutrino flux can be calculated from the observed gamma-ray flux. The second method is based on relating the source luminosity to the high energy interactions resulting in the production of high energy neutrinos. An example of a neutrino flux calculation using each method is presented.

1.4.1 Scaling from High Energy Gamma Rays

The following analysis of a neutrino flux as determined by scaling from a measured gamma-ray flux is based on Kolb, Turner and Walker (1985). Observed sources of high energy gamma-rays are also expected to be sources of high energy neutrinos as a result of the fact that both gamma-rays and neutrinos are products of the decay of pions as shown in figure 1.3. Hence, the neutrino spectrum will be related to the observed high energy gamma-ray spectrum. Assuming that the gamma-rays have a spectrum of the form:-

$$\frac{dS_\gamma}{dE_\gamma} = aE^{-\alpha} \tag{1.5}$$

and using the approximation that each π^0 produces two gamma-rays, each of energy $E_{\pi^0}/2$, then the spectrum of charged pions will then be given by equation 1.$\overset{6}{7}$.

$$\frac{dS_{\pi^0}}{dE_{\pi^0}} = a2^{\alpha-1}E^{-\alpha} \tag{1.6}$$

As charged pions are produced twice as often as neutral pions, the spectrum of charged pions is therefore given by equation 1.7.

$$\frac{dS_{\pi^\pm}}{dE_{\pi^\pm}} = 2\frac{dS_{\pi^0}}{dE_{\pi^0}} \tag{1.7}$$

A charged pion which decays in flight produces a neutrino, the energy of which is given by:-

$$E_\nu = E_\pi \frac{(1 - \frac{{m_\mu}^2}{m_\pi^2})}{2} \tag{1.8}$$

The neutrino source spectrum can therefore be represented by equation 1.9.

$$\frac{dS_\nu}{dE_\nu} = (1 - \frac{m_\mu^2}{m_\pi^2})^\alpha \frac{dS_\gamma}{dE_\gamma} \tag{1.9}$$

To calculate the neutrino spectrum at Earth we need to consider the propagation of neutrinos through the source target material. As an example, Cygnus X-3 is considered using the binary star model 'a' shown in figure 1.7. Neutrinos and gamma-rays are both absorbed in the companion star but, as gamma-rays are virtually totally absorbed in dense matter, they are only observed at Earth when the line of sight to the accelerator source just grazes the companion star. For Cygnus X-3 these points correspond to a small range of phases centred on ±0.25. Neutrinos, however, are not strongly absorbed in the companion star and the fraction of a period for which neutrinos are observed is correspondingly higher. Hence the neutrino flux at Earth is enhanced relative to the gamma-ray flux by a factor equal to $\frac{d\Psi_\nu}{d\Psi_\gamma}$, where $d\Psi_\gamma$ is the fraction of a cycle for which gamma-rays reach Earth and $d\Psi_\nu$ is the fraction of a cycle for which neutrinos reach Earth. The spectrum of neutrinos reaching Earth can now be expressed in terms of the measured gamma-ray spectrum at Earth according to equation 1.10.

$$\frac{dN_\nu}{dE_\nu} = (1 - \frac{{m_\mu}^2}{{m_\pi}^2})^{2.1} \frac{d\Psi_\nu}{d\Psi_\gamma}\frac{dN_\gamma}{dE_\gamma} \tag{1.10}$$

where $\frac{\mathrm{dN}_\nu}{\mathrm{dE}_\nu}$ = differential neutrino flux

$\frac{dN_\gamma}{dE_\gamma}$ = differential gamma – ray flux

m_μ = muon mass

m_π = pion mass

$\frac{d\Psi_\nu}{d\Psi_\gamma}$ = neutrino : gamma – ray enhancement factor

If we assume that gamma-rays from Cygnus X-3 are observable for a total phase of 0.05 and that neutrinos are observed for a total phase of 0.4, then the neutrino flux at Earth, based on the apparent gamma-ray flux measurements presented in Lloyd-Evans et al. (1983) and Samorski and Stamm (1983), is given by:-

$$\frac{dS_\nu}{dE_\nu} = 4.10^{-10}E^{-2.1}\mathrm{cm}^{-2}\mathrm{s}^{-1} \tag{1.11}$$

The possible error on this predicted neutrino flux is very large for several reasons. Firstly, the neutrino flux depends on the value of the neutrino:gamma-ray enhancement factor assumed. This factor can vary by as much as a factor of 10 depending on the binary system model used. Secondly, the assumed gamma-ray flux from Cygnus X-3, as determined by the Kiel and Haverah Park detectors, has not since been observed at these levels.

1.4.2 Neutrino Flux Calculated from Source Luminosity

The second method of calculating the neutrino flux is generally applied to active galactic nuclei and is described in detail in Szabo (1992). This approach is based on relating the measured luminosity of the source to the processes occuring in the AGN which produce high energy neutrinos. This information is contained in the differential luminosity factor which depends on the rate at which protons are injected into the accelerator and the differential neutrino spectrum resulting from interactions between accelerated protons and the target material. The differential neutrino luminosity can be expressed by equation 1.12.

$$\frac{dL_\nu}{dE_\nu}(E_\nu, L_c) = R_p^{inj}(E_{max})E_\nu \frac{dn_\nu}{dE_\nu}(E_\nu, E_{max}) \tag{1.12}$$

where $\frac{\mathrm{dL}_\nu}{\mathrm{dE}_\nu}$ = differential neutrino luminosity

E_ν = neutrino energy

L_c = infrared to X − ray continuum luminosity

R_p^{inj} = rate of proton injection into accelerator

E_{max} = maximum proton energy

$\frac{dn_\nu}{dE_\nu}$ = differential neutrino spectrum per injected proton

The continuum spectrum observed from the infra-red to the X-ray regions is thought to be due to the cascading of electrons, positrons and gamma-rays produced during and after acceleration. If the assumption is made that all of the energy channelled into these particles results in the continuum spectrum then the rate of proton injection can be related to the observed luminosity according to equation 1.13.

$$R_p^{inj}(E_{max}) = \frac{L_c}{W_{e\gamma}(E_{max})} \tag{1.13}$$

In this expression, $W_{e\gamma}$ is the energy per proton injected which goes into $e^{\pm}$ and γ production.

The differential neutrino flux reaching Earth from a neutrino source at redshift, z, can be expressed in terms of the differential neutrino luminosity and the luminosity distance to the source (d_l) according to equation 1.14 (Rowan-Robinson 1985).

$$\frac{dN_\nu}{dE_\nu} = \frac{(1+z)}{4\pi E_\nu {d_l}^2} \frac{dL_\nu}{dE_\nu}(E_\nu(1+z)) \tag{1.14}$$

$$\begin{aligned} \text{where } \frac{\mathrm{dN}_\nu}{\mathrm{dE}_\nu} &= \text{differential neutrino flux at Earth} \\ \frac{dL_\nu}{dE_\nu} &= \text{differential neutrino luminosity} \\ d_l &= R_0^2 r^2 (1+z)^2 \\ R_0 &= \text{scale factor of the universe} \\ r &= \mathrm{co-moving\ radial\ coordinate} \end{aligned}$$

The neutrino flux at Earth can therefore be calculated from equation 1.14 using the measured luminosity of the source and the known distance to the source.

1.4.3 Flux of Upward Muons at a Detector

A muon-neutrino which passes through the Earth will result in an upward travelling muon at a detector if the neutrino interacts with a nucleus and the resulting muon reaches the detector without being absorbed. Hence the muon flux at a detector depends on three factors:- the flux of parent neutrinos, the probability that a neutrino will interact to produce a muon, and the range of the resulting muon in rock. This muon flux is given by equation 1.15 (Gaisser and Grillo 1987).

$$S(> E_\nu) = \int_{E_\mu}^{\infty} P(E_\nu, E_\mu) \frac{dN_\nu}{dE_\nu} dE_\nu \tag{1.15}$$

The term dN_ν/dE_ν is the parent neutrino spectrum and $P(E_\nu, E_\mu)$ is the convolution of the charged current cross-section and the range-energy relationship of muons in rock. This term represents the probability that a neutrino of energy E_ν produces a muon which reaches the detector with an energy greater than E_μ. The term $P(E_\nu, E_\mu)$ is independent of the parent neutrino spectrum. Hence, once this factor is determined as a function of energy, the upward muon flux for any neutrino energy is given by the product of $P(E_\nu, E_\mu)$ and the neutrino flux at that energy.

$P(E_\nu, E_\mu)$ can be represented by equation 1.16.

$$P(E_\nu, E_\mu) = \int_{E_\mu}^{E_\nu} dE_\mu \int_{E_\mu}^{E_\nu} dE'_\mu \frac{d\sigma}{dE'_\mu} N_A \int_0^\infty dX \; g(X, E_\mu, E'_\mu) \tag{1.16}$$

Here, N_A is Avogadro's number, $d\sigma/dE$ is the differential charged current cross-section and g is the probability that a muon with energy E'_μ has a final energy in the range E_μ to $E_\mu + dE_\mu$ after passing through a thickness X. By substituting analytical expressions for the charged current cross-section and the range-energy dependence of muons in rock, the value of P as a function of neutrino energy can be determined.

1.4.3.1 Charged Current Cross-Section

One of the uncertainties in calculations of upward muons at neutrino detectors arises from assumptions made about the charged current interaction between neutrinos and nucleons at high energies. For neutrino energies greater than about $10^5 GeV$ the charged current cross-section is highly dependent on the nuclear model assumed and variations in this factor can lead to significant differences in the predicted fluxes of high energy neutrino-induced muons. The charged current cross-sections for two different nuclear models are compared in figure 1.10.

1.4.3.2 Range of Muons in Rock

When muons pass through matter they lose energy through a range of processes. Energy is continuously emitted due to ionisation of the medium. For relativistic

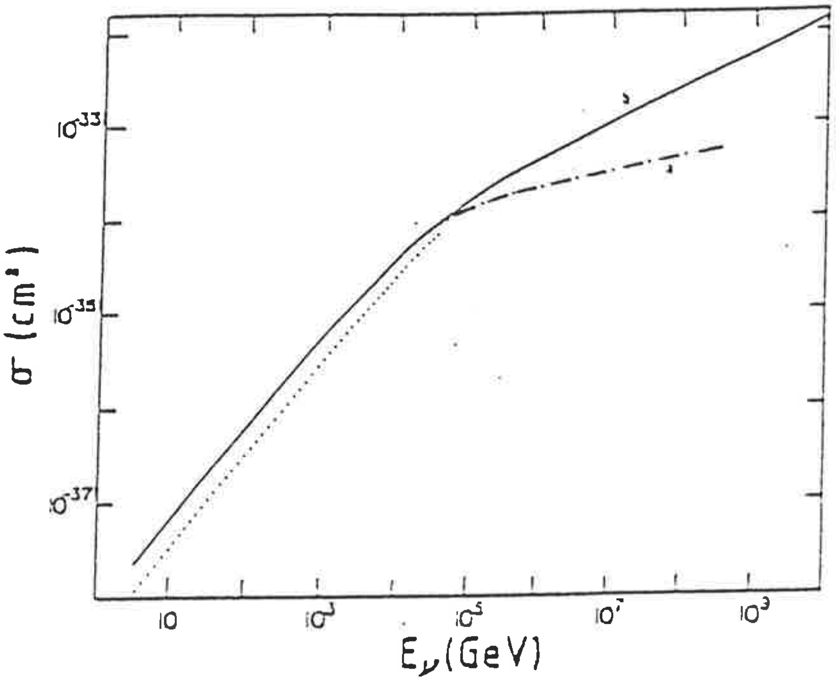

Figure 1.10: Charged current cross-section as a function of neutrino energy for different nuclear models (from Gaisser and Grillo 1987)

particles, this energy loss can be approximated by $dE/dx = -\alpha$ where $\alpha = 2\text{MeV/gcm}^{-2}$. Muons also lose energy via discrete processes such as bremsstrahlung, electromagnetic interactions with nuclei and pair production. These processes are significant only for high energy muons and on average the rate of energy loss by these processes is proportional to muon energy. The total energy loss of a relativistic muon can therefore be expressed by equation 1.17.

$$-\frac{dE}{dx} = \alpha + \beta E \qquad (1.17)$$

where $\beta = \beta_b + \beta_p + \beta_n$

β_b = bremsstrahlung coefficient/g^{-1}cm^2

β_n = coefficient for em interactions with nuclei/g^{-1}cm^2

β_p = pair production coefficient/g^{-1}cm^2

x = pathlength/gcm^{-2}

E = energy/MeV

$$\alpha = 2\mathrm{MeV/gcm^{-2}}$$

Hence the mean range of a relativistic muon in rock is given by:-

$$R = \frac{1}{\beta} ln(1 + \frac{\beta}{\alpha} E_i) \tag{1.18}$$

$$\begin{aligned} \text{where } \mathrm{E_i} &= \text{initial energy/MeV} \\ R &= \mathrm{range/gcm^{-2}} \end{aligned}$$

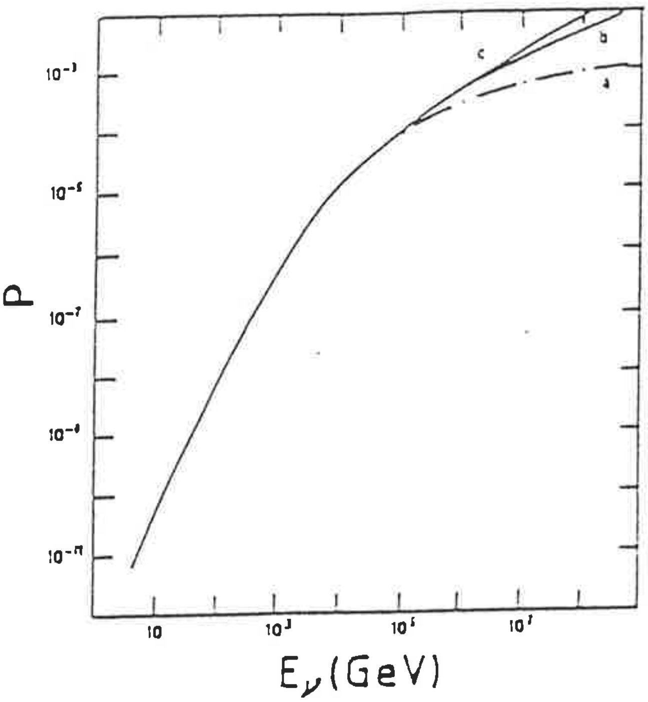

Figure 1.11: $P(E_\nu)$ as a function of neutrino energy for different nuclear structure models and for a minimum muon energy threshold of 2 GeV (from Gaisser and Grillo 1987)

From the values of charged current cross-section shown in figure 1.10 and the range of muons in rock given by equation 1.18 the value of $P(E_\nu, E_\mu)$ can be determined according to equation 1.16. The variation of this parameter with neutrino energy is shown in figure 1.11 for several nuclear structure models and for a minimum muon energy threshold of 2 GeV. The total predicted upward muon flux above 2 GeV, from a known neutrino spectrum, can then be found by convolving the neutrino spectrum with the factor $P(E_\nu)$.

To determine the energy spectrum of upward muons at a detector the integral in equation 1.19 is evaluated.

$$S = \int_{E_\mu}^{\infty} \frac{dP(E_\nu, E_\mu)}{dE_\mu} \frac{dN_\nu}{dE_\nu} dE_\nu \tag{1.19}$$

The expected relative upward muon spectra resulting from neutrino spectra with differential indices of 2.1 and 2.8 are shown in figure 1.12.

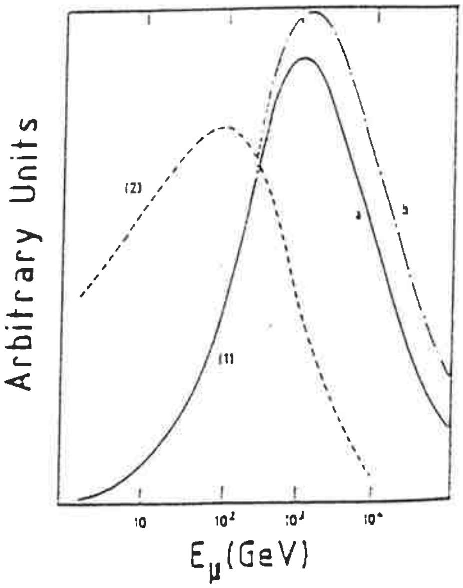

Figure 1.12: Number of upward muons, in arbitrary linear units, as a function of log of muon energy, for various neutrino source spectra (from Gaisser and Grillo 1987). The neutrino source spectra are of the form $\frac{dN}{dE} \propto E^{-\alpha}$. In plot(1) α =2.1, in plot(2) α =2.8, plots a and b represent 2 different nuclear structure models

A differential index of 2.1 corresponds to the spectrum from Cygnus X-3 and a differential index of 2.8 corresponds to that of atmospheric neutrinos. From this figure it can be seen that increasing the minimum energy threshold of a neutrino detector will increase the rate of neutrinos detected from sources such as Cygnus X-3 relative to the rate of atmospheric neutrinos detected.

The expected flux of upward muons from specific sources can vary considerably due to the fact that the assumed source neutrino spectrum is very model dependent and the charged-current interaction at high energies is not well known. As an example of how to determine the upward muon flux from a high energy neutrino source a calculation of the expected muon flux from Cygnus X-3 is presented.

1.4.4 Upward Muon Flux from Cygnus X-3

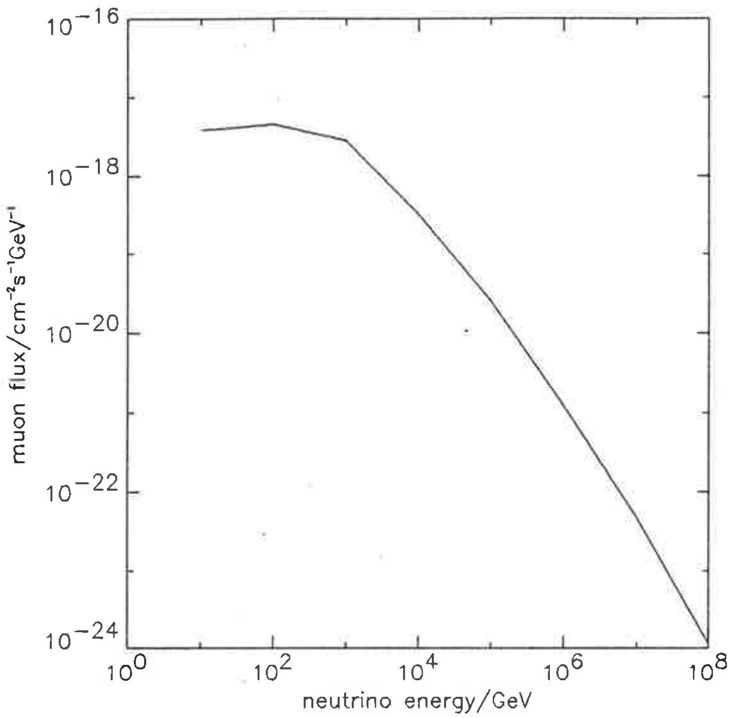

Figure 1.13: Upward muon flux from Cygnus X-3 as a function of neutrino energy, for a minimum muon energy threshold of 2GeV

The predicted neutrino spectrum from Cygnus X-3, based on the apparent gamma-ray flux measured by Samorski and Stamm (1983) and Lloyd-Evans et al. (1983), is given by equation 1.10. Assuming function 'c' in figure 1.11 as an upper limit for the parameter $P(E_\nu, E_\mu)$, the resulting upward muon flux as a function of neutrino energy is shown in figure 1.13. From these results, the expected flux of upward muons resulting from neutrinos from Cygnus X-3 is 2.3×10^{-15}cm^{-2}s^{-1}. This muon flux is an upper limit as it assumes that Cygnus X-3 is always within the viewing aperture of the detector and also that the attenuation of neutrinos in the Earth is negligible. This attenuation becomes significant at higher energies as the charged current cross-section increases, such that at neutrino energies greater than 10^{15}eV the Earth is virtually opaque to neutrinos (Reno and Quigg 1988). Considering these factors, it is uncertain whether this source would be observable above the flux of upwards muons resulting from atmospheric neutrinos in any of the proposed detectors.

The actual signal recorded in a neutrino detector depends on the upward muon flux at the detector, the fraction of time the astrophysical source is within the detector aperture (the duty factor) and the efficiency with which the detector records upward muon events (the effective area). The effective area of a neutrino detector is dependent on factors such as the detector geometry, the transmission of Cerenkov light through the detector medium and the triggering conditions which must be satisfied in order that an event is recorded. In chapter 4, the effective area of a proposed high energy neutrino detector is determined as a function of these factors. The aim of this is to calculate the expected rate of upward muons recorded from a neutrino source such as Cygnus X-3 and hence determine if the proposed detector will observe high energy neutrinos from point sources above the background noise.

Chapter 2

Review of Neutrino Detectors

2.1 Principles of Neutrino Detection

High energy neutrinos can be detected by observing the muons resulting from charged current interactions with nuclei in the earth. The cross-section for this reaction is extremely small, but if the neutrino flux is large, a significant number of neutrinos will produce muons as they pass through the earth. In the case of high energy neutrinos, the resulting muons will be highly relativistic and will produce Cerenkov radiation when they pass through a dielectric medium. Such muons can therefore be detected either by using a particle detector such as a scintillator counter, or by observing the Cerenkov radiation produced when they pass through a dielectric medium such as ice or water. The detection of high energy neutrinos via the secondary muons produced in the earth is shown schematically in figure 2.1.

The method of detecting muons directly using a particle detector is of limited use in high energy neutrino astronomy as the muon flux is so low that the area which would have to be instrumented is unfeasibly large. The method of detecting Cerenkov radiation produced by high energy muons has the advantage that this radiation can be detected at significant distances from the muon track, thus greatly reducing the amount of instrumentation required compared to a particle detector.

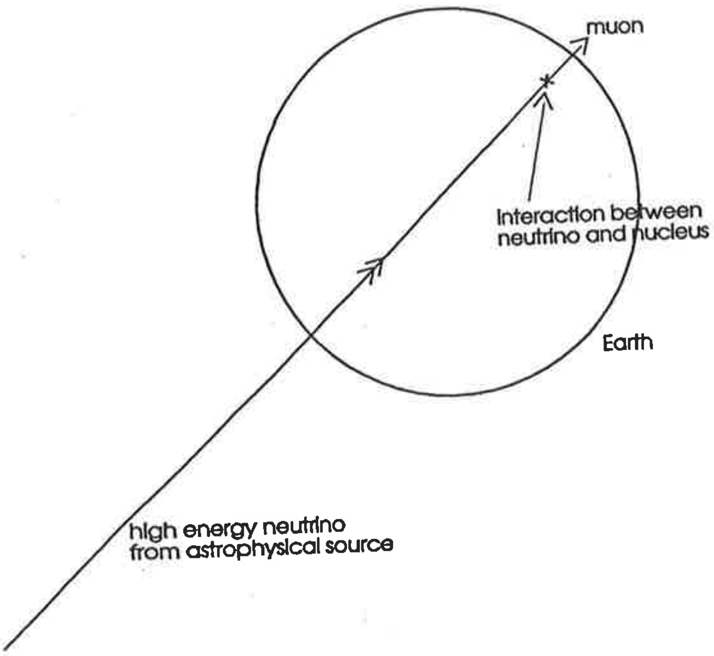

Figure 2.1: Schematic view of high energy neutrino detection

2.2 Cerenkov Radiation

When a charged particle passes through a dielectric medium, atoms along the particle trajectory are polarised, resulting in the emission of radiation. If the particle is travelling relatively slowly, this radiation is not observed due to destructive interference between emission centres. However, if the particle is travelling faster than the phase velocity of light in the medium, the wavelets from all emission sites along the particle track interefere constructively as shown in figure 2.2. In this figure, the phase of wavelets along the line BC is constant and hence coherent radiation (Cerenkov radiation) is observed emitted at an angle, θ, relative to the particle track. The condition for coherence along the line BC is that the time taken for light to travel from A to C must be the same as the time taken for the particle to travel from A to B. Hence, the angle, θ, is defined by equation 2.1.

$$cos(\theta) = \frac{1}{\beta n} \tag{2.1}$$

$$\text{where } \beta = v/c$$

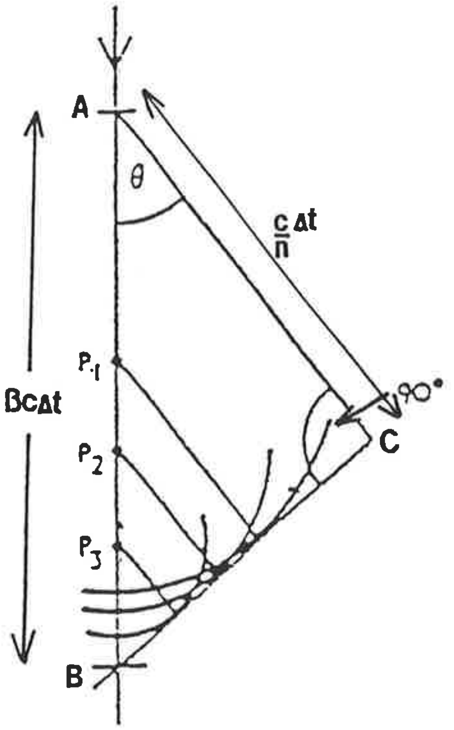

Figure 2.2: Production of Cerenkov radiation

v = particle velocity

c = speed of light

n = refractive index

For highly relativistic particles ($\beta = 1$) the emission angle is equal to $cos^{-1}(1/n)$. The radiation is therefore emitted as a forward travelling cone of semi-angle, θ, as shown in figure 2.3.

The total energy radiated per unit path length of muon track is given by equation 2.2 (Frank and Tamm 1937).

$$\frac{dE}{dl} = 4\pi^2 Z^2 e^2 \int_{\beta n>1} (1 - \frac{1}{\beta^2 n^2}) \frac{d\lambda}{\lambda^3} \tag{2.2}$$

where $\frac{\mathrm{dE}}{\mathrm{dl}}$ = energy radiated per unit path length/Jm^{-1}

Ze = charge/Coulombs

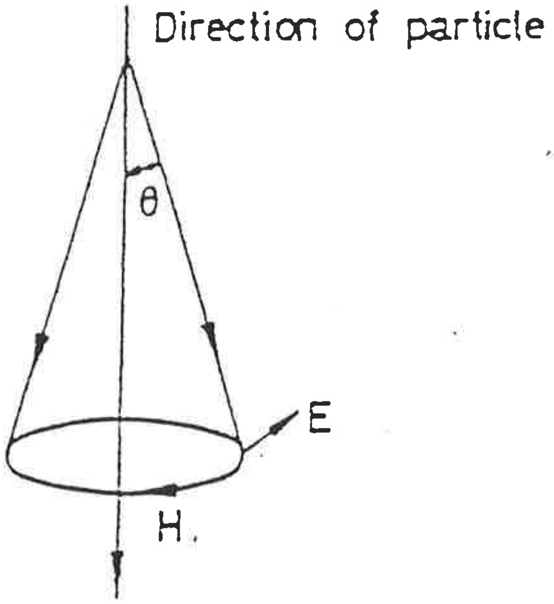

Figure 2.3: Emission cone of Cerenkov radiation for a relativistic particle. E and H are the electric and magnetic field vectors respectively

λ = wavelength/m

β, n = as defined in equation 2.1

Hence, for a relativistic muon, the total number of photons emitted along a track length, l, within a specific wavelength range, is given by equation 2.3.

$$N = 2\pi\alpha\, l\, (\frac{1}{\lambda_1} - \frac{1}{\lambda_2})\, sin^2\theta_c \qquad (2.3)$$

where N = number of photons

α = fine structure constant

θ_c = Cerenkov angle of emission

l = track length/m

λ_1 = minimum wavelength/m

λ_2 = maximum wavelength/m

The number of photons emitted per wavelength interval varies as $1/\lambda^2$ and hence the intensity of Cerenkov radiation increases rapidly towards the blue end of the spectrum.

2.3 Principles of Neutrino Detector Design

The new generation of high energy neutrino detectors is based on detecting the Cerenkov radiation from muons travelling upward through the earth and passing through water or ice. This radiation can be detected effectively by placing conventional photomultiplier tubes in the water or ice. A typical high energy neutrino detector would therefore consist of an array of downward looking photomultiplier tubes submerged in a body of water or ice. The angle of emission of Cerenkov light in water is 41.2° and in ice is 40.2°. Hence, Cerenkov light from an upward muon in water illuminates the photomultiplier tubes as shown in figure 2.4.

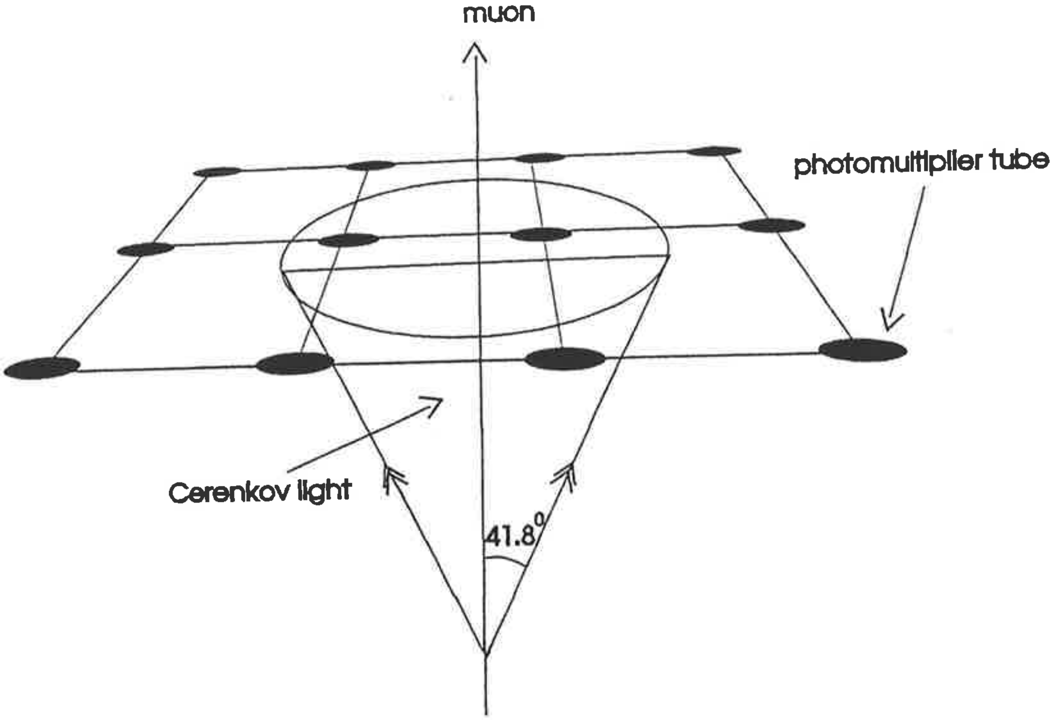

Figure 2.4: Schematic view of illumination of photomultiplier tubes by Cerenkov light from an upward travelling muon in water

The number of photomultiplier tubes which register a signal due to Cerenkov light depends on the amount of light transmitted through the water and the size and spectral response of the photomultiplier tubes used. The timing sequence in which the photomultiplier tubes register Cerenkov light is dependent on the direction of the muon. Hence the muon track can be determined from the relative times at which signals are recorded by each photomuliplier tube. A minimum number of three non-colinear photomultiplier tubes is required to reconstruct the muon trajectory. If more than 3 tubes register signals, the accuracy with which the muon direction is determined increases.

The main source of noise in such a detector results from the large flux of downward muons produced in the atmosphere by cosmic rays. To reduce this noise, high energy neutrino detectors require some degree of shielding from the atmospheric muon flux. This can be achieved by locating the detector under a depth of water or rock. In detectors with a low amount of shielding, many background muons still reach the detector and have to be discriminated from the upward travelling neutrino-induced muons. A simple example of an array geometry which enables discrimination between upward and downward travelling muons consists of two vertically separated layers of photomultiplier tubes as shown in figure 2.5.

Cerenkov light from upward travelling muons will be registered first by photomultiplier tubes in the lower layer and then by photomultiplier tubes in the upper layer. For the case of downward muons, the timing sequence in which the two layers are triggered will be reversed. Hence, a significant number of downward muon events can be eliminated by considering the relative times at which the two layers register Cerenkov light. In practice more complex up-down discrimination techniques are necessary to achieve the required signal to noise ratio and this aspect is addressed in chapter 4.

For a high energy neutrino detector to observe neutrinos from astrophysical point sources, the following criteria must be satisfied.

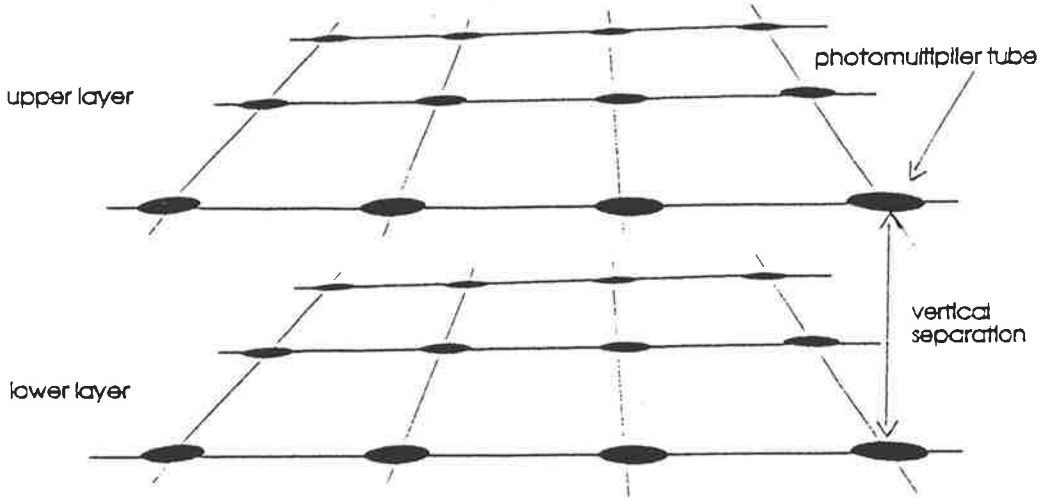

Figure 2.5: Geometry for discrimination between upward and downward travelling muons

1. The detector must be able to discriminate between the signal and the high flux of background events.

2. The angular resolution should be as high as possible in order to identify point sources and minimise the noise detected. The angular resolution which can be achieved is limited by the kinematics of the charged current interaction. For neutrino energies greater than about 1 TeV the maximum scattering angle between the neutrino and the resulting muon is about 1°. Hence, ideally, the angular resolution of a high energy neutrino detector should be of the order of 1°. The angular resolution increases with the number of photomultiplier tubes registering signals. Hence, in order that a sufficient number of tubes register Cerenkov light, the detector medium must exhibit a high transmission for Cerenkov radiation.

3. The effective area of the detector must be large enough to detect a reasonable rate of events from the low flux of upward muons. Current calculations of expected muon events from extraterrestrial neutrinos predict that the effective

area of a detector must be at least $10^4 m^2$ in order to detect tens of events in a year.

Several detector designs have been proposed which satisfy the above criteria, four of which (DUMAND, BAIKAL, AMANDA and NESTOR) are currently under construction. In the following section the history of neutrino astronomy and the designs of the major existing and proposed neutrino detectors are described.

2.4 Review of Neutrino Astronomy

The first neutrino detectors were the Kolar Gold Fields experiment (KGF) in India and the Case Western Reserve, Irvine experiment (CWI) in South Africa. These detectors were designed to observe atmospheric neutrinos. They were located in mines deep underground (7500 metres water equivalent (mwe) for KGF, 9000mwe for CWI) and hence were heavily shielded from background cosmic rays. They had a low threshold energy of 100MeV and poor angular resolution and hence could not observe neutrino point sources. However, the results obtained did set the first limits on the extraterrestrial neutrino flux (Crouch et al. 1978).

The first attempts to observe extraterrestrial neutrinos were made about a decade later using deep underground detectors originally designed for other purposes such as proton decay, monopole searches and high energy muon detection. These detectors have low threshold energies and small effective areas and hence are sensitive only to low energy neutrinos. They are used primarily to observe solar neutrinos and to study neutrino oscillations by observing atmospheric neutrinos. The main detectors with the capability of detecting low energy neutrinos are listed in table 1. The IMB detector and Kamiokande will be described in more detail as they are both water Cerenkov detectors and the designs served as prototypes for the new generation of high energy neutrino detectors.

Detector	Area/m^2	Design Function
KGF, South India	25-40	atmospheric neutrinos
CWI, South Africa	174	atmospheric neutrinos
BAKSAN, Caucasus	260	neutrino telescope
IMB, Ohio	400	proton decay
HPW, Utah	102	proton decay
Kamiokande I, II, Japan	160	proton decay
NUSEX, Mt.Blanc	12	proton decay
FREJUS, France/Italy	74	proton decay
SOUDAN I, Minnesota	10	proton decay
SOUDAN II, Minnesota	128	proton decay
MACRO, Gran Sasso	1100	monopoles
LVD, Gran Sasso	800	supernova neutrinos
SNO, Canada	180	solar neutrinos
SuperKamiokande, Japan	900	proton decay solar neutrinos

Table 2.1: Low energy neutrino detectors (from Sobel 1991)

2.4.1 Major Low Energy Neutrino Detectors

2.4.1.1 IMB (Irvine, Michigan, Brookhaven)

IMB is located at a depth of 1570mwe in a salt mine in Fairport, Ohio. It was originally designed to set a lower limit on the lifetime of the proton and consists of a tank of purified water surrounded on all sides by inward looking 8 inch photomultiplier tubes arranged on an approximate 1 metre grid as shown in figure 2.6.

The photomultiplier tubes record both the intensity and relative arrival times of Cerenkov light from which the vertex, direction and energy of a charge particle track can be determined. IMB is designed to detect contained neutrino events i.e. neutrinos which produce secondary muons within the detector. Discrimination between these contained events and cosmic ray events is achieved by calculating the interaction vertex and eliminating events with vertices occurring outside the detector. Low energy neutrinos have been observed with the IMB detector but searches for high energy neutrinos have been unsuccessful mainly because of the low effective area of the detector (Becker-Szendy et al. 1995).

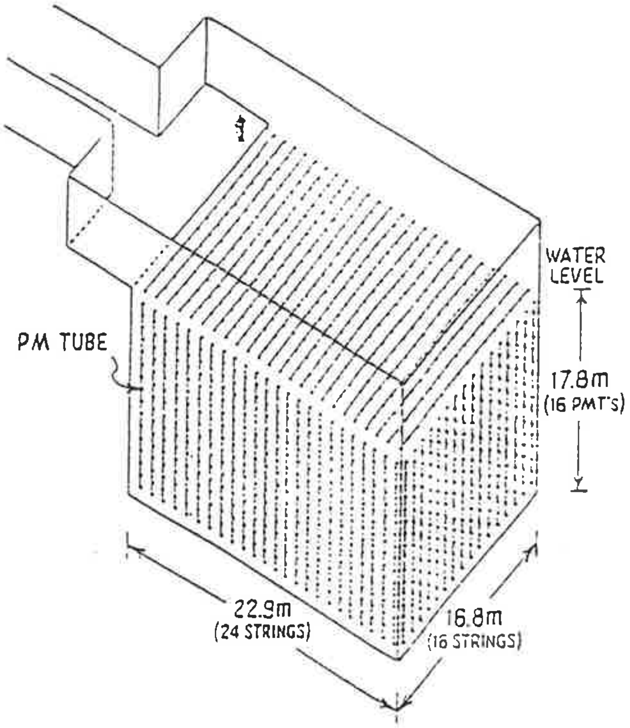

Figure 2.6: The IMB detector (from Koshiba 1992)

2.4.1.2 Kamiokande

Kamiokande was also originally designed as a proton decay experiment and was subsequently upgraded to operate as a solar neutrino detector. It is situated at a depth of 2700mwe in the Kamioke mine, Japan. The detector consists of a cylindrical tank containing purified water, the sides of which are covered with hemispherical photomultiplier tubes as shown in figure 2.7. The photomultiplier tubes were specifically designed for this detector to have a high quantum efficiency for Cerenkov radiation and a large collecting area. Hence, the light collection efficiency and the time resolution are greater than in standard photomultiplier tubes. The inner water tank is surrounded by a water Cerenkov anticoincidence unit which serves the double purpose of identifying cosmic ray muons and absorbing gamma-rays from the surrounding rock.

Low energy neutrinos have been observed in Kamiokande II and the next generation of Kamiokande detector, SuperKamiokande, is currently being developed.

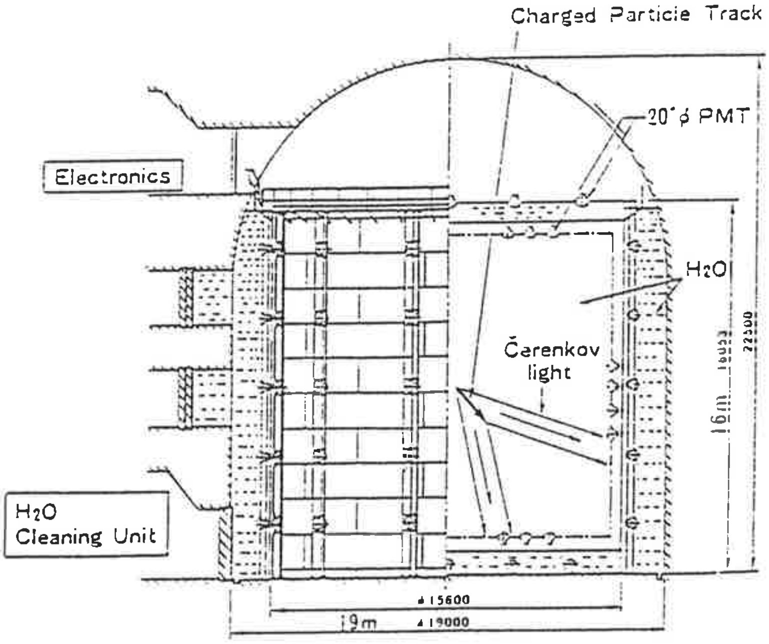

Figure 2.7: The Kamiokande detector (from Oyama 1989)

SuperKamiokande will have about 10 times the fiducial volume of Kamiokande II and will be capable of setting an upper limit on the diffuse neutrino flux (Koshiba 1992).

2.4.2 High Energy Neutrino Detectors

Neutrino astronomy really began with the detection of neutrinos from supernova SN1987a which appeared in the Large Magellenic Cloud on 24th February 1987. Statistically significant signals from SN1987a were observed by the Kamiokande II and IMB detectors (Bionta et al. 1987, Hirata et al. 1987). The measured fluxes agree with theoretical predictions of neutrino flux from this supernova to within a factor of two. The apparent success of these observations verified the feasibility of detecting neutrinos using the water Cerenkov technique and initiated the design of a new generation of detectors specifically intended to observe high energy neutrino point sources by observing upward travelling neutrino-induced muons.

The predicted flux of extra-terrestrial neutrinos falls off rapidly with energy. Hence high energy detectors require a much larger fiducial volume than existing low energy neutrino detectors. The fiducial volume of a high energy neutrino detector is the volume of instrumented ice or water plus the surrounding medium, up to a distance equal to the range of a high energy muon. From recent high energy neutrino flux calculations, a lower limit on the effective area of a high energy neutrino detector has been set at $10^4 m^2$. Existing low energy neutrino detectors are therefore not suitable for observing high energy neutrinos as they do not have the required surface area. Alternative designs were therefore developed for the new generation of detectors to facilitate the required increase in area.

One problem with increasing the effective area of such a detector is that the flux of background cosmic ray events also increases. The successful operation of a neutrino telescope depends on discriminating between the low flux of upward-travelling signal muons and the high background flux of downward travelling atmospheric muons. There are two main approaches to solving this problem. The first is to place the detector deep underwater or in ice such that most of the background atmospheric muons are absorbed in the water or ice above the detector (DUMAND, AMANDA, NESTOR and Lake Baikal). The second approach is to place the detector in a shallow body of water at the earth's surface and to discriminate electronically between the upward going signal and the downward background flux (GRANDE, LENA, NET, PAN). The relative merits and problems associated with deep underwater/ice detectors and surface detectors are discussed in the following section.

2.4.2.1 Comparison of Surface and Deep Underwater/Ice Detectors

The four neutrino detector projects currently underway are all deep underwater/ice detectors, namely DUMAND, AMANDA, NESTOR and the Lake Baikal Detector. The main disadvantage of all these detectors is the technical difficulty involved in working in the deep ocean or in Antarctic conditions. DUMAND has been funded for about 15 years, during which time many technical problems have been encountered and solved (Roberts 1992). The AMANDA project pioneered a technique for placing photomultipliers deep under ice, however the high cost of fuel for this procedure places stringent limits on the size of photomultiplier tubes that can be used. In the face of such technical obstacles a surface Cerenkov detector appears to be a way of building a neutrino detector in a more controlled environment using existing technology. In reality, the engineering costs of building a surface Cerenkov detector, such as GRANDE, are very high. Apart from the initial cost, the feasibility of expanding such a detector to provide a greater surface area is also limited by the engineering costs. As a way of reducing this cost and retaining the option of increasing the detector area, attention has turned to using natural lakes instead of custom-built facilities.

The major concern with surface Cerenkov detectors is the high level of up-down discrimination required to pick out the signal from the background noise. It is possible to achieve the required up-down discrimination using the timing and photon density information recorded by surface detectors. By considering both these factors, it is impossible, in principle, to confuse upward and downward going muons. In order to record the required timing and photon density information, a surface detector must be more densely intrumented than a deep underwater/ice detector. One advantage of this increased instrumentation density is that the energy of muons can be determined more effectively than in sparsely instrumented deep detectors. The GRANDE collaboration proposed to determine muon energies by applying total photoelectron number cuts to the signals recorded in each photomultiplier tube (Bratton et al. 1988). This technique would make the GRANDE detector sensitive to different source spectra.

If a surface detector is going to be capable of operating continuously, it has to be enclosed in a light-tight container. The effective area of the detector is defined by this enclosure. The threshold energy of the detector is the minimum energy of a muon which passes through all the planes of the detector and hence depends on the depth of water between the upper and lower layers. Above this threshold energy, the

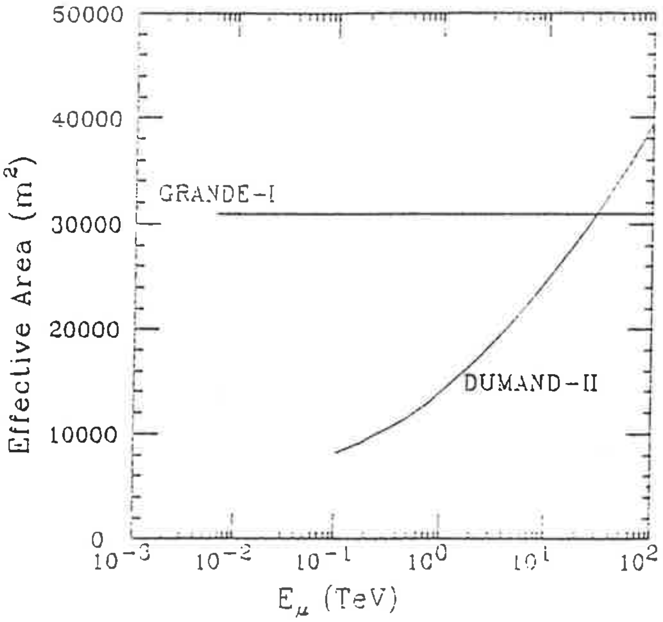

Figure 2.8: Effective area of DUMAND and GRANDE detectors as a function of muon energy (from Sobel 1993)

effective area of the detector is constant with muon energy. A deep underwater/ice detector, however, does not require a light-tight enclosure and can therefore detect Cerenkov light from muons which pass outside the array. As the track length of a muon increases with energy, the amount of light produced, and hence the effective area of the detector, also increases. A comparison of the effective areas of the GRANDE and DUMAND detectors, as a function of muon energy, is shown in figure 2.8. The different sensitivities of these two types of detector, as a function of muon energy, implies that they can provide complimentary information. For example, as the effective area of the DUMAND detector is greater than that of GRANDE at higher energies, then DUMAND will be more sensitive to sources which may have very hard neutrino spectra. GRANDE, on the other hand is best suited to observing sources which exhibit more conventional predicted neutrino spectra i.e. with a spectral index of about 2.1.

The large flux of atmospheric muons passing through surface detectors means that these detectors cannot observe muons close to the horizon or higher, as the signal would be swamped by background events. This leads to a viewing aperture for surface detectors of nadir angles from 0° to a maximum of about 80°. In deep

Detector	Area/m^2	Technique
DUMAND, Hawaii	2×10^4	Cerenkov-deep underwater
AMANDA, Antarctic	2×10^4	Cerenkov-deep ice
NESTOR	$\sim 3 \times 10^4$	Cerenkov-deep underwater
Baikal	2×10^3	Cerenkov-deep underwater
GRANDE	$\sim 3 \times 10^4$	Cerenkov-surface
LENA	3.6×10^3	Cerenkov-surface
NET	10^5	Cerenkov-surface
PAN	10^5	Cerenkov-surface
RAMAND	10^6	radio-deep ice
DUMAND		acoustic-deep underwater
SADCO		acoustic-deep underwater

Table 2.2: Major proposed and existing high energy neutrino detectors

detectors, however, the background flux is sufficiently attenuated for muons to be observed up to about 10° above the horizon. The solid angle viewed by deep underwater/ice detectors can therefore be up to 40% greater than for surface detectors.

Currently both deep/underwater and surface Cerenkov detectors are being developed, although no surface detector has yet reached the construction stage. Alternative forms of neutrino detection are also being considered, specifically the detection of acoustic and microwave radiation produced by neutrino induced showers. Proposed and existing high energy neutrino detectors are summarised in table 2.2 and are described in more detail in the remainder of this chapter.

Surface Cerenkov Detectors

2.4.2.2 GRANDE (Gamma-Ray and Neutrino Detector)

GRANDE was a proposed water Cerenkov facility which consisted of a high energy neutrino detector and an ultra-high energy gamma-ray detector. The proposed location was a quarry in Arkansas, USA, which is 70 metres deep with a surface area of $6.25 \times 10^4 m^2$. The expected rate of events due to neutrino-induced muons from a typical high energy neutrino source was of the order of tens per year and the predicted average angular resolution was 0.8° (Bratton et al. 1988).

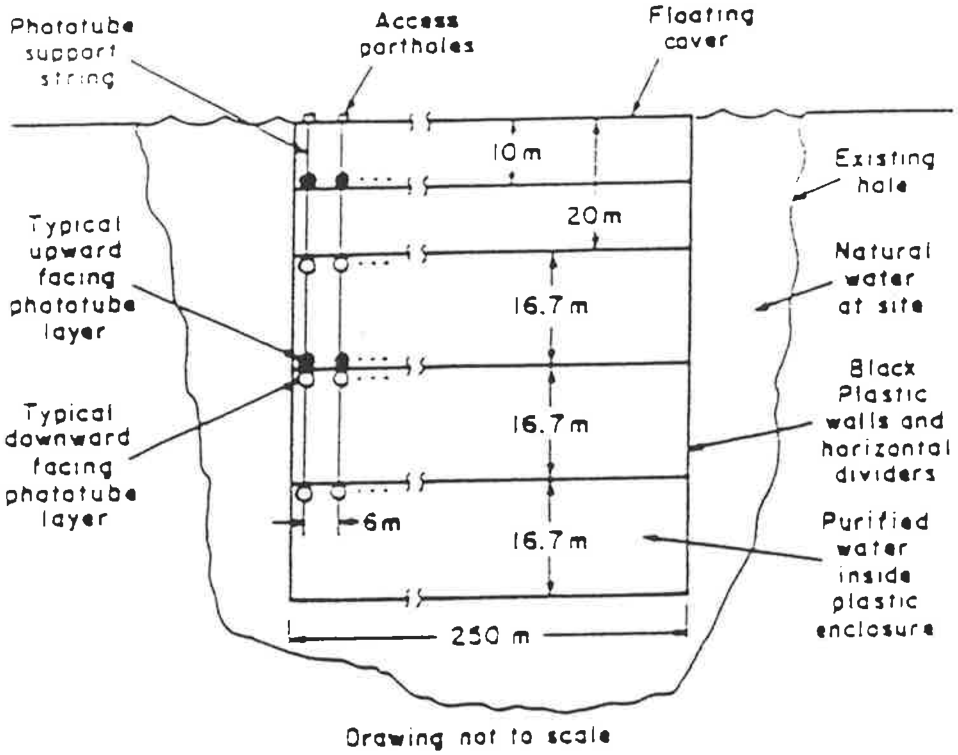

Figure 2.9: The GRANDE detector (from Bratton et al. 1988)

The design consisted of five layers of photomultiplier tubes as shown in figure 2.9. The photomultiplier tubes in each layer were arranged on a square grid of grid spacing 6 metres. The lower three layers consisted of downward looking tubes which constituted the neutrino telescope. The gamma-ray telescope consisted of the two upper layers of upward looking tubes which could also be used in anticoincidence with the neutrino telescope to eliminate triggers due to downward-travelling muons. The detector was to be enclosed in a light-tight plastic bag filled with purified water.

The main problem with surface Cerenkov detectors is the high flux of downward cosmic ray particles relative to the low flux of expected upward neutrino-induced muons. The soft component of cosmic rays, which consists mainly of electrons, is not very penetrating and most of these particles would be absorbed in the 20 metres of water above the neutrino detector. The hard component, however, consists mainly of muons and a significant flux of these particles would pass through the detector. Most of these events could be identified as downward travelling particles in the off-line analysis. However, if the on-line trigger rate due to downward muons was very high, the dead time of the detector would be prohibitively high. The on-line trigger rate was to be reduced in the GRANDE detector by applying a minimum coincidence requirement to each layer of photomultiplier tubes i.e. a layer of photomultiplier tubes would only trigger if greater than a minimum number of tubes registered signals. By applying this condition, the predicted on-line rejection ratio was $10^6 : 1$. Therefore, the detector dead time would be negligibly small.

At present, the GRANDE detector has not received funding for construction and the proponents of this detector are collaborating with the NET proposal.

2.4.2.3 LENA (Lake Experiment on Neutrino Astronomy)

LENA is a proposed water Cerenkov detector designed to observe both high energy neutrinos and gamma-rays. The proposed site is Lake Sugenuma in Gunma, Japan which is a mountain lake with a depth greater than 30m and an area greater than 10^4m^2. The detector consists of two layers of photomultiplier tubes arranged on the surface of a cylinder of radius 96 metres as shown in figure 2.10. The outer layer of photomultiplier tubes are outward looking while the inner layer are inward looking. The detector is surrounded by an array of air shower detectors which enable triggers due to air shower particles to be identified.

Although the status of the LENA project is uncertain an important test was performed using a prototype of the LENA detector installed in Lake Motosuto, Japan (Nishikawa et al. 1992). The aim of the prototype was to determine the accuracy with which muon tracks can be reconstructed and the efficiency of background rejection. The detector consisted of 30x30x30m of purified water enclosed in a PVC bag and instrumented with 3 layers of photomultiplier tubes as shown in figure 2.11.

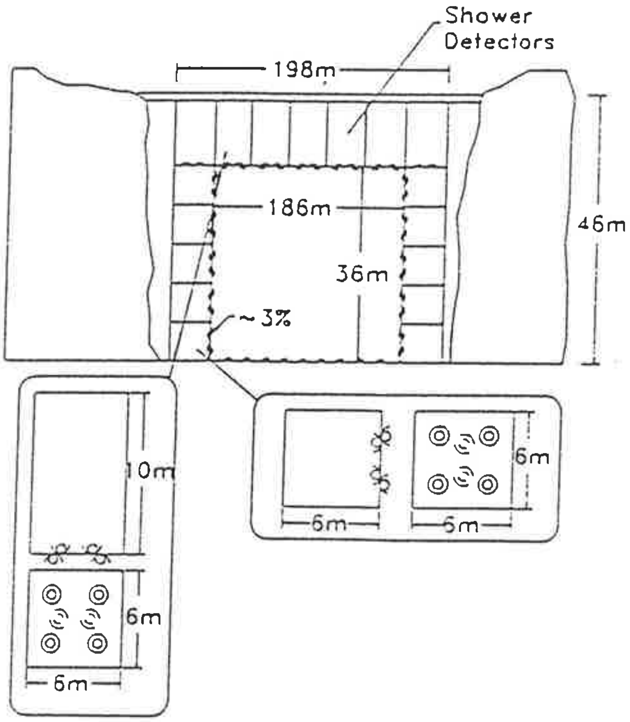

Figure 2.10: The LENA Detector (from Koshiba 1988)

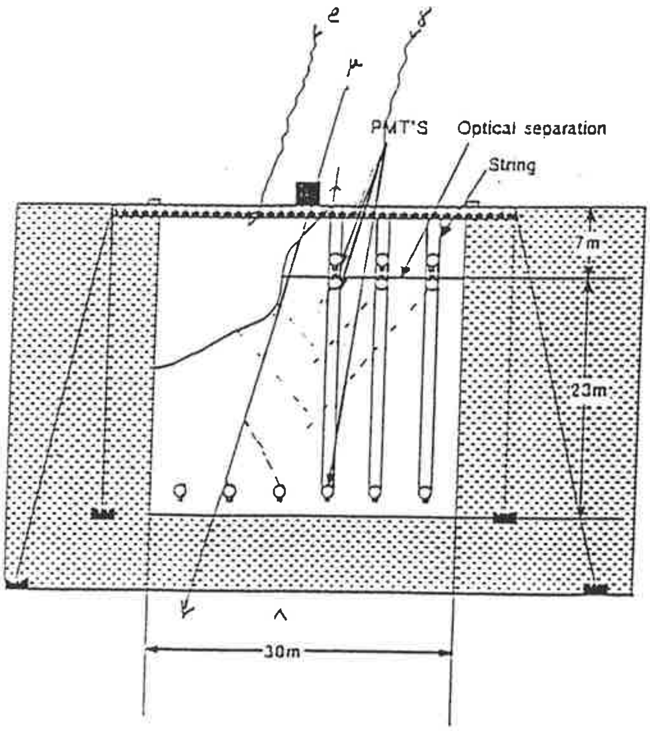

Figure 2.11: Schematic drawing of prototype of LENA detector (from Nishikawa et al. 1992)

The up-down discrimination capabilities were studied by observing atmospheric muons arriving close to the horizontal. From a total of 300000 events, muons close to the horizontal were selected and the direction of each muon was determined based on either timing information or pulse height analysis. The results showed that none of these muons were misinterpreted as upward travelling muons thus demonstrating that the large background rejection factor required in surface Cerenkov detectors can be achieved.

2.4.2.4 PAN (Particle Astrophysics in Norrland)

PAN is a proposed surface water Cerenkov detector to be located in Lake Tornetrask, Sweden. The detector is similar in design to GRANDE but the cost of providing a light-tight enclosure has been eliminated by operating the telescope only during the winter when the lake is covered with ice and the sun is below the horizon for most of the time. The status of this project is uncertain but interest has been shown in joining the AMANDA collaboration.

2.4.2.5 NET

NET is a proposed detector which is similar to GRANDE but with an area of $10^5 m^2$ (Bobsiut et al. 1991). The detector design is shown in figure 2.12 and consists of 3 layers of downward looking photomultiplier tubes. Like the GRANDE detector, the spacing between photomultiplier tubes in each layer is 6 metres and the vertical separation between layers is about 15 metres. It is proposed to locate the detector in a specifically constructed basin, filled with purified water, near the Gran Sasso laboratory in Italy.

This project is a colaborative effort between European groups and most of the groups involved in GRANDE. Funding is currently being sought and, if obtained, the detector is expected to be operating by 1998.

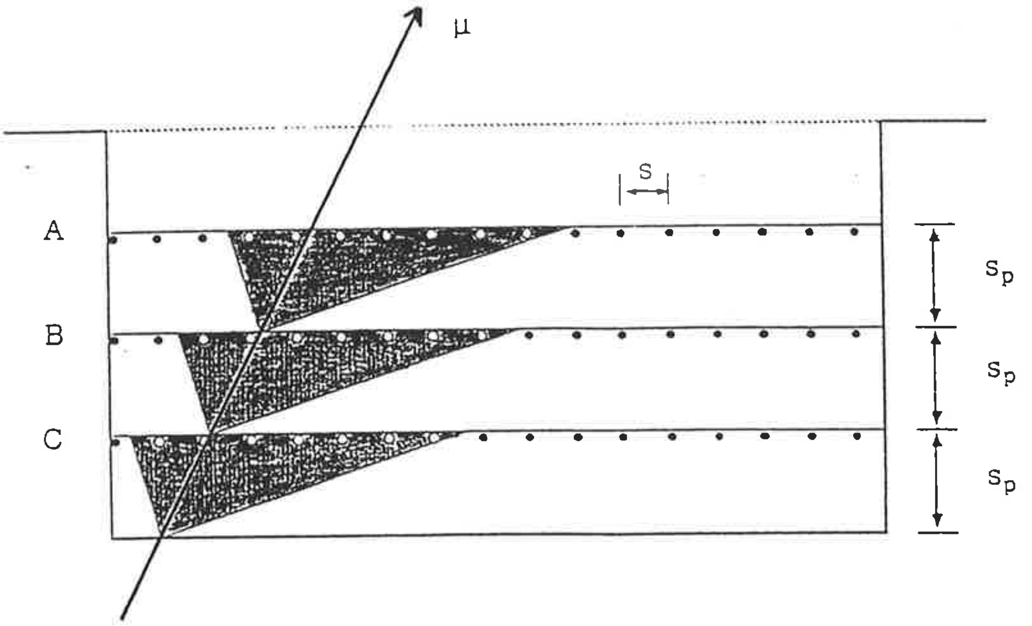

Figure 2.12: The NET detector (from Bobsiut et al. 1991)

Deep Underwater/Ice Detectors

2.4.2.6 Dumand (Deep Underwater Muon and Neutrino Detector)

DUMAND is a deep underwater neutrino detector located 4.5km below the ocean surface, 25 km off the west coast of Hawaii. At this depth, the flux of cosmic-ray muons is greatly reduced to about $3/m^2$/minute. The water at this depth appears to be surprisingly clear with an attenuation length of the order of 30 metres. Hence the light detectors can be spaced relatively far apart making it feasible to instrument a large volume of water. Locating the detector in the sea ensures that the detector area can be expanded if required. However, there are significant technical difficulties associated with working in a deep ocean environment. For a review of the DUMAND project see Roberts 1992.

The effective area of the DUMAND array is about $20000m^2$ and the predicted angular resolution is 1°. The detector design consists of 9 vertical strings of detectors anchored to the bottom of the ocean in an octagonal geometry as shown in figure 2.13.

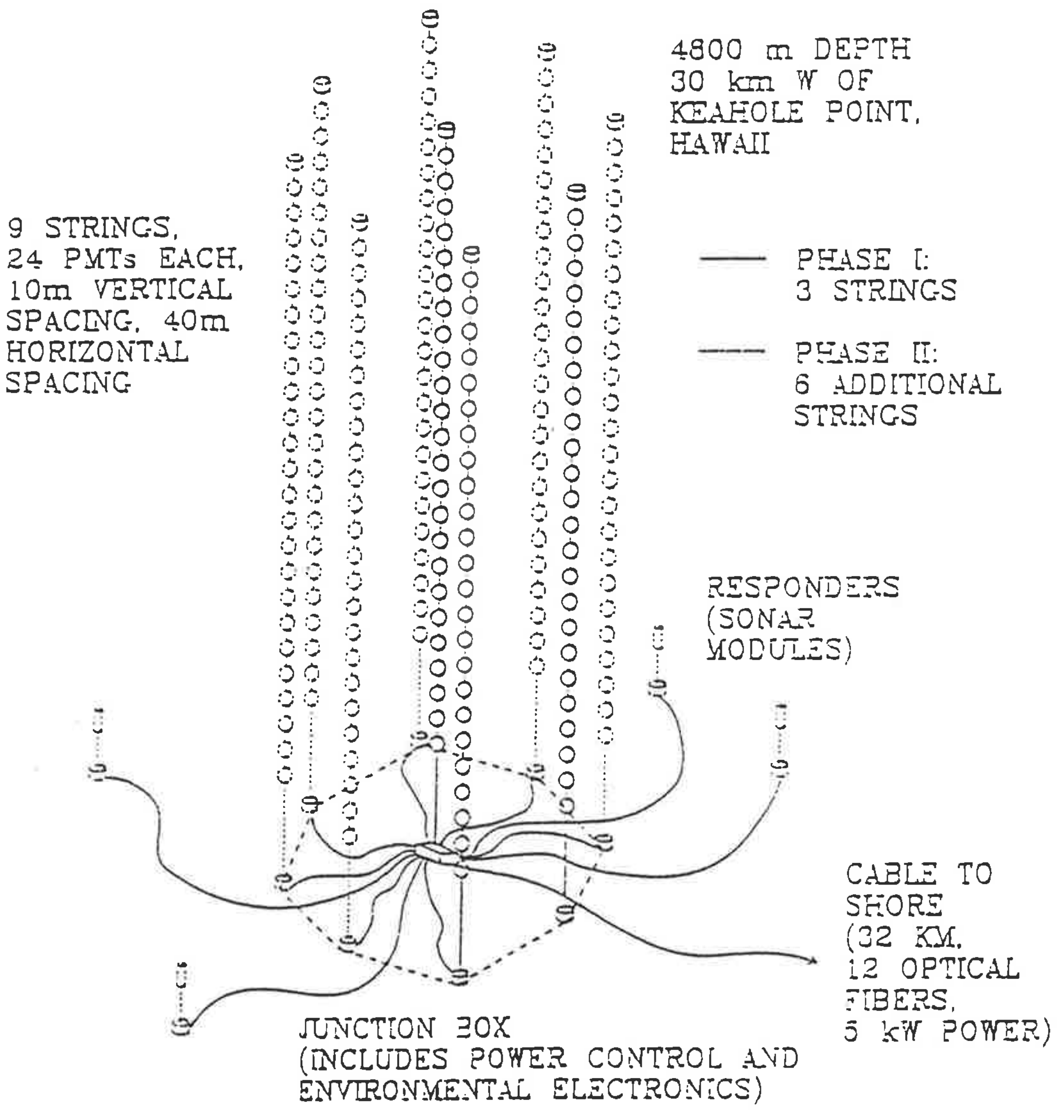

Figure 2.13: The DUMAND detector (from Wilkes 1994)

Each string supports 24 sensor modules containing downward looking hemispherical photomultiplier tubes. As the ocean environment is variable, conditions such as temperature, currents and the transmission properties of the water are continuously monitored via one environmental module and two calibration modules located on each string. The strings are anchored to the bottom of the ocean but can move as a result of ocean currents. The location of the strings is monitored by hydrophones and an acoustic transponder network. The data collected from the modules is transferred to shore via optical fibre links.

A prototype of the DUMAND array, the Short Prototype String, was tested in the ocean over a period of 6 years. This prototype consisted of a short string of 5 optical sensors which was suspended from a boat for a period of about two days at a time. The results from this prototype verified the expected flux and angular distribution of downward atmospheric muons in the ocean. The main problem identified was background light from bioluminescent organisms and the decay of K^{40}. This light is high enough to saturate some of the photomultiplier tubes and a trigger system has been designed to minimise the effects of this background light (Camerini et al. 1993).

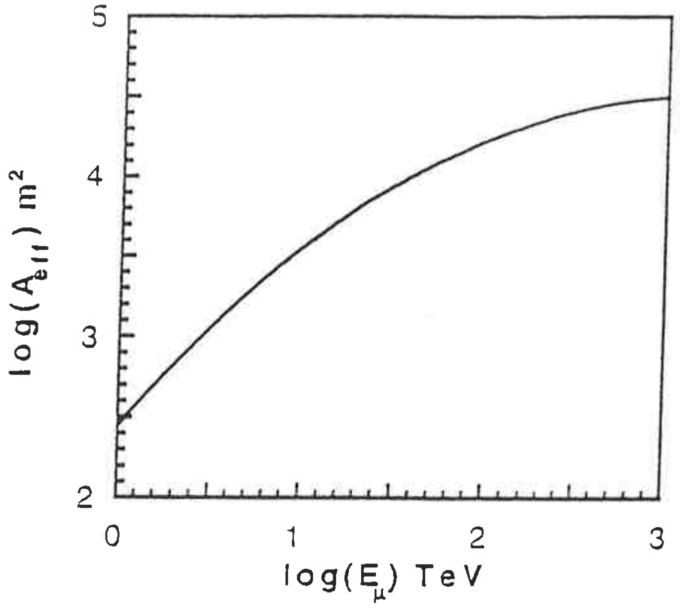

Figure 2.14: Effective area of the Triad as a fuction of muon energy (from Stenger 1993)

The first phase of the DUMAND detector, consisting of a 3 string array called the Triad, is scheduled to be deployed this year (1995). The strings are each 230 metres long with each string holding 24 optical modules and they will be anchored to the bottom of the ocean. Although the full nine strings are required to achieve the high effective area and angular resolution required, it is anticipated that the Triad will be capable of making limited high energy neutrino observations. The effective area of the Triad as a function of muon energy is shown in figure 2.14 from which it can be seen that an effective area of $10^4 \mathrm{m}^2$ is achieved only for muons of energy greater than about 30TeV.

The angular resolution is also energy dependent, with a median pointing accuracy of 5.5° at 1 TeV and 3.6° at 10TeV (Learned 1993). Current calculations indicate that the Triad has a marginal chance of detecting high energy neutrinos from active galaxies or other sources, with the uncertainty arising from the range of models and flux calculations for the possible sources.

2.4.2.7 Lake Baikal

A large underwater detector, designed to investigate neutrino astrophysics, cosmic ray physics and exotic particles, is currently under construction in Siberia. It is located in Lake Baikal, which is a large freshwater lake about 1450 metres deep. Near the bottom of this lake the transparency of the water is comparable to that of deep ocean water, with an attenuation length of about 20 metres at $\lambda = 480\mathrm{nm}$. The detector will be located at a depth of 1km as tests have shown that the natural luminescence is minimal at this depth. At this depth, the flux from downward cosmic ray muons is still high enough to restrict the maximum viewing angle to a nadir angle of 80°. The predicted median angular resolution is $1^\circ - 1.5^\circ$ and the minimum detectable flux of neutrinos from point sources with energies greater than 1TeV is about $10^{-9}\mathrm{s}^{-1}\mathrm{cm}^{-2}$ (Belolaptikov et al.1993).

The Lake Baikal detector is similar in design to DUMAND but several advantages are gained by locating the detector in a lake as opposed to the ocean, namely that the optical background in the lake is significantly lower than in the deep ocean and there is an absence of strong currents. The lake freezes over in the late winter facilitating the deployment of underwater equipment to the proposed site which is about 4.5km from the shore.

The proposed detector, named NT-200, consists of 8 vertical strings attached to a rigid umbrella-like frame as shown in figure 2.15. The positions of the strings are monitored using ultra-sonic emitters. Each string supports 12 pairs of optical modules. The optical modules in each pair point in the same direction and the pairs of modules are directed alternately upward and downward. The detector, therefore, has a symmetrical response to muons coming from above or below. A simple coincidence requirement between the two optical modules in each pair greatly reduces the rate of triggers due to random coincidences between photomultiplier tubes. When the array is triggered, the coordinates, trigger time and the summed charge for each pair of photodetectors are recorded.

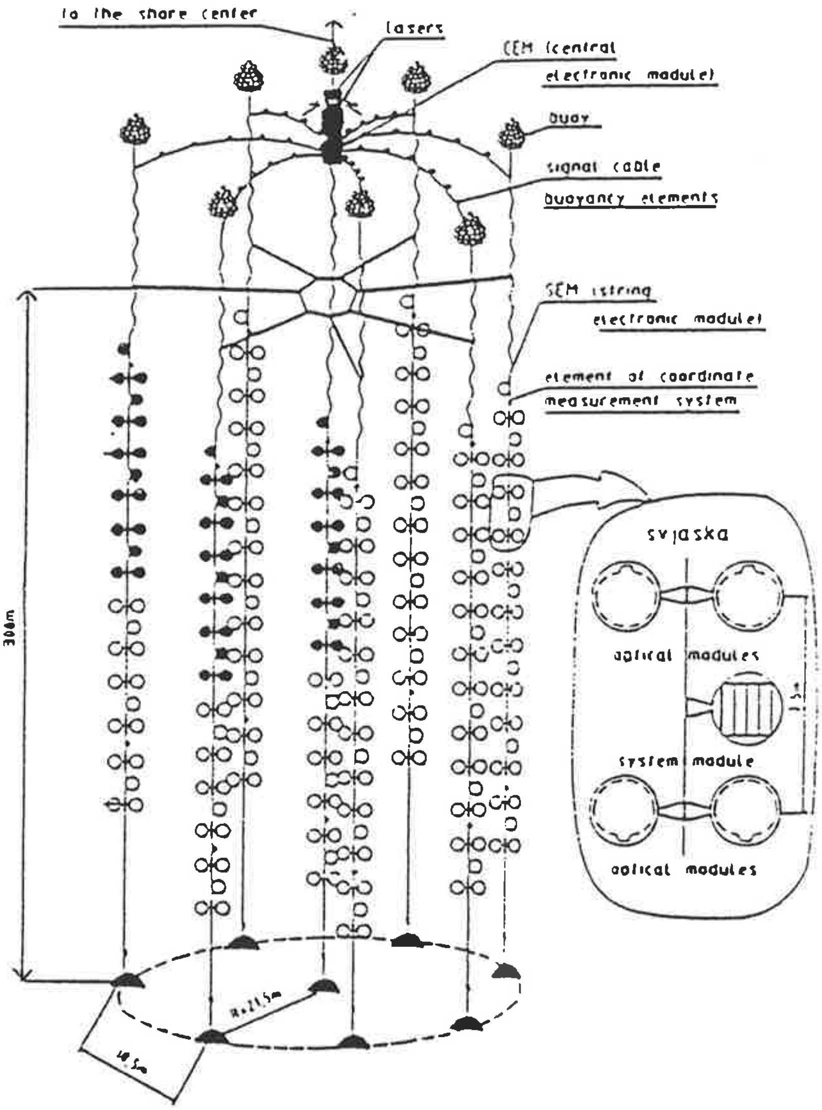

Figure 2.15: The Lake Baikal detector (from Belolaptikov et al. 1993)

A criticism of the Baikal project is that at a depth of 1km the background muon flux is still considerable and exceeds the upward muon signal by a factor of about

10^6. The algorithms for track reconstruction and background rejection in the Lake Baikal detector are described in (Belolaptikov et al. 1994a) and show that the required up-down discrimination factor is achievable.

The first module of the detector, consisting of 3 strings of photomultiplier tubes, was deployed in April 1993 and has been collecting data since that date. This module has been used to measure angular distributions of muons with depth, the results of which agree closely with published results of muon flux. Also, the background rejection algorithm has been optimised to give a signal to noise event rate ratio of 2:1 for a 72 photomultiplier tube array. The effects of water currents, sedimentation and other environmental factors have also been assessed. The results obtained from this first detector module are presented in Belolaptikov et al. (1994b). In March 1995, a 72 photomultiplier tube array was deployed and this array is scheduled to be upgraded in 1996.

2.4.2.8 AMANDA (Antarctic Muon and Neutrino Detector)

AMANDA is a proposed neutrino detector which will use ice instead of water as the detector medium. Deep ice is expected to have good optical transmission properties, especially in the ultra-violet region, while providing a rigid mechanical structure that maintains relatively constant photomultiplier positions. The detector will be located at the South Pole and will therefore view neutrinos from northern hemisphere sources. As most of the VHE and UHE gamma-ray detectors are in the northern hemisphere, this opens up the possibility of simultaneous gamma-ray and neutrino observations of the same sources.

The background noise in ice is expected to be less than in water due to the absence of background light resulting from bioluminescence and radioactive decay, and the reduction in thermal noise in the photomultiplier tubes due to the low −55°C temperature of the ice. These two factors are expected to reduce the background rates in single photomultiplier tubes by a factor of about 100 relative to photomultiplier tubes in deep ocean water (Barwick et al. 1992). Hence, in theory the AMANDA detector can define a muon trajectory to the same accuracy as DUMAND but using fewer coincidences. This implies that fewer photomultipler tubes are required in AMANDA to instrument the same effective area as in DUMAND. There is also no need for environmental and position sensors as the environment is relatively constant.

The major disadvantages with this proposal are the technical problems associated with working in Antarctic conditions and the difficulties involved in placing equipment deep under ice while maintaining good optical contact with the ice. This is achieved by boring a hole in the ice using a hot water drill, lowering the photomultiplier tubes into the hole and then allowing the water to refreeze under pressure. This technique has been successfully demonstrated during several field tests.

The proposed detector consists of an array of photomultiplier tubes embedded at a depth of about 1km in ice as shown in figure 2.16. The detector area is 10^4m^2 and the design consists of 9 strings of photomultiplier tubes surrounding a central string. Each string supports 20 downward looking hemispherical photomultiplier tubes.

Monte Carlo simulations of this array have shown that the angular resolution for muons of energy 1TeV is about 1° and the effective area range from 5000m^2 at 100GeV to 25000m^2 at 10^5GeV. The predicted rate of background events due to atmospheric neutrinos and misreconstructed atomospheric muons is of the order of 1 per year in a 1° angular bin (Tilav et al. 1993, Barwick et al. 1992).

In 1993-1994, 4 strings of 20 photomultiplier tubes were deployed at a depth of 800-1000m beneath the South Pole. It was found that ice at these depths was not completely bubble free, as expected, and this factor limits the effective volume of this module to about 10^6m^3. Since deployment, the electronics and data acquisition system have been upgraded such that this module can be used to look for high energy cascades from AGN neutrinos and supernova events.

A 6-string array is scheduled to be deployed in 1995-1996. These strings will be at a depth of 1500 metres where the ice should be bubble-free and hence exhibit very

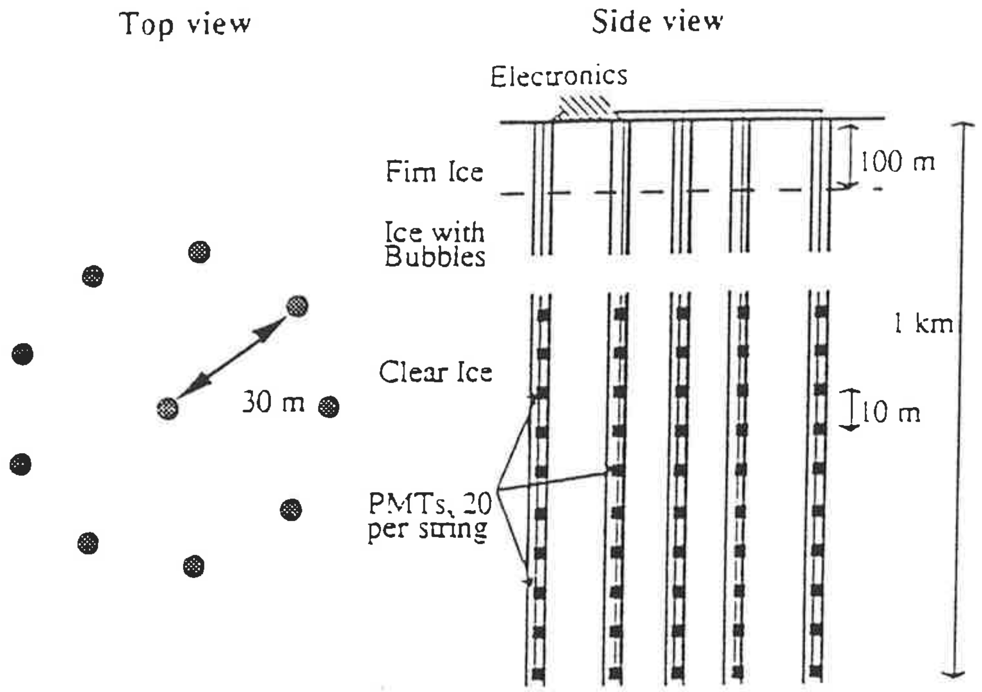

Figure 2.16: The AMANDA detector (from Lowder et al.1993)

high transmission for Cerenkov radiation. The ultimate aim is to deploy a second generation detector (AMANDA-MarkII) in the years 1996-1999. One possible design for this detector consists of 10 long strings surrounding the 6 string array of the 1995-1996 deployment. It is predicted that the effective volume of AMANDA-MarkII will exceed 1km^3 for TeV muons. The current status and results of recent field tests can be found in Mock et al. (1995) and Gray et al. (1995).

2.4.2.9 NESTOR (NEutrinos from Supernovae and TeV Sources)

NESTOR is a deep ocean detector to be located in the Mediterranean Ocean about 15km from Pylos in South West Greece. The site is a trench of depth greater than 5km in a protected bay. The detector will be located at a depth of 4km where the attenuation length of water at 450nm has been measured as 36-48 metres. The array will have a surface area of 10^{5}m^2 with the possibility of expanding further.

The design differs from DUMAND in that, instead of strings of optical units, NESTOR consists of towers of rigid hexagonal modules. Each module consists of a hexagonal frame of radius 16 metres supporting 6 optical units at the corners and one at the centre. Each optical unit consists of one upward and one downward looking hemispherical photomultiplier tube. The frame is made from titanium and expands to its full area when buoyant in water. Twelve hexagonal units are then stacked vertically to form a tower as shown in figure 2.17.

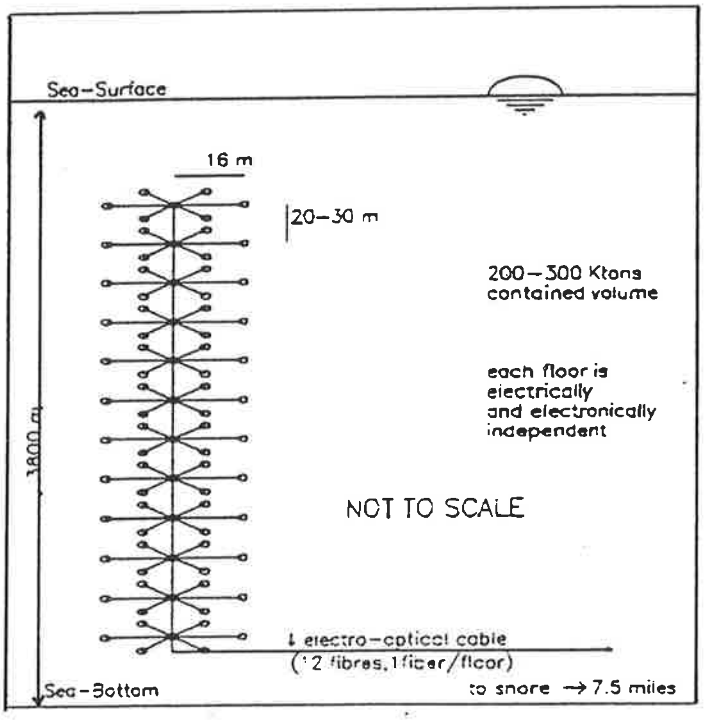

Figure 2.17: A tower of the NESTOR detector (from Resvanis 1994)

The angular resolution of one tower is insufficient to observe point sources. However, it is expected that a single tower will be capable of observing the diffuse neutrino background from AGNs with a predicted event rate of about 1 event per day at energies greater than 100 TeV (Resvanis 1992). The complete detector will have 7 towers arranged as shown in figure 2.18. The surface area of the NESTOR detector will be 4 times greater than the area of DUMAND II, with a predicted angular resolution of less than 1°.

In 1991 a half scale model of the basic hexagonal unit was deployed. Since then, in situ tests have been performed to measure factors such as the water clarity, sedimentation, underwater currents, background light and muon flux. The results of

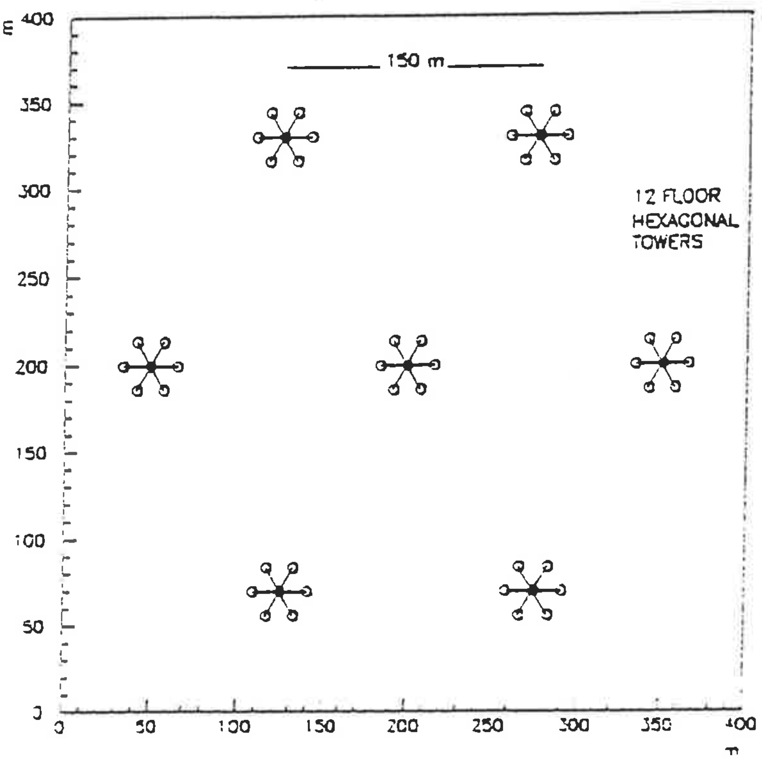

Figure 2.18: The NESTOR detector (from Resvanis 1994)

these tests have confirmed the suitability of the proposed site. At present, a complete tower of modules is being constructed and is expected to be deployed this year. Funding is currently being sought to construct a further 6 towers to complete the detector.

Alternative Designs

2.4.2.10 Acoustic Detection Techniques

The detection of high energy neutrino induced showers via the acoustic radiation produced is a technique being considered by the DUMAND collaboration and SADCO (Sea Acoustic Detection of Cosmic Objects), which will be located at the same site as the NESTOR detector. When a high energy shower develops in water, the energy is absorbed in a thin column of water which is heated and then expands adiabatically producing approximately cylindrical acoustic waves. If the original neutrino which induced the shower has an energy greater than 10^{15}eV, these acoustic waves can be detected by hydrophones. This method of detecting high energy neutrinos is appealing because very large detector volumes can be instrumented at low cost. The background noise level in the sea, however, is expected to be quite high but by using real-time Fourier techniques a signal to noise ratio of about 1 can be tolerated provided the noise is uncorrelated with the signal (Learned 1993a).

The DUMAND project proposes to use the 53 hydrophones which constitute the acoustical positioning system as a prototype for an acoustical high energy neutrino detector (Learned 1993). The expected deep ocean noise is calculated to be of the same order of magnitude as the signal from a $10^{16} eV$ cascade. Hence the threshold energy for this detector will be about $10^{16} eV$ and the event rate will be correspondingly low.

The SADCO detector (Karaevsky et al. 1993) will consist of 3 vertical strings separated by about 100 metres and located at a depth of 4 to 6km. Each string will support 8 subarrays of 16 hydrophones. The detector will have an effective area of 10^9m^3 for a 6×10^{15}eV neutrino. Preliminary tests were carried out in 1991 and 1992 using two test arrays to measure the background noise in the ocean and to determine the efficiency of sound generation by cascades in the ocean.

2.4.2.11 Radiodetection Techniques

The idea of detecting high energy neutrinos from the coherent radio signals emitted by the resulting high energy showers in dense media was first proposed 30 years ago (Askar'yan 1962). The power radiated by a particle passing through a dielectric medium is given by equation 2.2. If the radiation is incoherent then the power generated is simply proportional to the number of charged particles in a shower(N). However, if the wavelength of the radiation is comparable with the resulting shower dimensions then the resulting radiation is coherent and the power radiated is proportional to $(qN)^2$, where q is the average of the excess charge due to the ionisation of the medium. This radiated power can be detected using microwave antennae and the magnitude of power produced below 1GHz is given by equation 2.4 where E_0 is the total energy in the shower (Halzen, Zas and Stanev 1991).

$$W = 4.5 \times 10^{-14}[\frac{E_0}{1\mathrm{TeV}}]^2\mathrm{erg} \tag{2.4}$$

The Radiowave Antarctic Muon and Neutrino Detector (RAMAND), is a proposed radiowave detector to be located in a glacier close to the Soviet Vosto~~c~~k base (Boldyrev et al. 1991). The detector consists of an array of 100 microwave antennae spaced 100 metres apart to instrument an effective area of $1\mathrm{km}^2$ as shown in figure 2.19. The major drawback of this technique is that the neutrino threshold energy for the detection of signals above the background microwave noise is very high , of the order of 100TeV, and the expected event rate above this energy is low.

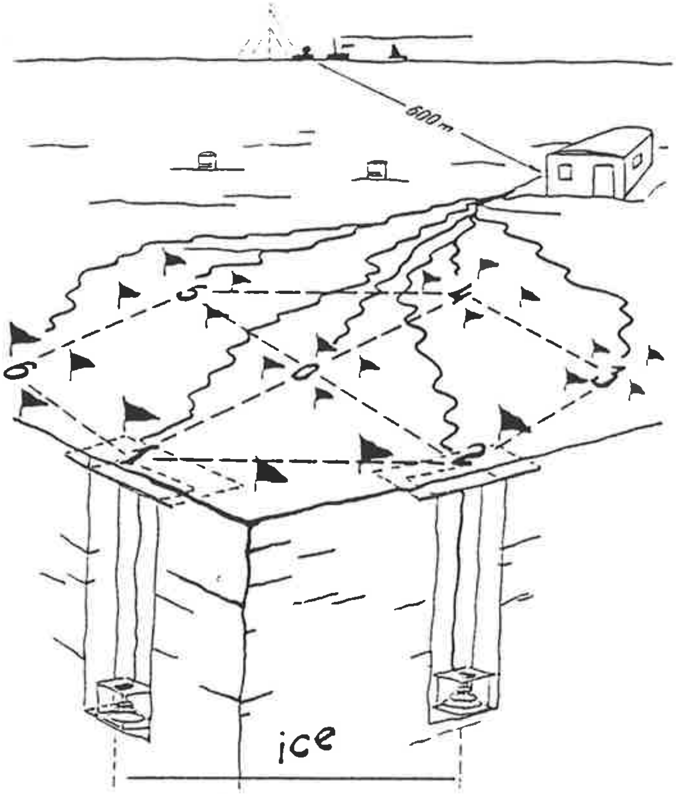

Figure 2.19: The RAMAND detector (from Boldyrev et al. 1991)

2.5 Concluding Remarks

In this chapter a review of proposed and existing high energy neutrino detectors has been presented. The majority of these detectors are based on detecting Cerenkov light produced by upward travelling neutrino-induced muons. These detectors fall into two categories:- deep underwater/ice detectors and surface detectors. Deep detectors have the advantages of increased viewing aperture, greater effective area to the highest energy muons and a low background flux of atmospheric muons. However, there are significant technical difficulties inherent in working at such depths in water and ice. Surface detectors can be constructed in much more controlled environments using existing technology. However, to date, no surface detectors are under construction. This is partly due to the high engineering costs involved.

The detector proposed in this thesis is a surface Cerenkov detector. In principle, the proposed detector is similar to the GRANDE detector but it would be located in a natural lake in South Australia. This would greatly reduce the engineering costs and, if the lake water is clear enought to transmit enough Cerenkov radiation, would also remove the need to provide purified water.

In the remainder of this thesis the design of the proposed detector is detailed. Possible sites for the detector are assessed and the detector performance characteristics are optimised using Monte Carlo simulations. Finally the feasibility of detecting muons via Cerenkov radiation produced in the proposed site is investigated using a custom built test device.

Chapter 3

Site Investigations

3.1 Introduction

Two natural lakes in Australia were considered as possible sites for a high energy neutrino detector : the Blue Lake in South Australia and Weebubbie Cave in Western Australia (see figure 3.1).

Figure 3.1: Map showing locations of detector sites considered

Both lakes have a surface area of at least 10^4m^2 and contain water which appears to be reasonably transparent to light. The efficiency of a neutrino detector is dependent on the transmission of light through the detector medium. Hence, in order to assess the suitability of these sites, the attenuation length of light in the water in both locations was measured.

In this chapter the relevant physical and chemical properties of the proposed sites are discussed. The theory and measurement of light attenuation in water is described and the measured values of light attenuation length for both sites are presented.

3.2 The Blue Lake

The Blue Lake is a surface volcanic crater lake situated at 38° South on the outskirts of Mt.Gambier, South Australia. The lake has a total surface area of about 10^6m^2 and a depth of about 70 metres across most of this area. A plan, showing depth contours of the Blue Lake, is shown in figure 3.2. The lake is part of an extensive aquifer system, most of which is underground. Water enters the lake primarily through groundwater seepage and the water level in the lake remains constant to within one metre. The lake is the main water reservoir for the surrounding towns and considerable infrastructure exists at the lake surface which would facilitate the deployment and operation of a neutrino detector.

The water in the lake changes colour from green in the winter to an intense blue in the summer. These variations in the optical characteristics of the water are closely related to the chemical and biological properties, some of which are regularly monitored by the state Engineering and Water Supply Department (E&WS). The optical clarity of the water is primarily affected by the density of biological particles (algae and phytoplankton). Biological particles tend to accumulate in regions of high temperature. It is therefore expected that the highest particle density and hence the lowest light transmission will occur in the warmer regions of the lake.

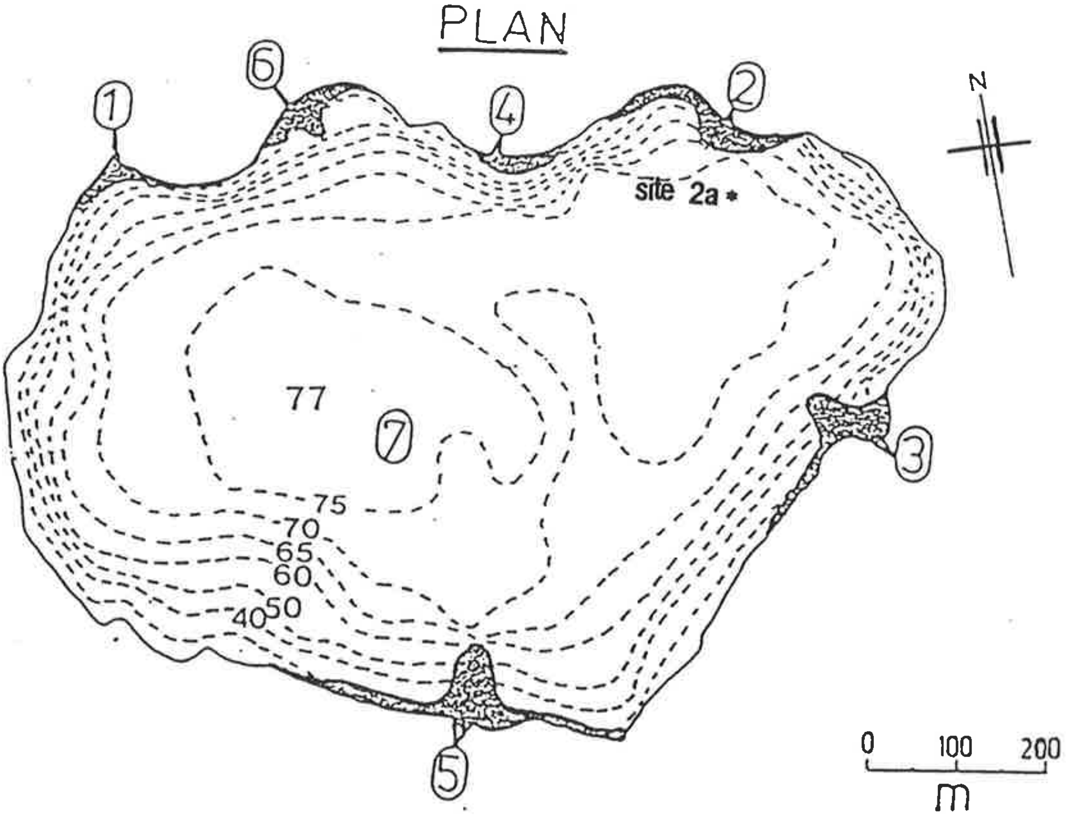

Figure 3.2: Plan of the Blue Lake showing depth contours in metres

The temperature of the lake, and hence the optical properties, vary seasonally. In winter the water in the lake is the same temperature at all depths and the density of biological particles is also relatively constant throughout the lake. In summer, when the air temperature increases, the surface layer of water in the lake heats up and an interface between this warmer upper water and the cooler deeper water is formed. Algae and plankton from the lower depths accumulate at this interface resulting in a relatively opaque layer of water which moves downwards through the lake during the summer. The water below this opaque layer is cooler and hence should exhibit good optical transmission characteristics.

Typical values of temperature and dissolved oxygen content as a function of depth in the Blue Lake, for one summer and one winter month are shown in figure 3.3. The density of biological particles is proportional to the dissolved oxygen content.

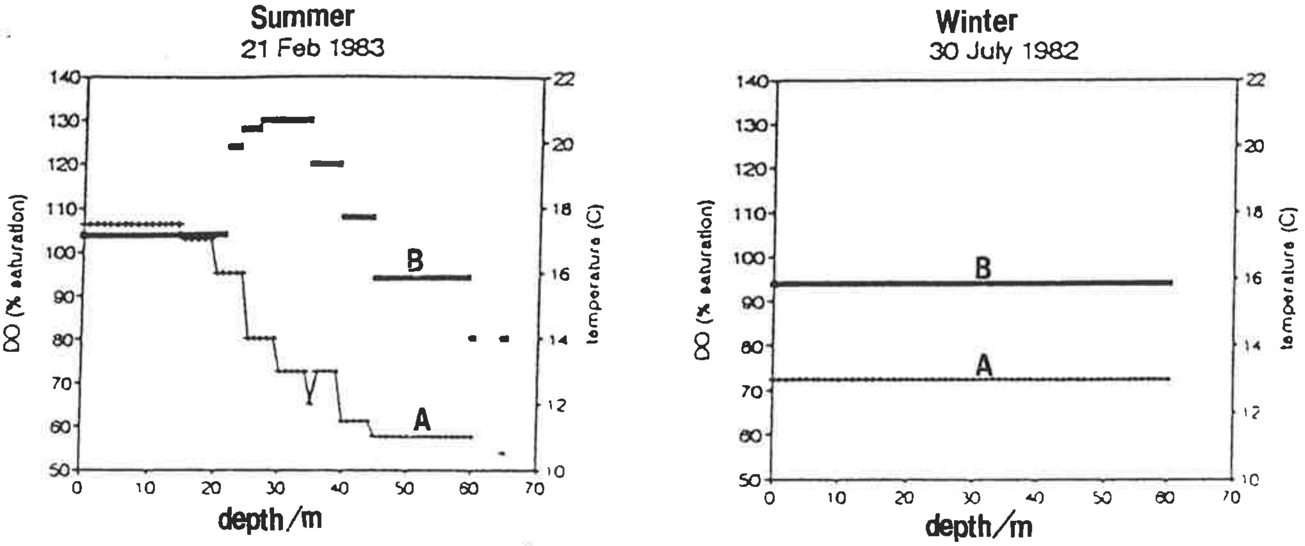

Figure 3.3: Temperature and dissolved oxygen content of Blue Lake water as a function of depth (Telfer 1993). Plot A = temperature, plot B = dissolved oxygen content.

From these results it can be seen that, in February, the density of biological particles decreased rapidly at depths greater than about 40 metres. Hence, we expect the highest light transmission to occur at these depths, during the summer months. The high density of biological particles from about 20 to 40 metres means there is a layer of water of low light transmission. The presence of this relatively opaque layer will reduce the amount of background light from the lake surface reaching the lower regions of the lake. During September, the temperature and the density of biological particles were constant throughout the lake. Hence, we expect the transmission of light to be approximately constant throughout the lake during winter.

3.3 Weebubbie Cave

Weebubbie cave is a water filled cavern located at 35° South under the Nullarbor Plain near Eucla, Western Australia. A map of the cave is shown in figure 3.4.

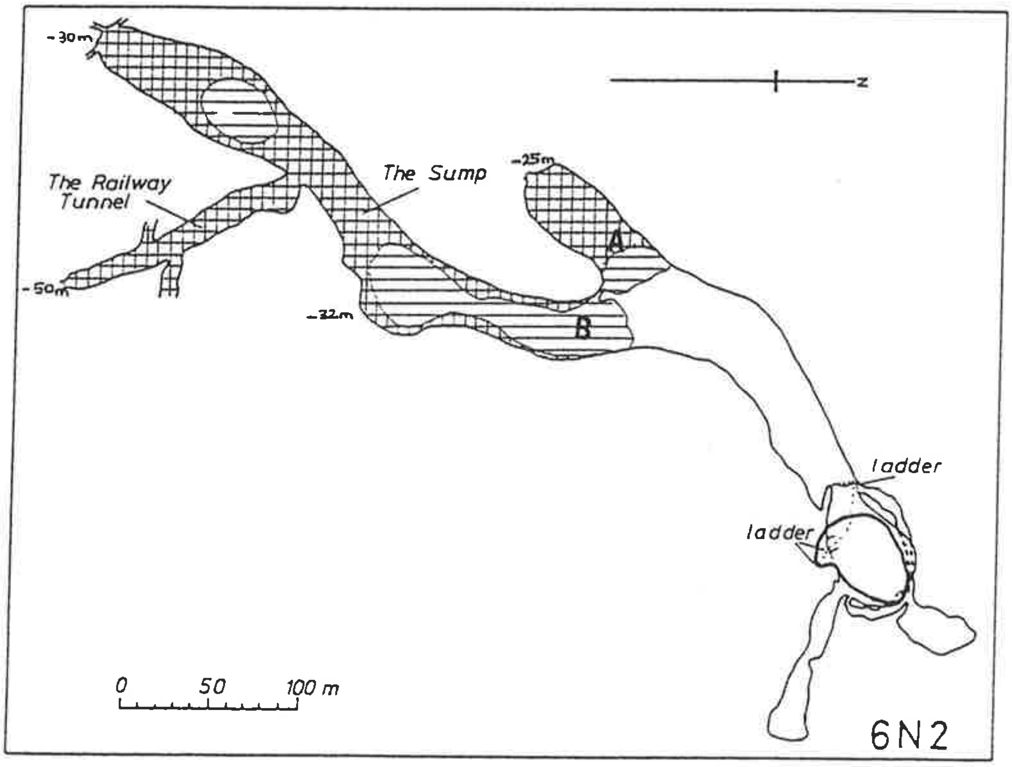

Figure 3.4: Map of Weebubbie Cave

The cave is located under 80 metres of rock and hence the flux of downward atmospheric muons reaching the cavern is significantly less than for a surface location such as the Blue Lake. The disadvantages of this site are that the water is shallow, reaching a maximum depth of only 10 metres, and the accessible surface area, ie regions of the cave not fully submerged, is of the order of $10^4\mathrm{m}^2$. This limits the size of a neutrino detector, at this location, to the predicted minimum size required to observe point sources. Despite these drawbacks, the cave was considered as a possible site because of the low background flux from atmospheric muons and the apparent clarity of the water.

3.4 Theory of Light Attenuation in Natural Water

The attenuation of a beam of light can be quantified in terms of a characteristic length, the attenuation length, which is defined by equation 3.1.

$$I = I_o e^{-r/\lambda_{att}} \tag{3.1}$$

$$\begin{aligned} \text{where I} &= \text{final intensity} \\ I_o &= \text{initial intensity} \\ r &= \text{pathlength} \\ \lambda_{att} &= \text{attenuation length} \end{aligned}$$

Light is attenuated by scattering and absorption processes. The characteristic lengths associated with attenuation, absorption and scattering are related according to equation 3.2.

$$\frac{1}{\lambda_{att}} = \frac{1}{\lambda_{abs}} + \frac{1}{\lambda_{sc}} \tag{3.2}$$

$$\begin{aligned} \text{where } \lambda_{\mathbf{abs}} &= \text{absorption length} \\ \lambda_{sc} &= \text{scattering length} \end{aligned}$$

Light can be absorbed in natural water by water molecules, dissolved matter or by particles in suspension. Absorption by water molecules is negligible in natural water across most of the electromagnetic spectrum. Dissolved matter and suspended inanimate particles exhibit similar absorption spectra, with an approximately $1/\lambda$ dependence (Jerlov 1976). The presence of biological particles is characterised by peaks in the absorption spectrum resulting from the presence of chlorophyll.

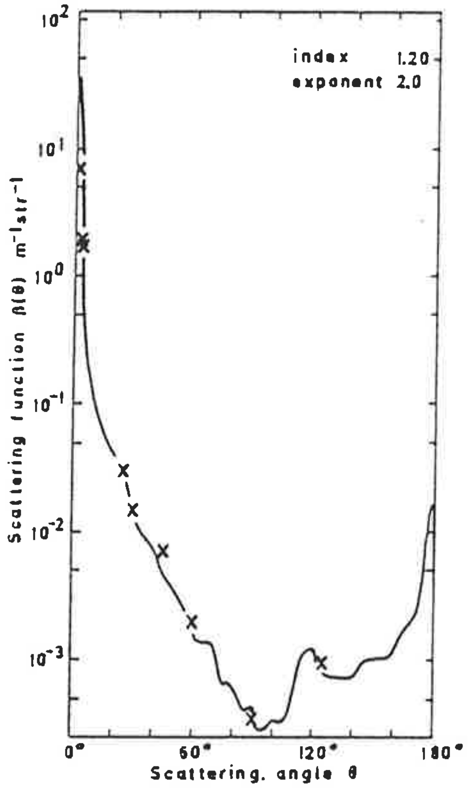

Figure 3.5: Volume scattering function measured in the Sargasso sea at a wavelength of 632.8nm (Kullenberg 1968)

The scattering of light is quantified by two parameters:- the scattering length which is a measure of the number of photons scattered, and the volume scattering function which defines the probability of the direction of the scattered photon. The type of scattering depends on the size of the scattering site compared with the wavelength of the light. When the size of the scatterer is smaller than or equal to the wavelength of the light, Rayleigh scattering occurs e.g. scattering of light off water molecules. This scattering shows a $1/\lambda^4$ dependence and the corresponding volume scattering function is strongly peaked in the forward and backward directions. When the scattering sites are much larger than the wavelength of light, Mie scattering occurs. This is the predominant form of scattering in natural waters. Mie scattering shows little variation with wavelength and the volume scattering function is strongly peaked in the forward direction with 50% of the scattered light lying within 5° of the forward direction (Bauer and Morel 1967). The scattering function is approximately constant for all natural waters and a typical function, measured at a wavelength of 632.8nm, is shown in figure 3.5.

3.5 Spectrometer Measurements

Two techniques were used to measure the attenuation length of water in the proposed detector sites. Firstly water samples were collected from each site and analysed on a laboratory spectrometer. The second technique employed a specifically designed device which was submerged in the water and measured the transmission of light *in situ.*

3.5.1 Principles of Spectrometer Measurements

A spectrometer records the fraction of light remaining in a beam after passing through a sample. The wavelength of the light is variable, hence the light transmission as a function of wavelength can be determined. The spectrometer employed was a differential spectrometer which recorded light transmission in terms of absorbance. Absorbance is defined by equation 3.3

$$A = log(\frac{I_o}{I_s}) \tag{3.3}$$

where I_o = initial intensity

I_s = final intensity after sample

A differential spectrometer measures the relative absorbance between two optical cells; the reference cell and the sample cell (see figure 3.6). If purified water is placed

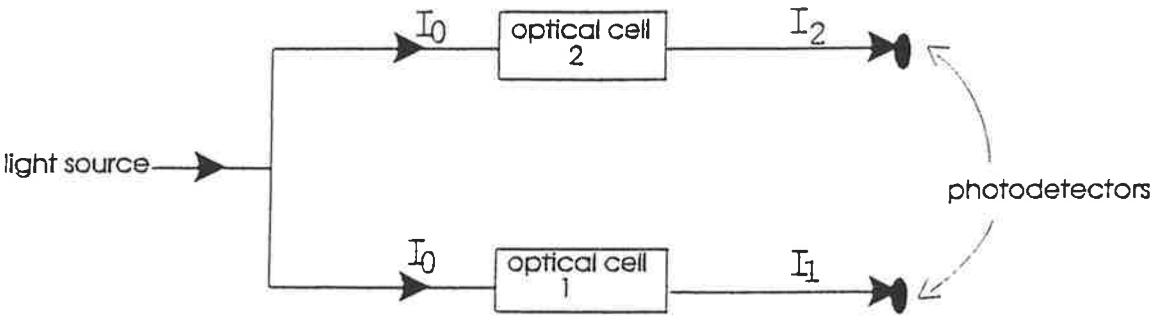

Figure 3.6: Schematic view of a differential spectrometer

in the reference cell (cell 2) and the water to be tested is placed in the sample cell (cell 1), then the relative absorbance recorded (A_{rel}) is given by equation 3.4.

$$A_{rel} = A_{s1} - A_{p2} = log(\frac{I_{p2}}{I_{s1}}) \tag{3.4}$$

where A_{s1} = absorbance of sample in cell 1
A_{p2} = absorbance of purified water in cell 2
I_{s1} = recorded intensity after sample in cell 1
I_{p2} = recorded intensity after purified water in cell 2

However, this relative absorbance includes effects due to differences between the two optical cells, such as differences in the transmission properties of the optical faces. To eliminate this factor, purified water is first placed in both the reference and sample cells and the relative absorbance, A_{pp}, is recorded. This is then repeated with the test sample in the sample cell and purified water in the reference cell to give the relative absorbance, A_{sp}. The difference between these relative absorbances, A_{diff}, is given by equation 3.5 and is independent of the reference cell.

$$A_{diff} = A_{sp} - A_{pp} = log(\frac{I_{s1}}{I_{p1}}) \tag{3.5}$$

where I_{s1} = final intensity after sample in cell 1

I_{p1} = final intensity after purified water in cell 1

The attenuation length of the test sample can thus be calculated from the measured value of A_{diff} according to equation 3.6.

$$\frac{1}{\lambda_{att}} = \frac{1}{\lambda_r} + 2.303\ \frac{A_{diff}}{r} \tag{3.6}$$

where λ_{att} = sample attenuation length/m

λ_r = reference attenuation length/m

r = pathlength/m

The error on this value of attenuation length is given by:-

$$\delta\lambda_{att} = -2.303\ \lambda_r^2\ r\ \frac{\delta A_{diff}}{(\lambda_r\ 2.303\ A_{diff} + r)^2} \tag{3.7}$$

where $\delta\lambda_{att}$ = error in sample attenuation length

δA_{diff} = error in relative absorbance

A_{diff} = relative absorbance

λ_r = reference attenuation length/m

r = optical pathlength/m

The absolute absorbance of the sample can, therefore, be determined providing the attenuation length of the reference sample is known. The reference medium used in the measurements presented is water purified by double osmosis, the spectral

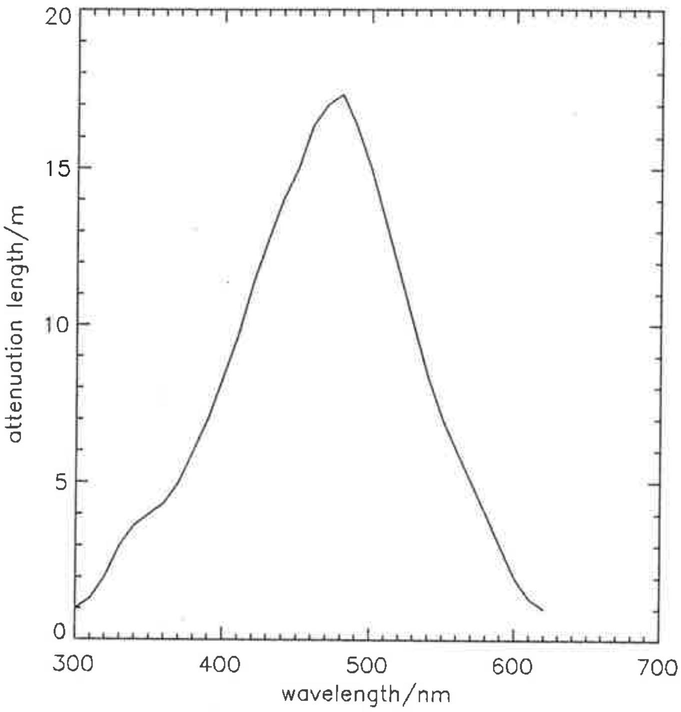

Figure 3.7: Attenuation length of purified water as a function of wavelength

attenuation length of which is shown in figure 3.7. This attenuation length function has been extrapolated from the results presented in Bratton et al. (1988).

The low absorbance of water over a 4cm pathlength means the spectrometer is extremely sensitive to temperature changes and variations within the water samples. To minimise these effects multiple measurements of sample and reference absorbances were taken. The attenuation length of the test sample is then determined from equation 3.6 using the average values of differential absorbances recorded. The error on this result is calculated from equation 3.7 assuming that the error in the difference between the sample and reference absorbances (δA_{diff}) is given by equation 3.8. This assumes that the errors are normally distributed and uncorrelated.

$$\delta A_{diff} = \sqrt{(\delta A_{sp}^2 + \delta A_{pp}^2)} \tag{3.8}$$

where $\delta \mathrm{A_{sp}}$ = standard deviation of relative sample absorbances, $\mathrm{A_{sp}}$

δA_{pp} = standard deviation of relative reference absorbances, $\mathrm{A_{pp}}$

3.5.2 Results of Spectrometer Measurements

Water samples were collected from depths of 0 to 60 metres at site 2a in the Blue Lake (see figure 3.2) over a period of 20 months and analysed on the differential spectrometer. The samples were stored in ice and kept in the dark to inhibit the growth of biological particles. The results of spectral attenuation length as a function of depth in the lake are shown in figure 3.8.

From these results it can be seen that, during the winter months, the attenuation length is relatively constant with depth (see results from August 1992). This indicates that the optical properties of water in the lake do not vary significantly with location during winter. It is also apparent from this figure that the highest values of attenuation length occur at the greatest depths during the summer months. However, the maximum value of attenuation length measured is of the order of only 5 metres. This is significantly lower than the attenuation length of water used in existing and proposed neutrino detectors such as DUMAND, GRANDE and IMB (Roberts 1992, Bratton et al. 1988, Koshiba 1992). Computer simulations have been used to assess if a neutrino detector can operate in water of such low attenuation length and the results of these simulations are presented in chapter 4. It should be noted that the optical properties of water in the Blue Lake are temperature dependent and will vary from year to year depending on the climate at the lake. Hence, a neutrino detector operating in the lake would need to continuously monitor the water attenuation length. In Weebubbie Cave, water samples were collected from the surface and at a depth of about 8 metres at locations A and B. The attenuation lengths measured from all 4 samples were identical and the resulting variation of attenuation length with wavelength is shown in figure 3.9.

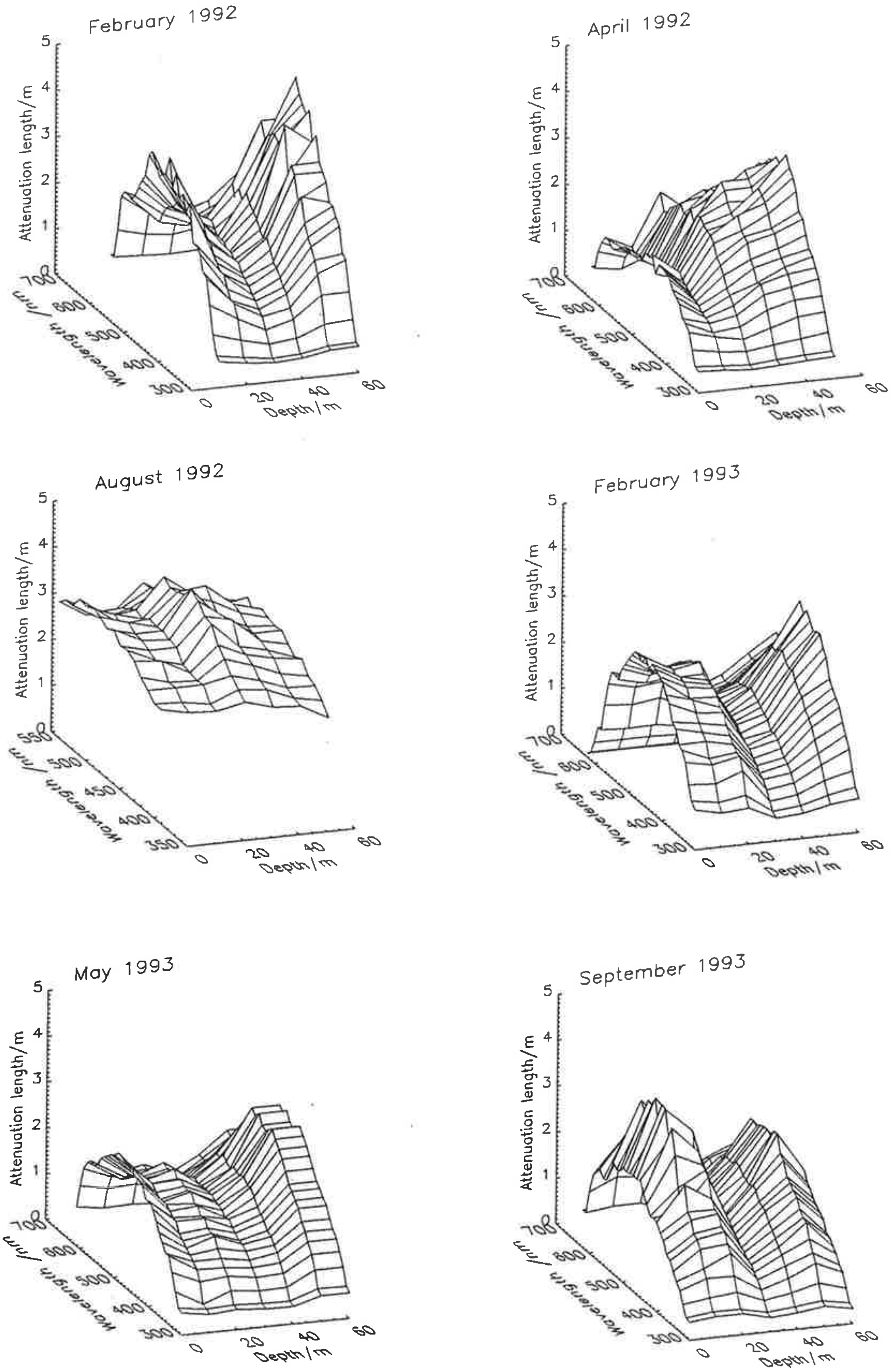

Figure 3.8: Attenuation length spectra as a function of depth for water samples collected in the Blue Lake from February 1992 to September 1993

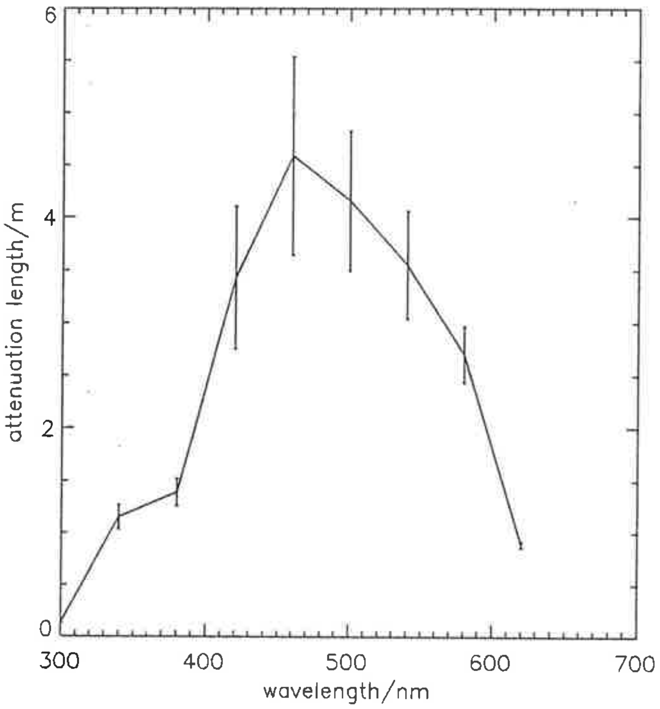

Figure 3.9: Attenuation length of water samples from Weebubbie Cave

3.5.2.1 Comparison of Cerenkov Light Transmission in the Blue Lake and Weebubbie Cave

The efficiency of a neutrino detector depends on the magnitude of muon-induced Cerenkov signals registered by a photomultiplier tube submerged in the detector medium. The magnitude of these signals is equal to the convolution of the Cerenkov light spectrum, the light transmission spectrum of the detector medium and the spectral response of the photocathode. To compare the Cerenkov signals that would be registered by a photomultiplier tube located in the Blue Lake and in Weebubbie cave, the ratio of signal magnitude in the Blue Lake to signal magnitude in Weebubbie cave was determined. In this calculation, the differential intensity of Cerenkov radiation varies as $1/\lambda^2$ (see equation 2.3) and the photocathode quantum efficiency used is the peak quantum efficiency of a S11 photocathode. The water attenuation length for Weebubbie Cave is as shown in figure 3.9. For the case of the Blue Lake, the attenuation lengths as a function of depth measured during February

1992 and September 1993 have been used (see figure 3.8). By using the attenuation results from these two months, results are obtained for one summer month and one winter month, representing the highest and lowest light transmission in the lake. The results in figure 3.10 show the ratio of Cerenkov signals in the Blue Lake to Cerenkov signals in Weebubbie Cave as a function of depth in the Blue Lake, for lake water attenuation lengths measured in February 1992 and September 1993.

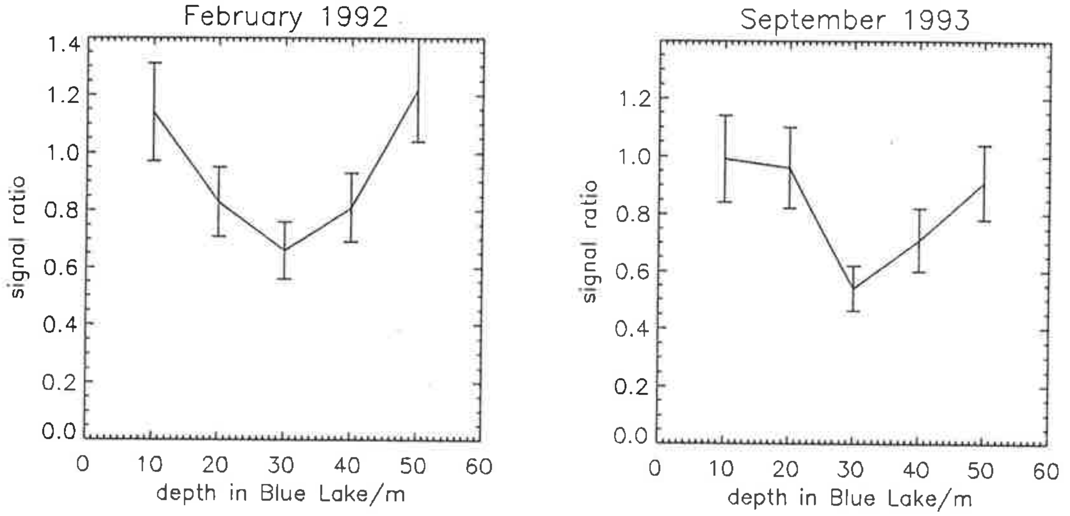

Figure 3.10: Predicted ratio of magnitude of Cerenkov signals in the Blue Lake to magnitude of Cerenkov signals in Weebubbie Cave as a function of depth in the Blue Lake, based on measurements taken in February 1992 and September 1993

From these results it can be seen that, for the month of September, Cerenkov signals registered in Weebubbie Cave were greater than or equal to those registered in the Blue Lake for all depths in the lake. This is due to the poor light transmission properties of Blue Lake water during the winter months. During February however, the signal in the Blue Lake was greater than the signal in Weebubbie Cave for depths in the lake greater than 40-50 metres, reaching a maximum value of about 1.2 times the signal in Weebubbie Cave. Hence, at depths greater than about 40 metres, the ratio of Cerenkov signal in the Blue Lake to Cerenkov signal in Weebubbie Cave varied from a maximum of about 1.2 in the summer to a minimum of 0.7 in the winter. Considering that this does not represent a significant overall difference in the magnitude of Cerenkov signals recorded in both sites, and also considering the limitations in surface area and accessibility of Weebubbie Cave, then the Blue Lake would be the more suitable location for a neutrino detector.

3.5.2.2 Measurements of Light Scattering

A spectrometer measures the fraction of light remaining in a thin beam, after passing through a sample, and is therefore sensitive to both absorption and scattering processes. The majority of light which is scattered will exit the light beam and hence will not be detected by the photocell. In the case of a neutrino detector located in a lake, the situation is different. The Cerenkov light can be considered as a plane wavefront which crosses the face of the photomultiplier tubes. Scattering in natural water is predominantly in the forward direction and hence it is likely that, while light will be scattered out of the field of view of a photomultiplier tube, a comparable amount of light will also be scattered into the field of view. Hence, the attenuation length measured on the spectrometer will be a minimum value corresponding to the extreme case of minimal scattered light being detected. If most of the light attenuation is due to scattering, then the effective attenuation length for a photomultiplier tube registering Cerenkov light may be much greater than is measured on a spectrometer.

To assess if this is the case in the Blue Lake, the proportion of light attenuation due to absorption and scattering processes was determined. The amount of scattering occurring is difficult to measure directly. However, the scattering pathlength can be deduced from the intensity of light emerging from a sample at 90° to the incident light beam. The proportion of incident light detected at 90° to the original direction is termed the nephelometric turbidity. This parameter can be measured on a turbiditimeter which consists of a light source directed at a sample and a photocell at 90^0 to the incident beam as shown in figure 3.11.

The turbidity in nephelometric turbidity units is approximately proportional to the reciprocal of the scattering pathlength with a constant of proportionality equal

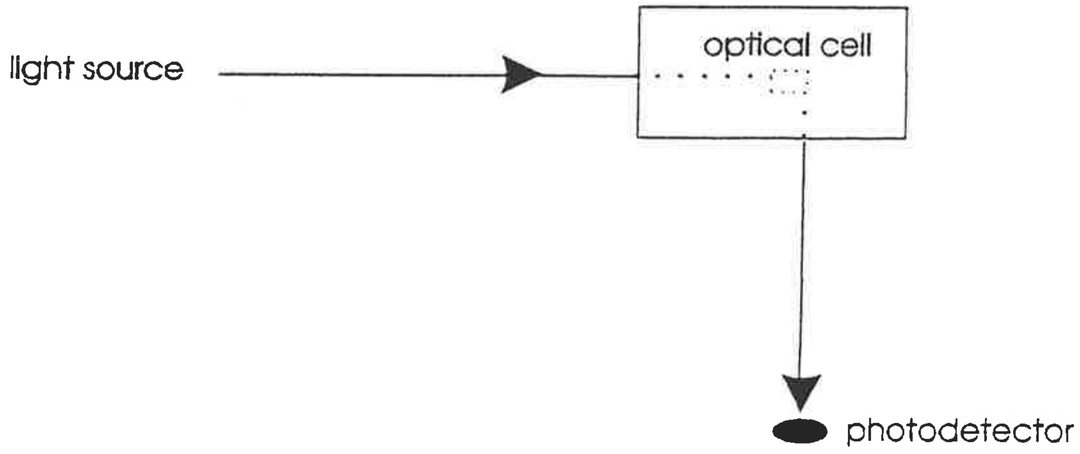

Figure 3.11: Schematic representation of a turbiditimeter

to about 1.1 (Kirk 1981). Once the attenuation and scattering lengths are known, the absorption length can then be determined from equation 3.2.

The turbidity, and hence the scattering length, was measured for water samples collected in the Blue Lake in May 1993. The turbiditimeter uses a tungsten bulb as a light source, and hence the values of scattering pathlength deduced from the turbidity measurements correspond to average values over the spectral range of the tungsten bulb. Using the spectrometer, the attenuation length is measured as a function of wavelength. Hence, to compare the attenuation lengths measured using the spectrometer with the scattering lengths as determined by the turbiditimeter, a value of attenuation length averaged over the spectrum of a tungsten bulb is calculated. To do this, the spectral attenuation lengths, measured on the spectrometer, are convolved with the light output spectrum of a tungsten bulb. The resulting attenuation length, averaged over the spectral output of a tungsten light source, is given by equation 3.9.

$$att_{av} = \frac{-x}{\ln \frac{\int W_1 d\lambda}{\int W_0 d\lambda}} \tag{3.9}$$

where $\mathrm{att_{av}}$ = average attenuation length/m

$$\begin{aligned}
x &= \text{optical pathlength/m} \\
weight(\lambda) &= W_0 = \text{spectral intensity of tungsten bulb} \\
W_1 &= weight(\lambda)\exp^{-x/att(\lambda)} \\
\lambda &= \text{wavelength/m} \\
att(\lambda) &= \text{spectral attenuation lengths from the spectrometer/m}
\end{aligned}$$

The main error on the resulting values of average attenuation length comes from the error in the values of spectral attenuation lengths measured on the spectrometer. The resulting error in the average attenuation length is given by equation 3.10.

$$\delta att_{av} = \frac{x^2\sqrt{\int {W_2}^2 d\lambda}}{(\ln\frac{\int W_1 d\lambda}{\int W_0 d\lambda})^2 \int W_1 d\lambda} \tag{3.10}$$

$$\begin{aligned}
\text{where } \delta \mathrm{att}_{\mathrm{av}} &= \text{error in average attenuation length/m} \\
\delta att(\lambda) &= \text{error in spectral attenuation length/m} \\
W_0, W_1, x &= \text{as defined in equation 3.9} \\
W_2 &= W_1 \frac{\delta att(\lambda)}{att(\lambda)^2}
\end{aligned}$$

Once the scattering length and the average value of attenuation length are known, the absorption length can then be calculated from equation 3.2. The resulting values of attenuation, absorption and scattering lengths as a function of depth for water samples collected from the Blue lake in ~~August~~ May 1993 are shown in figure 3.12.

From these results it can be seen that the absorption pathlength is significantly greater than the scattering pathlength at all the depths considered. These results show that light attenuation in the Blue Lake is dominated by scattering processes. This means that the values of attenuation length measured on the spectrometer represent a lower limit corresponding to the case of no scattered light being detected. In the proposed neutrino detector some scattered light will be registered. Hence the attenuation length corresponding to Cerenkov light detection in the proposed detector will be greater than the value measured on the spectrometer.

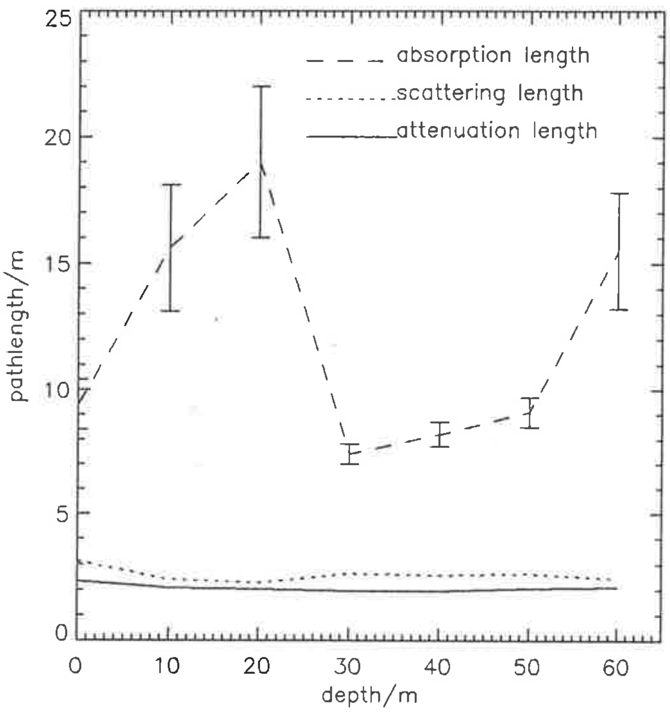

Figure 3.12: Attenuation, absorption and scattering pathlengths for Blue Lake water collected in ~~August~~ May 1993. Errors on the values of attenuation and scattering pathlengths are negligibly small on the scale shown.

3.6 Harvey I

The attenuation lengths of Blue Lake water samples, measured on the spectrometer, are low in terms of the water clarity required for a neutrino detector. However, it is possible that samples removed from the lake will have different optical properties from water in the lake. This can occur due to differences in factors such as temperature and exposure to light between the samples and the water remaining *in situ*. This may be significant as the optical properties of natural water depend on the concentration of biological particles, which is highly dependent on temperature and light exposure. To eliminate this uncertainty a device was designed and built, hereafter referred to as Harvey I, which measures light transmission *in situ*.

3.6.1 Principles of Attenuation Length Measurement using Harvey I

Harvey I consisted of a light source directed at a photomultipler tube such that the signal recorded by the photomultiplier tube depended on the attenuation length of the intervening medium. An absolute value of the attenuation length of this medium could be determined in two ways, as follows:-

1. Harvey I is submerged in a medium of known attenuation length, the reference medium, and the signal from the light source recorded. The device is then submerged in the sample medium and the light signal recorded. The sample attenuation length can then be determined from the known attenuation length of the reference medium and the ratio of light signals in the sample and reference media.

2. Several light sources are positioned at different distances from the photomultiplier tube. The attenuation length can be calculated from the relative signals recorded according to equation 3.11.

$$\lambda = \frac{-\delta x}{\ln \frac{I_1}{I_2}\frac{I_{o2}}{I_{o1}}} \tag{3.11}$$

where λ = attenuation length

δx = path difference between light sources

I_1 = signal detected from light source 1

I_2 = signal detected from light source 2

I_{o1} = light intensity of source 1

I_{o2} = light intensity of source 2

Hence, to calculate the sample attenuation length using this second method, the relative intensities of the light sources must be known.

The light sources used in Harvey I were blue light emitting diodes (LEDs). The light output from these LEDs was found to be variable with temperature making it difficult to obtain accurate values of the relative light intensities of several LEDs. Hence, the first technique listed to determine attenuation length was used, as this does not require that the relative intensities of the light sources are known. The reference medium used was water purified by double osmosis, the spectral attenuation length function of which is shown in figure 3.7. Three LEDs, located at different distances from a photomultiplier tube, were used to increase the accuracy of the attenuation length measurement by recording three independent signals. For each LED the attenuation length of the sample being tested is given by equation 3.12 and the error on this value can be determined from equation 3.13.

$$\frac{1}{\lambda_s} = \frac{-ln(\frac{I_s}{I_r})}{x} + \frac{1}{\lambda_r} \tag{3.12}$$

where λ_s = sample attenuation length/m

λ_r = reference attenuation length/m

I_s = intensity of sample beam

I_r = intensity of reference beam

x = pathlength/m

$$\delta\lambda_s = \frac{x\lambda_r}{[x - \lambda_r \ln(\frac{I_s}{I_r})]^2}\sqrt{x^2(\frac{\delta\lambda_r}{\lambda_r})^2 + \lambda_r^2 \ln(\frac{I_s}{I_r})^2 (\frac{\delta x}{x})^2 + \lambda_r^2[(\frac{\delta I_s}{I_s})^2 + (\frac{\delta I_r}{I_r})^2]} \tag{3.13}$$

I_s, I_r, λ_r, x = as defined in equation 3.12

$\delta\lambda_s$ = error in sample attenuation length/m

$\delta\lambda_r$ = error in reference attenuation length/m

δx = error in pathlength/m

δI_s = error in intensity of sample beam

δI_r = error in intensity of reference beam

The attenuation length of a sample of water was determined as follows. Firstly the device was submerged in the reference medium and the signals from each LED recorded giving the values of I_r in equation 3.12. In practice this calibration is performed by placing the device in a vertical pipe filled with purified water (the calibration pipe). The device is then submerged in the sample medium and the LED signals recorded giving the value of I_s, in equation 3.12.

The reference attenuation length, λ_r, used in equation 3.12, corresponds to the attenuation length which would be measured by Harvey I submerged in purified water. To calculate the value of this attenuation length, we need to determine the amount of light emitted by a blue LED which is detected by a 50mm RCA 8575 bialkali photomultiplier tube, after the light has passed through a known pathlength of purified water plus the glass window in front of the tube. This effective attenuation length can be calculated using equation 3.9 in which the parameter, $weight(\lambda)$, is equal to the product of the light intensity output of the LED, the transmission of the glass window and the peak quantum efficiency of the photocathode at each wavelength considered. The resulting effective attenuation length for purified water is 14.7 metres. This procedure is also used to compare the attenuation length of water samples, as measured on the spectrometer, with the *in situ* attenuation lengths measured using Harvey I.

3.6.2 Physical Description

Harvey I consisted of three blue LEDs located at distances of 0.5, 1.0 and 1.5 metres from a 50mm RCA 8575 photomultiplier tube as shown in figure 3.13. The LEDs were highly directional. Hence, diffusing lenses were placed in front of each LED to ensure that light hitting the photomultiplier tube remained constant if the LEDs moved slightly. The photomultiplier tube and associated electronics were contained in an aluminium pod with the PMT viewing the LED light through a glass window.

To take an *in situ* measurement of attenuation length, the whole device was suspended vertically from a winch on a boat. Two cables ran from the boat to the

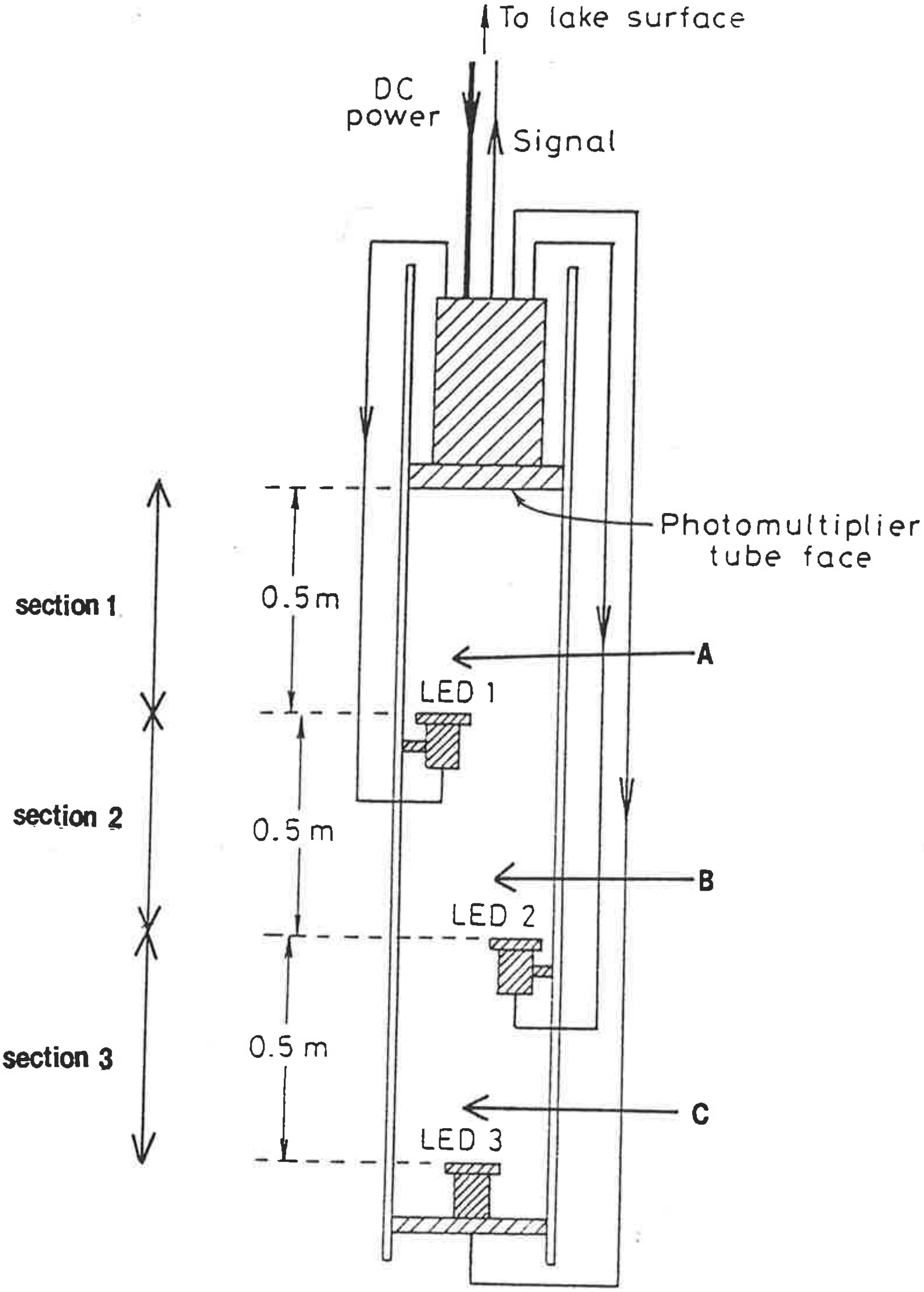

Figure 3.13: Schematic view of Harvey I

device:- one carrying 20 volts DC power from a battery located on the boat to the electronics in the aluminium pod, and the other carrying the photomultiplier signals from Harvey I to a multi-channel analyser (MCA) on the boat. The MCA recorded the frequency of signal pulses as a function of the pulse heights.

3.6.3 Electronics

As it was necessary that Harvey I be operated from a boat, all the electronics were powered by a 12 volt car battery. The 12 volt ouput from the car battery was input to a DC step-up transformer, thus providing the required 20 volts DC to power the electronics. The electronics contained in the photomultiplier tube pod of HarveyI consisted of a 1.5kV high voltage supply to power the photomultipler tube, a circuit controlling the light output from the LEDs, and a LeCroy TRA1000 amplifier which inverted and amplified signals from the photomultiplier tube. A block diagram of the electronics used in Harvey I is shown in figure 3.14.

The LEDs were set to flash succesively with pulse widths of $10\mu s$. The rate at which each LED is pulsed and the light output from each LED were variable parameters. The light output from each LED was set such that the 3 signals registered (one from each LED) had different amplitudes. This ensured that 3 distinct peaks were observed when the signals were recorded using the MCA. The position of each peak along the x-axis was proportional to the amplitude of the corresponding signal pulse. To identify which peak corresponded to which LED, the LEDs flashed at different rates. Each LED therefore corresponded to a specific pulse frequency. The LED signals could then be identified from the relative heights of the 3 peaks registered by the MCA.

The signals from the photomultiplier tube were inverted and amplified by the TRA1000 amplifier contained in Harvey I and then by the variable gain voltage amplifier on the boat. The amplified signals were then registered on the MCA. A typical signal registered on the MCA is shown in figure 3.15.

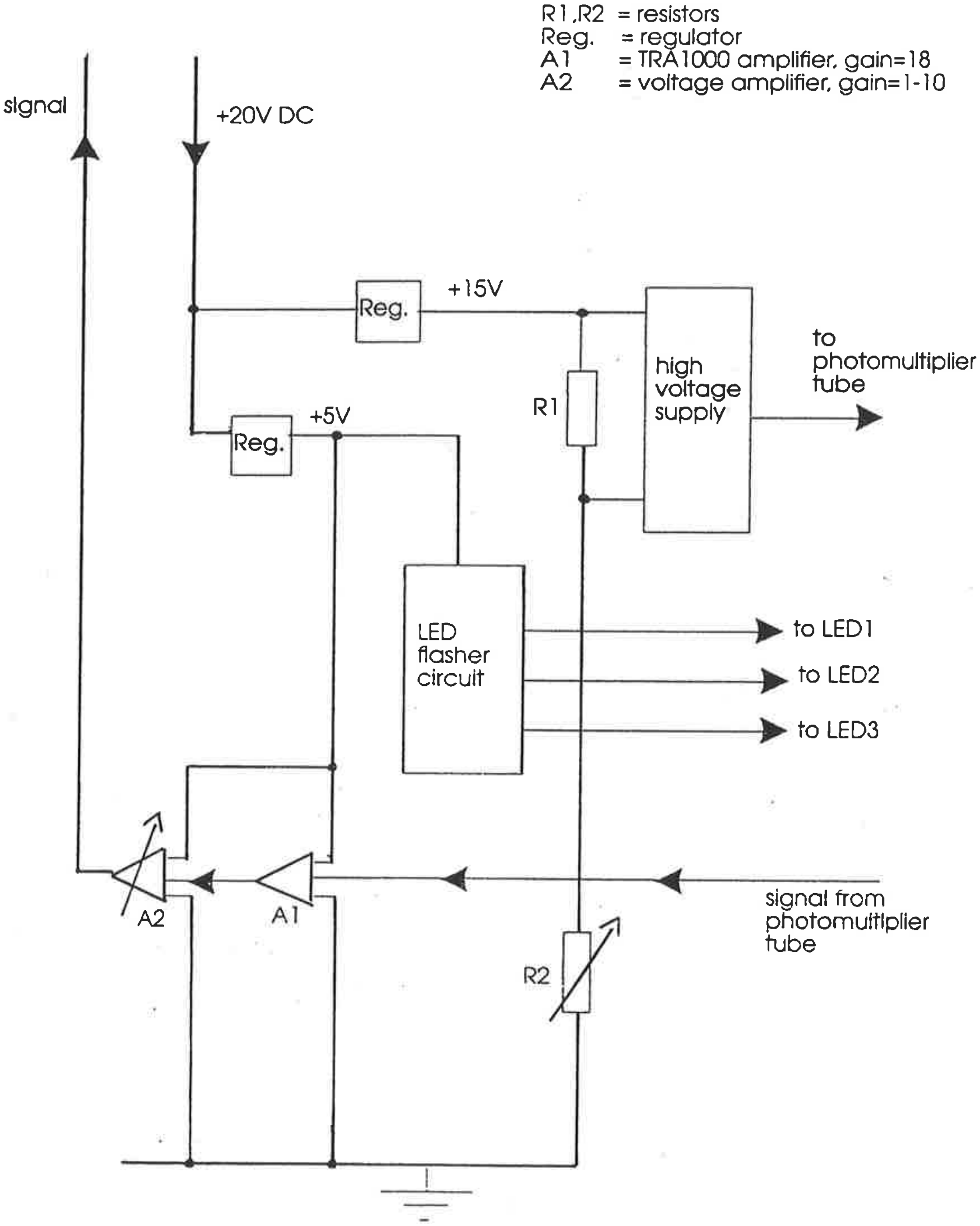

Figure 3.14: Block diagram of electronics for HarveyI

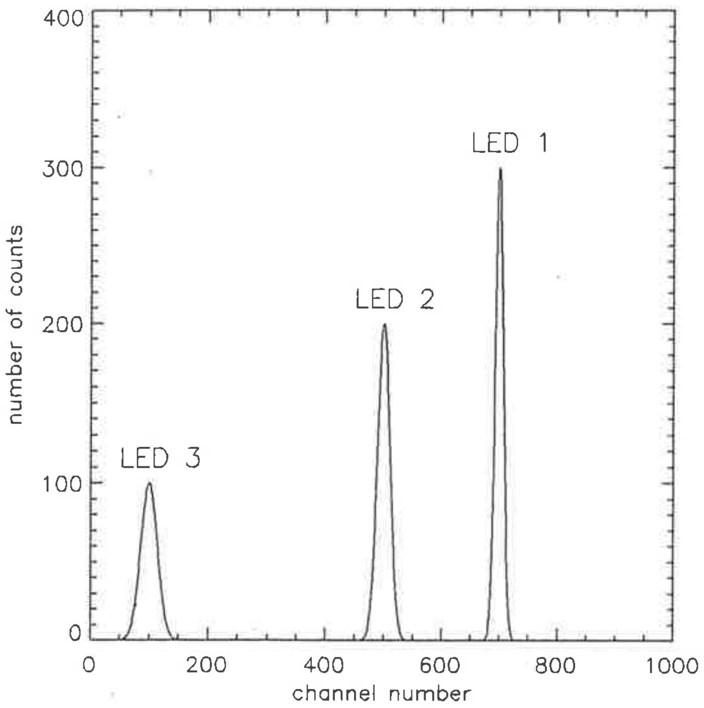

Figure 3.15: Typical signals from 3 pulsed LEDs registered using Harvey I

3.6.4 Preliminary Tests in Air

Harvey I was first tested in air in the laboratory. Several aspects of the device were investigated and are described below.

3.6.4.1 Linearity of Response

The proposed method of calculating attenuation length relies on the assumption that the intensity of light hitting the photomultiplier is proportional to the signal recorded on the MCA. This assumption holds only if the response of the photomultiplier tube is linear. The photomultiplier tube will show a non-linear response if the amount of light hitting the tube is too high, i.e. if the photomultiplier tube is saturated. To determine the range of light outputs for which the photomultiplier response is linear, the brightness of the closest LED was varied and the signals recorded when a range of filters were placed on the photomultiplier tube face. The ratio of signals with and without a specific filter in place will be constant for all LED outputs which do not cause the photomultiplier tube to saturate. For example, if we use a 50% filter, the ratio of the filtered to unfiltered signal will be 0.5, providing the photomultiplier tube is not saturating. If saturation is occurring then the gain of the photomultiplier tube is reduced and the ratio of filtered to unfiltered signals will be less than 0.5.

The ratio of filtered to unfiltered signals was measured for 3 filters placed on the photomultiplier tube face and for 7 different levels of brightness of the closest LED.

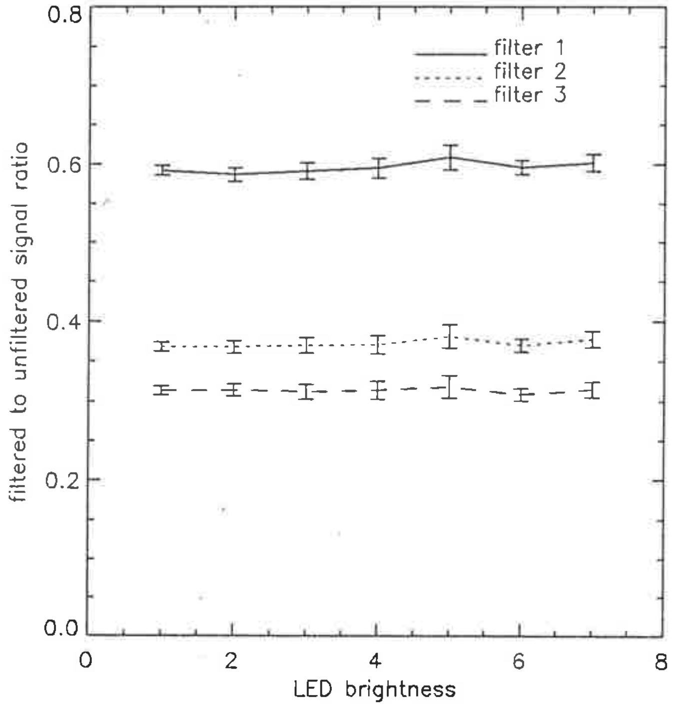

Figure 3.16: Ratio of filtered to unfiltered signal as a function of LED brightness, ranging from the maximum brightness level (1) to the minimum brightness level (7). The results shown are for 3 filters and for a photomultiplier tube voltage of 1500 volts

The results of signal ratio as a function of LED brightness, for the 3 filters considered, are shown in figure 3.16. The LED brightness is not known absolutely but ranges from the brightest possible setting, labelled 1, to the dimmest setting, labelled 7. The results shown are for a photomultiplier tube voltage of 1500 volts, which is the maximum voltage that can be applied to the photomultiplier tube in Harvey I. These results show that the ratio of filtered to unfiltered signal is constant, to within errors, for the full range of LED brightness considered. Hence, the photomultiplier tube response is linear across this range of LED outputs. The light levels of the three LEDs were then set within this range to produce three distinct signals on the MCA.

3.6.4.2 Variations with Temperature

The LED outputs and the response of the photomultiplier tube and associated electronics are all temperature dependent. During the summer, the temperature of water in the Blue Lake can vary by up to about 7°C from the surface to the bottom. To assess the effect of this variation in temperature on the signal levels registered by Harvey I, the temperature response of the complete system was measured. The LED signals for Harvey I, operating in air of ambient temperature ranging from 10°C to 23°C, were recorded and the results are shown in figure 3.17.

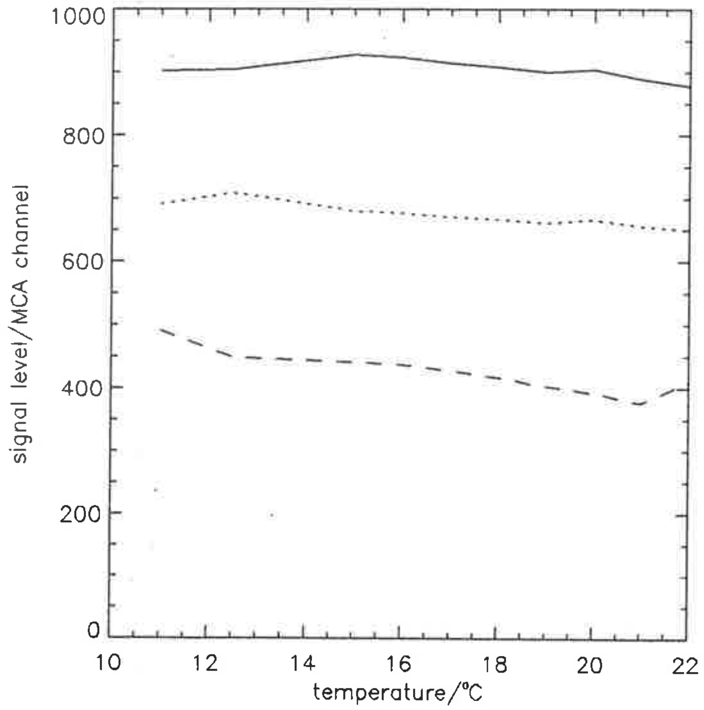

Figure 3.17: Signal levels as a function of air temperature for the three LEDs

From these results, the expected error in signal levels recorded in the lake, due to temperature variations, can be deduced. This error will be greatest during the summer when the water temperature in the lake shows the greatest variation.

During winter the water temperature is almost constant throughout the lake and the corresponding error in signal levels is negligible.

3.6.4.3 Variations due to Orientation

The light levels recorded in the laboratory were highly dependent on the orientation of Harvey I. This was found to be due to a combination of variations in the response of the photomultiplier tube due to changes in orientation relative to the Earth's magnetic field, and the effect of light scattering from the surroundings.

To separate out just the magnetic variations, a LED was placed directly on the photomultiplier tube face and the signals recorded as Harvey I was rotated about a horizontal axis along the length of the device as shown in figure 3.18.

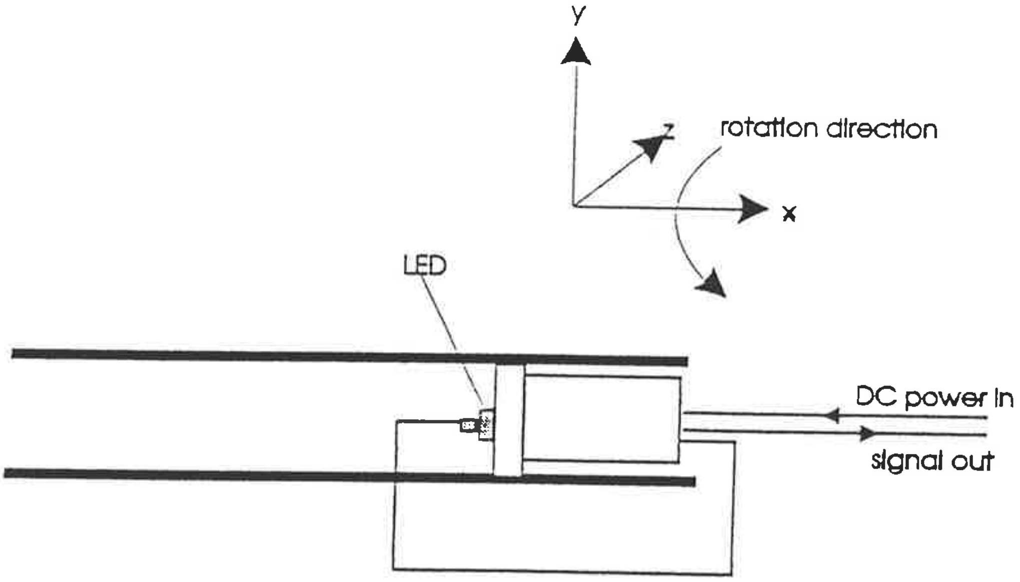

Figure 3.18: Experimental arrangement to measure signal levels as a function of rotation angle

The measurements were then repeated with the photomultiplier surrounded by mu-metal which provides shielding from magnetic fields. The results of both tests are compared in figure 3.19.

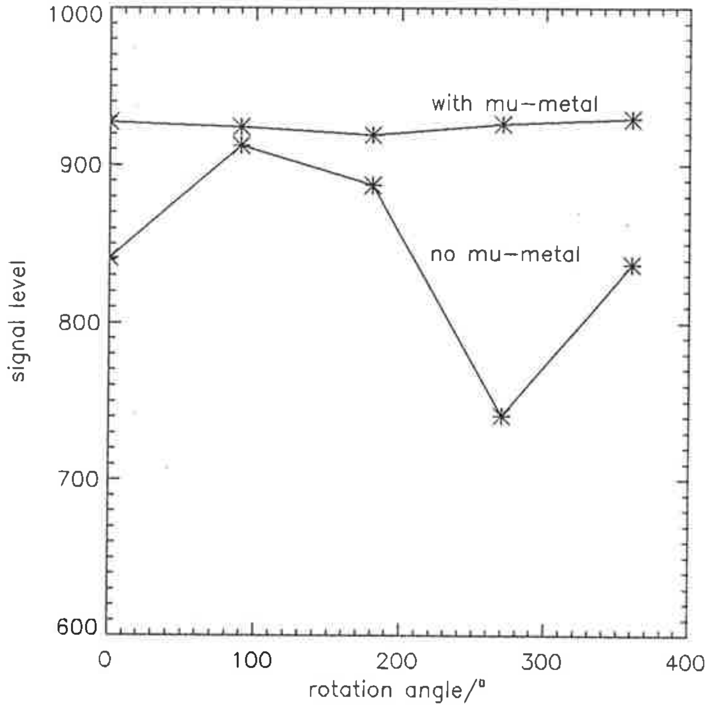

Figure 3.19: Signal levels in photomultiplier tube as a function of rotation angle with and without mu-metal shielding around the photomultiplier tube.

From these results it can be seen that the inclusion of magnetic shielding around the photomultiplier tube greatly reduces the variations in signal levels with orientation. However, there is still a residual magnetic effect. For this reason, the orientation of Harvey I during *in situ* measurements in the lake must be kept constant. The LED levels in the calibration pipe, which are used to determine the attenuation length of lake water, are recorded at the same orientation as Harvey I during measurements in the lake.

Having reduced the magnetic effects to a minimum, the LED signals recorded were still found to be dependent on the operating conditions of Harvey I. In particular, the signals recorded when the device was placed inside the calibration pipe were of the order of 25% higher than those recorded outside of the pipe. This indicated that light scattering from the surroundings is a significant factor. This is an undesirable effect as variations due to different amounts of light scattering in the calibration pipe and *in situ* in the lake may mask any effects due to light attenuation by the water. To reduce the amount of light scattered into the photomultiplier tube from the surroundings, the light from the LEDs was collimated by placing a series of apertures between the LEDs and the photomultiplier tube. The area of each aperture was the same as the area of the photomultiplier tube face. Collimating the beam in this manner significantly reduced the scattering effects in air and the difference between the signals recorded with Harvey I placed in and out of the calibration pipe was decreased to a maximum of 7%.

3.6.5 Preliminary Tests in Water

3.6.5.1 Measurement of Tap Water Attenuation Length

The proposed technique for determining attenuation length was tested in the laboratory by measuring the attenuation length of tap water using Harvey I. To do this, Harvey I was placed in the the calibration pipe and the LED signals were recorded with the calibration pipe filled first with purified water and then with tap water. The attenuation length of the tap water can then be determined from equation 3.12. The resulting values of attenuation length, calculated for each of the three LEDs are summarised in table 3.1.

Immediately after the signal levels of the LEDs in Harvey I were recorded, a sample of tap water was collected from the top of the calibration pipe and the attenuation length of this sample was measured on the spectrometer. The average attenuation length, corresponding to the detection of blue LED light using Harvey I, was then determined using equation 3.9 in which $weight(\lambda)$ is the product of the light output from a blue LED, the transmission of the glass window and the peak quantum efficiency of the photomultiplier tube at each wavelength considered. The resulting average attenuation length, as measured using the spectrometer, is also listed in table 3.1. From these results it can be seen that the attenuation length of tap water measured using the spectrometer and Harvey I agree to within errors.

		attenuation length/m
Harvey I	LED1	1.2 ± 0.2
	LED2	1.1 ± 0.3
	LED3	1.3 ± 0.2
spectrometer		1.1 ± 0.05

Table 3.1: Attenuation length of tap water determined using Harvey I and a spectrometer

3.6.5.2 Pool Tests

Prior to deploying Harvey I in the Blue Lake, the device was tested in a swimming pool. The tests were performed at night with the pool covered with opaque plastic to reduce the amount of background light present. In the pool, the signals recorded again showed a noticeable variation for different operating conditions of the device. In particular, the signal levels recorded when Harvey I was placed vertically in the centre of the pool and vertically at the side of the pool were significantly different. Hence, although the effect of scattering in air was negligible there was still a significant scattering effect in water. A series of tests were performed to investigate ways of reducing this scattering. Increasing the number of apertures along the light beam had a negligible effect, hence it was decided to surround Harvey I with a rigid black plastic shield. This removed any remaining effects due to light scattering. The final design of Harvey I, as used in the Blue Lake measurements, consisted of the original device as shown in figure 3.13 with five apertures along the light path and the whole device surrounded with a black plastic shield (see figure 3.20). The plastic shield is open at the top and bottom so that water can still pass through the device.

3.6.6 *In Situ* Measurements in the Blue Lake

A series of *in situ* measurements in the Blue Lake were taken over a period of a year. A description of the measurement technique and the results of the two major field tests are presented.

3.6.6.1 Measurement Technique

The aim of the *in situ* measurements was to determine the attenuation length of Blue Lake water as a function of depth. The measurements were performed at night from a boat anchored at site 2a on the lake (see figure 3.2). Harvey I was attached to a winch on the boat and suspended vertically with the photomultiplier tube looking downward to minimise the flux of background light hitting the photomultiplier (see figure 3.20).

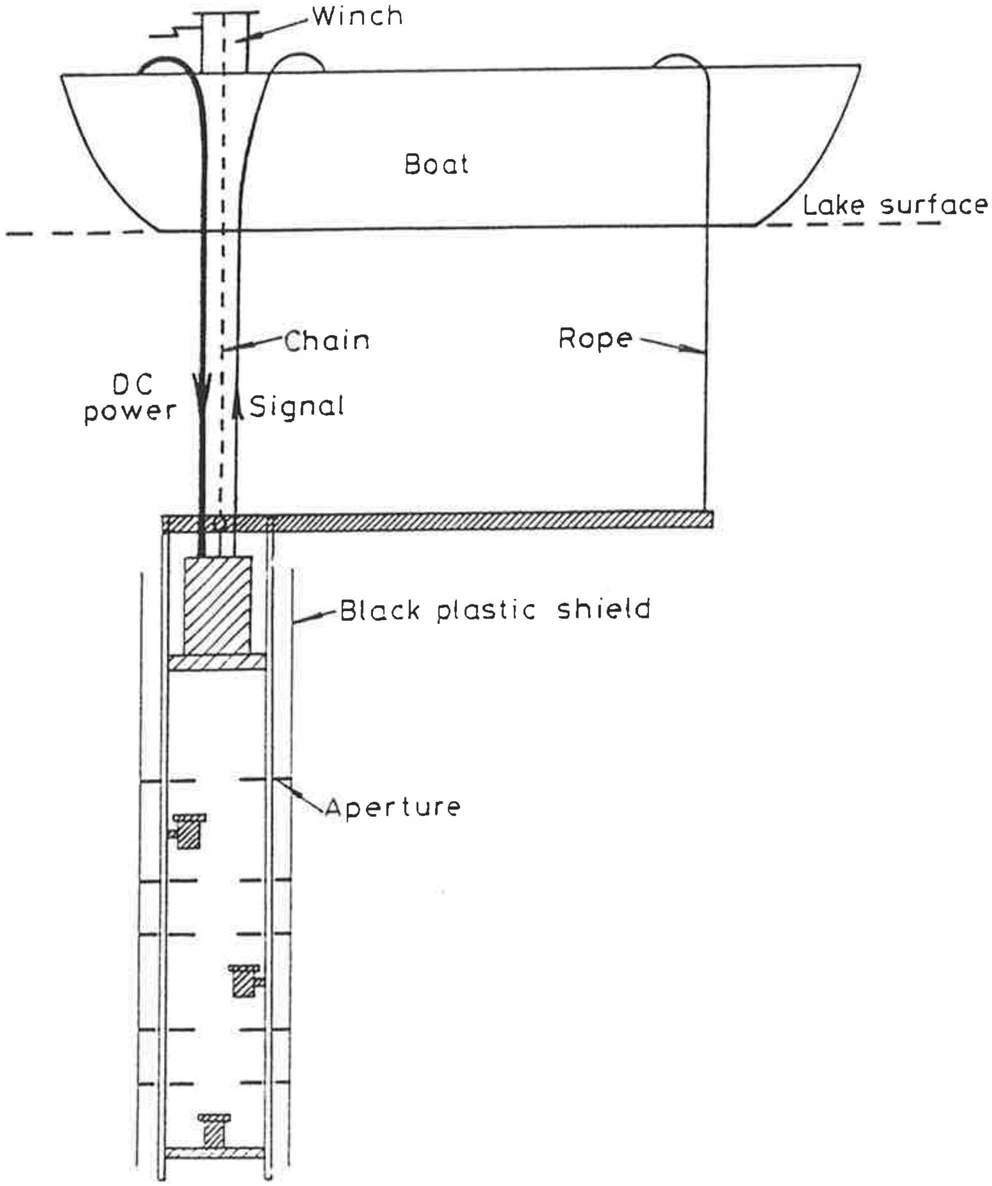

Figure 3.20: Cross-section of Harvey I during *in situ* measurement

The horizontal bar was present to prevent the device from rotating about the vertical axis and hence ensure that the orientation of Harvey I remained constant at all depths. The bar was attached to the boat via a rope which was released concurrently with the winch cable. A typical set of measurements was taken by lowering Harvey I from the lake surface to the bottom and recording the LED signals at 10 metre intervals. This process was then repeated while Harvey I was raised from the bottom of the lake back up to the surface. Hence, two sets of results are obtained for each depth in the lake:- one set corresponding to Harvey I being lowered through the lake and the other set corresponding to Harvey I being raised through the lake. The orientation of Harvey I in the lake was recorded to enable signal levels in the calibration medium to be recorded at the same orientation as the measurements taken in the lake.

Harvey I was calibrated at the side of the lake by placing it in the calibration pipe filled with purified water. Ice made from purified water was added to the water in the calibration pipe to reduce the temperature of the calibration medium to approximately the same temperature as the water in the lake. The device was rotated about the vertical axis and the LED signals recorded at approximately 45° intervals (see figure 3.21).

The attenuation length of lake water, calculated for each LED, can then be determined using equation 3.12 in which I_s is the LED level recorded in the lake, I_r is the LED level recorded in the calibration pipe at the same orientation as the lake measurements, λ_r is the attenuation length of purified water averaged over the spectral response of Harvey I, and x is the distance between the LED and the photomultiplier tube face.

3.6.6.2 Results of *In Situ* Measurements

December 1992

The first results presented correspond to measurements taken on 2nd December 1992. This was one of the first *in situ* tests using Harvey I and results were obtained

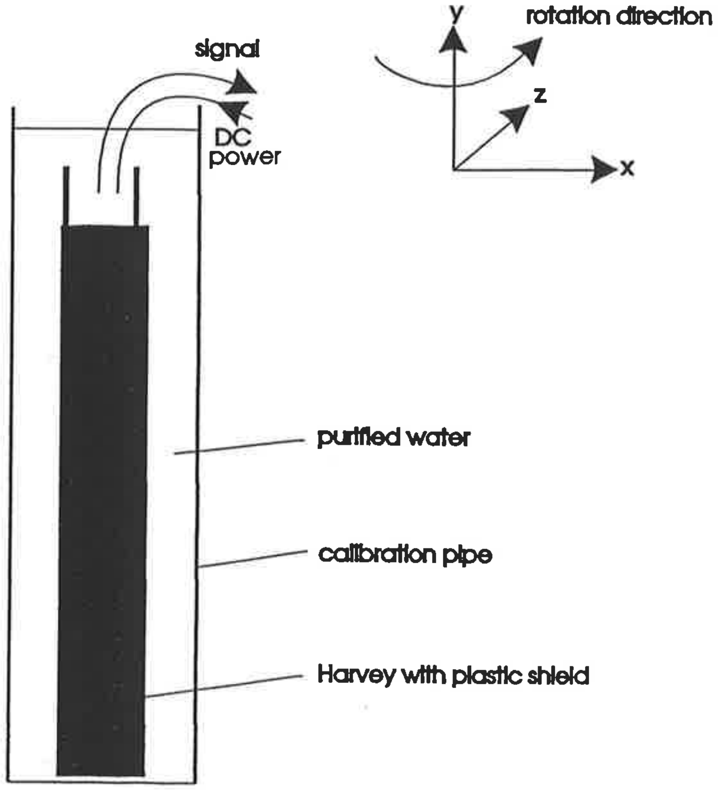

Figure 3.21: Schematic of calibration pipe showing rotation direction for calibration measurements

for depths from 30 metres to 65 metres. The device was placed in the lake and the signal levels recorded at 5 metre intervals while being lowered and then raised through the lake. The signal levels recorded from each LED are shown in figure 3.22. The signal levels registered from LED2 and LED3 were indistinguishable.

Harvey I was then calibrated in purified water and the resulting signal levels as a function of rotation angle are shown in figure 3.23. The variations in the calibration levels are due to the residual magnetic field which is not shielded out by the mu-metal around the photomultiplier tube.

From the results shown in figures 3.22 and 3.23 it can be seen that the signal levels in the lake were higher than those recorded in the calibration pipe. This implies that either the lake water was clearer than distilled water or that the optical properties of the calibration water deteriorated in the calibration pipe. To determine if the calibration water did change when put into the calibration pipe, a sample of water was collected from the top of the calibration pipe at the same time the

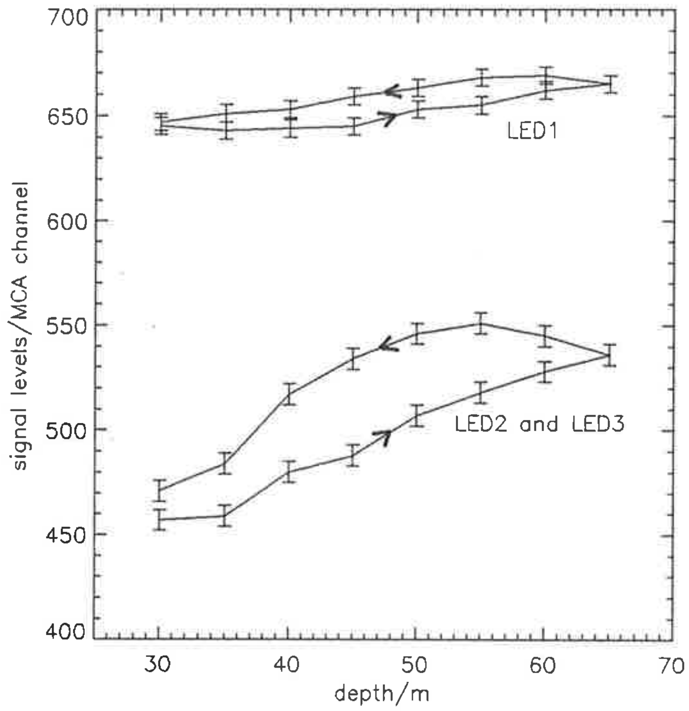

Figure 3.22: Signal levels recorded using Harvey I in the Blue Lake as a function of depth. Results are presented for Harvey I being lowered and then raised through the lake

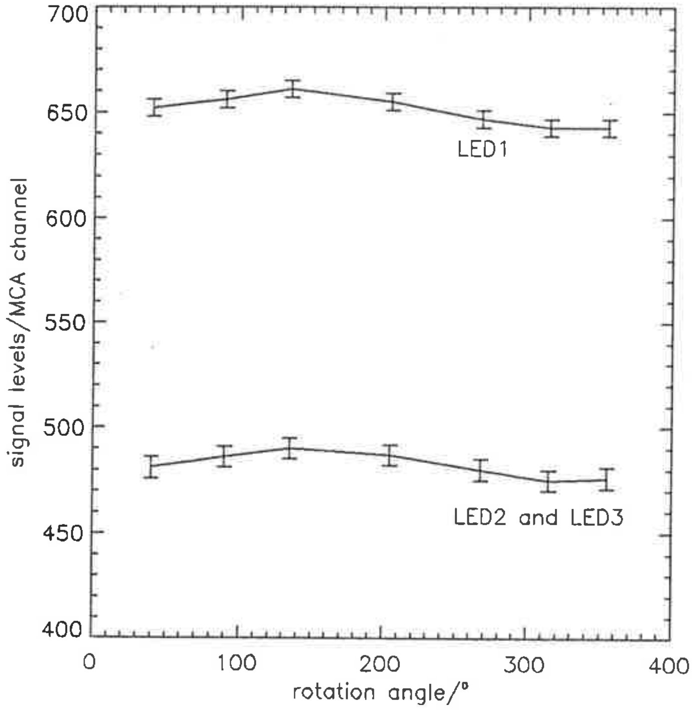

Figure 3.23: Signal levels recorded using Harvey I during calibration as a function of rotation angle

calibration measurements were recorded. The attenuation length of this sample was measured on the spectrometer. The resulting spectral attenuation lengths are shown in figure 3.24 and correspond to an attenuation length, averaged over the spectral response of Harvey I, of 4.1 ± 0.1 metres. This is significantly lower than the predicted average attenuation length of purified water which was calculated to be 14.7 metres. Hence the purified water does become contaminated when placed in the calibration pipe, resulting in a decrease in the attenuation length of the calibration medium. This deterioration in optical transmission of the calibration water occurs despite steps which were taken to minimise this effect, including rinsing both the calibration pipe and Harvey I with distilled water prior to the calibration procedure.

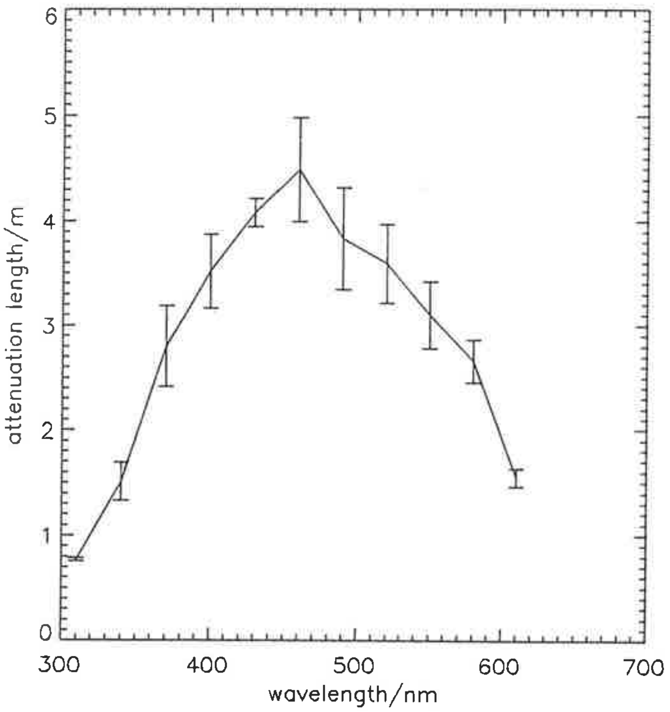

Figure 3.24: Attenuation length of water in calibration pipe as a function of wavelength

Assuming that the attenuation length of the calibration water was 4.1 ± 0.1 metres, the attenuation length of water, at each depth tested in the lake, was calculated using equation 3.12 and the results are shown in figure 3.25.

These results show that the measured attenuation lengths in the lake are dependent on whether the device is being lowered or raised. The cyclic variation of

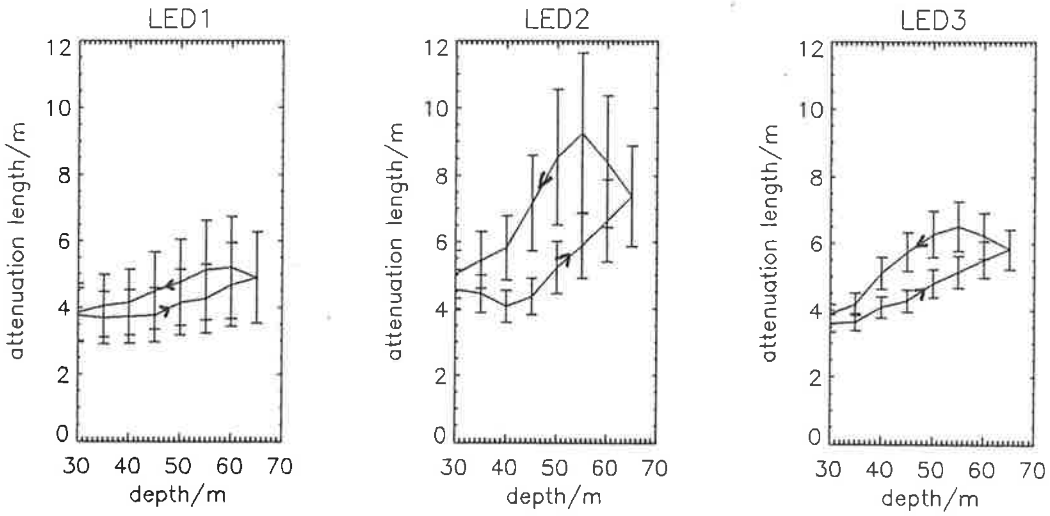

Figure 3.25: Attenuation lengths measured using Harvey I during February 1993. Results are presented for Harvey I being lowered and then raised through the lake

the measured values is consistent with the possibility that water circulation inside the plastic shield around the device is restricted such that water is not mixing completely as the position of the device is changed. Harvey I was originally designed to operate without being enclosed in a plastic shield, thus allowing a free flow of water between the LEDs and the photomultiplier tube. However the presence of the plastic shield in combination with the apertures, which were included to minimise the effects due to light scattering, greatly reduced the circulation of water. It is therefore possible that water is dragged along with the device as it is moved through the lake, resulting in the hysteresis pattern apparent in figure 3.25. To improve the flow of water in subsequent tests the plastic shield was increased in radius and spaced further from the apertures.

The conclusions reached at the end of this field trip were that the calibration water degrades significantly in the calibration pipe and hence it cannot be assumed that it has the same optical properties as purified water. To determine the attenuation length of the calibration water, a sample of water from the calibration pipe must be collected simultaneously with the recording of the LED levels during the calibration procedure. The attenuation length of this sample can then be measured on a spectrometer.

Also, it is likely that water inside the device is not mixing sufficiently as the depth at which Harvey I is located is changed. Hence, different attenuation lengths are measured at the same position in the lake depending on whether the device is being lowered or raised. In subsequent tests the shielding surrounding the device has been spaced further from the apertures to attempt to increase the circulation of water through the device.

September 1993

The following results correspond to the final field tests performed on the 2nd September 1993. The measurement procedure was similar to that used in the December tests. Harvey I was submerged in the lake and the LED signal levels recorded at intervals of 10 metres while the device was first lowered and then raised through the lake. The resulting LED signals as a function of depth are shown in figure 3.26.

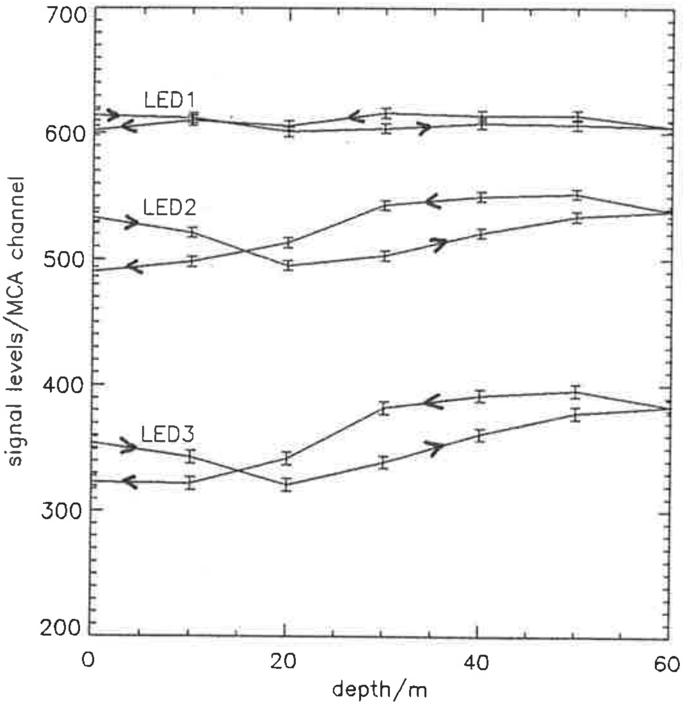

Figure 3.26: LED levels as a function of depth for field tests in September 1993. Results are presented for Harvey I being lowered and then raised through the lake

At each depth considered, a sample of lake water was collected. The attenuation length of each sample was later measured on a spectrometer, thereby providing a direct comparison between the attenuation lengths determined using Harvey I and the spectrometer. Harvey I was then submerged in purified water contained in the calibration pipe and the LED levels were recorded with Harvey I at the same orientation as for the measurements taken in the lake. To assess the degradation of the optical properties of the calibration water, the LED levels in the calibration pipe were recorded over a period of about 40 minutes. The results are shown in figure 3.27.

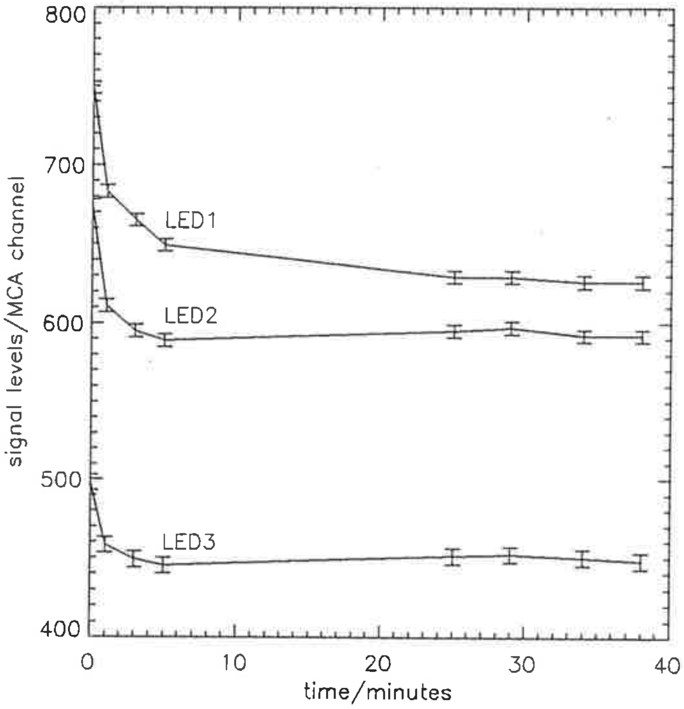

Figure 3.27: LED levels as a function of time as recorded in the calibration pipe in September 1993

While the LED signals in the calibration pipe were being recorded, 3 water samples were collected from the calibration pipe at times of 29 minutes and 38 minutes. The samples were taken from just in front of each of the 3 LEDs at positions A,B and C shown in figure 3.13. For each sample, the attenuation length as a function of wavelength was measured on the spectrometer. The average attenuation length corresponding to the measurement of blue LED light using

	Attenuation length/m		
	sample A	sample B	sample C
time=29mins	5.8 ± 0.3	8.5 ± 1.2	7.3 ± 0.5
time=38mins	6.9 ± 0.3	7.0 ± 0.7	6.8 ± 0.3

Table 3.2: Effective attenuation length of water samples collected from in front of each LED in the calibration pipe at time periods of 29 and 38 minutes, measured using a spectrometer

Harvey I was then calculated using equation 3.9 in which $weight(\lambda)$ is the product of the spectral output from the blue LEDs, the peak quantum efficiency of the photocathode and the spectral transmission of the glass window. The resulting values of average attenuation length for the 3 samples collected at positions A,B and C in the calibration pipe, at the 2 times considered, are listed in table 3.2.

From these results it can be seen that the optical properties of the calibration water vary with time and with position in the calibration pipe. Hence, when calculating the attenuation length of lake water using equation 3.12, the value of attenuation length of the calibration water used (λ_r) will be different for each LED and will also depend on the time at which the calibration signal levels are recorded by Harvey I. To take account of these factors in determining the attenuation length of lake water, the following procedure was used. The signal levels recorded in the calibration pipe (I_r) were measured simultaneously with the collection of water samples from in front of each LED. Harvey I was considered to be in three sections of length 0.5 metres as shown in figure 3.13. It was assumed that the average attenuation length of the water in section 1 of Harvey I was equal to the effective attenuation length of the water samples collected from position A, and similarly, that the attenuation lengths of water in sections 2 and 3 were equal to that of the water samples collected from positions B and C respectively. The attenuation length of calibration water that would be measured by each LED (λ_r in equation 3.12) is then given by equation 3.14. The resulting values of calibration water attenuation length, as would be measured by each LED in Harvey I, are listed in table 3.3. From these results it can be seen that the attenuation length corresponding to each LED depends on the position of the LED and also on the length of time the water has been in the calibration pipe.

$$\begin{aligned}\lambda_{r1} &= att(A) \\ \lambda_{r2} &= \frac{2 \times att(A)att(B)}{att(A) + att(B)} \\ \lambda_{r3} &= \frac{3 \times att(A)att(B)att(C)}{att(A)att(B) + att(A)att(C) + att(B)att(C)}\end{aligned} \qquad (3.14)$$

where λ_{r1} = calibration attenuation length for LED1
λ_{r2} = calibration attenuation length for LED2
λ_{r3} = calibration attenuation length for LED3
$att(A)$ = attenuation length of water sample from A
$att(B)$ = attenuation length of water sample from B
$att(C)$ = attenuation length of water sample from C

	Attenuation length/m		
	LED1	LED2	LED3
time=29mins	5.8 ± 0.3	6.9 ± 0.4	7.0 ± 0.2
time=38mins	6.9 ± 0.3	6.9 ± 0.4	6.9 ± 0.1

Table 3.3: Attenuation length of calibration water corresponding to each LED after 29 and 38 minutes in the calibration pipe

The attenuation length of lake water can then be calculated from equation 3.12 and the error on these values is given by equation 3.13. The attenuation length of lake water was calculated for the two sets of calibration measurements:- the first taken at 29 minutes and the second at 38 minutes in the calibration pipe. For each calibration measurement, 3 values of attenuation length were determined corresponding to the 3 LEDs. The values of signal levels in the lake (I_s) are shown in figure 3.26, the values of signal levels in the calibration pipe (I_r) correspond to the signal levels recorded at 29 minute and 38 minutes and are shown in figure 3.23, and the attenuation length of the calibration water for each LED (λ_r) is listed in table 3.3. The resulting values of attenuation length of lake water as a function of depth, for the two calibrations considered, are shown in figures 3.28 and 3.29. Also shown in these figures is the average attenuation length as a function of depth, for the water samples collected in the lake and analysed on the spectrometer.

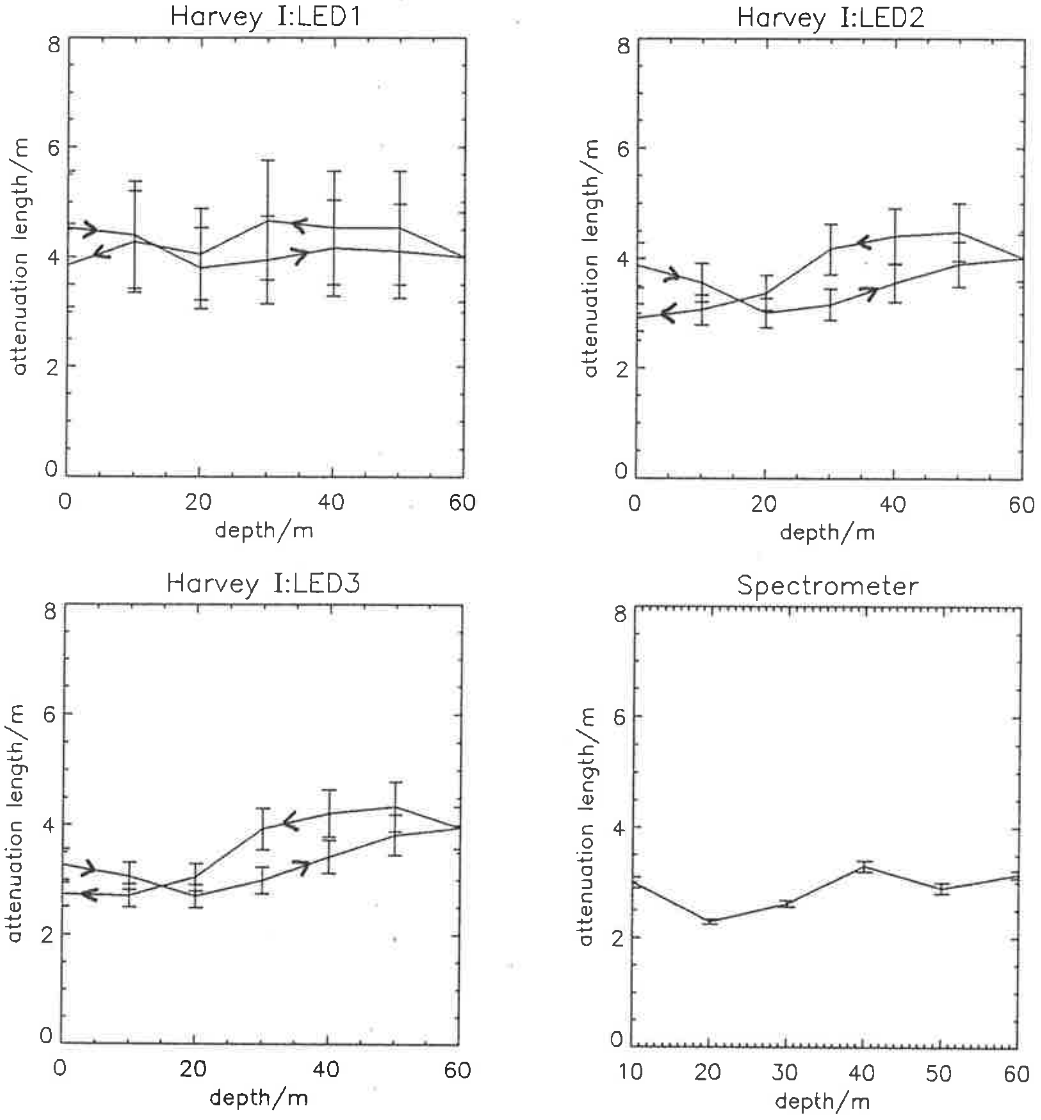

Figure 3.28: Attenuation length as a function of depth as measured using Harvey I and the spectrometer during September 1993 field tests. The Harvey I results correspond to the device being lowered and then raised through the lake. Calibration measurements taken after 29 minutes in the calibration pipe

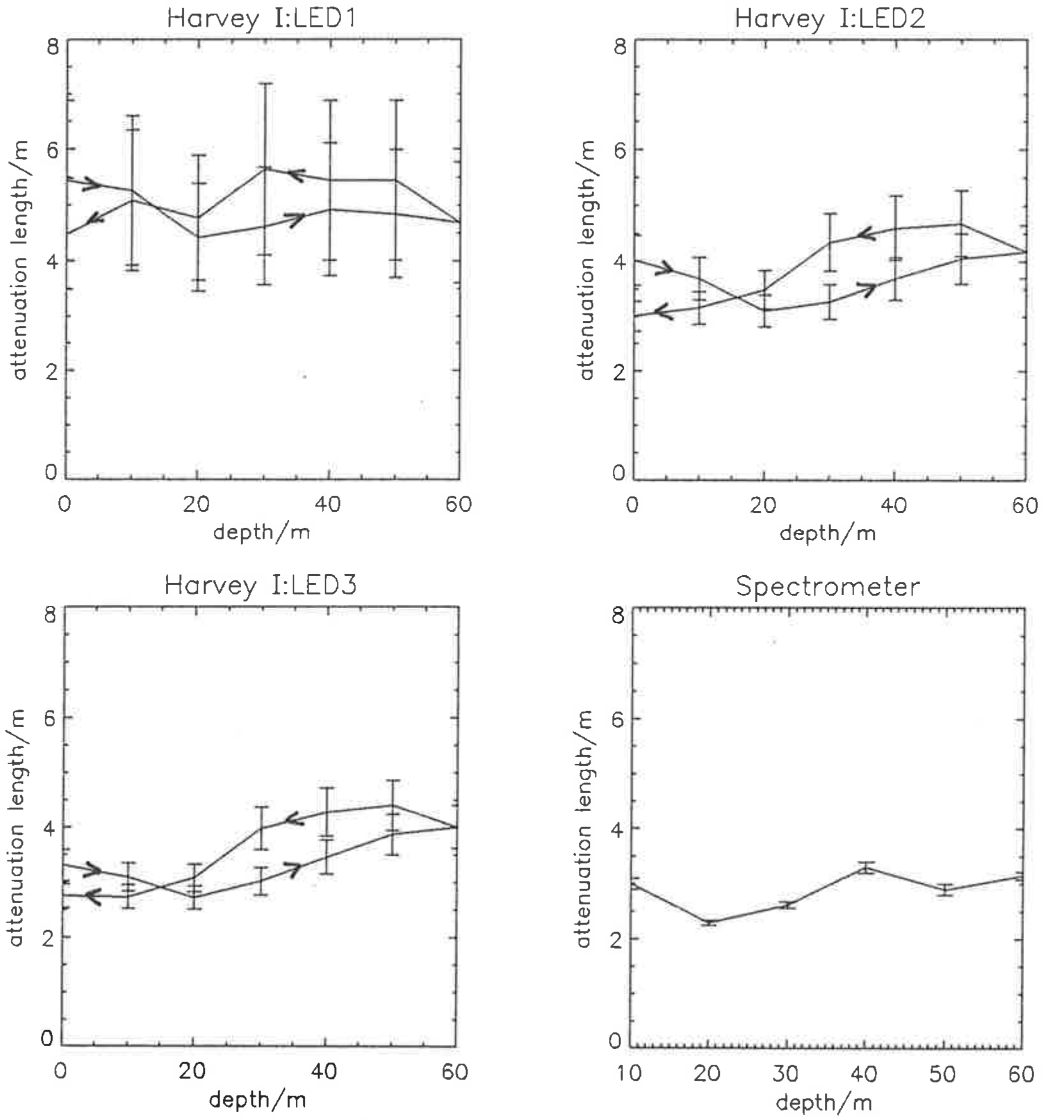

Figure 3.29: Attenuation length as a function of depth measured using Harvey I and a spectrometer during September 1993 field tests. The Harvey I results correspond to the device being lowered and then raised through the lake. Calibration measurements taken after 38 minutes in the calibration pipe

From these results it can be seen that the attenuation length of lake water measured by Harvey I differs for each LED. Also, the two calibrations used result in different values of lake water attenuation length, particularly in the case of the closest LED. Both these factors may be due to the uncertainty in the value of calibration water attenuation length used. It has been shown that the optical properties of the calibration water vary with time and with position in the calibration pipe. In calculating the attenuation length of lake water, the calibration water attenuation length was determined from water samples collected in front of each LED in the calibration pipe. The resulting calibration water attenuation lengths are approximate values based on the assumption that the attenuation length of the water samples, collected in front of each LED, are equal to the average attenuation length of water in the corresponding section of Harvey I. The resulting error in the assumed values of calibration water attenuation length can result in different values of lake water attenuation length for each LED and, also, different results for different calibrations.

The variation in lake water attenuation length, determined using the two calibrations at 29 minutes and 38 minutes as shown in figure 3.28 and figure 3.29, can be used to estimate the the error due to the uncertainty in the attenuation length of the calibration water. For each LED, it can be assumed that the correct value of lake water attenuation length lies somewhere between the attenuation length values predicted using the two calibrations. The resulting range of attenuation lengths for each LED, calculated by combining the results for both calibrations, are shown in figure 3.30.

From these results it can be seen that the ranges of attenuation lengths measured by each LED overlap. Hence, it is possible that the apparent discrepancy between the attenuation length values determined for each LED is due to the uncertainty in the attenuation length of the calibration water. However, the resulting range in measured values of lake water attenuation length is large. Hence, it is difficult to obtain accurate values of lake water attenuation length using Harvey I.

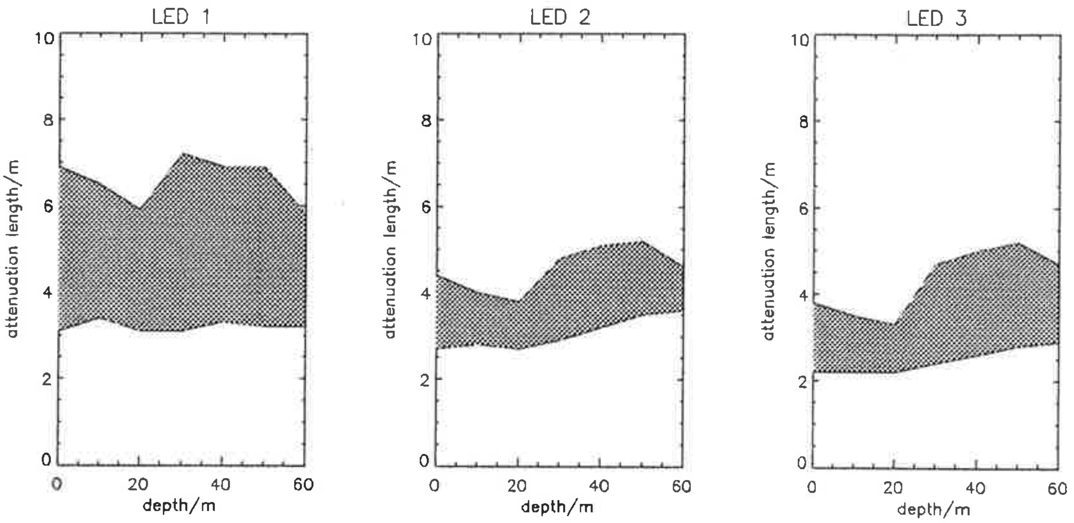

Figure 3.30: Range of attenuation lengths of lake water as a function of depth, for each LED in Harvey I

It is also apparent that the attenuation lengths predicted by Harvey I are consistently higher than those measured using the spectrometer. This will occur if Harvey I registers a greater amount of light transmitted through lake water than does the spectrometer. One explanantion for this is that Harvey I registers more scattered light than the spectrometer. This is likely as, in order to increase the water circulation through Harvey I, a gap was left between the enclosing plastic shield and the apertures. Hence, the light within Harvey I is not totally collimated and it is possible for LED light to be scattered into the field of view of the photomultiplier tube. This cannot occur in the spectrometer. Therefore, the attenuation length measured by Harvey I will be greater than the attenuation length measured on the spectrometer.

The accuracy with which the attenuation length of lake water can be determined using Harvey I is also reduced by the effects of incomplete water mixing, resulting in the hysteresis patterns shown in figures 3.28 and 3.29. This effect has been reduced relative to the results obtained during the field tests in December 1992. However, the difference between attenuation lengths calculated at the same depth when the device is being lowered and raised is still significant. This effect is difficult to eliminate totally while the flow of water through Harvey I is restricted by the presence of the enclosing plastic shield.

3.7 Conclusions

The attenuation lengths of water samples collected from the Blue lake and Weebubbie Cave, measured on the spectrometer, indicate that the water in both locations exhibits similar light transmission properties. Additionally, the water in the Blue Lake shows a seasonal variation in optical properties which is related to the water temperature. The clearest water occurs at depths greater than about 40 metres during the summer months. At these depths the Blue Lake exhibits better light transmission properties, with respect to Cerenkov light detected by photomultiplier tubes, than the water in Weebubbie Cave. From the values of attenuation lengths measured in the Blue Lake over a period of 18 months, the clearest water was recorded at a depth of 50 metres in the lake during February 1992. Using this value of lake water attenuation length, the expected Cerenkov signal in the Blue lake would be 1.2 times greater than the corresponding Cerenkov signal in Weebubbie Cave. Considering the similarity in water attenuation length at both sites, and also considering the accessibility and available surface area, then depths greater than 40 metres in the Blue Lake would be the better location for a neutrino detector.

The water in the Blue lake was also analysed *in situ* using Harvey I. The final results of attenuation length as a function of depth in the Blue Lake, as determined using Harvey I, are shown in figure 3.30 and the corresponding spectrometer results are shown in figure 3.28. The errors on the results determined using Harvey I are large due to the error in the assumed value of attenuation length of water used to calibrate the device. This error limits the accuracy with which the attenuation length of lake water can be determined using Harvey I.

The attenuation lengths as a function of depth in the lake, calculated using Harvey I, exhibit a hysteresis effect due to the restricted flow of water through the device.

Hence, the attenuation length measured at a particular depth in the lake depends on whether the device is being lowered or raised through the lake. The attenuation length measured by Harvey I does not, therefore, accurately represent the water at that position in the lake. The restricted water flow is due to the presence of apertures along the length of Harvey I in combination with the opaque shield around the device. These factors were included to minimise the effects of light scattering effects. The reduction of light scattering effects in Harvey I and the resulting errors due to restricted water circulation are conflicting aspects in the design of the device.

The attenuation lengths determined using Harvey I are consistently higher than those measured using the spectrometer. This indicates that Harvey I registers some scattered light due to the incomplete collimation of light within the device, whereas the spectrometer registers a negligible amount of scattered light. The scattering pathlength as measured on a turbiditimeter (see figure 3.12) is of the same order of magnitude as the attenuation length and hence, light attenuation in the lake is dominated by scattering processes. We would therefore expect the amount of light scattered in lake water to be significant. A device such as Harvey I, which detects scattered light, will therefore register a greater attenuation length than a spectrometer which detects practically no scattered light. In the proposed neutrino detector, uncollimated Cerenkov light will be detected by photomultiplier tubes. This detector will therefore record a greater proportion of scattered light than Harvey I. The water attenuation length relevant to the proposed neutrino detector is therefore expected to be higher again than the attenuation length measured by Harvey I.

In light of the fact that neither the spectrometer or Harvey I measure the full effect of light scattering corresponding to the proposed detector, and considering the problems associated with water mixing inherent in the design of Harvey I, a test device was designed and built which tracks individual muons and registers the resulting Cerenkov radiation. This device therefore reproduces the expected Cerenkov signals in the proposed neutrino detector. A detailed description of this device and the measurements recorded using it are presented in chapter 5.

Chapter 4

Simulations of Detector Performance

4.1 Introduction

The proposed neutrino detector will observe high energy neutrinos from astrophysical point sources, provided that a) the number of genuine signal events registered is significantly greater than the uncertainty in the number of background events and b) the detector angular resolution is sufficient to resolve point sources. Background events are any events, not due to muons produced by astrophysical neutrinos, which trigger the detector. The ratio of signal event number to uncertainty in the number of background events can be seen as a signal to noise ratio. Assuming that the number of background events registered obey Poisson statistics, then the uncertainty in the background number is proportional to the square root of the total number of background events. The signal to noise ratio is therefore given by equation 4.1.

$$\frac{S}{N} = \frac{R_s}{\sqrt{R_b}} \tag{4.1}$$

where $\frac{\mathrm{S}}{\mathrm{N}}$ = signal to noise ratio

R_s = number of signal events in a solid angle, Ω

$$R_b = \text{number of background events in a solid angle, } \Omega$$

For the detector to successfully observe signal events, the signal to noise ratio should be at least of order 3, in which case there is only a 0.1% probability that the excess events from a given direction are due to an upward fluctuation of the background count.

The angular resolution is a measure of the accuracy with which the parent neutrino direction can be determined. For an angular resolution of 1σ (defined as the standard deviation of a 2-dimensional error distribution) it can be shown that for maximum signal to noise, data should be accepted within an error circle of radius 1.6σ. This error circle will contain 72% of the signal events. The number of background events registered within the angular resolution is given by equation 4.2.

$$N_{bg} = \frac{dN}{d\Omega}\pi\theta^2 \tag{4.2}$$

where N_{bg} = number of background events within error circle

$\frac{dN}{d\Omega}$ = number of background events per solid angle

θ = error circle radius in radians

Hence, the number of background events registered, and thus the fluctuations in background event number, will increase as the angular resolution becomes worse. The signal to noise ratio and the angular resolution are therefore inter-related.

The signal to noise ratio and the angular resolution depend on parameters such as the detector geometry and the triggering conditions required to register an event. Both these factors can be assessed using Monte Carlo techniques to simulate the response of the detector. By modelling the response as a function of the detector geometry and the triggering conditions, the optimum design can be determined.

In this chapter the design and performance characteristics of a high energy surface neutrino detector are discussed. Monte Carlo simulations are used to optimise this design for a detector to be located in the Blue Lake as follows. Firstly, simulated values of angular resolution for various detector configurations are presented. Next, the expected detection rate of upward muons resulting from astrophysical neutrinos (the signal rate) is determined as a function of the geometry of the detector and the triggering conditions. The main sources of background events are then discussed and the corresponding detection rates of these events are calculated. The signal to noise ratio can thus be calculated for any running period. Finally, an optimum design for a high energy neutrino detector to be located in the Blue Lake is proposed.

4.2 Principles of the Proposed Detector

The proposed high energy neutrino detector records the Cerenkov light emitted by upward travelling muons passing through the Blue Lake. The light is detected by a three-dimensional array of photomultiplier tubes submerged in the water. The direction of the muons can be determined from the relative times at which the photomultiplier tubes register light. The proposed detector is based on a geometry of horizontal layers of downward looking photomultiplier tubes with the photomultiplier tubes in each layer arranged on a square grid as shown in figure 4.1. The number of layers, the vertical separation between the layers and the grid spacing in each layer are variable parameters which affect the detector response.

4.2.1 Registering an Upward Travelling Muon

In the proposed detector an upward travelling muon will produce Cerenkov light which directly hits some of the photomultiplier tubes in each layer. Signals are also recorded in the photomultiplier tubes as a result of photomultiplier tube noise, background light and Cerenkov light from other relativistic particles passing through the detector. The main problem with surface neutrino detectors is discriminating between the real signal and the background noise signals. This is achieved by applying a combination of on-line hardware conditions which must be met in order

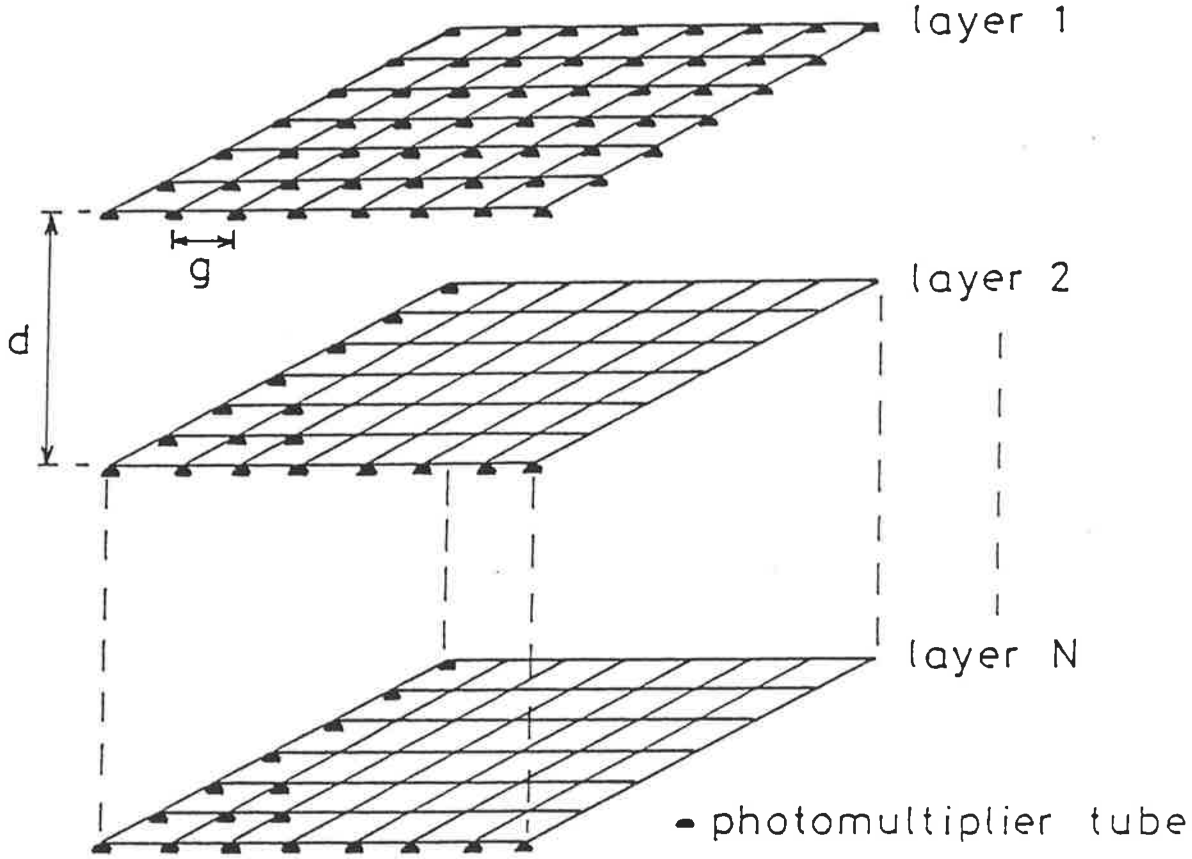

Figure 4.1: Geometry of the proposed neutrino detector

for the detector to register an event (the triggering criteria) and off-line software analysis which differentiates between the events registered which are due to upward travelling muons and the background events which also trigger the detector.

The triggering scheme for the proposed detector is designed to preferentially detect upward going muons which pass through the array. An upward travelling muon will pass through each layer sequentially from the lowest layer upwards and will illuminate several adjacent photomultiplier tubes in each layer as shown in figure 4.2

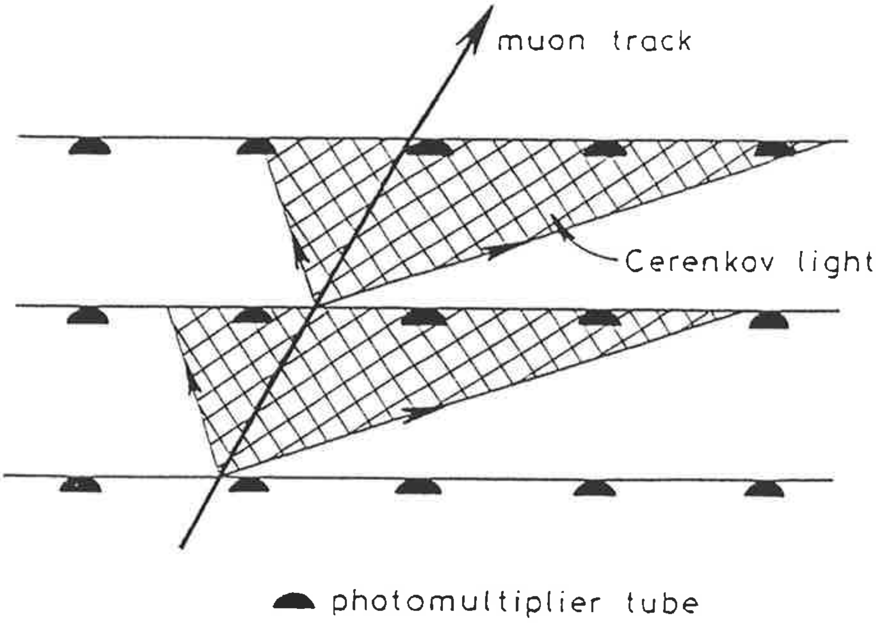

Figure 4.2: Schematic view of muon travelling upwards through the detector

There are two time periods associated with the identification of an upward muon signal. The first corresponds to the time taken for a muon to travel through the detector, t_{flight}, and the second relates to the time interval during which photomultiplier tubes in a single layer register signals above a specified threshold level (the lower level discriminator). The inclusion of a lower level discriminator reduces the number of low amplitude noise pulses recorded.

When a photomultiplier tube in the lowest layer registers a signal, a time window, t_{layer}, is opened and the number of photomultiplier tubes in this layer which register signals within this time window are counted. The layer is considered as 'triggered' if greater than a specified number of photomultiplier tubes register a 'hit' within the time window, t_{layer}. If the lowest layer is triggered a second time window, t_{flight}, is opened. Each photomultiplier tube layer in the detector is then tested to determine if greater than the minimum number of photomultiplier tubes in each layer are hit. If each layer is triggered within the time taken for a muon to pass through the detector, an event is registered. The amplitude of the photomultiplier tube signals and the relative times at which each photomultiplier tube registered a signal are then recorded.

The number of photomultiplier tubes which register Cerenkov light in each layer and the time interval during which this light illuminates a layer depend on the attenuation length of the water, the lower level discriminator and the arrival direction of the muon. Figure 4.3 shows contours of constant photoelectron numbers and constant relative arrival times across a single layer of photomultiplier tubes for the two cases of upward muons at nadir angles of 0° and 70°. The photoelectron contours are in units of photoelectron numbers and the arrival time contours are in units of nanoseconds. In these results 200mm diameter photomultiplier tubes, with bialkali photocathodes, located on a square grid of grid spacing 4 metres have been assumed. The phototube spectral response used in this simulation is the quantum efficiency for a bialkali photocathode. A grid spacing of 4 metres was selected as this is the optimum grid spacing for the proposed detector. The optimisation of this parameter is described in section 4.4.2.2. The attenuation length of the lake water corresponds to the spectrometer measurements of Blue Lake samples collected at a depth of 50 metres during February 1993 (see figure 3.8). As explained in chapter 3, these attenuation lengths represent lower limits on the actual values of lake water attenuation length due to the fact that the spectrometer registers practically no scattered light.

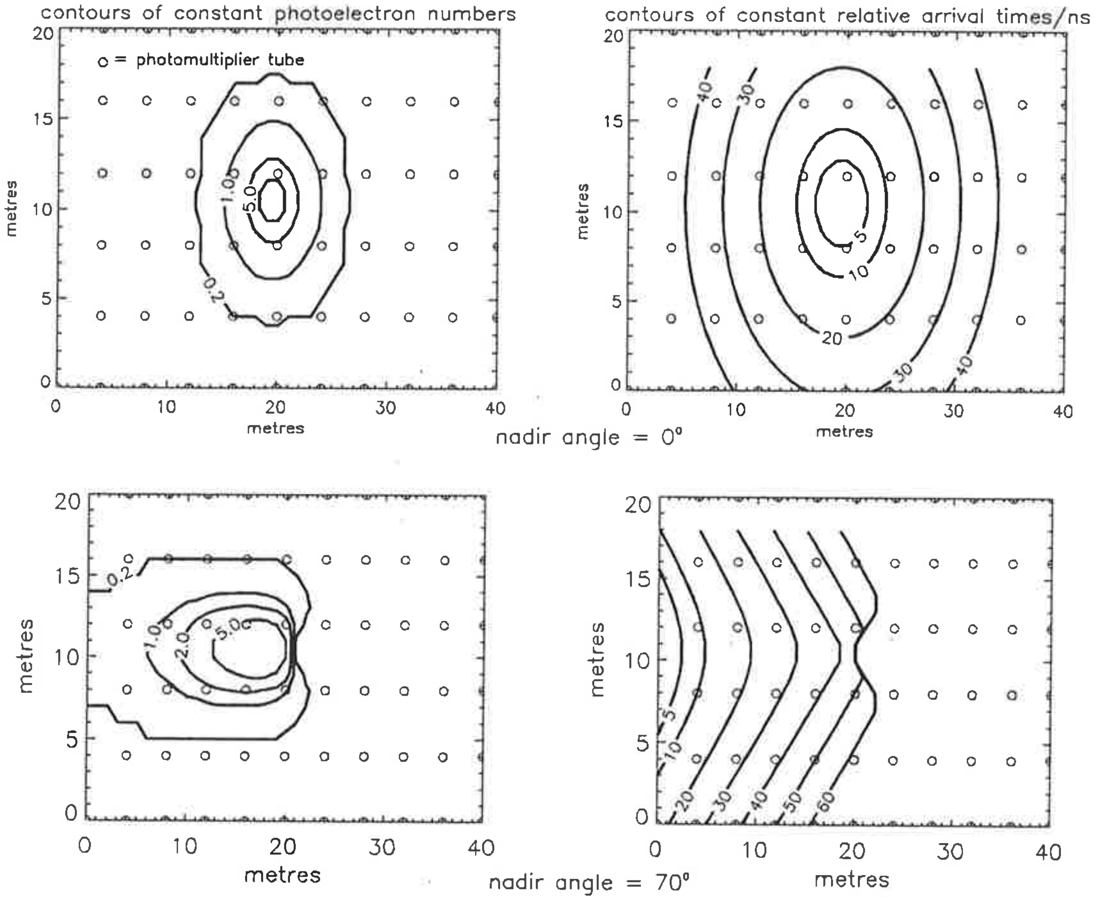

Figure 4.3: Contours of constant photoelectron numbers and relative arrival times in nanoseconds for upward travelling muons at nadir angles of 0° and 70°

From these contour plots it can be seen that if the lower level discriminator is set at one photoelectron and we require that all the photomultiplier tubes above this threshold are counted, then the corresponding spread in arrival times is about 10ns for a nadir angle of 0° and about 30ns for a nadir angles of 70°. Hence, to detect muons up to a nadir angle of 70° the coincidence time window, t_{layer}, has to be of the order of 30ns. The time taken for a muon to travel through the detector also depends on the arrival direction of the muon and the corresponding coincidence time window, t_{flight}, ultimately sets the maximum viewing angle of the detector.

The triggering scheme for the proposed detector is shown schematically in figure 4.4 along with the pulse trains corresponding to muons arriving at nadir angles of 0° and 70°. The detector geometry corresponding to this triggering scheme is shown in figure 4.1.

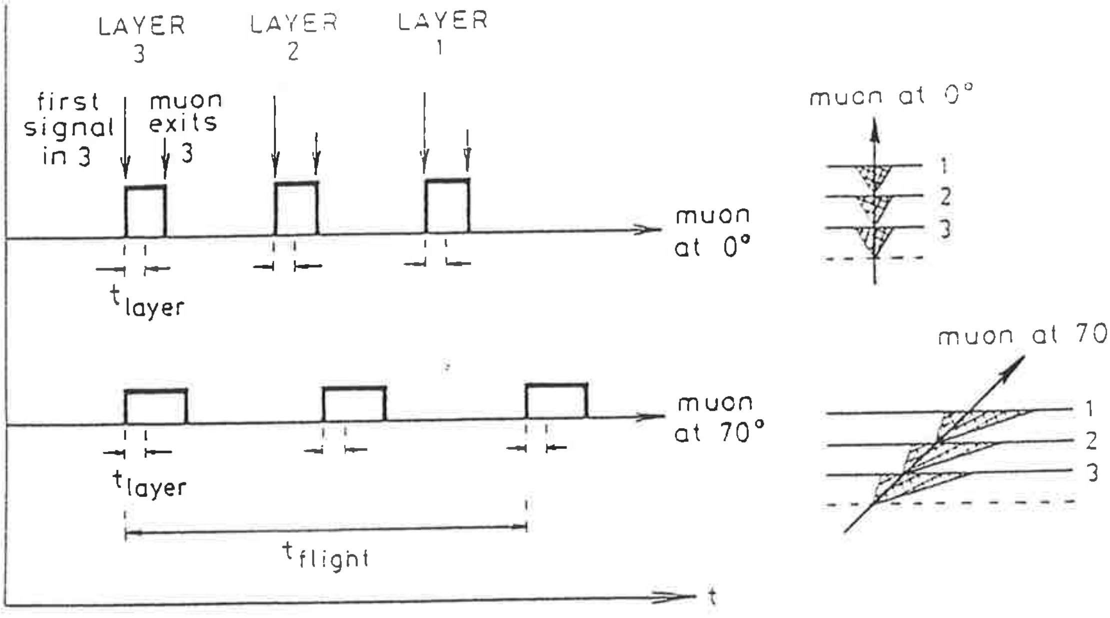

Figure 4.4: Schematic representation of detector triggering scheme

4.3 Angular Resolution

The angular resolution is a measure of the error between the reconstructed direction and the real direction of a high energy neutrino. Ideally, the error circle (defined as a circle of radius 1.6σ where σ is the angular resolution) should be as small as possible in order to maximise the signal to noise ratio. There are several sources of uncertainty in the reconstruction process which are outlined below.

1. There is an error in calculating the muon trajectory from the detector signals. This is termed the detector angular resolution and is dependent on the detector configuration used. The method of determining the detector angular resolution using Monte Carlo simulations is described in Hill (to be published). The algorithm for determining angular resolution uses both the photon density and timing information from photomultiplier tubes which are triggered. In the simulation used, the effects of the timing resolution of the photomultiplier tubes and Poisson fluctuations in the photon numbers have been included. Any effects due to muon-induced showers have also been considered. However, no photomultiplier tube noise has been included. Hence, the resulting values of detector angular resolution should be treated as best case results corresponding to no photomultiplier tube noise. The resulting values of angular resolution for various detector configurations are presented in table 4.1.

2. There is an uncertainty due to the scattering angle between a neutrino and the resulting muon and, also, an uncertainty in the muon direction at the detector due to multiple Coulomb scattering in rock. These combined uncertainties are termed the interaction angular resolution. The fraction of muons arriving at a detector, as a function of the angular deviation from the parent neutrino direction is shown in figure 4.5. The results shown are for various neutrino source spectra and for a detector of muon energy threshold equal to 6GeV. Both the effects of the neutrino-muon scattering angle and multiple scattering of the resulting muon have been considered.

		1σ angular resolution/°
grid spacing/m	2	0.20
	4	0.42
	6	1.37
photocathode diameter/m	0.1	1.60
	0.14	0.79
	0.2	0.42
lower level discriminator/pe	1	0.42
	2	0.43
	3	0.33
minimum no.PMTs/layer	3	0.42
	4	0.39
	5	0.39

Table 4.1: Detector angular resolution for various detector configurations. The fixed values of detector parameters used, when not being varied, are grid spacing=4 metres, photocathode diameter=0.2 metres, lower level discriminator=1 photoelectron, minimum number of photomultiplier tube hits per layer=3

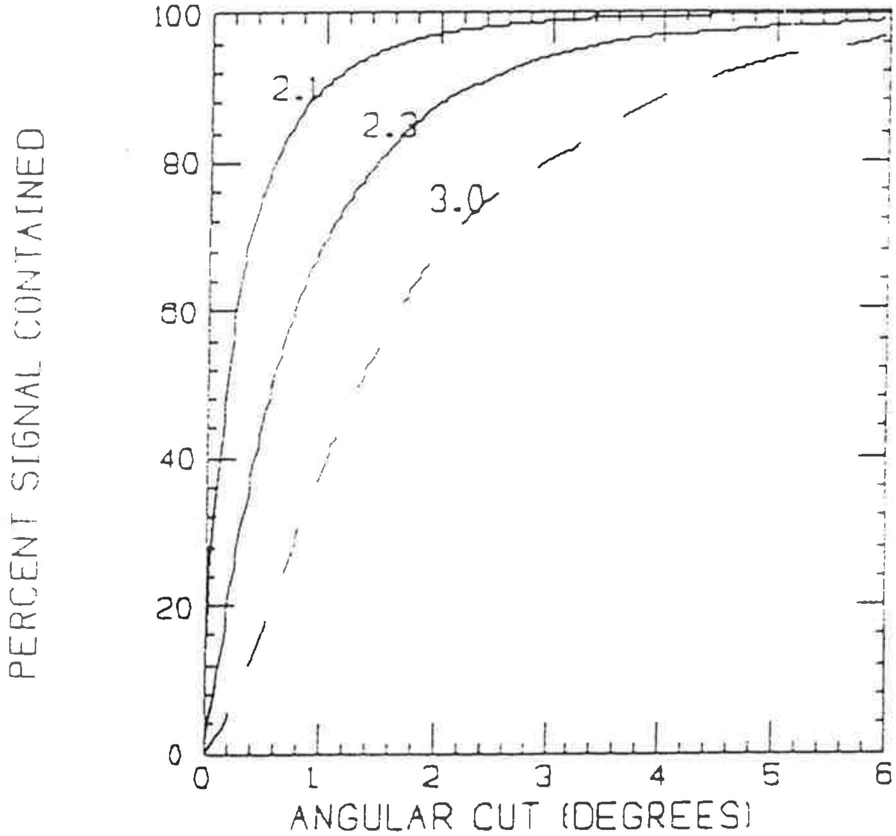

Figure 4.5: Fraction of muons arriving at a detector as a function of angular deviation from the parent neutrino direction. Three values of source spectral index are shown (Sobel 1991)

From figure 4.5 it can be seen that, for the case of Cygnus X-3 i.e. a source spectral index of 2.1, 50% of muons (1σ of a 2-dimensional Gaussian distribution) arrive within an angle of about 0.2°. Hence, we can assume that the interaction angular resolution for neutrinos from Cygnus X-3 is equal to 0.2°

The total angular resolution is given by equation 4.3.

$$\theta = \sqrt{{\theta_d}^2 + {\theta_i}^2} \tag{4.3}$$

where θ = total angular resolution
θ_d = detector angular resolution
θ_i = interaction angular resolution

The values of angular resolution for various detector configurations, calculated using this equation, are presented in table 4.2. An error circle of 1.6 times these values is used to maximise the signal to noise ratio.

4.4 Signal Events

The rate of upward muons detected by the array depends on the upward flux of muons passing through the detector as calculated in section 1.4.4 and the effective area of the detector. The effective area is the product of the geometric area of the detector and the efficiency of registering upward travelling muons, and depends on factors such as the position of the detector in the lake, the geometry of the photomultiplier tube array and the triggering criteria. Monte Carlo simulations have been used to determine the effective area of the proposed detector to upward muons as a function of these parameters.

		angular resolution/°
grid spacing/m	2	0.28
	4	0.47
	6	1.38
photocathode diameter/m	0.1	1.60
	0.14	0.80
	0.2	0.47
lower level discriminator/pe	1	0.47
	2	0.47
	3	0.39
minimum no.PMTs/layer	3	0.47
	4	0.44
	5	0.44

Table 4.2: Total angular resolution for various detector configurations. The fixed values of detector parameters used, when not being varied, are grid spacing=4 metres, photocathode diameter=0.2 metres, lower level discriminator=1 photoelectron, minimum number of photomultiplier tube hits per layer=3

4.4.1 Monte Carlo Simulation to Determine Detector Response

The Monte Carlo technique employed simulates upward travelling muons passing through the detector and determines what fraction of these muons satisfy the triggering criteria for an event to be registered. The fraction of muons which trigger the detector is referred to as the detection efficiency and the effective area is the product of this efficiency and the geometric area of the detector modelled. The main steps of the simulation are outlined below.

1. The muon path is randomly selected assuming that the muon crosses the lowest detector plane and that the muon energy is above the lower energy threshold of the detector. Muons from astrophysical sources will arrive at a range of nadir angles as the source tracks across the sky. As the detector response varies significantly with nadir angle, the effective area is determined for a range of nadir angles from 0° to 70°. The azimuthal angle is randomly selected in the range 0° to 360°.

2. Once the muon direction has been selected, the length of muon track viewed by each photomultiplier tube is determined. The intensity of Cerenkov photons emitted along this segment of muon track for wavelength bins of width 20nm from 300 to 620nm is calculated according to equation 2.3. This assumes that the muon energy is greater than the Cerenkov threshold along the track segment and that showering does not occur. The emitted photons are spread over an annulus in a plane perpendicular to the muon track as shown in figure 4.6.

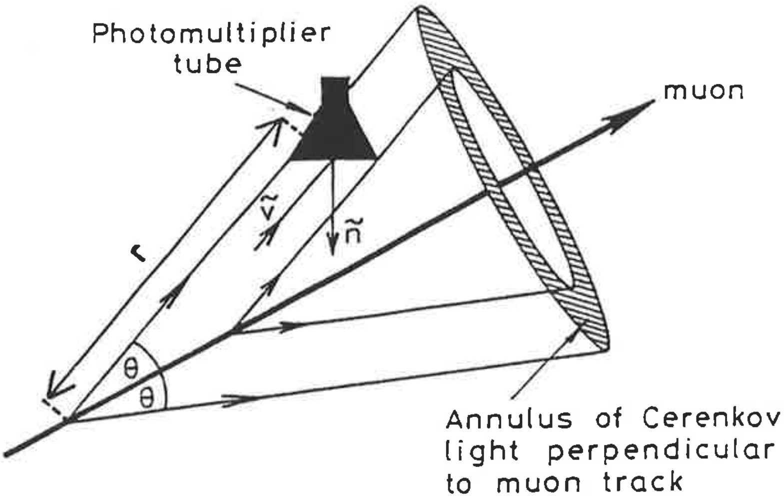

Figure 4.6: Geometry for calculating photon density at photomultiplier tube

By calculating the photon density in the disc perpendicular to the muon track and resolving this density onto the plane of the photomultiplier tube, the photon density at the photomultiplier tube can be determined. The number of photons hitting the photomultiplier tube face is equal to this photon density multiplied by the projected surface area of the photocathode and is given by equation 4.4.

$$N = \alpha \left(\frac{1}{\lambda_1} - \frac{1}{\lambda_2}\right) ds\ \tilde{v}.\tilde{n}\ \frac{e^{-r/att}}{r} \tag{4.4}$$

where N = photon number

α = fine structure constant

λ_1 = minimum wavelength

λ_2 = maximum wavelength

ds = photocathode area

$\tilde{v}$ = unit vector of lightpath from muon track to photomultiplier tube face

$\tilde{n}$ = unit area vector of photomultiplier face

r = distance light travels from muon track to photomultiplier

att = attenuation length of water

3. The resulting signal in the photomultiplier tube depends on the transmission properties of the glass window and the quantum efficiency of the photocathode. The number of photoelectrons produced is given by the convolution of the spectral distribution of Cerenkov photons, the transmission of the glass window and the quantum efficiency of the photocathode. For each photomultiplier tube viewing a segment of the muon track, the number of photoelectrons produced is calculated including the effect of fluctuating the photon numbers and the photoelectron numbers according to Poisson statistics.

4. The photoelectron numbers in each photomultiplier tube are then tested to determine if the triggering criteria are satisfied. A photomultiplier tube is considered as 'hit' if the signal registered is greater than the minimum threshold level. The number of photomultiplier tubes hit in each layer is counted and a layer is considered as triggered if this number is greater than the specified minimum number of photomultiplier tube hits required. An event is registered by the detector if every layer is triggered.

5. The detection efficiency is equal to the number of events registered divided by the total number of muons simulated.

4.4.2 Results of Detector Response Simulations

The simulated efficiency of detecting upward muons was determined as a function of the detector location, the detector geometry and the triggering criteria, for muons arriving at nadir angles from 0° to 70°. The geometrical parameters which have been considered are the photocathode area and the spacing between photomultiplier tubes in each layer (the grid spacing). The triggering criteria modelled are the lower level discriminator setting and the number of photomultiplier tubes in each layer which must register a signal in order to trigger the detector. The default values of these parameters are as follows:-

photocathode diameter = 0.2 metres
grid spacing = 4 metres
layer separation = 9 metres
photoelectron threshold = 1 photoelectron
no. of tubes hit per layer = 3

The attenuation length of Blue Lake water used in these simulations is that measured at a depth of 50 metres in February 1993, as shown in figure 3.8. The optical prop~~o~~erties of the water in the lake vary seasonally and maximum light transmission occurs at depths greater than 40 metres during the summer months. Hence the simulated values of detection efficiency represent the maximum possible efficiency of the proposed detector in the Blue Lake using the light attenuation lengths measured on the spectrometer. However, these attenuation lengths do not include any effects due to light scattering and, as such, the resulting detector efficiencies should be treated as lower limits.

4.4.2.1 Location of the Detector in the Blue Lake

Depth in the Lake

The amount of Cerenkov light registered, and hence the detector efficiency, is maximised by using the clearest water available. Hence the optimum position for a detector in the Blue Lake is at a depth greater than 40 metres. It is also advantageous to locate the detector as deep as possible to reduce the flux of downward atmospheric muons which pass through the detector. The lowest layer of photomultiplier tubes should therefore be located close to the bottom of the lake while allowing for a sufficient depth of water below this layer to ensure that Cerenkov light from upward muons is viewed by a sufficient number of photomultiplier tubes to trigger the lowest layer.

The optimum position of the lowest layer was determined by simulating the response of a single layer of photomultiplier tubes to upward muons as a function of the distance of the layer above the bottom of the lake. As before, an optimised grid spacing of 4 metres was assumed and the arrival direction of each muon was selected from an isotropic nadir angle distribution of 0° to 70°. The results shown in figure 4.7 show the efficiency of a single layer of photomultiplier tubes located at various depths and for a range of triggering conditions.

From these results it can be seen that the detection efficiency remains approximately constant down to a certain depth beyond which the number of photomultiplier tubes registering Cerenkov light, and hence the efficiency, decreases due to the 68 metre maximum depth of the lake (see figure 4.8).

The depth at which this decrease in efficiency occurs depends on the triggering conditions. For the minimum triggering condition of a lower level discriminator of 1 photoelectron and a minimum number of 3 photomultiplier tubes registering signals, the efficiency decreases only when the layer is positioned less than about 5 metres above the lake bottom. However, increasing the minimum number of photomultiplier hits required to 5 results in a decrease in efficiency when the layer is less than about

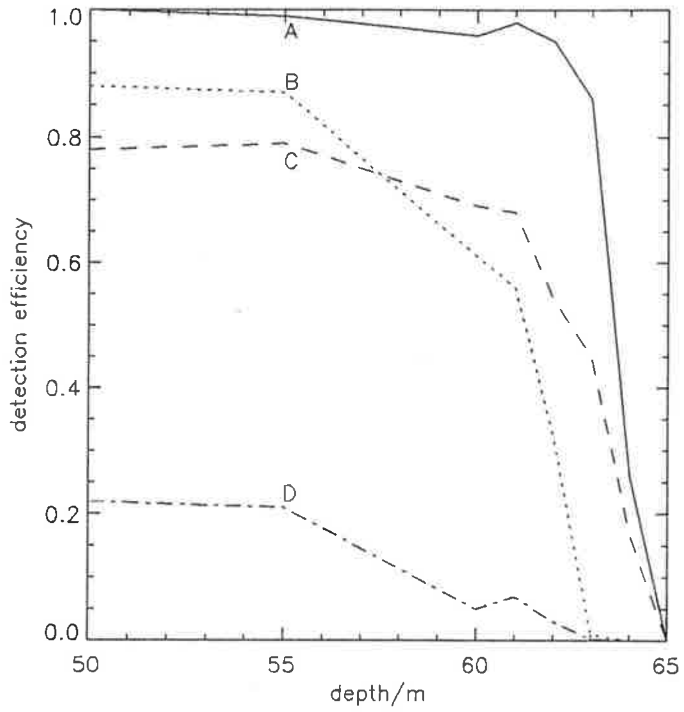

Figure 4.7: Detection efficiency as a function of depth for a single layer. A=at least 3 photomultiplier tubes (PMTs) per layer with at least 1 photoelectron (pe), B=at least 5 PMTs with at least 1 pe, C=at least 3 PMTs with at least 2 pes, D=at least 5 PMTs with at least 2 pes.

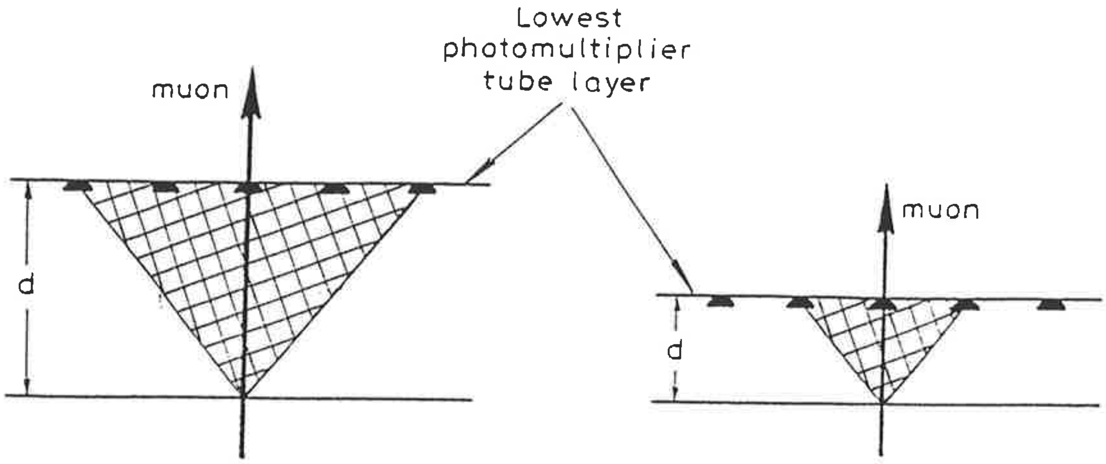

Figure 4.8: Schematic showing effect of depth on number of illuminated photomultiplier tubes

13 metres above the bottom of the lake. Hence, locating the lowest layer as far as possible above the bottom of the lake maximises the range of triggering conditions that can be used without significantly decreasing the detection efficiency. The optimum location in the lake is determined by maximising the detection efficiency for a sufficient range of triggering conditions while ensuring that all three photomultiplier tube layers are located at depths greater than 40 metres.

Separation Between Photomultiplier Tube Layers

The maximum separation between three equally spaced layers below 40 metres is 9 metres. From the results of detection efficiency as a function of depth of water below a single photomultiplier tube layer shown in figure 4.~~10~~7 it can be seen that for a depth of water of 9 metres the detection efficiency is significantly reduced only for one of the triggering conditions considered i.e. a threshold equal to 2 photoelectrons and a minimum number of photomultiplier tube hits per layer of 5. This sets a limit on the triggering conditions that can be used in a detector consisting of photomultiplier tube layers separated by 9 metres in the Blue Lake without significantly decreasing the detection efficiency.

Each layer of photomultiplier tubes must be optically isolated from the other layers to ensure that Cerenkov light viewed by one layer will not also illuminate the next layer up. This is an important factor in discriminating between upward and downward travelling muons. If we consider the downward travelling muon shown in figure 4.9 the resulting Cerenkov light will illuminate the upper layer first and then the lower layers sequentially. The muon can be identified as downward going from this timing sequence.

If, however, the photomultiplier layers are not optically isolated such that light from the same position on the muon track can illuminate several layers, e.g. ray A in figure 4.9, then the pattern of signals is indistinguishable from that produced by an upward travelling muon.

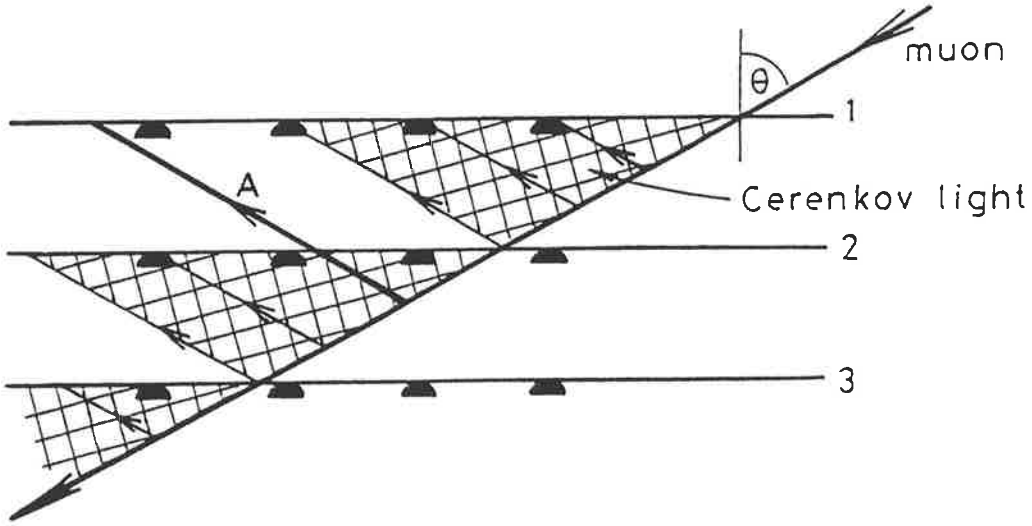

Figure 4.9: Downward travelling muon passing through the detector

Optical isolation between layers can be achieved by placing light-tight barriers above each layer of downward looking photomultiplier tubes. However, if the transmission of light through the water is low then it may be possible to achieve the desired optical isolation by placing the layers far enough apart such that light crossing one layer is attenuated by water before reaching the next layer.

To determine whether a layer separation of 9 metres is sufficient to optically isolate the layers the response of two layers of photomultiplier tubes to downward muons was simulated. For each muon registered as an event, the number of photomultiplier tubes in the upper layer which register Cerenkov light emitted from below the lower layer are counted. If this number is greater than the minimum number of photomultiplier tube signals required per layer then the upper layer will be triggered after the lower layer and the resulting event will be indistinguishable from an upward muon event. The simulated rate of these false events was determined as a function of separation between the layers and hence, the minimum separation required to provide the necessary optical isolation deduced. When observing a signal from a point source, only muons arriving within a 1.6σ error circle are considered. Hence, assuming that these background events occur isotropically, then the rate of such events is equal to the total rate times $(1 - cos[1.6\sigma])$ where σ is the total angular resolution as listed in table 4.2. Figure 4.10 shows the expected rate of such events occurring within the 1.6σ error circle as a function of the separation between the two layers. The minimum triggering conditions of a lower level discriminator equal to 1 photoelectron and at least 3 photomultiplier tubes triggered per layer have been assumed. Also shown in this figure is the expected rate of signal events resulting from high energy neutrinos emitted from Cygnus X-3 for the same detector configuration and triggering conditions. The method of calculating the expected rate of neutrino events registered from Cygnus X-3 is described in section 4.4.3.

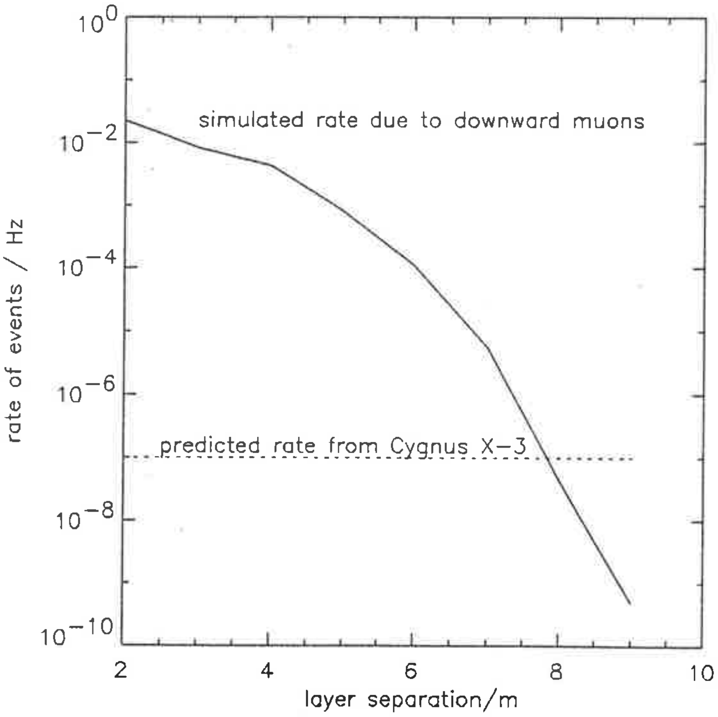

Figure 4.10: Rate of downward muons registered as upward muon events as a function of separation between photomultiplier tube layers. Also shown is the predicted event rate from Cygnus X-3. Grid spacing=4 metres, photocathode diameter=0.2 metres, minimum number of photomultiplier tube hits per layer=3, lower level discriminator=1 photoelectron

From figure 4.10 it can be seen that for a layer separation of 9 metres the rate of background events due to Cerenkov light illuminating several layers is approximately one hundredth of the rate of expected signal events from Cygnus X-3. By applying more stringent triggering conditions than a lower level discriminator of 1 photoelectron and a minimum number of photomultiplier tubes hit per layer of three, the rate of false triggers due to Cerenkov light hitting several layers will be further reduced. This result indicates that layers of photomultiplier tubes in the Blue Lake separated by 9 metres are sufficiently optically isolated as a result of light attenuation in the water. However, this result assumes lower limit values of light attenuation as determined using the spectrometer. If there is a significant amount of light scattering in the lake water then the actual values of attenuation length will be correspondingly higher and it may be necessary to include additional optical isolation between the layers of photomultiplier tubes. The final optimum location of the detector in the Blue Lake is shown in figure 4.11.

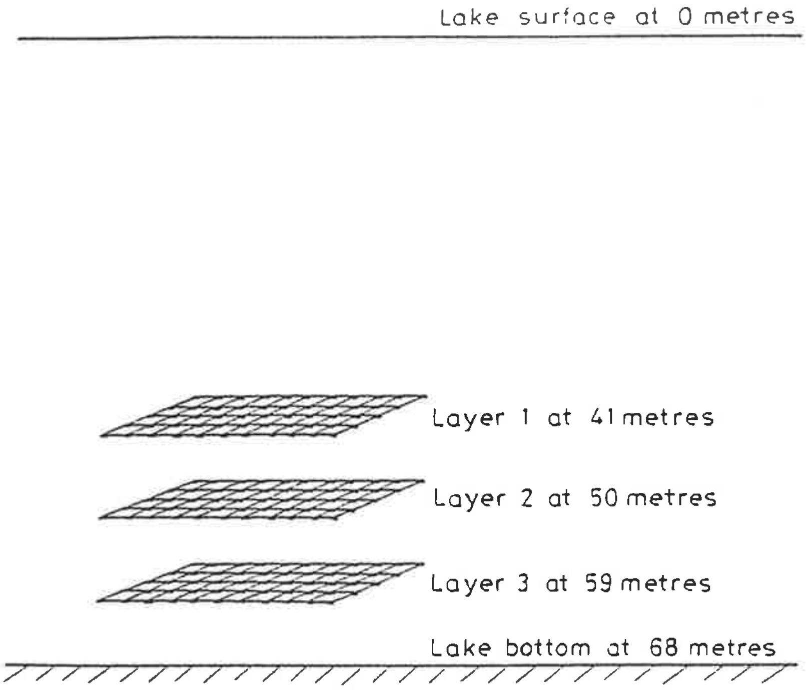

Figure 4.11: Location of proposed neutrino detector in the Blue Lake

Energy Threshold

A muon is registered only if it passes through all the layers of the detector before being absorbed. Hence the distance between the bottom of the lake and the top layer of the detector determines the lower energy threshold of the detector. For the detector location shown in figure 4.11 the shortest distance taken for a muon to pass through the detector is 27 metres and hence from equation 1.17 the minimum energy threshold is approximately 5.4GeV.

Detector Aperture

The detector will record an event if all three layers are triggered within the coincidence time window, t_{flight}. Hence only muons which pass through the detector in a time equal to t_{flight} or less will be registered and this condition sets the maximum nadir angle at which muons will be detected. Increasing t_{flight} will increase the viewing aperture but will also increase the rate of random coincidences recorded (see section 4.5.1). For a detector with layers separated by 9 metres a viewing aperture of 70° corresponds to a coincidence time window of 263 ns.

4.4.2.2 Detection Efficiency as a Function of Detector Geometry and Triggering Conditions

To determine the optimum detector geometry and triggering conditions the response of the detector shown in figure 4.11 to upward travelling muons was simulated. The detector assumed consists of three layers of optically isolated photomultipliers, the area of each layer being $1.17 \times 10^4\text{m}^2$. The predicted minimum effective area required to observe high energy neutrino point sources is of the order of 10^4m^2 and hence the simulated detector would need to have an efficiency of about 1. If the efficiency is less than 1 then the required effective area can be obtained by increasing the geometric area of the detector.

In addition to the location of the detector in the lake and the separation between the layers of photomultiplier tubes already discussed, the aspects of the detector geometry which have been considered are the photocathode area and the spacing between the photomultiplier tubes in each layer. The triggering criteria which have been considered are the lower level discriminator threshold in all the photomultiplier tubes and the minimum number of photomultiplier tubes per layer which must record a signal above the lower level discriminator for a layer to be triggered. The simulated detection efficiency as a function of these parameters is presented below.

Photocathode Area

The efficiency of detecting upward going muons as a function of photocathode diameter is shown in figure 4.12. In these results the grid spacing is 4 metres, the minimum number of photomultiplier tubes hit per layer is 3 and the lower level discriminator is 1 photoelectron. The number of photons detected and hence the amplitude of signals in the photomultiplier tubes increases with increasing photocathode area. This results in an increase in the detection efficiency. Increasing the photocathode area will also improve the angular resolution. The error in the calculated muon direction increases as the relative error in the magnitude of signals recorded in the photomultiplier tubes increases (Hill, to be published). For a signal of N photoelectrons the relative error is equal to $1/\sqrt{N}$ and hence increasing the value of N by using a larger photocathode will reduce the error in the calculated muon direction and improve the angular resolution. In practice the photocathode area used is limited by the size and cost of available photomultiplier tubes and the maximum size considered corresponds to a diameter of 200 mm.

From the results shown in figure 4.12, some trends in detection efficiency as a function of nadir angle can be identified. These trends are also apparent in the subsequent results presented in figures 4.14 to 4.16. There are 2 main effects which occur as the nadir angle increases. Firstly, the muon track passes closer to the photomultiplier tubes in each layer and, as a result, the number of photons hitting the photomultiplier tubes varies. For nadir angles greater than about 50° there is a significant increase in the number of photons registered and this results in an

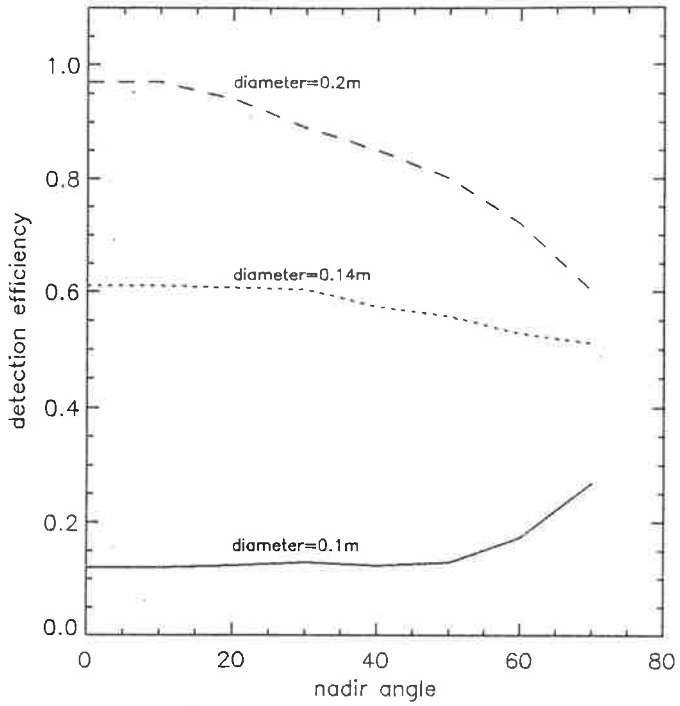

Figure 4.12: Detection efficiency as a function of photocathode area. Grid spacing=4 metres, minimum number of photomultiplier tubes hit per layer=3, lower level discriminator=1 photoelectron

increase in the detection efficiency. To illustrate this effect, consider the 2-dimensional arrangement shown in figure 4.6 in which Cerenkov light is registered by a single photomultiplier tube. The number of Cerenkov photons hitting the tube is given by equation 4.4. The relative number of photons registered as a function of nadir angle was calculated assuming the attenuation length of the water is 4 metres and that the muon track intersects the plane of the photomultiplier tube face at a distance of 4 metres from the phototube. The results are shown in figure 4.13.

From these results it can be seen that there is a significant increase in the number of photons detected at nadir angles greater than about 50°. Hence, we would expect an increase in the detection efficiency at large nadir angles. This effect is most obvious in the results for phototube diameters of 0.1m in figure 4.12, a grid spacing of 6 metres in figure 4.14, lower level discriminator of 3 photoelectrons in figure 4.15 and a minimum of 5 phototubes hit per layer in figure 4.16. In all these cases the detection efficiency at small nadir angles is low (less than about 0.5) indicating that

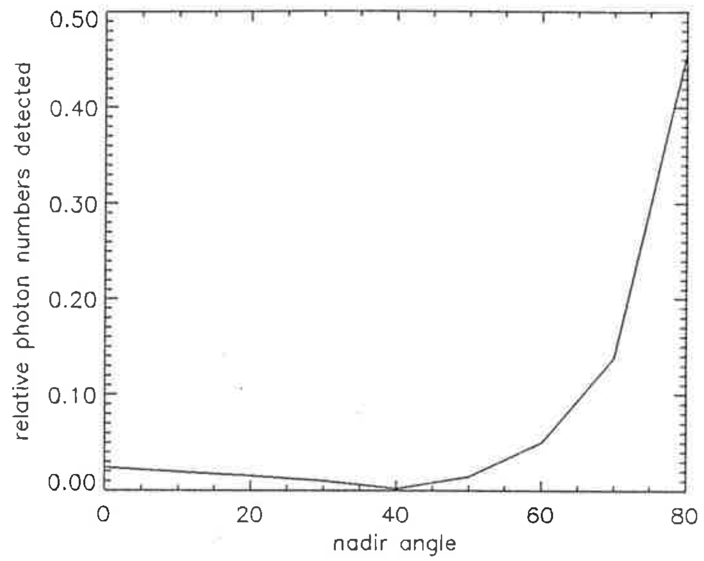

Figure 4.13: Relative number of Cerenkov photons detected by a photomultiplier tube as a function of nadir angle assuming the detector geometry shown in figure 4.6. Water attenuation length=4 metres, distance between photomultiplier tube and muon track in the plane of the photomultiplier tube face=4 metres

a significant proportion of the muons considered resulted in an insufficient number of photons hitting the photomultiplier tubes for the detector to trigger. However, there is a noticeable improvement in the detection efficiency at large nadir angles due to the increased number of photons registered.

The other major effect which occurs at large nadir angles is that a muon which passes through the lowest layer of photomultiplier tubes may not pass through the upper layers. This will occur if the muon intersects the lowest plane close to the edge of the detector. As all three detector layers are required to trigger for an event to be recorded, then we would expect the detection efficiency to decrease at large nadir angles. This effect can be seen in all the plots shown in figures 4.12, 4.14, 4.15 and 4.16 for which the detection efficiency at small nadir angles is close to 1.0. For the detector conditions corresponding to these plots, the number of photons registered is sufficient to trigger the detector, even at small nadir angles. Hence, any increase in photon numbers detected at large nadir angles has no noticeable effect on the detection efficiency. However, the fact that an increasing number of muons will not trigger all three photomultiplier tube layers as the nadir angle increases results in a gradual decrease in efficiency with nadir angle.

Grid Spacing

The grid spacing between photomultiplier tubes in a layer is largely determined by the attenuation length of the water. If the water has a low attenuation length then most of the Cerenkov light is absorbed and the photomultipliers must be spaced closely together if a sufficient number of tubes are to register Cerenkov light. Reducing the grid spacing will increase the number of photomultiplier tubes recording signals but the number of photomultiplier tubes required to instrument the detector volume increases rapidly. The efficiencies of detection of upward muons for grid spacings from 2 to 6 metres are shown in figure 4.14.

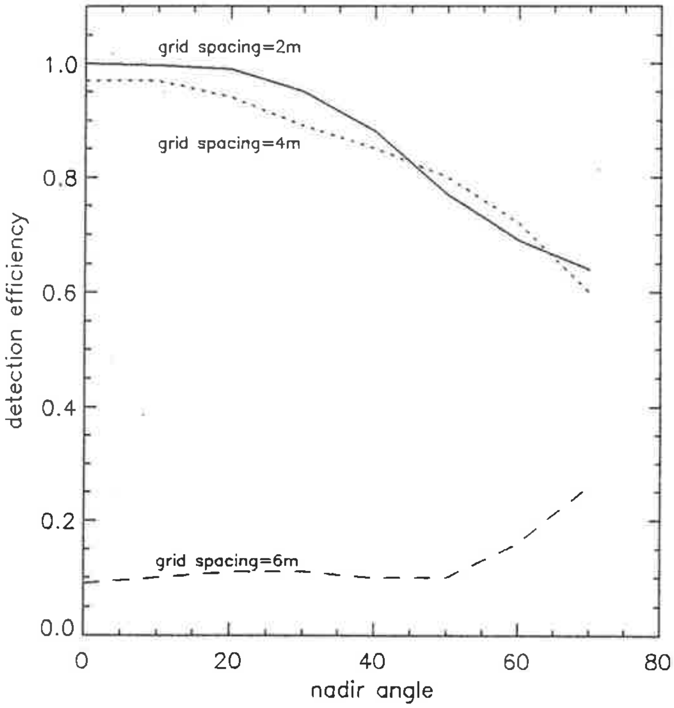

Figure 4.14: Detection efficiency as a function of grid spacing. Photocathode diameter=0.2 metres, minimum number of photomultiplier tube hits per layer=3, lower level discriminator=1 photoelectron.

From these results it can be seen that increasing the grid spacing to 6 metres results in a significant drop in detection efficiency, whereas grid spacings of 2 and 4 metres result in approximately equal detection efficiencies. A grid spacing of 2 metres would require 9075 photomultiplier tubes to instrument a 3 layer detector, whereas a 4 metres grid spacing would require 2352 photomultiplier tubes. This indicates that a spacing of 4 metres would result in the best ratio of detection efficiency to number of photomultiplier tubes required and is therefore selected as the optimum grid spacing in the proposed detector.

Lower Level Discriminator

The lower level discriminator is the photoelectron threshold in each photomultiplier tube below which signals are ignored. Including a lower level discriminator eliminates low level noise pulses while retaining most of the signal pulses. Ideally this discriminator should be set just below the minimum signal amplitude which is to be retained. In the Blue Lake, the attenuation of light in water is such that the expected Cerenkov signals can be as low as a few photoelectrons. Hence the lower level discriminator must be correspondingly low. The efficiency of detecting upward muons as a function of lower level discriminator setting is shown in figure 4.15.

Reducing the lower level discriminator increases the efficiency of detecting a real Cerenkov signal, in particular the difference in efficiency for photoelectron thresholds of one and two photoelectrons is significant. However reducing the lower level discriminator also increases the rate of noise pulses registered and hence the rate of background events recorded. This effect is discussed in section 4.5.

Number of Photomultiplier Tubes Per Layer Registering a Signal

Each layer of the detector is triggered if greater than a minimum number of photomultiplier tubes in each layer register signals above the photoelectron

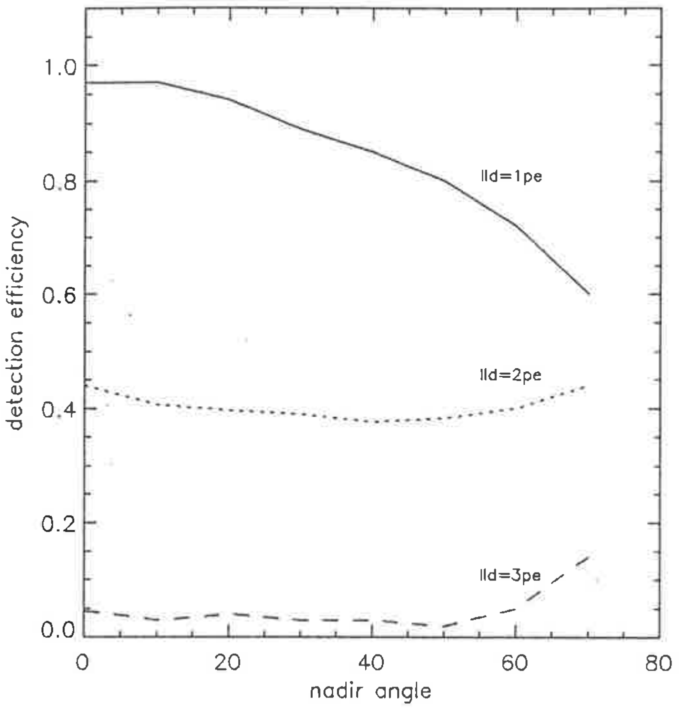

Figure 4.15: Detection efficiency as a function of lower level discriminator. Photocathode diameter=0.2 metres, grid spacing=4 metres, minimum number of photomultiplier tube hits per layer=3.

threshold. The efficiency as a function of the number of photomultiplier tubes hit per layer is shown in figure 4.16. The minimum number of photomultiplier tubes required per layer in order to determine muon trajectories is three. The efficiency increases as the minimum number of tubes required decreases and hence if we are considering only the number of signal pulses detected, the optimum number of tubes required to register a hit in each layer is three. However reducing the minimum number of tube hits required also increases the rate of background events detected, as discussed in section 4.5.

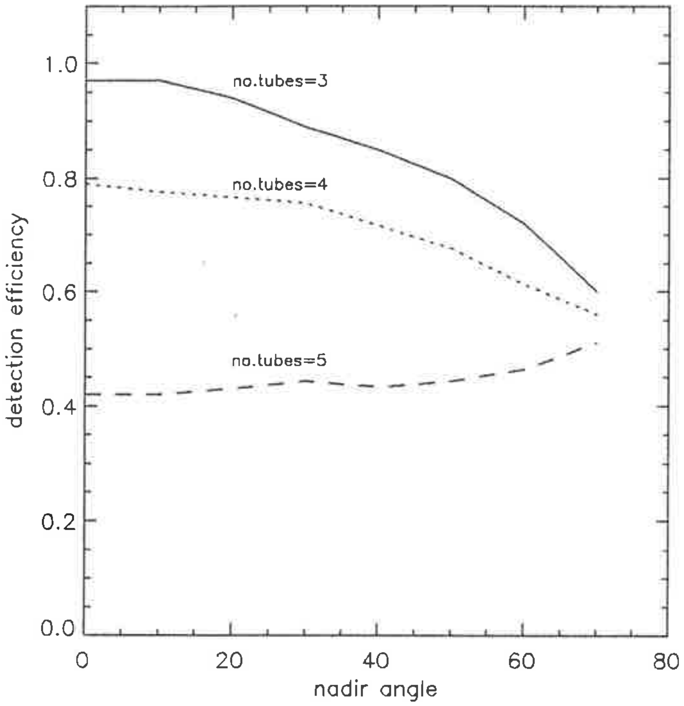

Figure 4.16: Detection efficiency as a function of minimum number of photomultiplier tubes hit per layer. Photocathode diameter=0.2 metres, grid spacing=4 metres, lower level discriminator=1 photoelectron.

4.4.3 Expected Rate of Neutrino Events from Cygnus X-3

The rate of events registered due to high energy neutrinos from astrophysical sources depends on the resulting upward muon flux at the detector, the efficiency of detecting these muons and the angular resolution of the detector. This event rate is given by the product of the upward muon flux within the 1.6σ error circle and the effective area of the detector. The total predicted upward muon flux from Cygnus X-3 is calculated in section 1.4.4 using the apparent gamma-ray fluxes measured by Samorski and Stamm (1983) and Lloyd-Evans et al.(1983), and has a value of $2.3 \times 10^{-15}\mathrm{cm}^{-2}\mathrm{s}^{-1}$. Assuming that only muons arriving within the 1.6σ error circle of the detector are registered, then the muon flux from Cygnus X-3 arriving within this error circle is equal to $1.7 \times 10^{-15}\mathrm{cm}^{-2}\mathrm{s}^{-1}$. The effective area of the detector varies according to the nadir angle of the muon track and hence varies according to the position of the source relative to the detector. The effective area used in the

		event rate/year
grid spacing/m	2	2.9
	4	2.8
	6	0.7
photocathode diameter/m	0.1	0.5
	0.14	1.9
	0.2	2.8
lower level discriminator/pe	1	2.8
	2	1.3
	3	0.1
minimum no.PMTs/layer	3	2.8
	4	2.3
	5	1.4

Table 4.3: Simulated rate of neutrino-induced events from Cygnus X-3 arriving within a 1.6σ error circle. The fixed values of parameters used, when not being varied, are grid spacing=4 metres, photocathode diameter=0.2 metres, lower level discriminator=1 photoelectron, minimum number of photomultiplier tube hits per layer=3.

calculation of event rate is therefore equal to the average effective area over the range of nadir angles for which the source is within the viewing aperture of the detector. The expected rates of high energy neutrino-induced events from Cygnus X-3, as registered by the proposed Blue Lake detector, are listed in table 4.3 for various detector geometries and triggering conditions. The results in this table correspond to a detector consisting of 3 layers of photomultiplier tubes arranged on a square grid and located as shown in figure 4.11. Each layer has a geometrical area of $1.17 \times 10^4 m^2$. It should be noted that the error on these predicted event rates can be as much as a factor of 10, even assuming that the gamma-ray observations are real, due to uncertainties in the model assumed for neutrino production in a binary system and hence in the neutrino flux spectrum from Cygnus X-3. In this thesis the neutrino flux spectrum calculated by Kolb, Turner and Walker (1985) has been assumed.

The expected neutrino fluxes from Cygnus X-3, listed in table 4.3, will be observed by the proposed detector providing the genuine neutrino-induced events can be discriminated from the background events registered. To determine if this is the case, the expected sources and fluxes of background events are discussed in the following section.

4.5 Background Events

Background events in the proposed detector arise from two main sources:- random noise pulses due to photomultiplier tube noise and background light, and cosmic ray particles in the atmosphere which pass through the detector. The success of the detector depends on its ability to differentiate signal events from background events. To achieve this it must be possible either to discriminate between the signal patterns corresponding to real events and those corresponding to background events, or the flux of background events must be significantly less than the flux of signal events. In this section the predicted flux of background events from the two main sources are presented.

4.5.1 Random Noise Pulses

The main sources of random noise pulses in the Blue Lake detector are electronic noise in the photomultiplier tubes and fluctuations in the background light. Any noise pulses in the photomultiplier tubes, or fluctuations in the ambient light of magnitude greater than the lower level discriminator, will be recorded as signal pulses. If the noise pulses in each photomultiplier tube are uncorrelated then an event will be registered only if noise pulses occur randomly in a pattern that satisfies the triggering criteria. If the triggering condition for a single layer is that at least n tubes out of a total number of N tubes in the layer must register signals within a time period, δt, then the rate of triggers due to random coincidences is given by equation 4.5.

$$f_r = \frac{N!}{(N-n)!}\, f_1 f_2 ...... f_n \, \delta t^{n-1} \tag{4.5}$$

f_r = rate of random coincidences

n = number of photomultiplier tubes required for coincidence

N = total number of photomultiplier tubes

f_i = rate of noise pulses in tube i

δt = coincidence time window

The coincidence time window for a single layer is 30ns, the total number of photomultiplier tubes, N, is 784 for a grid spacing of 4 metres, and the number of photomultiplier tubes required to register signals, n, depends on the trigging criteria for a single layer. The expected random rate can therefore be determined if the rate of noise pulses in individual photomultiplier tubes, f_i, is known. This rate depends on the photomultiplier tube used and also on the amount of background light, which varies with time. If the background light is high then the rate of fluctuations will result in a rate of random coincidences which is much higher than the rate of signal events. If this is the case then the detector will only operate successfully if it is surrounded by light-tight shielding.

To assess if it would be necessary to shield the proposed detector from background light the expected rate of events due to random coincidences was calculated using a measured noise spectrum to obtain an approximation for the expected rate of noise pulses registered in each photomultiplier tube. The noise spectrum used was recorded on a moonless night using a 180mm EMI 9623B photomultiplier tube looking downwards at 60 metres in the Blue Lake (see section 5.5.1.2). This noise spectrum is shown in figure 5.13 and the total rate of noise pulses registered, above a lower level threshold of 2 photoelectrons, is approximately 3.4×10^4Hz. Hence, assuming that the gain of the proposed detector is comparable to the gain of the system used to record this noise spectrum and that all the photomultiplier tubes in the proposed detector are firing at this measured rate, then the rate of random triggers of a single layer can be calculated according to equation 4.5. In this calculation the assumed triggering criteria for a single layer are a lower level threshold of 2 photoelectrons and a minimum number of 3 photomultiplier tubes registering signals. In section 4.4.3 it was shown that the expected rate of signal events from Cygnus X-3 for these triggering conditions is about 4.0×10^{-8}Hz. Hence, for this signal to be observable, the rate of random events registered within the 1.6σ error circle must be significantly less than this signal rate.

From equation 4.5 the rate of random coincidences for a single layer of photomultiplier tubes is 1.7×10^{7}Hz. This random rate can be reduced using the fact that the photomultiplier tubes triggering in a layer will be adjacent. Therefore we can restrict the total number of photomultiplier tubes considered from 784 to, for example, 16 adjacent tubes. This will reduce the rate of random coincidences per layer to 120Hz.

For an event to be recorded by the complete detector each layer must register a noise pulse within the time window corresponding to a muon passing through the detector. Also, using the triggering scheme described in section 4.2.1, the layers must trigger sequentially from the lowest layer upwards for an event to be registered. The rate of random coincidences satisfying this triggering condition for a detector with three photomultiplier tube layers is given by equation 4.6.

$$f_r = f_1\, f_2\, f_3\, \delta t^2 \tag{4.6}$$

f_r = rate of random coincidences

f_1, f_2, f_3 = trigger rates of layers $1, 2, 3$

δt = time window = $\mathrm{t_{flight}}$ = 263ns

If the rate of random triggers per layer is 120 Hz, then the rate of events recorded by the detector due to random coincidences between noise pulses is of the order of 1.2×10^{-7}Hz. Assuming that these random events occur isotropically, then the rate of such events arriving within the 1.6σ error circle of the detector is given by equation 4.2, in which $\frac{dN}{d\Omega}$ equals the total number of background events divided by

2π. From table 4.1 it can be seen that a detector configuration of a grid spacing of 4 metres, photocatode diameter of 0.2 metres, lower level discriminator of 2 photoelectron and a minimum number of photomultiplier tube hits per layer of 3 has a 1.6σ error circle of 0.75°. Hence, the rate of random events registered within the angular resolution is 1.0×10^{-11}Hz. This random rate can be further reduced in the off-line analysis by requiring that the positions at which the muon crosses each layer are collinear. This condition can reduce the random rate by a factor of about 1/100 (Bratton et al.1988) giving a rate of random noise events of about 1.0×10^{-13}Hz which is significantly less than the expected signal rate from Cygnus X-3. Hence, in principle it would be possible to operate the proposed detector on moonless nights without shielding out background light. It should be noted that this assumes the photomultiplier tubes in the proposed detector will register background light signals at a rate comparable to about 30kHz. The actual rate will depend on the photomultiplier tubes used, the gain of the final detector and the position of the lower level discriminator, none of which are known at this stage. However, by assuming that the rate of events recorded due to random coincidences must be less than 1/10th of the expected signal rate from Cygnus X-3, an upper limit on the rate of single noise pulses recorded in each photomultiplier tube can be set. This maximum rate is 66kHz, assuming an error circle of radius 0.75°. Hence, if the trigger rate of individual photomultiplier tubes in the proposed detector is greater than 66kHz, the detector will have to be shielded from background light to reduce the rate of random noise events registered to a tolerable level. In practice the detector would have to operate virtually continuously in order to record a reasonable event rate from point sources such as Cygnus X-3 and hence the detector would have to be enclosed in a light-tight container to facilitate operation during daylight.

4.5.2 Cosmic Ray Particles

Any particle travelling through the detector at relativistic speeds will produce Cerenkov radiation which may trigger the detector and be recorded as a neutrino event. At ground level there is a high particle flux as a result of interactions between cosmic rays and particles in the atmosphere. An incoming cosmic ray particle interacting with a nucleus high in the atmosphere gives rise to a cascade of particles which continues through the atmosphere in approximately the same direction as the original cosmic ray. The initiating particle may be a proton or a heavier nucleus that produces mainly pions as secondary particles. Kaons are also produced, but in much smaller numbers (about 1/10). The charged pions decay to muons and neutrinos and, as the lifetime of the pion is increased due to time dilation, some of the pions will interact with other nuclei before decaying thus contributing to the hadron cascade. The muons lose energy only through ionisation at a rate of about $2\mathrm{MeV/g/cm^2}$ and, although the decay lifetime is only $2.2 \times 10^{-6}s$, this is enhanced due to time dilation and most muons survive to ground level. The π^os will decay to photons and, if the energy of these photons is sufficiently high, i.e. at least twice the rest mass of an electron, e^+e^- pairs are produced building up an electron-photon cascade. A typical hadronic cascade is shown schematically in figure 4.17.

The number of particles in an air shower increases to a maximum value as it traverses the atmosphere. Beyond this there is a continuous decrease in particle number due to absorption and decay processes. The atmospheric depth of this maximum is proportional to the logarithm of the energy of the primary particle (Gaisser 1990). Hence for low primary energies the shower dies out before reaching ground level. However, the penetrating muon component persists and this flux of uncorrelated muons is the dominant portion of the total particle flux at ground level and a major consideration in the design of neutrino detectors located close to ground level. Atmospheric muons have absorption path lengths of up to several kilometres in rock. Hence a significant flux of downward travelling atmospheric muons will pass through the water in the Blue Lake and reach the detector. Additionally, muon-neutrinos produced in cascade showers above other parts of the earth may result in background events if they interact with nuclei in the earth to produce upward going muons which pass through the detector. Hence the main sources of

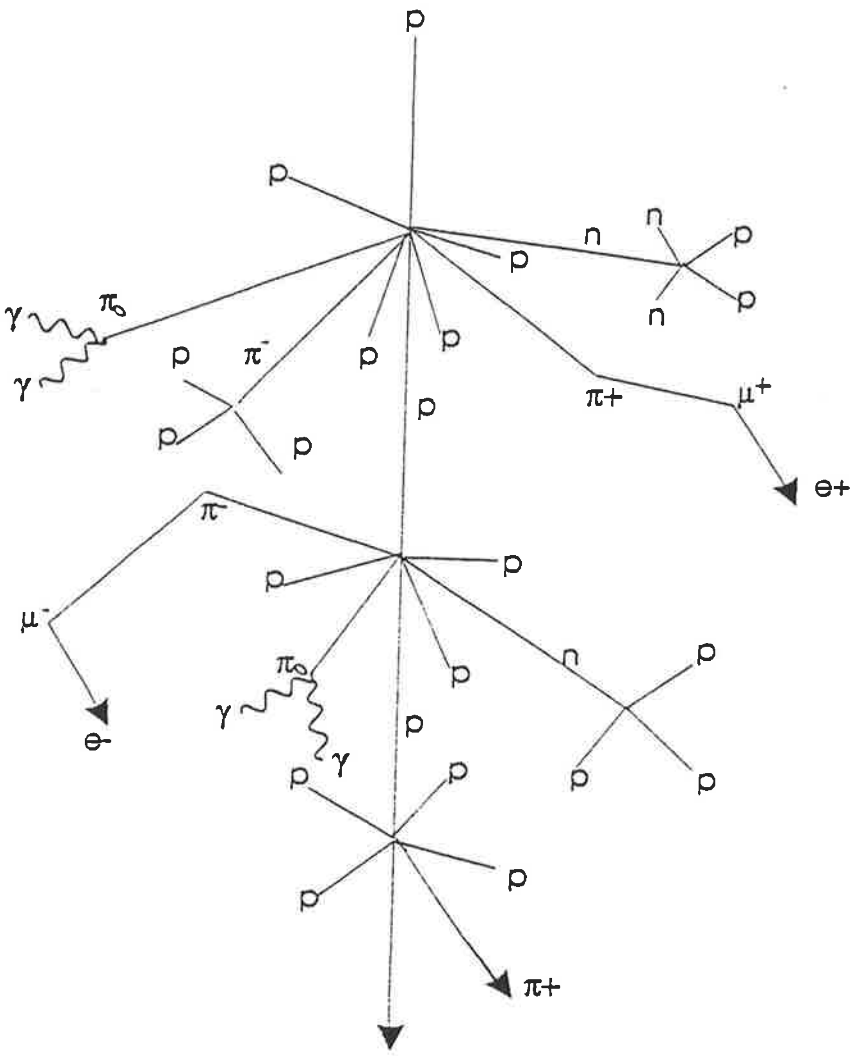

Figure 4.17: Schematic view of a hadronic cascade (Allkofer 1975). Note that the transverse scale is greatly exaggerated and that neutrinos have not been included

background particles which can result in events being registered in a surface neutrino detector are downward travelling uncorrelated atmospheric muons and atmospheric muon-neutrinos which travel upwards through the earth.

Another possible source of background events is correlated particles occurring in a cascade shower which reaches ground level. If several particles, which are correlated in time, pass through the detector then it is possible that the resulting photomultiplier tube signals will look like the signals corresponding to a single muon passing upwards through the detector. Air showers consist of three components:- the nuclear component which includes the original particle and resulting hadrons; the electromagnetic component consisting of electrons, positrons and photons; and the muonic component which consists of muons and neutrinos. The nuclear component accounts for only about 1% of air shower particles at ground level and is narrowly distributed about the shower core. The electromagnetic component is almost totally absorbed in a few metres of water. The muons, however, are significantly more penetrating and there may be a sufficient flux of correlated muons passing through the detector to result in coincident pulses occurring in several photomultiplier tubes. The expected rates of background events resulting from atmospheric neutrinos, uncorrelated muons and correlated muons in air showers are discussed in the following sections.

4.5.2.1 Atmospheric Neutrinos

Atmospheric neutrinos which interact with nuclei in the earth to produce upward going muons will produce a signal in the detector which is indistinguishable from the extraterrestrial neutrino signal. It is this atmospheric neutrino flux which ultimately limits the sensitivity of neutrino detectors. Figure 4.18 shows the total atmospheric neutrino flux and the atmospheric neutrino flux within a 1° error circle, compared with the expected neutrino flux from Cygnus X-3 (Gaisser and Stanev, 1985).

The differential atmospheric neutrino spectrum is steeper than the extraterrestrial neutrino spectrum, falling off as $E^{-3.7}$. For neutrino energies greater than about

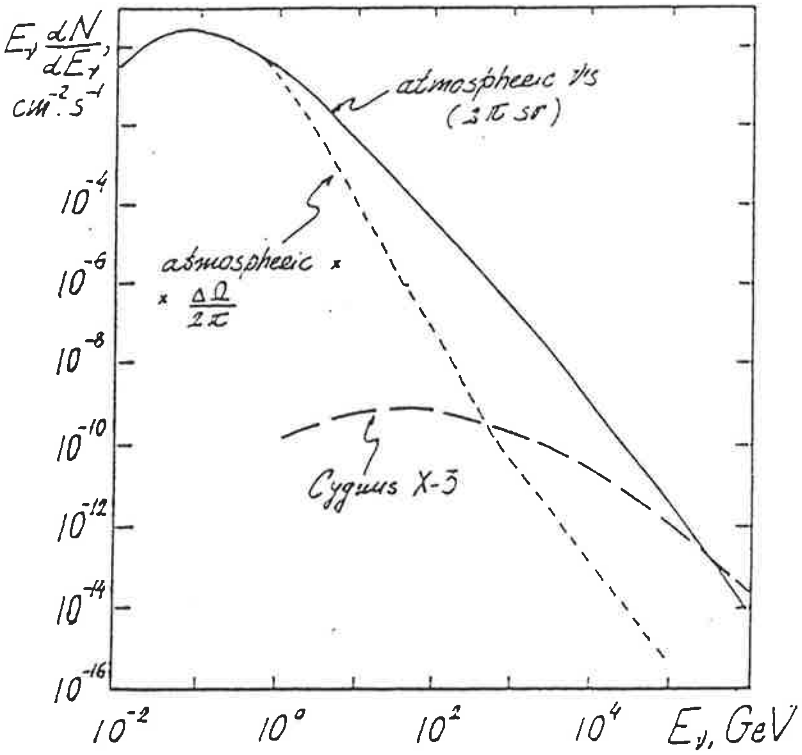

Figure 4.18: Atmospheric neutrino flux within 1° angular resolution compared to predicted neutrino flux spectrum from Cygnus X-3 (Gaisser and Stanev, 1985)

1TeV, the ground level neutrino flux is dominated by extraterrestrial neutrinos. Hence increasing the lower energy threshold of a neutrino detector will improve the ratio of extra-terrestrial to atmospheric neutrinos detected.

The expected flux of atmospheric neutrino-induced muons greater than 2GeV is equal to about $1.6 \times 10^{-12}\text{cm}^{-2}\text{s}^{-1}$ over 2π steradians (Gaisser and Stanev, 1984). The error on this flux is of the order of 20%, resulting from the error in the assumed atmospheric neutrino flux as derived by Volkova (1980). When observing a neutrino point source only muons arriving within the 1.6σ error circle of the detector are considered. The nadir angular dependence of the atmospheric neutrino-induced muon flux is approximately isotropic (Svoboda 1990). Hence the atmospheric neutrino background in the observing window is proportional to the solid angle viewed. The expected rate of atmospheric neutrino-induced muons passing through the proposed detector as a function of the 1.6σ error circle is shown in figure 4.19 from which it can be seen that the expected rate of neutrino-induced muons from

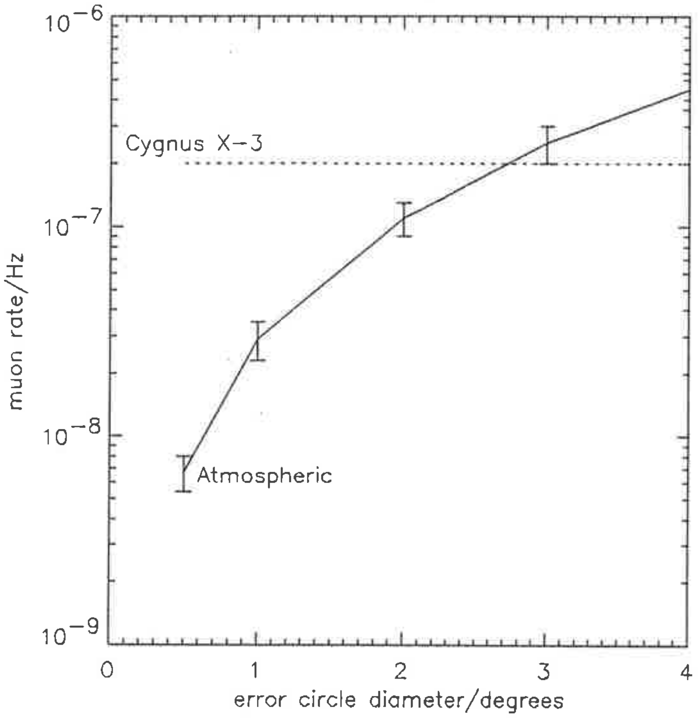

Figure 4.19: Rate of background atmospheric neutrinos viewed by the detector as a function of the 1.6σ error circle diameter. Also shown is the predicted muon flux from Cygnus X-3 falling within the error circle

Cygnus X-3 is approximately ten times greater than the rate of atmospheric neutrino-induced muons if the error circle is 1°.

The actual rate of events recorded due to atmospheric neutrinos depends on the flux of muons arriving within the detector error circle and also on the effective area of the detector to upward travelling muons. Both these factors vary with the detector parameters. The effective area as a function of the muon nadir angle is determined using a Monte Carlo simulation as described in section 4.4.1. Assuming atmospheric neutrino-induced muons arrive isotropically and continuously, then the average effective area for a detector aperture of nadir angle 0° to 70° is given by equation 4.7.

$$\mathrm{effarea} = \sum_{0^\circ}^{70^\circ} \mathrm{area}(\theta)\ \sin\theta\ \Delta\theta \tag{4.7}$$

where effarea = average effective area of the detector

area(θ) = effective area as a function of nadir angle

		event rate/year
grid spacing/m	2	0.10 ± 0.02
	4	0.27 ± 0.05
	6	0.30 ± 0.06
photocathode diameter/m	0.1	0.47 ± 0.09
	0.14	0.53 ± 0.11
	0.2	0.27 ± 0.05
lower level discriminator/pe	1	0.27 ± 0.05
	2	0.12 ± 0.02
	3	0.009 ± 0.002
minimum no.PMTs/layer	3	0.27 ± 0.05
	4	0.19 ± 0.04
	5	0.11 ± 0.02

Table 4.4: Predicted rate of background events due to atmospheric neutrinos for an angular resolution of 1.6 sigma. The fixed values of parameters used, when not being varied, are grid spacing=4 metres, photocathode diameter=0.2 metres, lower level discriminator=1 photoelectron, minimum number of photomultiplier tube hits per layer=3.

$$\theta = \text{nadir angle}$$

The rate of atmospheric neutrino-induced muons registered by the detector is then given by the product of the total flux of these muons arriving within the detector error circle and the average effective area calculated from equation 4.7.

The predicted rate of background events due to atmospheric neutrinos, arriving within the 1.6σ error circle, has been calculated for a range of detector geometries and triggering conditions. The results are presented in table 4.4. The error on these event rates is approximately 20% due to the error in the atmospheric neutrino flux spectrum calculated by Volkova (1980).

4.5.2.2 Uncorrelated Atmospheric Muons

The most significant flux of particles passing through the detectors is due to uncorrelated atmospheric muons. The upward atmospheric muon flux is negligible due to absorption in the earth. However, the downward muon flux at detectors located close to the earth's surface is very high. Downward muons can be differentiated from upward travelling muons from the timing pattern of photomultiplier tubes which view the resulting Cerenkov light. However, if the flux of muons triggering photomultiplier tubes is very high then the dead time of the detector may be prohibitively high and also the rate of triggers due to accidental coincidences will become significant.

The downward muon flux as a function of depth in the lake can be determined using a Monte Carlo technique to simulate downward travelling muons passing through water. The main steps of the simulation are as follows:-

1. The point where the muon crosses the surface of the lake is randomly selected across an area, A.

2. The energy of the muon is randomly selected from the integral atmospheric muon spectrum which varies as $E^{-1.1}$ for muon energies greater than a few GeV. The minimum muon energy considered is 12GeV which is the minimum energy required for a downward muon to reach a depth of 60 metres in water without being absorbed.

3. The muon trajectory is determined assuming that the azimuthal angular dependence is isotropic and that the zenith angle dependence is given by equation 4.8.

   $$P(\theta) = cos^n\theta \tag{4.8}$$

   where n is a function of the muon energy as shown in figure 4.20 (Allkofer 1975).

4. The distance each muon travels to reach a specific water depth is determined and a muon is counted if the absorption length in water is greater than this distance. The fraction of total muons simulated which reach the depth considered can then be determined.

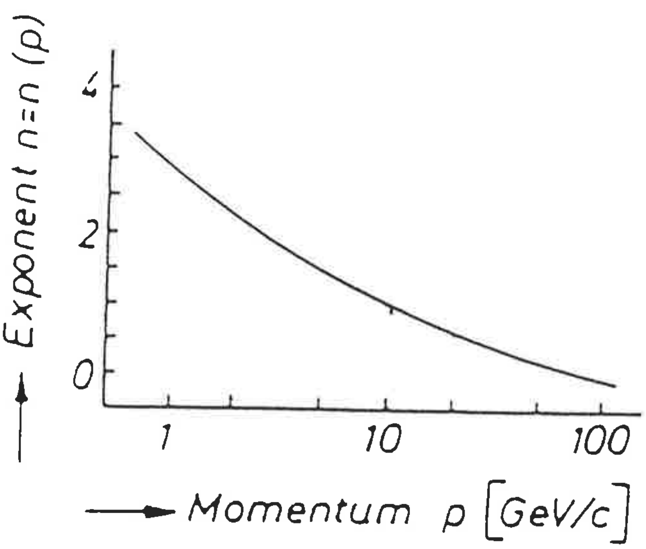

Figure 4.20: Variation of n as a function of muon energy

5. The absolute value of muon flux at depth is equal to the fraction of simulated muons reaching the depth multiplied by the total ground-level flux of muons considered. The total muon flux, adjusted to account for the effect of geographical latitude, is taken from Wolfendale (1973).

The downward muon flux as a function of depth in water is shown in figure 4.21.

These uncorrelated, downward-travelling muons can produce signals in downward looking photomultiplier tubes in several different ways. Muons with energies greater than the Cerenkov threshold in water ,which arrive at zenith angles greater than 48°, will emit Cerenkov light which directly illuminates some of the photomultiplier tubes. For muons arriving at less than 48° a signal will be recorded in two cases. Firstly, the muon can be backscattered in the rock surrounding the detector, in which case the resulting event will look identical to an event due to an upward-travelling muon. Secondly, Cerenkov light can be backscattered into the viewing aperture of photomultiplier tubes. Light scattering in natural water occurs predominantly in the forward direction as discussed in section 3.4. Hence, the number of photons which are backscattered into the viewing apertures of the photomultiplier tubes is expected to be very small. Also, any events registered in

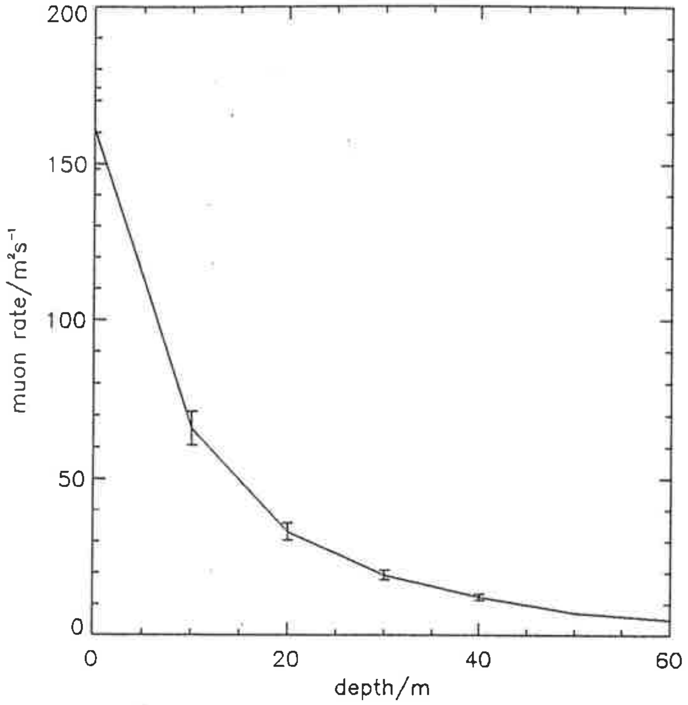

Figure 4.21: Downward muon flux as a function of depth in water

this manner can be identified as due to downward travelling muons from the timing sequence in which the layers of photomultiplier tubes are triggered. Hence the rate of events, due to backscattered Cerenkov light, which are indistinguishable from genuine signal events can be assumed to be negligibly small. For the case of muons arriving at zenith angles greater than 48°, the resulting signals can be identified as originating from a downward-travelling muon. However, this discrimination may occur off-line, in which case a large number of downward muons will satisfy the on-line triggering conditions causing the detector to register an event. The rate of such events must be within the acquisition speed of the electronics to ensure that the detector dead time is not too high. To assess this factor the flux of background events due to downward atmospheric muons which satisfy the hardware triggering criterion that each layer of photomultiplier tubes is triggered within the time window, t_{flight}, has been calculated.

Note that only single muons have been considered. The simulation does not include muon bundles or bremsstrahlung, both of which may affect the more highly biased trigger rates.

Atmospheric Muons Arriving at Zenith Angles Greater than 48°

Muons arriving at zenith angles greater than 48° will directly illuminate downward looking photomultiplier tubes as shown in figure 4.9. The expected rate of events registered as a result of Cerenkov light from downward muons directly hitting photomultiplier tubes is equal to the product of the muon flux through the detector at zenith angle greater than 48° and the effective area for detecting these downward-travelling muons. The total muon flux is shown in figure 4.21 and the flux at angles greater than 48° is equal to about 0.3 of this total flux. The effective area was calculated by adapting the Monte Carlo simulation used to determine the effective area to upward muons described in section 4.4.1. For the case of downward muons, the energy is selected from the integral muon spectrum which varies as $E^{-1.1}$ and the arrival direction is selected according to equation 4.8 and, as only Cerenkov light from muons arriving at zenith angles greater than 48° can directly illuminate downward looking photomultiplier tubes, the zenith angles were selected in the range 48° to 90°. The rate of background events was determined as a function of geometrical parameters (the grid spacing between photomultiplier tubes in a layer and the photocathode area) and triggering conditions (the photoelectron threshold in each photomultiplier and the minimum number of photomultipliers per layer which register signals). The results of background event rate as a function of each variable considered are shown in figure 4.22.

These events will be identified as downward travelling muons either in the hardware triggering conditions or in the subsequent software analysis. However if the rate of these events is very high then the dead time of the detector may become unreasonably high. In the worst case we can assume that all the events due to downward muons are registered by the detector and are not eliminated until the software analysis. Hence for each event recorded the detector is effectively dead for a period of 263ns. In order to ensure that the detector dead time is low, the rate of background events recorded must be significantly less than 1/263 ns i.e. less than about 3.8 MHz. From the results shown in figure 4.22 it can be seen that the maximum predicted rate of background events due to downward travelling muons is 1kHz. This low event rate is a result of the very low effective area of the detector to downward travelling muons. Hence, the proposed detector will be capable of operating successfully even if there are no hardware cuts to eliminate triggers due to downward travelling muons. However, a background trigger rate of 1kHz would prove challenging in terms of data acquisition and analysis. It is likely that intelligent on-line filtering could be implemented.

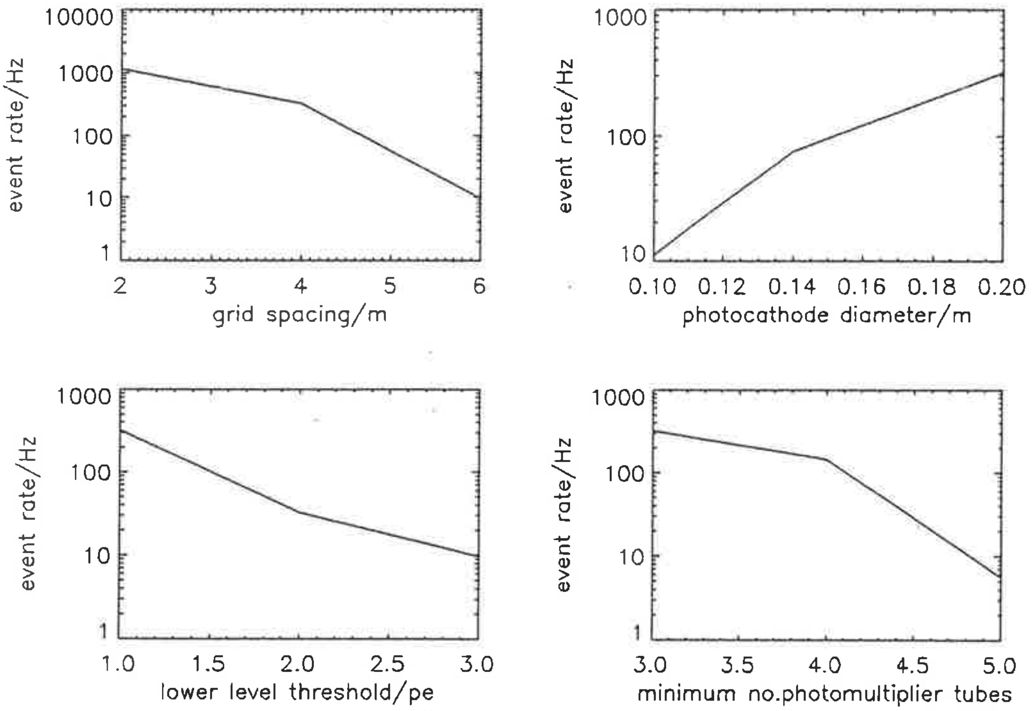

Figure 4.22: Predicted rate of background events due to downward travelling muons. When not being varied, the fixed values of the parameters used in these simulations are grid spacing=4 metres, photocathode diameter=0.2 metres, lower level threshold=1 photoelectron, minimum number of photomultiplier tube hits=3.

Random Coincidences due to Background Particles

A single muon passing downwards through the detector can be identified as downward travelling from the sequence of photomultiplier tube hits. However, if several downward muons pass through the detector within the time window of 263ns then the resulting signals could be misinterpreted as originating from an upwards travelling muon. The large flux of downward muons at the detector means that each photomultiplier tube layer may be triggering at a high rate and hence the rate of random coincidences between all three layers may be significant. An event will be recorded if each layer is triggered within the time window in a timing sequence consistent with an upward travelling muon. An illustration of how this can occur is shown in figure 4.23.

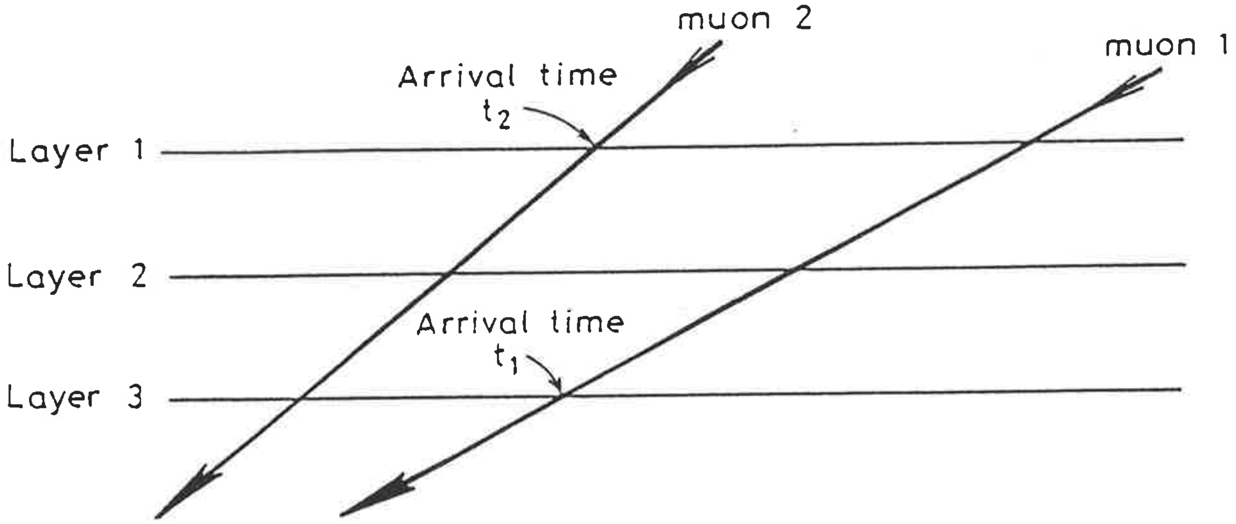

Figure 4.23: Geometry for misidentification of downward travelling muons. t_1=time at which muon 1 crosses layer 3, t_2=time at which muon 2 crosses layer 1.

In this figure the Cerenkov signals recorded will look like those due to an upward travelling muon if the arrival time, t_1, is less than the arrival time, t_2, and providing that $t_2 - t_1$ is less than the coincidence time window ,t_{flight}.

The rate of events due to random coincidences between downward muons is given by equation 4.6 in which the rate of triggers per layer, f_1, f_2, f_3, corresponds to the rate of triggers per layer due to Cerenkov light from downward muons directly illuminating photomultiplier tubes. This trigger rate per layer was calculated by simulating downward muons crossing a single layer of photomultiplier tubes and

		event rate/year
grid spacing/m	2	1.8 ± 0.4
	4	$2.0 \times 10^{-1} \pm 0.5 \times 10^{-1}$
	6	$9.2 \times 10^{-4} \pm 2.2 \times 10^{-4}$
photocathode diameter/m	0.1	$4.3 \times 10^{-2} \pm 1.0 \times 10^{-2}$
	0.14	$5.7 \times 10^{-1} \pm 1.4 \times 10^{-1}$
	0.2	$2.0 \times 10^{-1} \pm 0.5 \times 10^{-1}$
lower level discriminator/pe	1	$2.0 \times 10^{-1} \pm 0.5 \times 10^{-1}$
	2	$6.2 \times 10^{-3} \pm 1.5 \times 10^{-3}$
	3	$2.8 \times 10^{-4} \pm 0.7 \times 10^{-4}$
minimum no.PMTs/layer	3	$2.0 \times 10^{-1} \pm 0.5 \times 10^{-1}$
	4	$3.9 \times 10^{-2} \pm 0.9 \times 10^{-2}$
	5	$1.0 \times 10^{-2} \pm 0.2 \times 10^{-2}$

Table 4.5: Rate of random coincidences due to downward travelling muons within a 1.6σ error circle. The fixed values of parameters used, when not being varied, are grid spacing=4 metres, photocathode diameter=0.2 metres, lower level discriminator=1 photoelectron, minimum number of photomultiplier tube hits per layer=3.

determining the fraction of muons resulting in Cerenkov signals in the photomultiplier tubes which satisfy the triggering conditions for a single layer. The resulting rate of events registered due to random coincidences between the three layers, within the 1.6σ error circle of the detector, was then calculated for various triggering conditions and the results are presented in table 4.5. The predicted event rates listed in table 4.5 can be further reduced by requiring that the points at which muons cross each layer are colinear.

Atmospheric Muons Arriving at less than 48° - Muon Scattering

A downward travelling muon which is scattered in the rock surrounding the detector such that it then travels upwards through the detector will be indistinguishable from a genuine upward muon event. The expected rate of backscattered muons has been investigated by the GRANDE collaboration using experimental results from three muon detectors:- the IMB detector, a magnetic spectrometer experiment, MUTRON and the Baksan neutrino detector (Bratton et.al.1988). Scaling the results from the GRANDE proposal to the proposed Blue

Lake detector gives an upper limit on the predicted rate of backscattered muons, arriving within a 1.6σ error circle of 1°, of 4.3×10^{-9} Hz. This rate is approximately 50 times less than the predicted rate of upward neutrino-induced muons from Cygnus X-3. Hence the rate of these background events can be assumed to be negligible.

4.5.2.3 Correlated Muons in Cosmic Ray Air Showers

Muons arriving at zenith angles less than 48° will not directly illuminate downward looking photomultiplier tubes. However a muon actually passing through a photomultiplier tube may produce a signal above the photoelectron threshold. For an event to be registered several muons must pass through a sufficient number of photomultiplier tubes within the coincidence time windows of the detector. This is possible in the case of muons in a cosmic ray shower which will reach ground level at approximately the same time. The rate of background events due to muons in air showers arriving at less than 48° which pass through photomultiplier tubes has been determined using the simulation described below.

Monte Carlo Simulation for Correlated Muons

In this simulation cosmic ray showers are randomly generated in the atmosphere. The path of the primary particle is selected by choosing the zenith angle from the cosine dependence of cosmic ray showers (Allkofer 1975) and the azimuthal angle from an isotropic distribution. The location of the shower core at ground level is selected within an area significantly larger than the detector as an air shower can extend for hundreds of metres laterally at ground level.

Having determined the path of the shower core, the primary particle energy is selected from the primary energy spectrum shown in figure 4.24.

The size of the air shower at ground level can then be calculated by determining the depth in the atmosphere at which the air shower maximum occurs and the number of air shower particles at this point (Protheroe and Patterson 1984). The

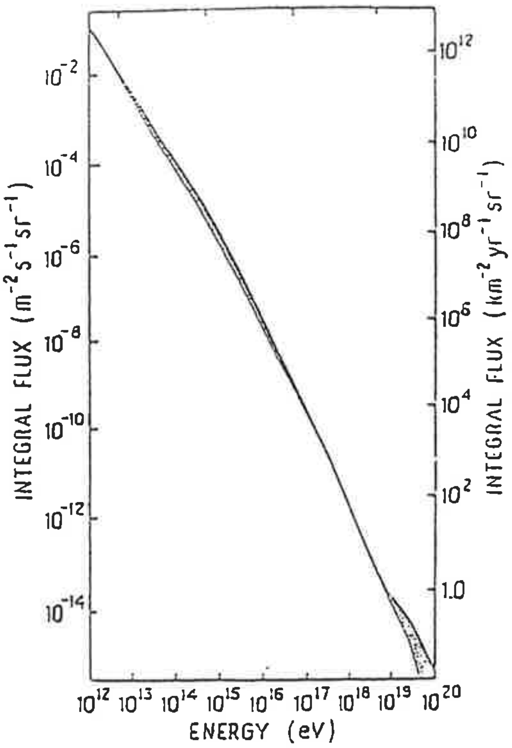

Figure 4.24: Cosmic ray primary particle integral energy spectrum (Jones, 1985)

size of the shower at ground level is then calculated according to equation 4.9.

$$N = N_{\mathbf{max}} e^{-\mathbf{xatmos}/185} \tag{4.9}$$

where N = shower size at ground level

$N_{\mathbf{max}}$ = maximum shower size

xatmos = distance from air shower maximum to ground level/gcm^{-2}

The density of muons in a shower front depends on the muon energy, the air shower size at ground level and the lateral distance from the shower core. This muon density is given by equation 4.10 (Khrenov and Linsley 1981).

$$\rho(> E_\mu, r) = \frac{5 \times 10^3}{(E_\mu + 250)^{1.4}} \, r^{-0.55\, \psi^{0.1} \phi^{0.07}} \, e^{\frac{\psi^{0.62} r}{80}} \, \psi^{0.78} \, \phi^{0.78} \tag{4.10}$$

where ψ = $(E_\mu + 2)/12 \; for \; 5 < E_\mu < 6 \times 10^3 \; GeV$

$$\begin{aligned}
N_e &= \text{shower size} \\
\phi &= \frac{N_e}{2 \times 10^5} \; for \; 3 \times 10^4 < N_e < 10^6 \\
E_\mu &= \text{muon energy/GeV} \\
r &= \text{lateral displacement from core/m} \\
\rho &= \text{muon density/number m}^{-2}
\end{aligned}$$

Using equation 4.10 the density of muons in each photomultiplier tube in the detector is calculated. The minimum muon energy in equation 4.10 is assumed to be the energy of a muon which just reaches the photomultiplier tube before being absorbed in the water. The number of muons in each photomultiplier tube, including the effects of Poisson fluctuations, can then be calculated and the number of tubes recording more than one muon are counted. It is assumed that a muon passing through a photomultiplier tube will produce a pulse above the photoelectron threshold. Hence a layer will be triggered if greater than the minimum required number of photomultiplier tubes have at least one muon passing through them. An event will be recorded if this occurs in all three layers. The rate of such events is equal to the product of the fraction of air showers simulated which are registered as an event and the total rate of air showers considered in the simulation. The rate of air showers is derived from the energy spectrum in figure 4.24 and the main source of error in the simulated event rates results from the error in this air shower rate. The simulated rate of background events due to correlated air shower muons as a function of grid spacing and for a minimum of 3 photomultiplier tubes per layer registering at least 1 muon is shown in figure 4.25.

These events can be identified as downward travelling muons from the timing sequence in which each layer is triggered. However, such correlated muons can be misinterpreted as an upward-going muon event in two ways. Firstly, if several air showers pass through the detector within the coincidence time window of 263ns then the 3 layers may trigger randomly in the correct sequence. The expected rate of such

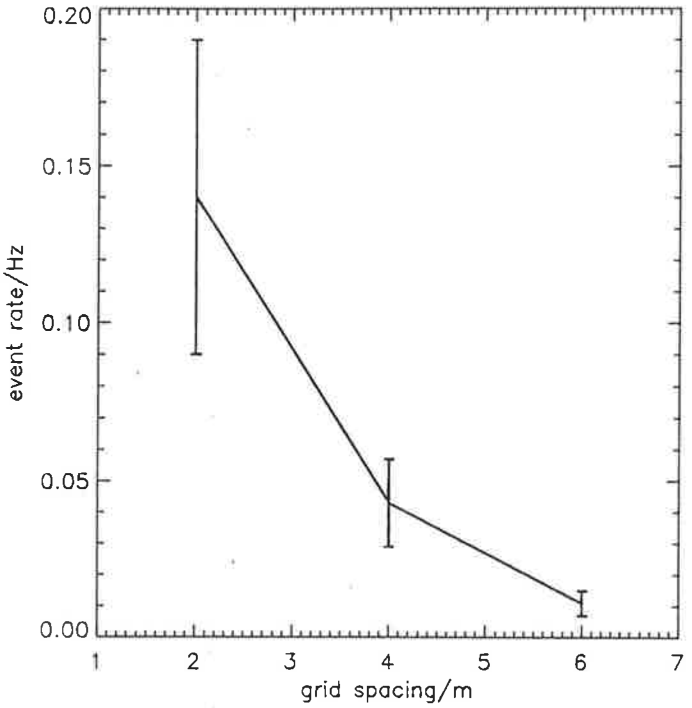

Figure 4.25: Rate of background events due to correlated muons in cosmic ray showers

events can be calculated from equation 4.6 in which f_1, f_2 and f_3 are the rate at which layers 1,2 and 3 are triggered by air shower muons. The highest rate of these random triggers will occur for a grid spacing of 2 metres and a minimum number of 3 photomultiplier tubes registering at least 1 muon. The rate of triggers of a single layer of photomultiplier tubes for these conditions is 0.14 Hz. Hence, the rate of events registered due to random coincidences between 3 such layers is equal to 1.9×10^{-16}Hz which is negligible compared to the expected rate of signal events.

The second way in which a correlated muon event can be interpreted as an upward travelling muon is if the muons in an air shower front arrive over a period of time comparable to the detector coincidence window, i.e. 263ns. If this is the case then it is possible that some muons in the air shower will arrive at the lower detector layer before the upper layers are triggered. The spread in arrival times of particles in a shower front has been investigated by Linsley (1985). This spread in arrival times increases as the lateral distance from the shower core increases. For a dispersion in arrival times of 280 ± 12ns the corresponding distance from the shower core is about

650 metres. If the number of muons passing through photomultiplier tubes located about 650 metres from an air shower core is sufficiently large, then it is possible that an event would be recorded which would be indistinguishable from a genuine signal event. The density of muons at a distance of 650 metres from a shower core can be determined using equation 4.10 assuming that the minimum muon energy equals 12GeV (the energy required to reach a water depth of 60 metres). The muon density and hence the expected number of muons in a photomultiplier tube of diameter equal to 200mm has been determined for a range of cosmic ray primary particle energies. This calculation assumes that the ratio of primary particle energy, in electronvolts, to the number of shower particles is 10^{10}. The resulting plot of muon density as a function of primary particle energy is shown in figure 4.26. From these results it can

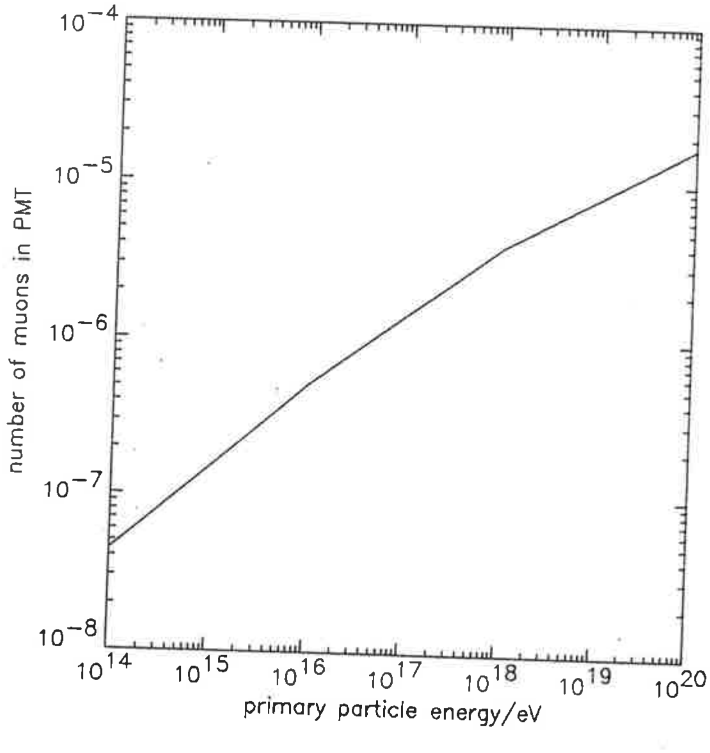

Figure 4.26: Muon density as a function of primary particle energy at a distance of 650 metres from the shower core

be seen that for a primary particle energy of 10^{20}eV the number of muons in a photomultiplier tube 650 metres from the shower core is 1.02×10^{-5}. Hence for energies up to this value, the muon density at 650 metres from the shower core is about 10^5 times too low to trigger any of the photomultiplier tubes. This muon density will increase as the primary particle energy increases, however, the flux of air showers due to primary particles with energies greater than 10^{20}eV is of the order of 1/km^2/century. Hence it can be assumed that the rate of cosmic ray air showers which would result in the required spread in arrival times and the required muon density of at least 1 muon in 3 photomultiplier tubes per layer is negligibly small.

4.5.3 Summary of Background Fluxes

Background events registered by the proposed neutrino detector fall into two categories. Firstly there are background events resulting from downward travelling muons which emit Cerenkov light which is detected by the photomultiplier tubes or which actually pass through photomultiplier tubes causing signals to be registered. These events will trigger the layers of photomultiplier tubes sequentially from the top layer to the bottom layer and hence can be identified as downward travelling muons from this timing sequence. These events will only cause a problem if the flux is high enough to significantly affect the dead time of the detector. For this to occur the flux of background events due to downward muons would have to be of the order of 3.8MHz. It has been shown that the predicted flux of these events is significantly less than 3.8MHz even if they are not eliminated due to timing considerations until the off-line software analysis. Hence, the events registered due to downward travelling muons will have a negligible effect on the dead time of the detector.

The second class of background events are those which are indistinguishable from genuine signal events due to upward travelling muons produced by high energy extra-terrestrial neutrinos. These background events can result from several sources namely:-

1. atmospheric neutrinos

		event rate/year
grid spacing/m	2	1.9 ± 0.4
	4	0.47 ± 0.07
	6	0.30 ± 0.06
photocathode diameter/m	0.1	0.51 ± 0.09
	0.14	1.1 ± 0.2
	0.2	0.47 ± 0.07
lower level discriminator/pe	1	0.47 ± 0.07
	2	0.13 ± 0.02
	3	0.009 ± 0.002
minimum no.PMTs/layer	3	0.47 ± 0.07
	4	0.23 ± 0.04
	5	0.12 ± 0.02

Table 4.6: Summary of predicted background events. The fixed values of parameters used, when not being varied, are grid spacing=4 metres, photocathode diameter=0.2 metres, lower level discriminator=1 photoelectron, minimum number of photomultiplier tube hits per layer=3.

2. random coincidences between photomultiplier tube signals resulting from photomultiplier tube noise, background light, downward travelling atmospheric muons and air shower muons

3. downward travelling muons which are backscattered

As these events cannot be differentiated from upward-travelling muon events, the rate of such background events arriving within the 1.6σ error circle of the detector must be less than the rate of signal events. The predicted total rate of background events arriving within the angular resolution, from all the noise sources considered and for a range of detector geometries and triggering conditions are summarised in table 4.6. This total rate is dominated by the event rates due to atmospheric neutrinos and random coincidences resulting from downward travelling atmospheric muons passing through the detector.

However, the background rejection of downward going muons needs to be investigated further to take into account factors such as muon bundles, bremsstrahlung and the actual effects of background light and electronic noise.

		signal to noise ratio
grid spacing/m	2	2.1 ± 0.2
	4	4.1 ± 0.3
	6	1.3 ± 0.1
photocathode diameter/m	0.1	0.70 ± 0.06
	0.14	1.8 ± 0.2
	0.2	4.1 ± 0.3
lower level discriminator/pe	1	4.1 ± 0.3
	2	3.6 ± 0.3
	3	1.1 ± 0.1
minimum no.PMTs/layer	3	4.1 ± 0.3
	4	4.8 ± 0.4
	5	4.0 ± 0.3

Table 4.7: Signal to noise ratio for a 1.6σ error circle. The fixed values of parameters used, when not being varied, are grid spacing=4 metres, photocathode diameter=0.2 metres, lower level discriminator=1 photoelectron, minimum number of photomultiplier tube hits per layer=3.

4.6 Signal to Noise Ratio

In order that the proposed neutrino detector observes neutrinos from point sources the signal to noise ratio should be at least 3, and the absolute rate of signal events must be at least a few events per year to produce a positive result in a reasonable time frame. The signal to noise ratio is defined by equation 4.1. This parameter can be determined for the case of Cygnus X-3, from the predicted signal event rates listed in table 4.3 and the total background event rates listed in table 4.6. The resulting signal to noise ratios, for various detector configurations, are presented in table 4.7.

From these results it can be seen that four of the detector configurations considered resulted in a signal to noise ratio greater than 3 for the case of Cygnus X-3. Ideally we would select the detector configuration with the highest signal to noise ratio, provided that the absolute event rate is at least a few events per year and the angular resolution is less than 1°. The highest signal to noise ratio is achieved for the case of grid spacing=4m, photocathode diameter=0.2m, lower level discriminator=1 photoelectrons and a mimimum of 4 photomultiplier tube hits per layer. The resulting signal to noise ratio is 4.8 ± 0.4 and the predicted event rate from Cygnus X-3 is 2-3 per year. The 1σ angular resolution is 0.47°. This configuration therefore satisfies all of the three conditions required to observe point sources and is selected as the optimum detector configuration. Again it should be noted that there is a large uncertainty in the predicted signal rate.

4.7 Conclusion

In this chapter Monte Carlo simulations have been used to optimise the design of a high energy neutrino detector to be located in the Blue Lake. The criteria which must be satisfied in order that the detector observes neutrinos from point sources are as follows:-

1. The rate of signal events should be at least a few events per year
2. The signal to noise ratio should be at least 3
3. the 1σ angular resolution should be less than 1°

The expected rate of signal events was assessed by simulating the detector response to upward travelling muons resulting from high energy neutrinos emitted from Cygnus X-3. The predicted event rates from this source are listed in table 4.3. In order to determine the expected background rate, various sources of background events were considered. The main contributions to the total rate of background events were found to be due to atmospheric neutrino-induced muons passing upwards through the detector, and random coincidences between photomultiplier tube signals resulting from Cerenkov light emitted by downward travelling atmospheric muons. All other sources of background events either produce signals which can be differentiated from the signals due to upward travelling muons, or occur at negligibly low rates compared to the signal event rate. Table 4.7 lists the predicted signal to noise ratios for a range of detector geometries and triggering conditions. These results show that for four of the detector configurations considered, the signal to noise ratio is greater than 3 and hence, in these cases, it should be possible to observe high energy neutrino-induced muons above the background flux.

The results of the simulations indicate that the optimum design, in terms of the three criteria listed, is a detector located at a depth greater than 40 metres and consisting of three layers of photomultiplier tubes as shown in figure 4.11. The photomultiplier tubes in each layer are arranged on a square grid of grid spacing 4 metres. The photocathode diameter of each tube is 0.2 metres and the triggering conditions for the detector are that at least 4 photomultiplier tubes per layer register signals of greater than 1 photoelectron. For this detector design the 1σ angular resolution is 0.47° and it is assumed that only events arriving within an error circle of radius equal to 1.6σ are considered. The expected rate of signal events from Cygnus X-3 is 2-3 per year, assuming the Kolb, Turner and Walker model for neutrino production in Cygnus X-3 (Kolb, Turner and Walker, 1985). The predicted signal to noise ratio is 4.8 ± 0.4.

Chapter 5

Feasibility Tests

5.1 Introduction

In order to assess the feasibility of observing muons in the Blue Lake by the detection of the induced Cerenkov radiation, a test device was designed and built (hereafter referred to as Harvey II) to track individual muons and record the emitted Cerenkov light. Harvey II consists of a muon telescope and a light detector arranged as shown in figure 5.1 such that the Cerenkov light from muons which pass through the telescope is registered by the light detector.

The aim of this device was to record the magnitude of muon-induced Cerenkov pulses. As no timing information was to be used, it was decided to use slow electronics i.e. slow amplifiers and a multi-channel analyser to record the data. The advantage of using slow electronics was that existing electronics and data acquisition equipment used in Harvey I could be easily adapted for use in Harvey II. However, the amount of noise registered using a slow system is greater than in a fast system. Hence, if the background light level in the Blue Lake is high it may be difficult to identify Cerenkov signals from noise pulses. This factor proved to be a major limitation in the design of Harvey II. As discussed in this chapter, it was possible to detect Cerenkov signals using Harvey II. However, the background light level in the lake was surprisingly high, even when operating at depths of 60 metres during moonless nights and the signal to noise ratio of the system was correspondingly low. The signal to noise ratio could be significantly improved by using fast electronics.

The muon telescope consists of two vertically separated pods with each pod containing a scintillator optically coupled to a photomultiplier tube. A muon passing through the scintillator produces a light pulse which is detected by the photomultiplier tube. By separating the two pods and requiring that both pods must register a light pulse within a time window corresponding to the time of flight of a muon between the pods, one can ensure that only muons arriving within a known solid angle will trigger the telescope. Hence the direction of muons triggering the telescope is known to within the limits set by the angular acceptance of the telescope.

The light detector is a photomultiplier tube positioned as shown in figure 5.1. The photomultiplier tube face is oriented at 42° to the vertical so that Cerenkov light produced by a muon passing vertically downwards through the telescope will hit the light detector normally, hence maximising the effective area of the light detector.

The test device was primarily intended to observe downward-going atmospheric muons in the Blue Lake by pointing the light detection pod upwards as in figure 5.1 and recording the light pulses observed when the muon telescope was triggered. The aim of this was to assess if it would be possible to observe muons in the Blue Lake via the emitted Cerenkov light and also to determine the transmission properties of Cerenkov light in Blue Lake water from the amplitudes of the light pulses recorded.

The attenuation length of water in the lake, measured using the transmission spectrometer and Harvey I as described in chapter 3, is of the order of 4 metres. If this attenuation is mainly due to absorption then the grid spacing of the proposed neutrino detector has to be about 4 metres. However, if there is a large scattering component in the light attenuation then a significant number of photons may be scattered into the viewing apertures of the photomultiplier tubes, causing larger signals to be registered than in the case of light attenuation via predominantly absorption processes. This increase in the amount of light detected would make it possible to space the photomultiplier tubes further apart than 4 metres. The

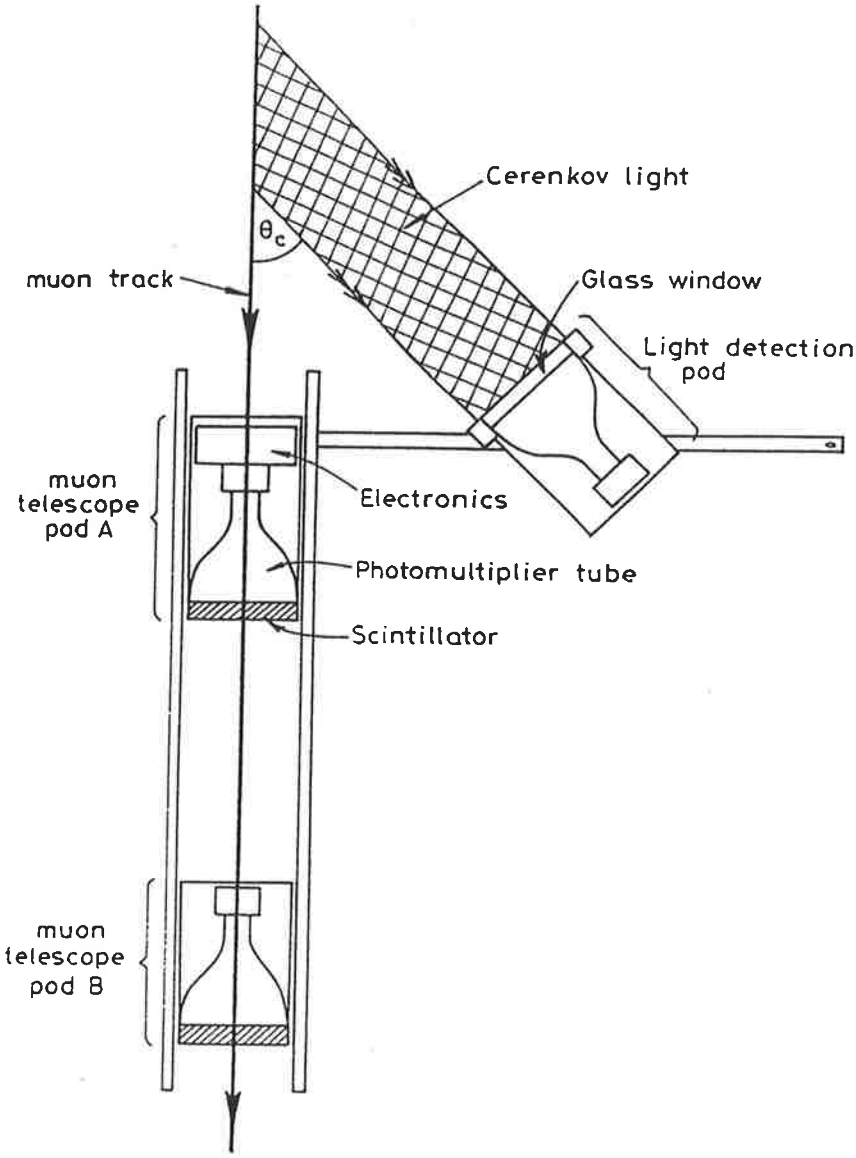

Figure 5.1: Cross-section of Harvey II

previous measurements of light attenuation as described in chapter 3 were performed using collimated light beams and hence most of the effects due to light scattering were eliminated. Harvey II was designed to observe the plane wave fronts of Cerenkov light emitted by muons and hence reproduce the expected signals in the proposed neutrino detector, including any effects due to light scattering. The signals registered by Harvey II therefore yield information on the attenuation length of lake water corresponding to the detection of Cerenkov light pulses in the proposed neutrino detector.

Another aspect of the proposed neutrino detector, investigated using Harvey II, is the background light level as a function of depth in the lake. If the ambient light level in the lake is high then the gain of the photomultiplier tubes in the detector, and hence the amplitude of the signals registered, will be reduced. Also, fluctuations in the background light will be recorded as light pulses and, if the DC light level is high, the frequency and magnitude of these noise fluctuations may swamp the Cerenkov signals from muons. Currently all the proposed surface neutrino detectors are to be located within light tight enclosures to eliminate the problem of background light. One function of Harvey II was to assess if it would be possible to operate a neutrino detector in the Blue Lake at night without shielding the detector from background light. The background light levels in the lake were measured by recording all the light pulses registered by the light detection pod.

The flux of atmospheric muons at various depths in the lake can be determined from the rate at which the muon telescope is triggered. The variation of muon flux with depth in water is well known and verification of this function is a test of the operation of the muon telescope.

5.2 Physical Description of Harvey II

5.2.1 The Muon Telescope

The muon telescope consists of two pods each containing a 5cm thick, 22cm diameter scintillator disk optically coupled to a 125mm diameter RCA 8055 photomultiplier tube. The scintillators are coated with reflective paint to maximise the amount of light hitting the photomultiplier tube face. The pods are aligned vertically with the separation between them variable from 0 to 1.5m. The separation between the pods determines the angular acceptance of the telescope. Increasing the separation between the pods reduces the range of zenith angles accepted and hence improves the accuracy with which muon tracks can be determined. However, reducing the solid angle acceptance also reduces the rate of muons detected. The spacing between the telescope pods is chosen to give an acceptable angular resolution while maintaining a reasonable event rate.

5.2.2 Light Detection Pod

The light detection pod consists of a 180mm diameter EMI 9623B photomultiplier tube which views Cerenkov light through a 2.5cm thick glass window. The pod can be positioned looking upwards or downwards at a variable distance from the muon telescope. The number of photons per unit wavelength reaching the photomultiplier tube depends on the attenuation length of the water and the distance of the photomultiplier tube from the muon track and is given by equation 5.1 for a muon passing straight through the centre of the telescope.

$$\frac{dN}{d\lambda} = \frac{\pi\alpha}{4R\lambda^2}\, tan\theta_c\, d^2\, e^{\frac{-R}{\lambda_a sin\theta_c}} \tag{5.1}$$

where α = fine structure constant

d = photomultiplier tube diameter/m

R = perpendicular distance from muon track to photomultiplier tube/m

λ_a = attenuation length/m

θ_c = Cerenkov angle

N = photon number

λ = wavelength/m

5.2.3 Mechanical Considerations

The construction of Harvey II was subject to a number of practical design constraints which were addressed as follows. The pods and connecting cables had to be watertight to a maximum pressure of 7 atm (60m of water plus atmospheric pressure) while keeping the total weight of the device as low as possible. The pods were made from 22cm diameter PVC pipe with a wall thickness of 5mm. Cables were connected into the pods via feedthroughs which were encased in epoxy under vacuum and then screwed into the aluminium end plates. The muon telescope pods were supported by three brass rods and the separation between the pods could be varied from 0m to 1.5m. The light detection pod was supported on a brass arm perpendicular to the telescope axis and the position of the light detection pod could be varied along this arm from 0m to 1.5m. When operated in the lake the whole device was suspended by a single cable attached to a winch in a boat as shown in figure 5.2. The buoyancy of the device was counteracted by a 10kg lead weight attached to the lowest telescope pod. To ensure that the device did not rotate as it was lowered, a rope was connected to the end of the horizontal arm and was released at the same rate as the winch cable.

5.3 Electronics

In order to minimise the number of cables going from the lake surface to the device, most of the electronics was contained in the upper pod of the muon telescope. Three

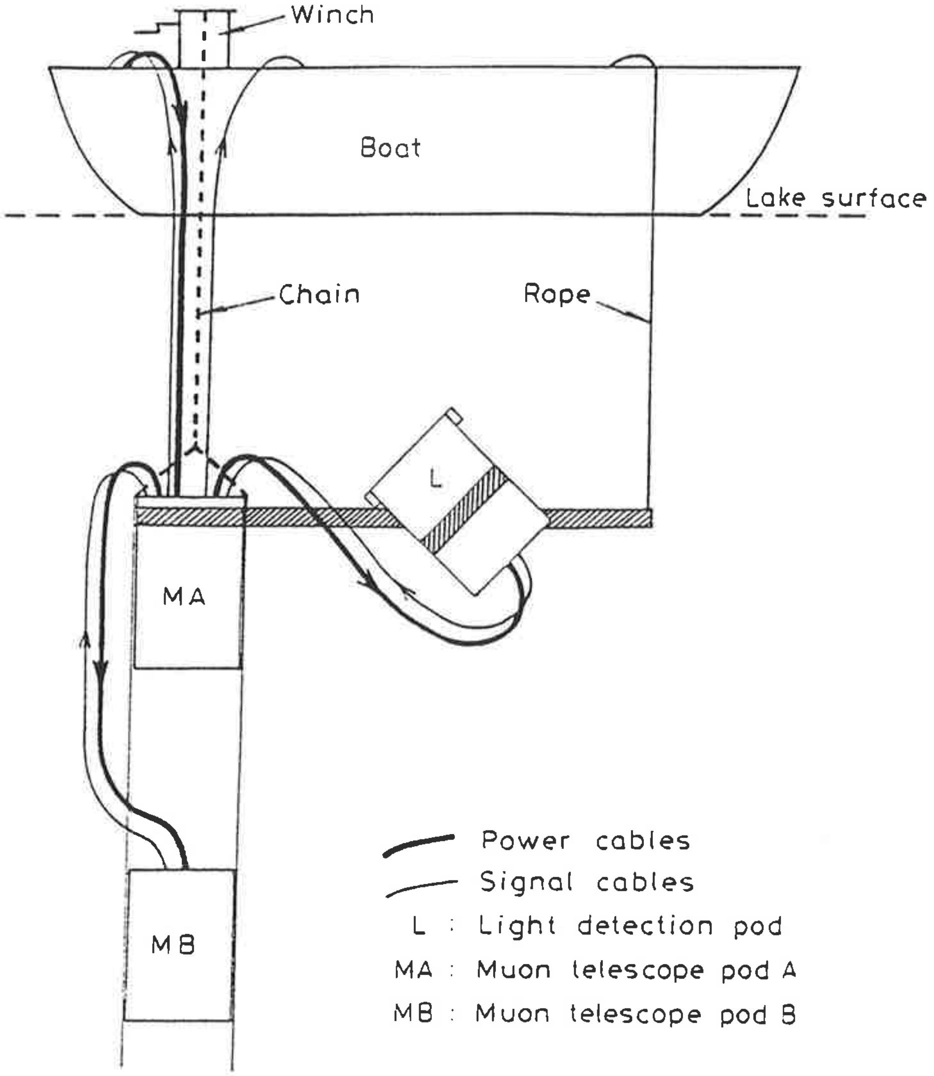

Figure 5.2: Schematic view of Harvey II during in-situ measurements

cables were required between the boat and Harvey II :- one to carry 20 volts DC supply from the surface to the electronics in the upper telescope pod, one signal cable to carry the trigger pulses from the muon telescope and a second signal cable to carry the pulses registered by the light detection pod. As Harvey II had to be portable, all the electronics were powered from two 12 volt car batteries located in the boat. The computer which records the data collected also resided on the boat. An overview of the electronics is shown in figure 5.3.

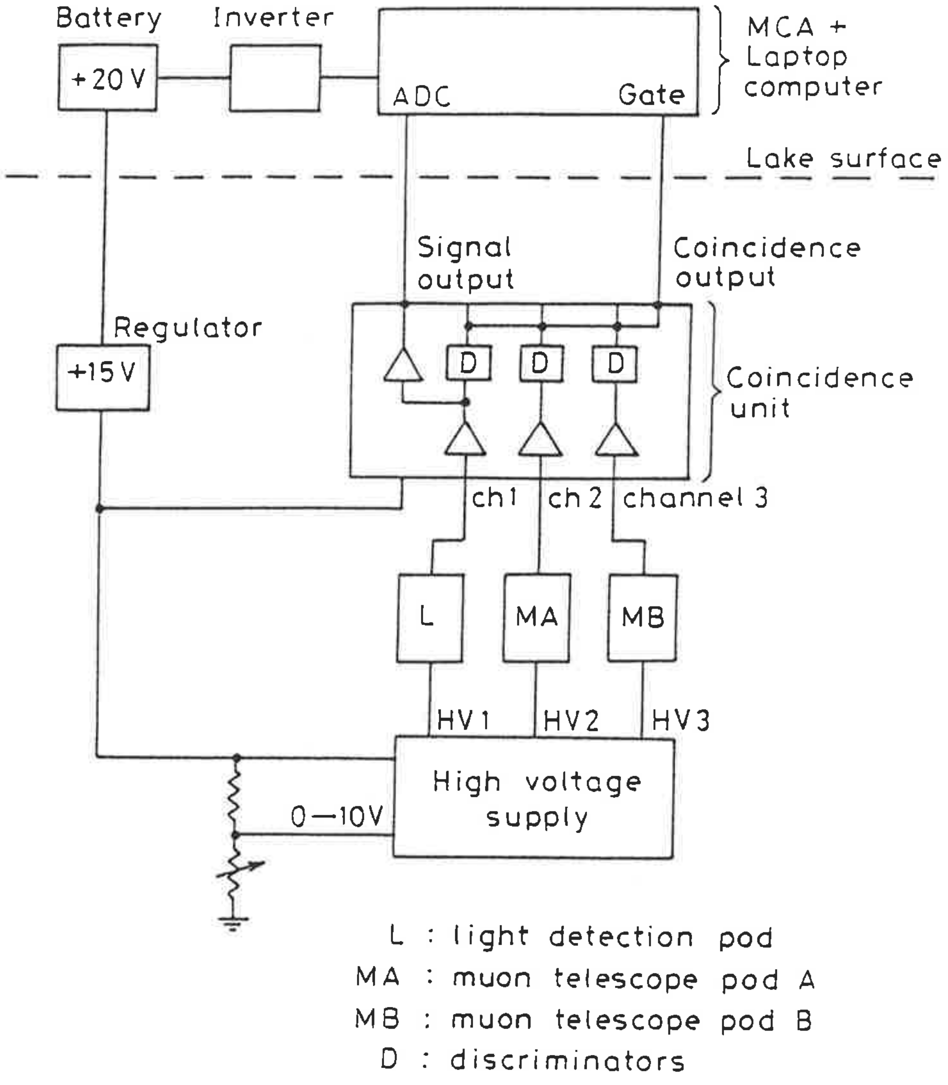

Figure 5.3: Overview of electronics for Harvey II

The electronics contained in the top telescope pod consisted of two high voltage supplies which could provide up to 1580V to each of the three photomultiplier tubes, and a coincidence unit built in Adelaide by Neville Wild. Signals registered by the three photomultiplier tubes were input to the coincidence unit in which they were inverted and amplified as shown in figure 5.3. The amplified pulses then passed through discriminators in which pulses with amplitudes less than the pre-set discriminator levels were ignored. A pulse with amplitude greater than the discriminator threshold setting resulted in a transistor-transistor logic (TTL) pulse of duration $0.5\mu s$ output from the discriminator unit. The TTL outputs from the discriminators were then tested for coincidences. A variety of coincidence conditions could be selected ranging from the requirement that a TTL pulse was output only on channel 1 to the requirement that all channels registered TTL pulses within a time window of $1\mu s$. If the coincidence conditions were satisfied, a TTL pulse of variable length up to $20\mu s$ was output from the coincidence unit.

In order to record the amplitude of pulses registered by the light detection pod, the signal into channel 1 also passed through a second amplifier of variable gain. The output of this amplifier was a positive pulse which could be registered by a multi-channel analyser (MCA).

Both the TTL pulses output from the coincidence unit and the amplified pulses output from the light detection pod were input to a multi-channel analyser in the computer on the boat. The MCA was operated in peak height sensing mode and displayed the frequency of pulses detected as a function of the peak amplitudes of the pulses.

In order to record light pulses in coincidence with the muon telescope triggering, the signal from the light detection pod was connected to channel 1 as in figure 5.3 and the resulting amplified signal was connected to the analogue to digital conversion (ADC) port on the MCA. The two signals from the muon telescope pods were connected to channels 2 and 3 as in figure 5.3, a coincidence between channels 2 and 3 was specified, and the output coincidence pulse was connected to the gate input of the MCA. If the MCA was operated in gated mode a pulse on the ADC channel would be registered only when a pulse also occured on the gate channel.

Hence pulses from the light detection pod were recorded only when the gate input to the MCA was enabled by a coincidence pulse from the muon telescope. A schematic representation of typical pulses which would result in an event being recorded while operating in this gated mode are shown in figure 5.4.

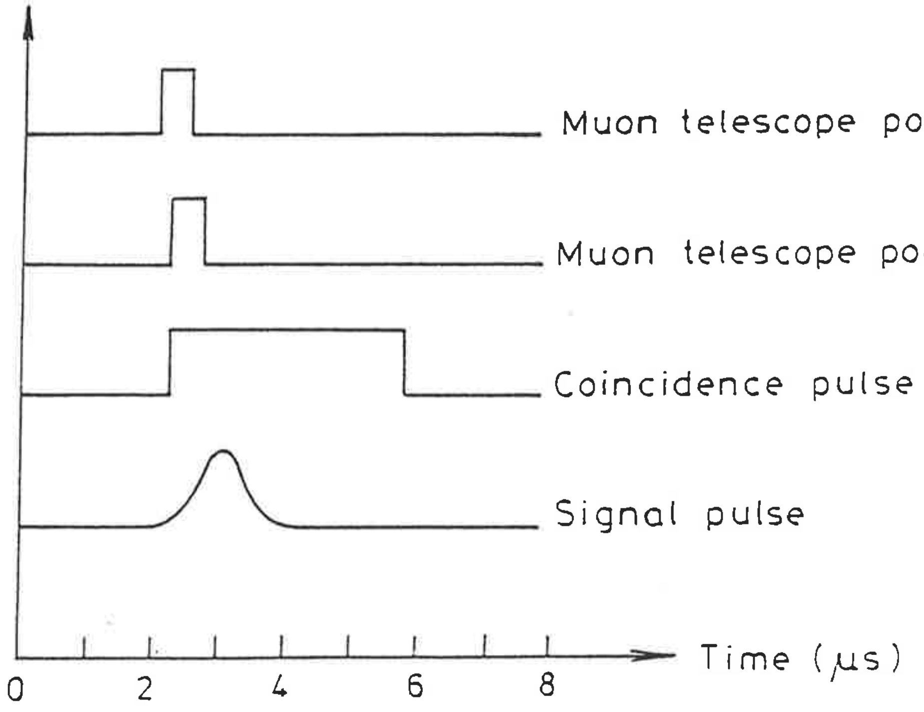

Figure 5.4: Typical pulses resulting in an event recorded in gated mode operation

To record background light spectra the MCA was operated in normal mode i.e. all pulses registered on the ADC input were recorded. The rate of muons triggering the muon telescope was determined by connecting the coincidence pulse from the muon telescope to the ADC input on the MCA and counting the number of events recorded in a specified time period.

5.4 Laboratory Measurements

The variable factors in the electronics such as photomultiplier tube voltages, amplifier gains and discriminator levels, were set by operating Harvey II in the laboratory. In this section the procedure for optimising the electronics is described, and the calibration of the light detection pod in terms of number of photons corresponding to a channel on the MCA display is presented.

5.4.1 Muon Telescope Settings

The muon telescope triggers if a muon passes through both scintillators. A false trigger will be recorded if pulses in both of the muon telescope photomultiplier tubes randomly occur within the coincidence time window of $1\mu s$. The rate of such false triggers can be reduced by raising the lower level discriminator hence decreasing the rate at which each photomultiplier tube registers pulses. Ideally the discriminator level for a specific tube voltage should be set as high as possible to reduce the rate of low amplitude noise pulses registered, but low enough to ensure the majority of genuine signal pulses are retained.

The discriminator levels for each telescope pod were set by recording the pulse height spectrum due to single muons passing through each scintillator. Muons arriving at zenith angles from 0° to 90° will produce pulses in the scintillators and the resulting pulse height spectra show no obvious peaks due to the wide range of possible track lengths through the scintillator. If a limited range of muon directions is accepted by requiring that two vertically separated scintillators register light pulses within a coincidence time window then the gated pulse height spectrum for each scintillator exhibits a peak corresponding to the light pulses from single muons passing through both scintillators. A typical spectrum recorded in this way is shown in figure 5.5. The optimum position for the lower level discriminator is just below the single particle peak as shown in figure 5.5.

The single muon peak for each telescope pod was recorded by separating the pods vertically by 93 cm and recording the gated spectrum for each scintillator in coincidence with the other scintillator as shown in figure 5.6. The voltages applied to each photomultiplier tube were first set to give a pulse detection rate in each photomultiplier tube of the order of 100 times the expected coincidence rate of

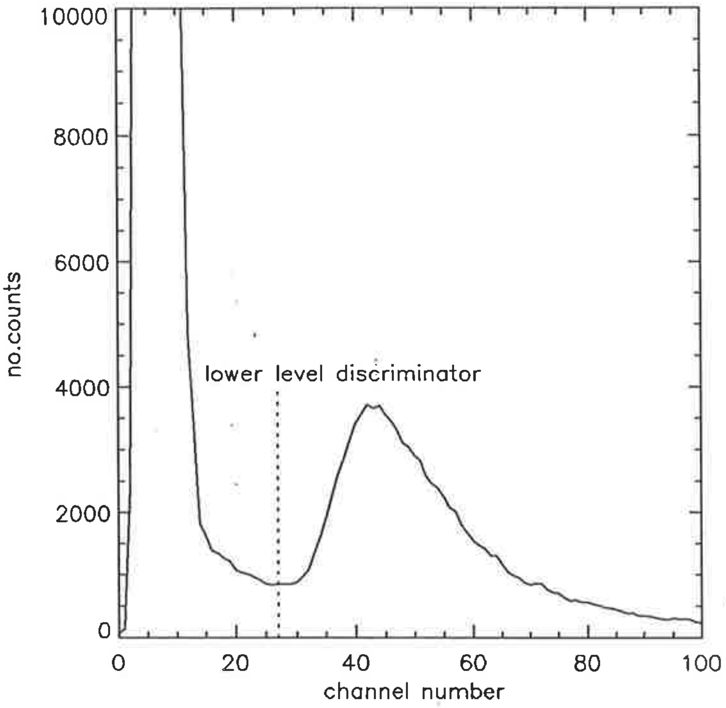

Figure 5.5: Typical single particle peak for muons passing through scintillator

2.3 ± 0.2Hz. The single muon peaks were then recorded and the lower level discriminators set as shown in figure 5.5.

5.4.2 Muon Rate Measurement

The efficiency of the muon telescope can be assessed by measuring the rate of muon coincidences as a function of separation between the two telescope pods and comparing these measured rates with the expected rates as determined using a Monte Carlo simulation. The Monte Carlo simulation generates muons with random directions which pass through the top scintillator and counts how many of these also pass through the lower scintillator. The arrival directions of the muons are selected from the zenith and azimuthal angle distributions for atmospheric muons as described in section 4.5.2.2. The predicted rates of coincidences are calculated from the fraction of simulated muons triggering the telescope and from the fluxes of muons at sea-level listed in Wolfendale (1973). There is an uncertainty in the simulated muon rates due to factors such as errors in measuring the areas and

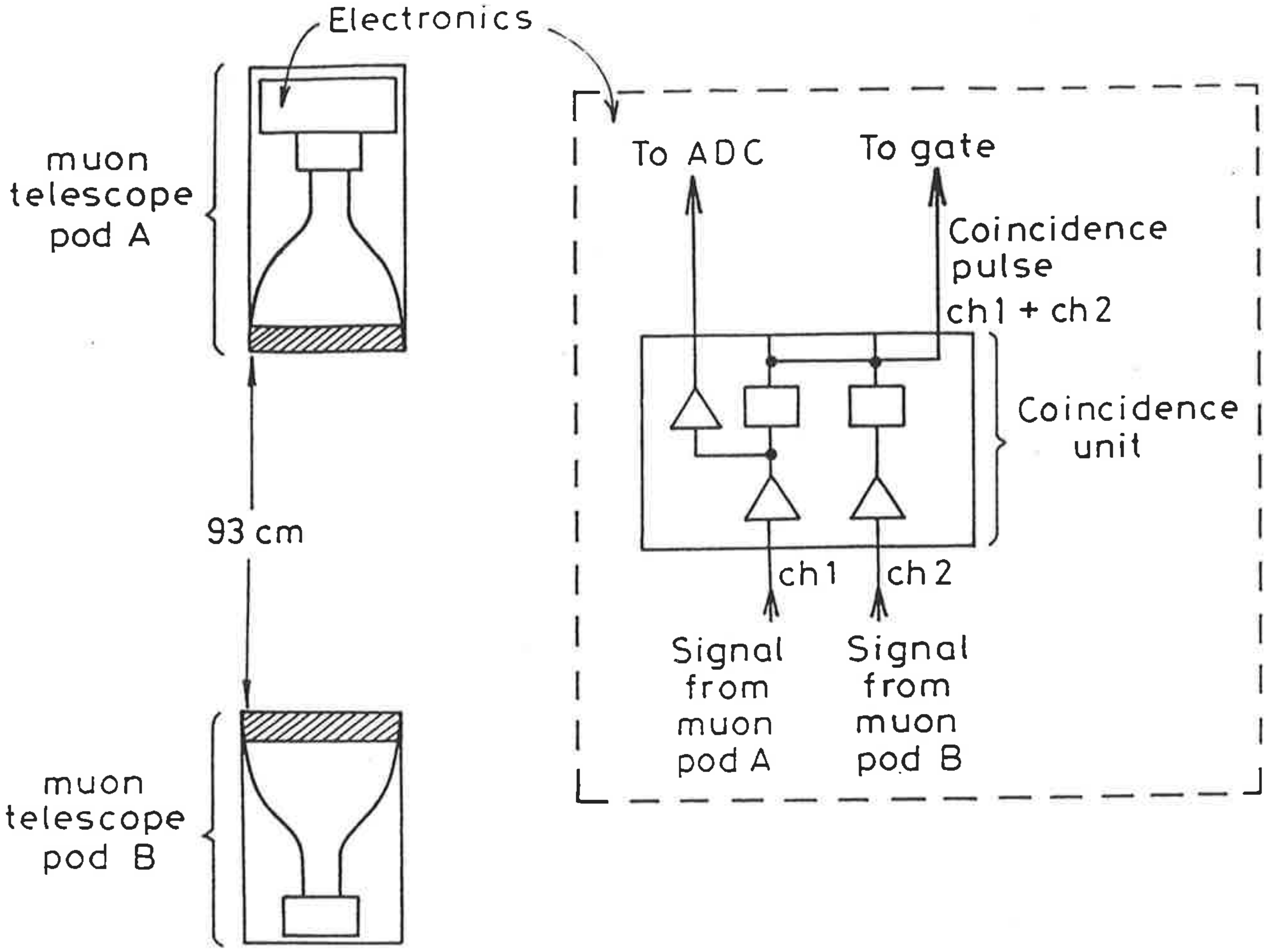

Figure 5.6: Schematic of experimental arrangement to record single muon peak

separations of the scintillators. However, the dominant source of error is the variation in the assumed flux of muons at ground level at different latitudes. This variation with latitude is due to the effect of the earth's magnetic field on the trajectories of cosmic ray particles. For each location and direction on the Earth's surface there is a minimum energy below which charged particles entering the earth's magnetic field will not pass through the atmosphere. This results in a pronounced variation in the intensity of lower energy cosmic ray primary particles with latitude, which leads to a variation in the intensity of cosmic ray-muons observed at ground level. This effect is described in detail in Allkofer (1975) and measured muon rates at various latitudes are presented in Wolfendale (1973). From these results it can be deduced that the integral muon intensity at 35° South is equal to $7.8 \pm 0.6 \mathrm{cm}^{-2}\mathrm{s}^{-1}\mathrm{sr}^{-1}$. The results of measured and simulated trigger rates due to muons as a function of separation between the scintillators are shown in figure 5.7.

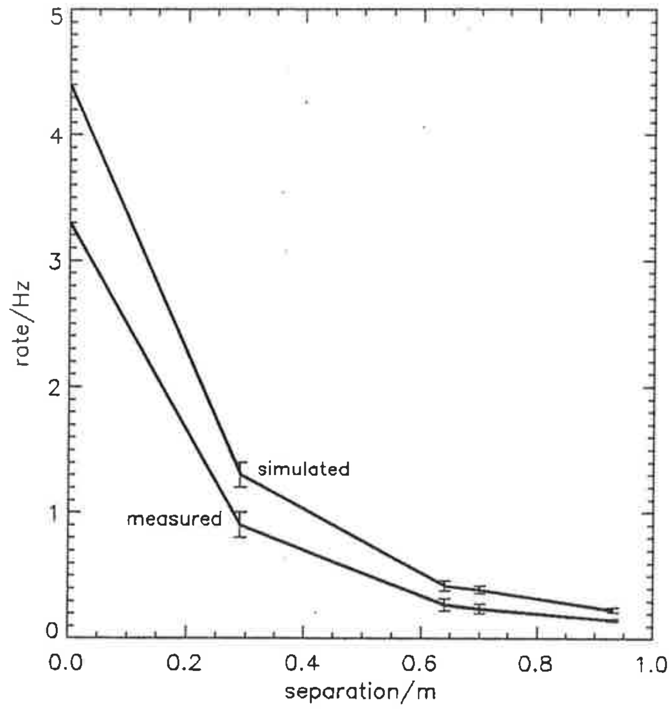

Figure 5.7: Coincidence rates in muon telescope for various scintillator separations

From these results it can be seen that the measured rate of muon triggers is consistently less than the predicted rate. This indicates that the efficiency of the muon telescope is less than 100%. This is probably due to the presence of muon-induced light pulses which have amplitudes less than the lower level discriminator settings in the coincidence unit and hence are not recorded.* One way of quantifying the efficiency of the muon telescope is to assume the scintillators have an effective area to muons which is less than their geometrical area. The value of this effective area can be determined by simulating the muon trigger rate for various values of scintillator radius and determining which effective radius results in predicted muon rates which best agree with the measured rates. The simulated rates for various effective radii are shown in figure 5.8 from which it can be seen that close agreement with the measured rates is achieved if an effective radius of 0.10 metres is assumed.

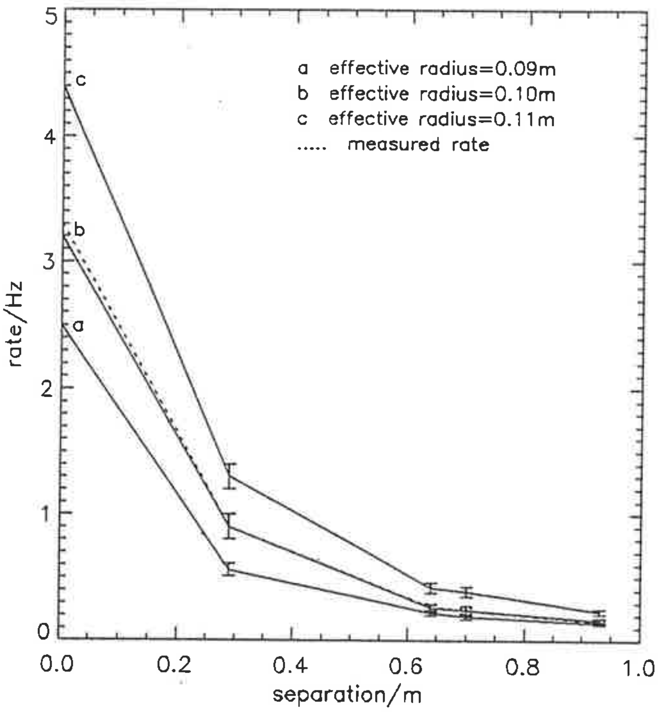

Figure 5.8: Trigger rates for various scintillator radii

5.4.3 Calibration of Cerenkov Light Pod

Light pulses registered by the light detection pod are recorded on the MCA as a spectrum of pulse frequency against pulse height. To determine the magnitude of the

---

*Another possible explanantion is a variation in the muon flux due to solar modulation. The muon flux can vary by a factor of 2 at 1GeV/amu over a 22 year period.

pulses registered, it is necessary to calibrate the MCA output in terms of photon numbers per MCA channel. This calibration is performed by illuminating the light detection pod with light pulses of known intensity and recording the resulting signals on the MCA. Hence the number of photons corresponding to the position of a peak recorded on the MCA can be determined. Two light sources were used, namely the Cerenkov pulses resulting from muons passing through a glass disk and through a perspex disk. By using Cerenkov light pulses to calibrate the system the intensity spectrum of the expected signal in the lake is replicated and hence the spectral quantum efficiency of the photomultiplier tube does not need to be known.

The calibration is performed by aligning the light detection pod between the two muon telescope pods as shown in figure 5.9. The glass or perspex disk is placed on top of, and optically coupled to, the upward pointing photomultiplier tube face. Each disk is surrounded by reflective foil on all sides which are not in contact with the photomultiplier tube so that all light produced in the disk is reflected into the photomultiplier tube face. Any particle which passes through both of the muon telescope pods will also pass through the light detection pod producing Cerenkov light in the glass/perspex disk. Hence recording the light pulses registered when both telescope pods are triggered results in a spectrum of pulse heights due to single muons passing through the glass/perspex disk and arriving within a range of directions defined by the angular acceptance of the muon telescope. The resulting spectrum exhibits a peak which corresponds to muons travelling downwards at zenith angle equal to 0°. The relationship between the number of photons in a pulse and the corresponding MCA channel in which the signal is registered can therefore be deduced from the position of the peak in the gated spectrum and the known number of Cerenkov photons produced by a muon passing through the dielectric disk at a zenith angle of 0°.

The pulse recorded when a muon passes through the light detection pod is made up of two components:- the Cerenkov light produced in the glass/perspex disk and the photoelectron pulse resulting from the interaction between the muon and the

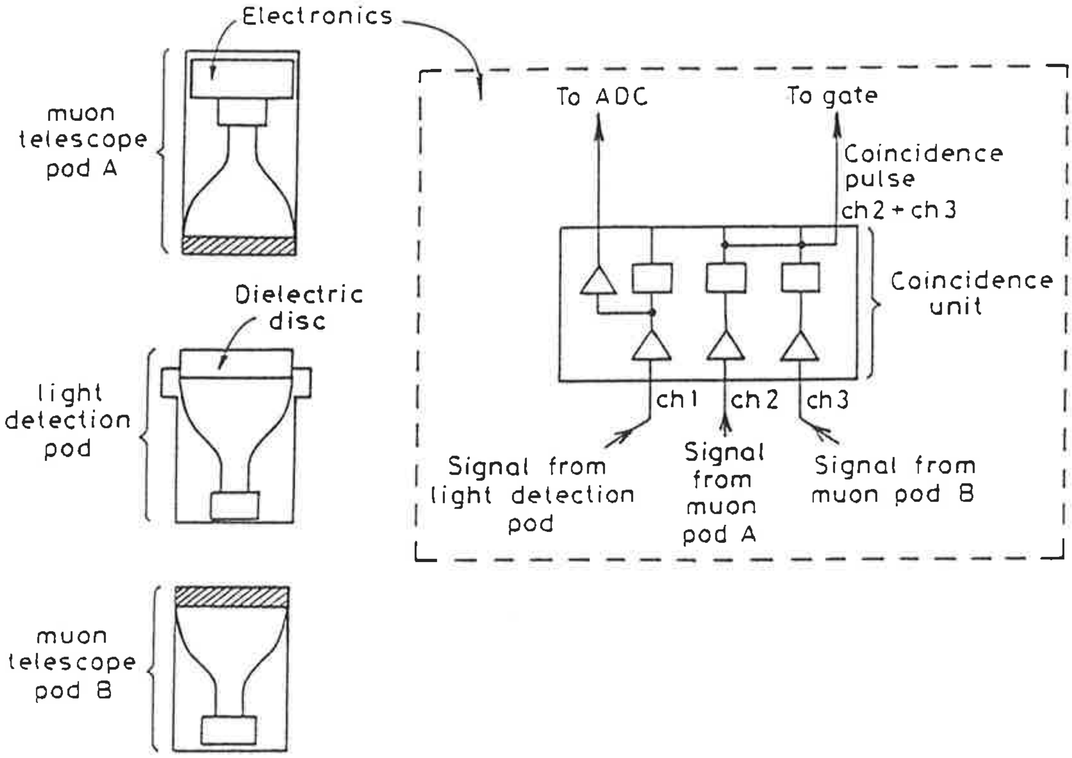

Figure 5.9: Experimental arrangement for calibration measurements

photocathode. During in-situ measurements, Harvey II records the Cerenkov light produced by muons which pass close to the light detection pod but which do not actually go through the photocathode. Hence when calibrating the light detection pod as described, the component of each pulse due solely to the muon passing through the photocathode must be subtracted from the total signal. This component can be determined using the experimental set-up shown in figure 5.9 with no glass/perspex disk on the photomultiplier tube face. The gated spectrum recorded is solely due to muons passing through the photocathode.

The results summarised in table 5.1 represent the positions of the peaks in the spectra of light pulses recorded in the light detection pod operating at 1580 volts, in coincidence with the muon telescope for the three cases of the glass disk, the perspex disk and no disk on the photomultiplier tube face. In all three spectra the peak corresponds to the signals induced by muons travelling downwards at zenith angle equal to 0°. The proportion of the signal due to Cerenkov light produced by vertical muons passing through a dielectric disk is given by the difference between the peak position in the spectra recorded with the dielectric disk in place and the peak position in the spectrum recorded with no disk in place. For example, with the glass disk on the photomultiplier tube face the resulting signal from vertical muons is made up of a pulse of magnitude equivalent to channel 39 on the MCA due to the interaction between the muon and photocathode, and a pulse of magnitude equivalent to channel 29 due to the muon-induced Cerenkov light in the glass disk. Hence, channel 29 on the MCA corresponds to a Cerenkov pulse the magnitude of which is equal to the number of Cerenkov photons produced by a muon travelling through the glass disk at a zenith angle of 0° which hit the photocathode.

	peak positions
glass	68 ± 5
perspex	110 ± 10
photocathode	39 ± 5

Table 5.1: Positions of peaks in gated spectra

The number of Cerenkov photons produced as a muon passes vertically downwards through the dielectric disks can be calculated from equation 2.3 in which the pathlength (l) is equal to the thickness of the disk. However, the actual number of photons reaching the photocathode will depend on the transmission of Cerenkov radiation through the dielectric. The number of photons registered will be given by the convolution of the spectrum of Cerenkov photons produced and the spectral transmission of the dielectric material. The resulting predicted number of Cerenkov photons reaching the photomultiplier tube face in the wavelength range of 300 to 620nm are 826 for the glass disk and 1873 for the perspex disk giving calibrations of 28.5 ± 3.9 photons per channel and 26.4 ± 4.1 photons per channel respectively. The actual calibration value used in the analysis of Blue Lake measurements is the average of these calibrations i.e. 27.5 ± 5.7 photons per channel.

5.4.3.1 Noise Spectrum

The dark noise spectrum of the photomultiplier tube in the light detection pod was recorded by placing the light detection pod in a dark box. The resulting ungated spectrum taken over a period of 10 seconds of live time for a tube voltage of 1580 volts is shown in figure 5.10.

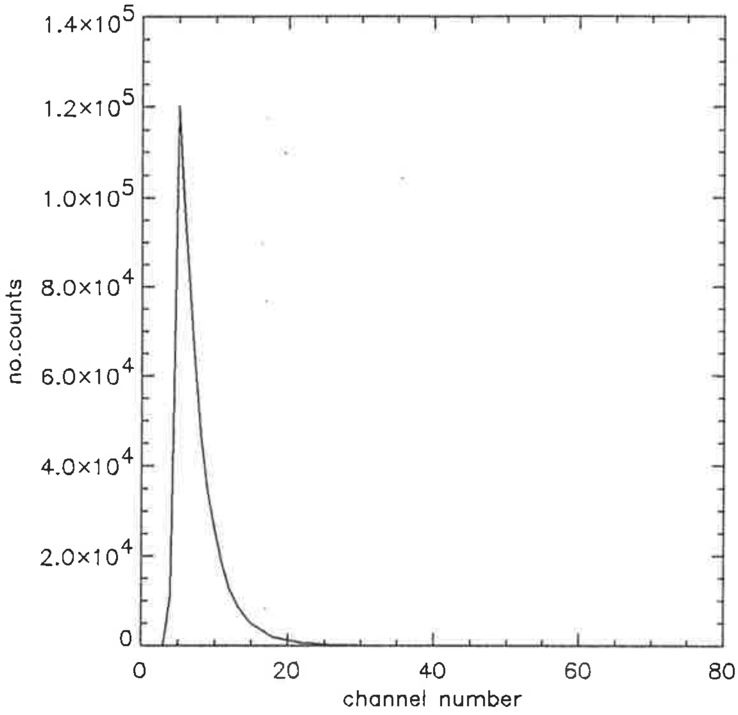

Figure 5.10: Dark noise spectrum of photomultiplier tube in light detection pod at 1580 volts

5.5 Blue Lake Measurements

A series of four field tests was performed at the Blue Lake using Harvey II. The results presented in the following sections correspond to measurements taken during field tests in April and October 1994. The results from the April field test represent the final results using the initial design of Harvey II as described in the previous sections. Following this field test the device was modified to reduce the effects of background noise. The data collected in October are the final measurements to date using this modified version of Harvey II.

5.5.1 Results from April 1994

During April 1994 Harvey II was operated over a period of two nights during the new moon. On the first night measurements were taken of the rate of muons triggering the muon telescope and also of the background light levels as a function of depth in the lake. On the second night pulse height spectra of light pulses registered by the light detection pod in coincidence with the muon telescope were collected at two depths. During these measurements the voltage applied to the photomultiplier tube in the light detection pod was 1580 volts and the duration of the coincidence pulse used to gate the MCA was set at $20\mu s$.

5.5.1.1 Muon Rate Measurement

To measure the rate of muons triggering the muon telescope, Harvey II was suspended from a boat as shown in figure 5.2 and positioned at various depths from the surface to 60 metres. The separation between the telescope pods was set such that the distance between the two scintillators was 130 cm. At each depth the rate at which the muon telescope was triggered was determined by recording the number of coincidences between the two muon telescope pods in a given time interval. The resulting measured muon rate as a function of depth is shown in figure 5.11 along with the predicted rate as determined using the Monte Carlo simulation described in section 5.4.2 with the inclusion of the effect of absorption of muons in water and assuming that the scintillators have an effective radius to muons of 0.1 metres.

From these results it can be seen that the measured and simulated rate of muons triggering the telescope agree to within errors. This result verifies the accuracy of the Monte Carlo simulations used to determine muon rates.

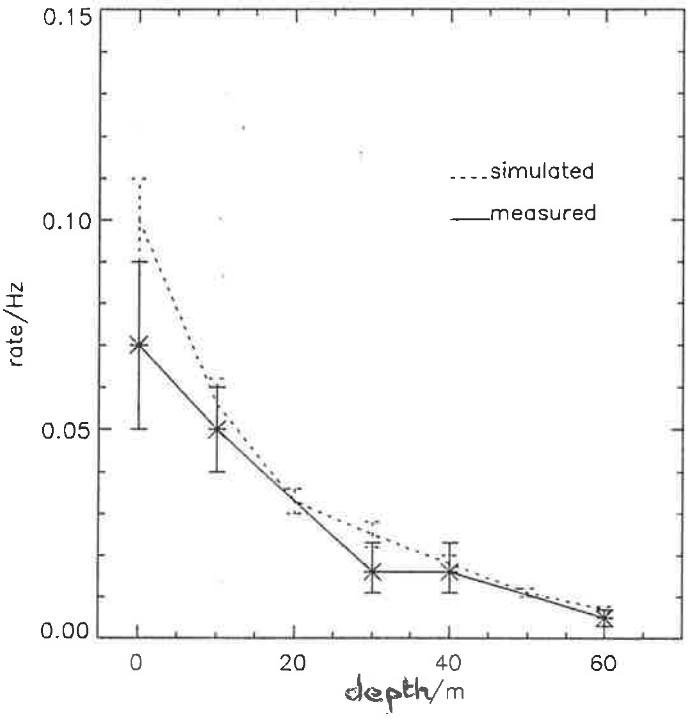

Figure 5.11: Rate of muons triggering the muon telescope as a function of depth in the Blue Lake

5.5.1.2 Background Light Measurements

At each depth considered the background light level was recorded by operating the light detection pod independently from the muon telescope. Two measurements were taken at each depth; one with the light detection pod pointing upwards as shown in figure 5.1 and the other with the light detection pod looking downwards as shown in figure 5.12. The pulse height spectra collected at each depth over a period of 10 seconds of live time for the light detection pod looking upwards and downwards are shown in figure 5.13. From these results it appears that the amount of background light registered increases with depth from 0 to 50 metres for the case of the light detection pod pointing upwards, and from 0 to 30 metres with the light detection pod pointing downwards. Beyond these depths the background light level decreases as expected. This apparently anomalous increase in light with depth occurs as a result of the decrease in gain of the photomultiplier tube when exposed to high DC light levels. This effect is known as saturation. The gain of a photomultiplier tube is

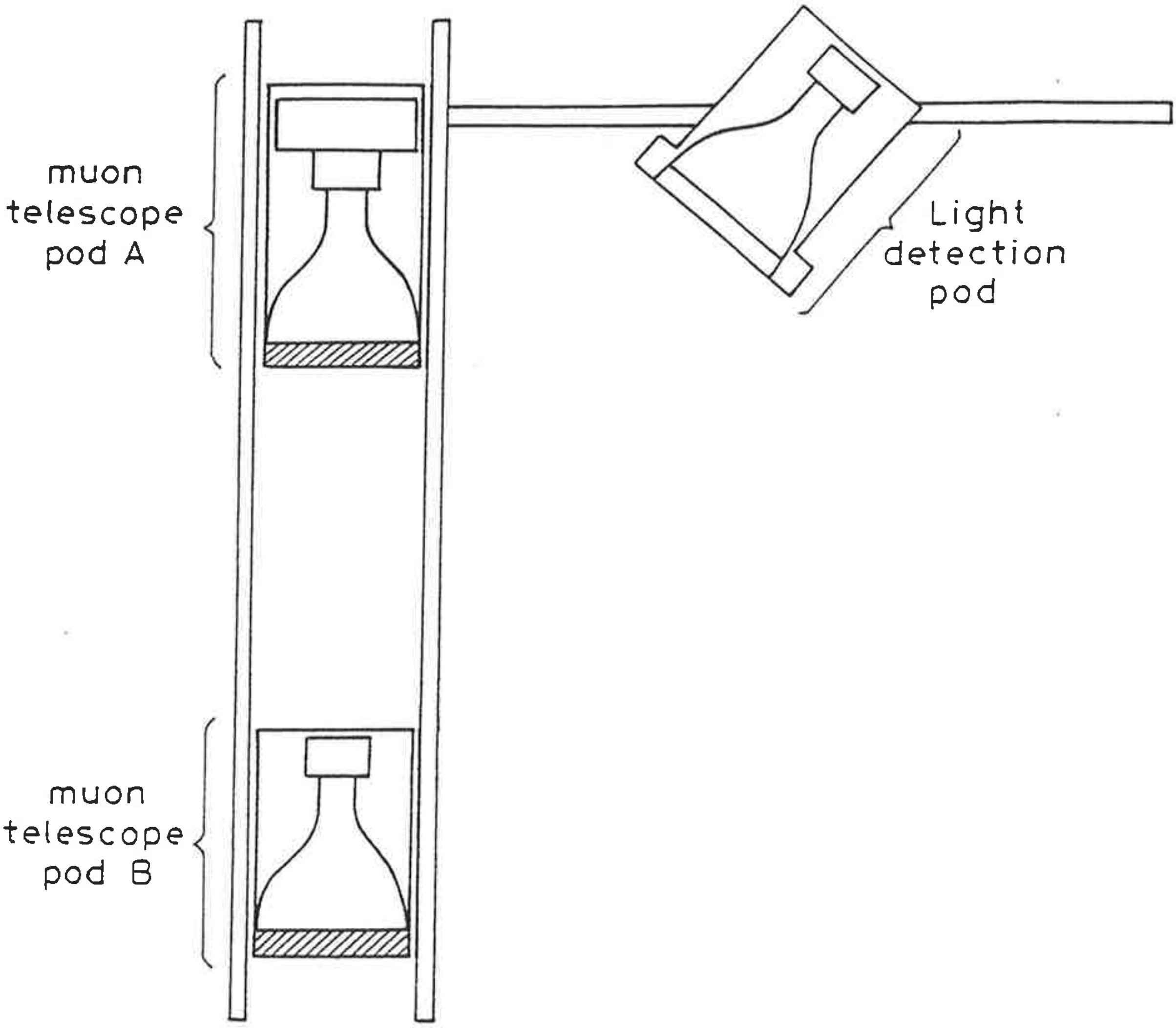

Figure 5.12: Arrangement of Harvey II for downward light measurements

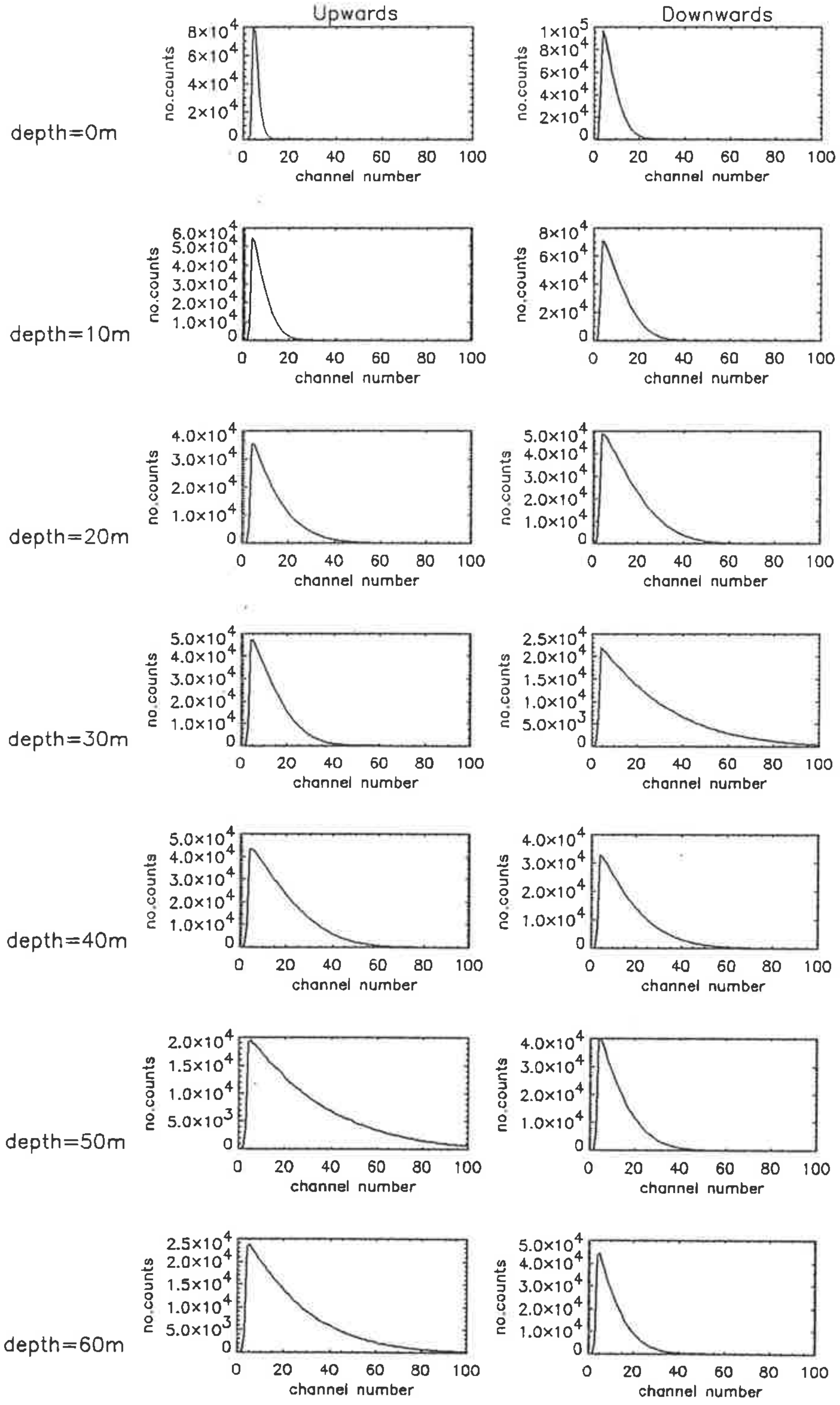

Figure 5.13: Noise spectra at various depths in the Blue Lake each recorded for 10 seconds live time

determined largely by the voltage drop between the anode and the first dynode stage. If the anode current is high then a correspondingly high current is induced in the first dynode stage resulting in an increased voltage across the section of the dynode chain between the first dynode and the cathode. As the total voltage across the dynode chain is constant this increase in voltage results in a decrease in the voltage between the anode and first dynode, and hence a decrease in the gain of the photomultiplier tube. This effect is described in detail in Engstrom (1980).

Harvey II therefore has to be operated at depths greater than about 40 metres when the light detection pod is pointing upwards, to ensure that the photomultiplier tube is not operating in saturation. Even at these depths the rate at which noise pulses are recorded is high. At 60 metres this rate is approximately 3 times greater than the rate with no DC light present as determined from the dark noise spectrum shown in figure 5.10. The effect of this high background light level on the detection of muons is discussed in the following sections.

5.5.1.3 Measurement of Cerenkov Light from Downward Muons

To measure the Cerenkov light from downward muons the light detection pod was oriented pointing upwards and operated in coincidence with the muon telescope. Hence only light pulses occurring when a muon passes through the telescope were registered. The relative positions of the telescope pods and the light detection pod used in this measurement are shown in figure 5.14. Spectra of light pulses recorded in coincidence with triggers from the muon telescope were collected at depths of 40 metres and 60 metres. A gated spectrum was also recorded at 60 metres with the light detection pod pointing downwards. The resulting spectra are shown in figure 5.15. Also shown in this figure are the ungated pulse height spectra (i.e. the total noise registered by the light detection pod) recorded at both depths immediately before each gated spectrum was collected.

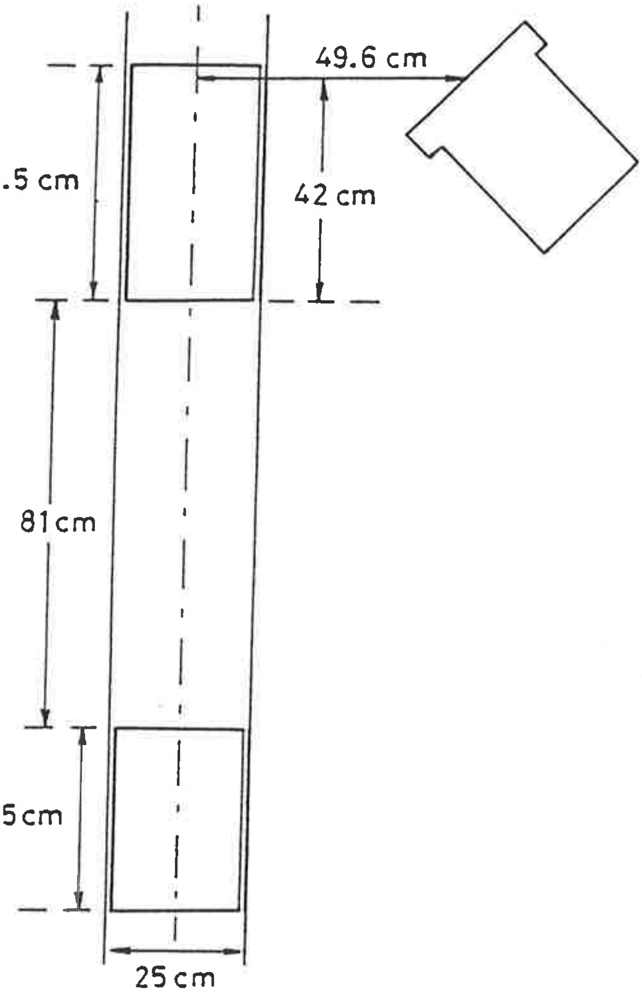

Figure 5.14: Arrangement of Harvey II for measurement of gated spectra

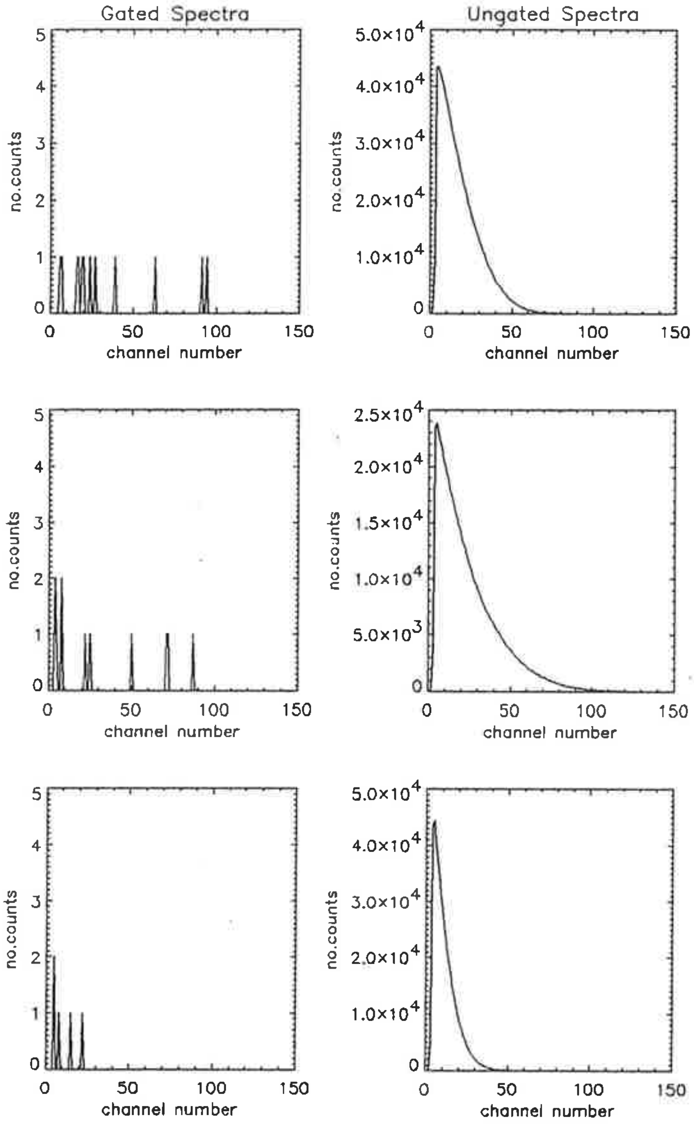

a. 40m upwards

b. 60m upwards

b. 60m downwards

Figure 5.15: Spectra recorded at depths of 40 and 60 metres in the Blue Lake during April 1994

The predicted gated spectra can be determined by simulating downward travelling muons, selecting those which trigger the telescope and calculating the number of Cerenkov photons produced which will hit the face of the photomultiplier tube in the light detection pod. The number of photons reaching the photomultiplier tube face depends on the attenuation length of the water. Simulated spectra for a range of values of water attenuation length are shown in figure 5.16. These simulated spectra do not include any effects due to the presence of DC light. The measured and simulated gated spectra shown in figures 5.15 and 5.16 are significantly different.

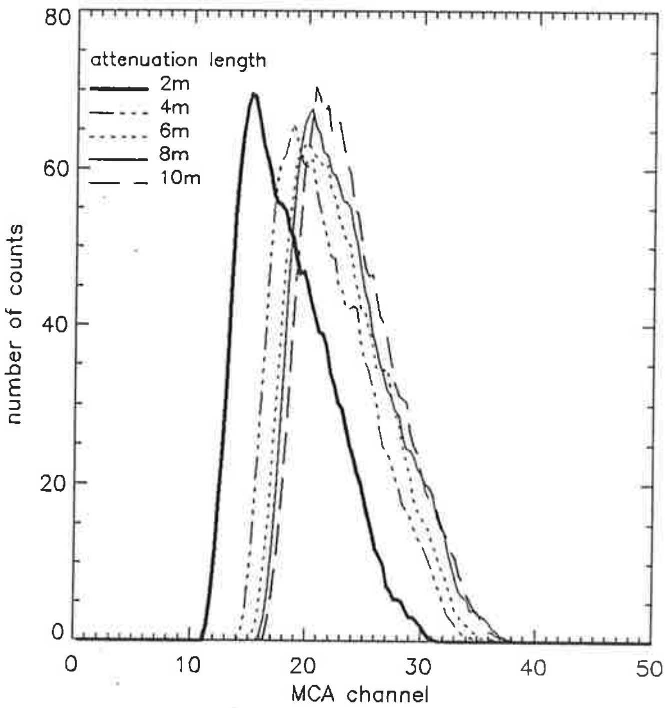

Figure 5.16: Simulated gated spectra for various water attenuation lengths

The measured gated spectra exhibit no significant peaks and are similar in shape to the ungated noise spectra recorded. This suggests that a significant number of noise pulses are being registered instead of the Cerenkov light pulses from muons.

For a pulse to be recorded on the MCA there must be a coincidence pulse from the muon telescope which enables the MCA. The MCA will then register the first peak detected during this coincidence pulse. Fluctuations in the DC noise level can affect the gated spectra recorded in two ways. Firstly, if a peak in the DC light level occurs within the coincidence time window and before the Cerenkov pulse then only the amplitude of the noise fluctuation will be recorded. If this does not occur then the amplitude of the Cerenkov pulse is recorded. However, this amplitude will be modulated according to the variations in the DC light level. The response of Harvey II to fluctuations in the DC light level has been measured and is described in detail in section 5.5.3.2. For the purpose of this analysis we use the results from this section that for a delay between the start of the gating pulse and the peak of the Cerenkov pulse equal to $6\mu s$ (which corresponds to the electronics used in the April measurements) two thirds of the pulses recorded in the gated spectrum are noise fluctuations and the remaining third are Cerenkov pulses, the amplitudes of which are fluctuated according to the DC light level fluctuations. It has also been shown in section 5.5.3.2 that the magnitude of the fluctuations in the Cerenkov signal amplitudes are equal to the magnitude of the fluctuations in the background light level. Hence gated spectra, including the effects of background light, can be simulated by randomly selecting two thirds of the events from the noise distribution and selecting the remaining one third of the events from the predicted spectrum due to Cerenkov pulses and fluctuating each Cerenkov pulse by the amplitude of a randomly selected noise pulse. The simulated gated spectra corresponding to the three gated spectra recorded in the Blue Lake in April are shown in figure 5.17. Also shown are the background light spectra measured at each location considered.

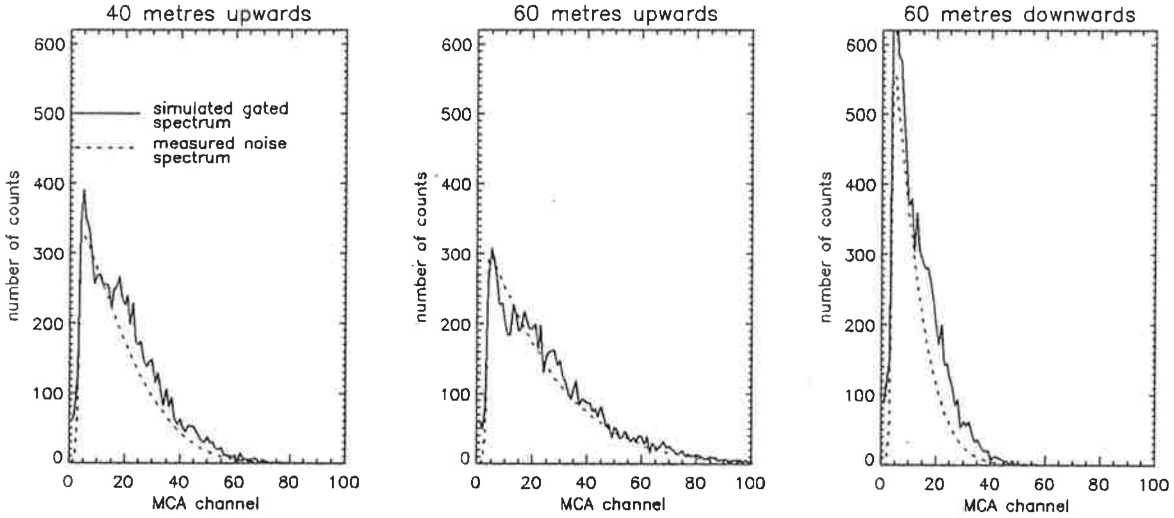

Figure 5.17: Simulated gated spectra including effect of background light

From these results it can be seen that the expected gated spectra are very similar to a random sample of pulses from the corresponding background noise spectra. For the case of 60 metres looking downwards, the predicted gated spectrum and the background light spectrum do differ noticeably at pulse amplitudes greater than about channel 25 on the MCA. Hence there is an identifiable contribution from

Cerenkov light pulses in this gated spectrum. This is apparent only in this spectrum, due to the relatively lower background light level recorded looking downwards at 60 metres. In the other two spectra any Cerenkov signals are indiscernible from noise pulses.

The effect of DC light on the detection of Cerenkov signals and the possibility of discriminating between noise pulses and Cerenkov signals was further investigated in the laboratory as described in the following section.

5.5.2 Laboratory Measurements of Effects of Background Light

The effect of background light on the detection of a signal was simulated in the laboratory using the components of Harvey II arranged as shown in figure 5.9 with the addition of a DC light source located in the dark box. The light source used was a green LED, the light output from which is varied by adjusting the DC current applied to the LED. By altering the current applied to the LED and matching the resulting pulse height spectrum with the background light spectra recorded in the Blue Lake, the DC light conditions in the lake can be reproduced. The Cerenkov signal in the lake was approximately reproduced by Cerenkov pulses produced by muons passing through a glass disk optically coupled to the photomultiplier tube face.

The aim of these tests was to determine if it is possible to derive any information about muon-induced Cerenkov signals from the gated spectra recorded in the Blue Lake. The light conditions in the lake were reproduced by adjusting the brightness of the LED such that the noise spectrum was identical to the background light spectrum recorded with the light detection pod pointing upwards at 60 metres in the lake. Two gated spectra of light pulses in coincidence with muon telescope triggers were then recorded. For the first spectrum the perspex disk was placed on the photomultiplier tube face and for the second spectrum the perspex disk was removed. If there is a significant contribution to the gated spectra from the Cerenkov light produced by muons then the spectrum with the perspex disk in place will be noticeably different from the equivalent spectrum with no perspex present. The two spectra recorded are shown in figure 5.18.

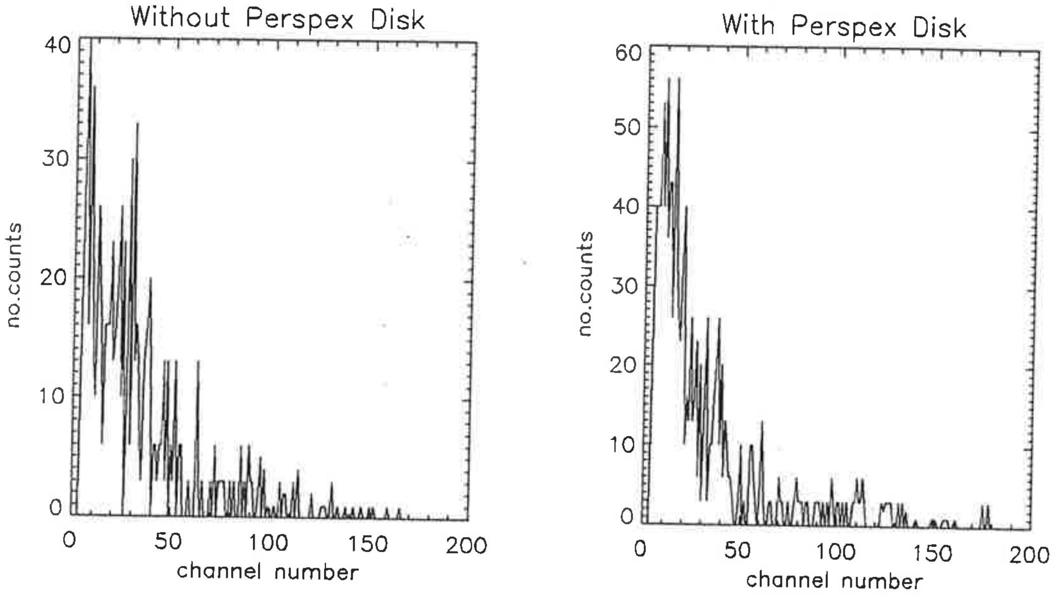

Figure 5.18: Gated spectra recorded using DC light levels equal to DC light level in the Blue Lake

From these results it can be seen that there is no discernible difference between the gated spectra with and without the perspex disk on the photomultiplier tube face. In particular there is no evidence of the presence of a single particle peak in the spectrum recorded with the perspex in place. Hence any signals due to muon induced Cerenkov pulses are not sufficiently different in amplitude to the noise pulses to be identifiable in the gated spectra recorded. This result shows that in the gated spectra collected in the Blue Lake looking upwards at 60 metres, any genuine Cerenkov signals which are present are indistinguishable from the random noise pulses registered.

In the laboratory tests the signals used are the Cerenkov pulses due to muons passing through the perspex disk. These pulses are of the order of three times larger than the expected Cerenkov signals in the Blue Lake. Hence it is expected that the effect of noise in the Blue Lake results will be more extreme than the effect measured in the laboratory tests. Hence, as the Cerenkov signal in the laboratory tests cannot be observed above the background noise, then it would not be expected to be possible to observe the predicted Cerenkov signals in the Blue Lake using Harvey II operating in the measured DC light conditions.

5.5.2.1 Conclusions from April 1994 Field Tests

The results of the measurements taken in the Blue Lake during this field trip in conjunction with the subsequent laboratory tests showed that the high DC light level in the Blue Lake prohibits the detection of muon induced Cerenkov pulses using Harvey II. Given this conclusion, there are two approaches one could take to reduce the effect of background light in the lake measurements. The first is to reduce the amount of background light by enclosing the test device in a light-tight container. The second is to reduce the coincidence time window during which a pulse can be registered by the MCA. This would reduce the rate of noise fluctuations occurring before the genuine Cerenkov signal and hence the effect of background light would be predominantly to modulate the amplitude of registered Cerenkov pulses. Assuming these fluctuations can be simulated from the measured background light spectrum then it would be possible to derive information about the Cerenkov pulses from the measured gated spectra. The second approach, of reducing the coincidence time window, was used because of the mechanical difficulties in eliminating background light at 60 metres in the Blue Lake.

The coincidence time window was reduced by decreasing the rise time of the Cerenkov pulses which are input to the ADC port of the MCA and also by reducing the delay between the start of these Cerenkov pulses and the start of the coincidence pulse from the telescope. By altering these factors the coincidence time window was reduced to about $1\mu s$. The duration of the coincidence pulse used to gate the MCA was also reduced from $20\mu s$ to $6\mu s$ to eliminate any possibility of more than one pulse being registered during each gating pulse. As the dead time of the MCA is of the order of $15\mu s$ then it is highly unlikely that two pulses would occur within the gating pulse separated in time by at least $15\mu s$ thus resulting in both pulses being registered. However, setting the length of the gate pulse to much less than the MCA dead time ensures that this never occurs.

There are several uncertainties in the analysis of the results from this field trip. On returning from the Blue Lake the trigger rate of the muon telescope and the calibration of the light detection pod were re-measured. It was found that the calibration of the photomultiplier tube in the light detection pod differed from the equivalent calibration performed before the field trip. The single muon peak in the glass window was now occurring at channel 55 as opposed to the previous result of channel 68. This shift in system gain was identified as being due to a drop of 60 volts in the voltage output from the high voltage supply driving this photomultiplier tube.

The calibration performed after the field trip gives a result of 33 ± 1 photons/channel. Hence the absolute photon numbers corresponding to the spectra measured in the lake are uncertain, lying somewhere between the two values given by the calibrations before and after the field trip. The effect of this uncertainty in the gain of the system does not significantly affect the conclusions reached about the effect of the high background light level on the Cerenkov signals registered. To illustrate this, the expected signals in the lake, including the effect of background light, were simulated for the two calibration values of 27.5 and 33 photons per MCA channel. In this simulation the spectrum due to muon-induced Cerenkov light was first calculated in terms of photon numbers. This spectrum was then translated to channels on the MCA according to the calibration value assumed. Hence the simulated Cerenkov pulse spectrum varies according to the calibration value and hence the system gain. This Cerenkov spectrum was then combined with the background light spectrum as described in section 5.5.1.3. The background light spectrum used was recorded directly on the MCA during field tests in the lake and is therefore unaffected by any subsequent changes in system gain. The attenuation length of lake water was assumed to be 4 metres and the background noise spectrum used was that recorded looking upwards at 60 metres. The resulting spectrum for each calibration value is shown in figure 5.19 From this figure it can be seen that the two simulated spectra are virtually identical and that any variation in the predicted amplitudes of Cerenkov pulses, resulting from the uncertainty in the calibration of the light detection pod, is insignificant compared to the effect of background noise pulses.

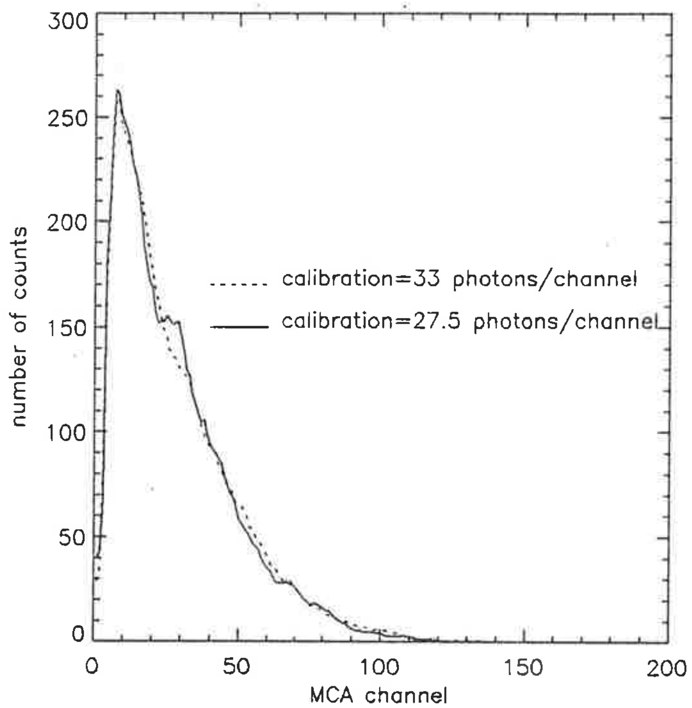

Figure 5.19: Simulated gated spectra for calibrations of 27.5 and 33 photons per MCA channel

The drop in the gain of the system resulted in several additional changes to the test equipment to try to eliminate and/or identify such variations in gain which may occur during future measurements. One possible cause of a decrease in gain of the photomultiplier tube in the light detection pod is that exposure to high DC light levels at a high tube voltage may result in damage to the photocathode. Hence the voltage applied to this photomultiplier tube was dropped from 1500 volts to 1360 volts and, in order to maintain the signal amplitude, the amplification of the signal out of this photomultiplier tube was increased by a factor of 5. Also, a temperature stabilised LED was used in future tests as a means of determining whether the gain had changed. The portable nature of this device (designed by B.Dawson and modified by G.Hill) enabled checks on the gain of the system to be performed at the Blue Lake immediately before submerging and after de-submerging the device.

5.5.2.2 Upgraded Version of Harvey II

The conclusions reached as a result of the analysis of measurements taken during the April field trip led to several changes being made to the electronics of the test equipment with the aim of reducing the effect of background light. To summarise these changes:- the coincidence time window during which pulses are recorded on the MCA was reduced from $6\mu s$ to about $1\mu s$, the voltage applied to the photomultiplier tube in the light detection pod was decreased from 1500 to 1360 volts, the amplification of the signal from this photomultiplier tube was increased by a factor of 5, and the duration of the gate pulse into the MCA was decreased from $20\mu s$ to $6\mu s$.

This upgraded version of Harvey II was calibrated according to the calibration technique described in section 5.4.3. The results of this calibration are shown in figure 5.20. The device was then used to take measurements in the Blue Lake on two field trips, the first in September 1994 and the second in October 1994. During both these tests a limited amount of useful data was collected due to problems arising as a result of water leaking into the equipment. The results of the final test in October are presented in the following section.

5.5.3 Results from Field Trip in October 1994

Harvey II was tested over a period of 2 nights in the Blue Lake. On both nights the device was located at 60 metres and a series of gated spectra alternated with ungated noise spectra were collected. The resulting spectrum of total events recorded in gated

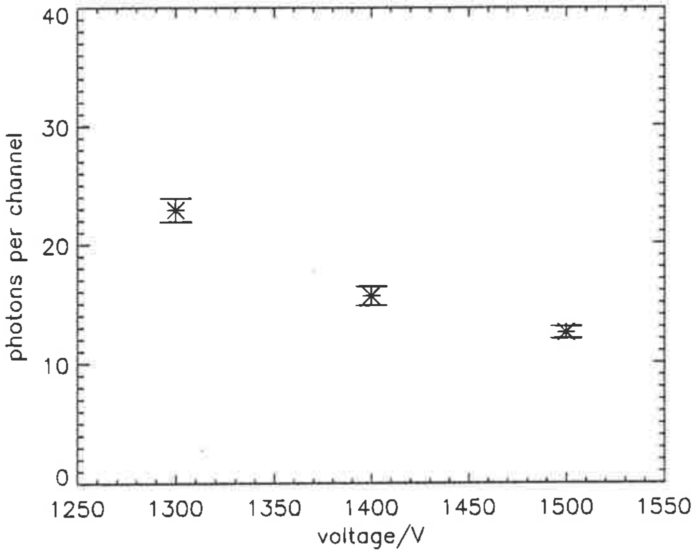

Figure 5.20: Calibration of light detection pod in Harvey II

mode and the corresponding ungated noise spectrum at 60 metres are shown in figure 5.21.

Following this field trip the device was recalibrated in the laboratory and the results obtained agreed closely with the initial calibration performed before the field trip. Hence there was no significant change in gain of the system during this field test and the calibration value of 15.6 photons/channel at 1360 volts can be applied to the results.

5.5.3.1 Analysis of Results

The predicted gated spectrum is determined using the algorithm outlined in section 5.5.1.3 to simulate the Cerenkov light pulses registered, and then including the effects of the presence of DC light. As the electronics are AC coupled and hence register light pulses and not DC levels, then only the fluctuations in the DC light level will be recorded.

These light fluctuations can affect the recorded spectra in two ways. Firstly if a noise pulse occurs well before a Cerenkov pulse then the amplitude of the noise pulse

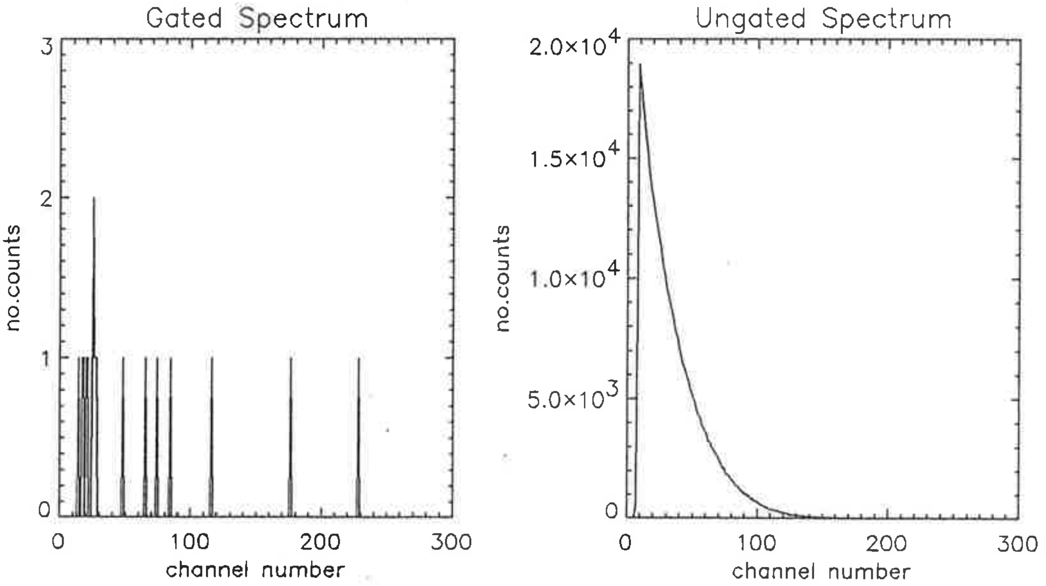

Figure 5.21: Results from October 1994 field trip

will be recorded. For the current system we can assume that for this to occur the noise pulse must occur within $1\mu s$ of the start of the gate pulse.

A second way in which noise can affect the signals registered occurs if the noise pulse and the signal pulse overlap significantly. In this case the amplitude recorded will correspond to some combination of the noise pulse and the Cerenkov pulse. If the coincidence time window is large, as in the original settings of the device, then the majority of noise pulses registered will be complete pulses which occur before the Cerenkov pulse and hence the gated spectrum will be very similar to the ungated noise spectrum as was observed. However this cannot be assumed for the upgraded device which has a reduced coincidence time window of $1\mu s$.

5.5.3.2 Investigation of Effects of Noise Pulses in Upgraded Version of Harvey II

To accurately predict the gated spectrum observed, the effect of DC light on a signal registered by the upgraded version of Harvey II system must be quantified. To do this the experimental configuration shown in figure 5.22 was used.

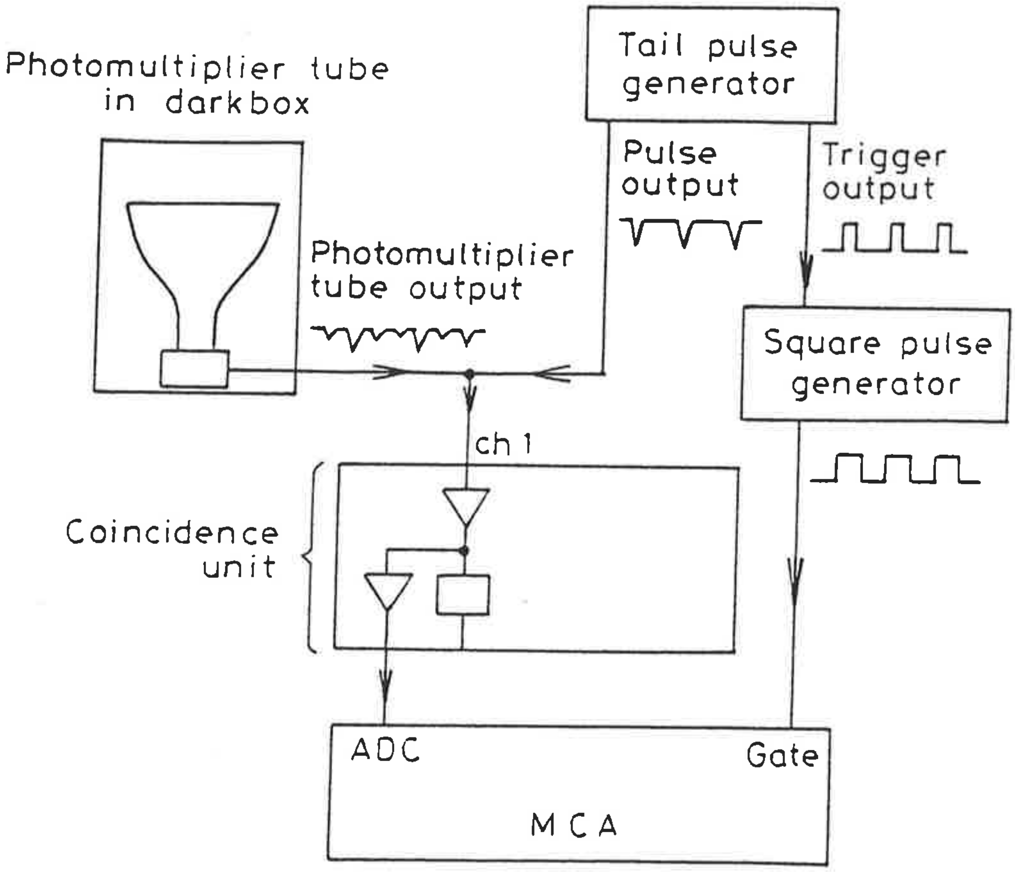

Figure 5.22: Experimental arrangement for measuring noise response of Harvey II. Pulses from the tail pulse generator are combined with noise pulses from the photomultiplier tube and pass through the coincidence unit to the ADC input on the MCA. The MCA is gated by trigger pulses from the tail pulse generator

A pulse from a tail pulse generator, similar in rise time and magnitude to light pulses out of the photomultiplier tube in the light detection pod, is connected to channel 1 on the coincidence unit. This signal passes through the amplifier and is connected to the ADC channel on the MCA. The trigger pulse which is output from the tail pulse generator is too short to be registered by the MCA and is therefore connected to a second pulse generator which outputs a TTL pulse with an increased width of about $6\mu s$. This is equivalent to the gate pulse used in Harvey II. This TTL pulse is then connected to the gate input of the MCA. Hence a gated spectrum recorded using this configuration represents the periodic tail pulse from the pulse generator in coincidence with itself. This spectrum is a delta function on the MCA of width equal to 2 channels. The effect of noise on this delta function can be determined by combining the periodic pulses with a DC noise signal. The DC noise source used is the dark noise from the photomultiplier tube in the light detection pod operating at 1360 volts but with the gain of the variable amplifier in the discriminator unit set to a minimum value of 1. In order to reproduce as much as possible the conditions in the lake the repetition rate of the square pulse from the signal generator was set as low as possible i.e. about 10 Hz. The delta function recorded with the addition of background noise from the photomultiplier tube is shown in figure 5.23. Also shown in this figure is the spectrum corresponding to a random selection of noise pulses for a time period equal to that of the delta function spectrum.

From this figure it can be seen that the effect of noise on the tail pulse is to modulate the amplitude of the tail pulse resulting in a spread in width of the delta function recorded. By comparing the two spectra in figure 5.23 it can be seen that the delta function spectrum is symmetrical and that each half of this spectrum is almost identical in shape to a random sample of pulses from the noise distribution. The shape of this spectrum can be understood by considering the response of the photomultiplier tube to DC light levels.

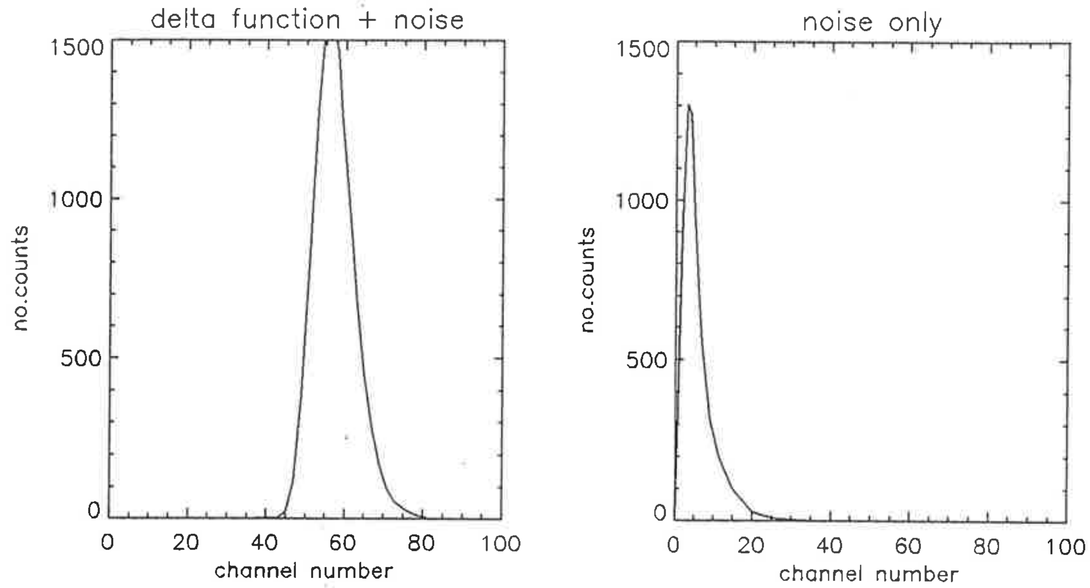

Figure 5.23: Delta function response of Harvey II

Noise pulses which are registered by the photomultiplier tube correspond to fluctuations in the DC level of background light. These fluctuations can be either positive or negative, with a positive fluctuation corresponding to an increase in light level and hence an increase in the signal out of the photomultiplier tube. As the signals out of the photomultiplier tube are always negative voltages, then an increase in the light level will produce an increased negative voltage. The photomultiplier tube is AC coupled such that the DC light level corresponds to a signal of 0 volts. Hence the output from the photomultiplier tube will be a series of positive and negative voltage pulses centred around 0 volts. These signals are inverted and amplified, and only the resulting positive voltage pulses are registered by the MCA. Hence the background noise spectrum is asymmetric due to the fact that only positive fluctuations in the DC light level, resulting in negative voltage pulses out of the photomultiplier tube, are recorded on the MCA.

When a gated spectrum of signal pulses plus background noise is recorded, each pulse registered will be a combination of the signal pulse and any noise fluctuations occurring within the coincidence time window. The fact that the shape of the delta function and the noise spectrum shown in figure 5.23 are almost identical indicates that the the amplitude of the signal pulses are modulated by an amount equal to the magnitude of coincident background noise fluctuations. In other words, if a signal pulse and a noise fluctuation occur within the coincidence window then the resulting pulse will have a magnitude equal to the sum of the magnitudes of the individual pulses. In this case, positive fluctuations in the noise level will increase the amplitude of the signal pulse and negative fluctuations will decrease it. Hence the resulting spectrum is symmetrical about a signal level equivalent to the amplitude of the unfluctuated signal pulse and is identical in shape to the noise spectrum.

To determine if this result is true for all amplitudes of signal pulses, the amplitude of the pulse from the tail pulse generator was varied and the resulting spectrum of signal plus noise pulses was recorded for each amplitude considered. In all the resulting spectra, the spread in the delta function was identical to the corresponding noise spectrum. Hence, the effect of DC noise on signal pulses, for a coincidence time window of $1\mu s$, can be modelled by modulating each signal pulse amplitude by an amount equal to the magnitude of a noise pulse randomly selected from the known noise distribution. The expected gated spectrum at 60 metres in the lake, including the effect of background noise, can therefore be determined by first simulating the gated spectrum due solely to Cerenkov pulses with no background noise present, and then fluctuating each event in this spectrum by the amplitude of a noise pulse randomly sampled from the noise spectrum recorded at 60 metres in the Blue Lake. The resulting predicted spectra for a range of water attenuation lengths are shown in figure 5.24.

To determine if the 17 events recorded in the lake during the October field tests contain information on muon-induced Cerenkov signals, the measured events are compared with the simulated distributions shown in figure 5.24. The degree to which the distribution of measured events matches a simulated distribution of events can be quantified by defining some function of the measured events and the simulated distribution. The value of this function, hereafter referred to as the 'goodness of fit' parameter, varies with the distribution of measured events. Comparing the goodness

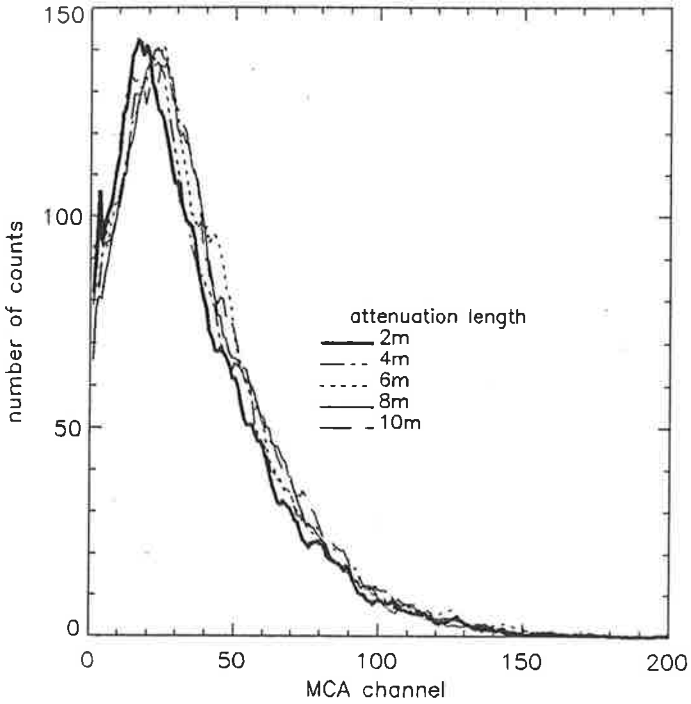

Figure 5.24: Simulated gated spectra at 60 metres in the Blue Lake

of fit parameter for the measured events with the expected distribution of this parameter for a large number of sets of 17 events, randomly selected from the simulated distribution, is a means of determining how closely the measured events match the simulated distribution. For example, if the distribution of the goodness of fit parameter for sets of 17 events is a normal distribution and the goodness of fit parameter for the set of measured events lies at the 3σ point on this distribution, then we can say that the probability of randomly selecting sets of 17 events from the simulated spectrum with goodness of fit parameters less than the measured events is 0.01.

In this analysis the goodness of fit parameter is defined as the logarithm of the total probability that a specific set of 17 events are randomly selected from the simulated distribution. This parameter is represented by equation 5.2 in which g is the goodness of fit parameter and P_n is the probability that an event is randomly selected from the simulated distribution.

$$g = log \prod_{n=1}^{17} P_n \tag{5.2}$$

If a measured event is recorded at, say, channel 50 on the MCA then P_n for this event is the probability that an event selected randomly from the simulated distribution will occur at channel 50. This probability is proportional to the amplitude of the simulated spectrum at channel 50. The goodness of fit parameter is therefore determined by first finding the amplitude of the simulated spectrum corresponding to each measured event and then calculating the product of these amplitudes. This represents the total probability that the 17 events are randomly selected from the simulated distribution. The logarithm of this factor is then calculated as the variation in the total probability is very large.

By randomly selecting a large number of sets of 17 events from the simulated spectrum and calculating the goodness of fit parameter for each set, the distribution of this parameter can be determined. Figure 5.25 shows the distributions of goodness of fit parameter for sets of 17 events sampled from two spectra, namely, the simulated gated spectrum of events recorded in the lake at 60 metres for a water attenuation length of 2 metres (see figure 5.24), and the measured noise spectrum at 60 metres in the lake (see figure 5.21). Also shown in this figure are the goodness of fit parameters corresponding to the set of 17 measured events.

For the case of the simulated spectrum of events in the lake, the goodness of fit distribution peaks at a value of about 4. Hence a set of 17 events with a goodness of fit parameter equal to 4 would have a very high likelihood of being sampled from the simulated spectrum. The 17 events recorded in the lake have a goodness of fit parameter equal to -1.7 which lies on the tail of this distribution. Of the 100 000 events considered about 100 had goodness of fit parameters less than -1.7. Hence, we can say that the probability of randomly selecting 17 events from the simulated spectrum with goodness of fit parameters less than the measured events is about 1 in 1000. For the case of the noise spectrum, the goodness of fit parameter for the

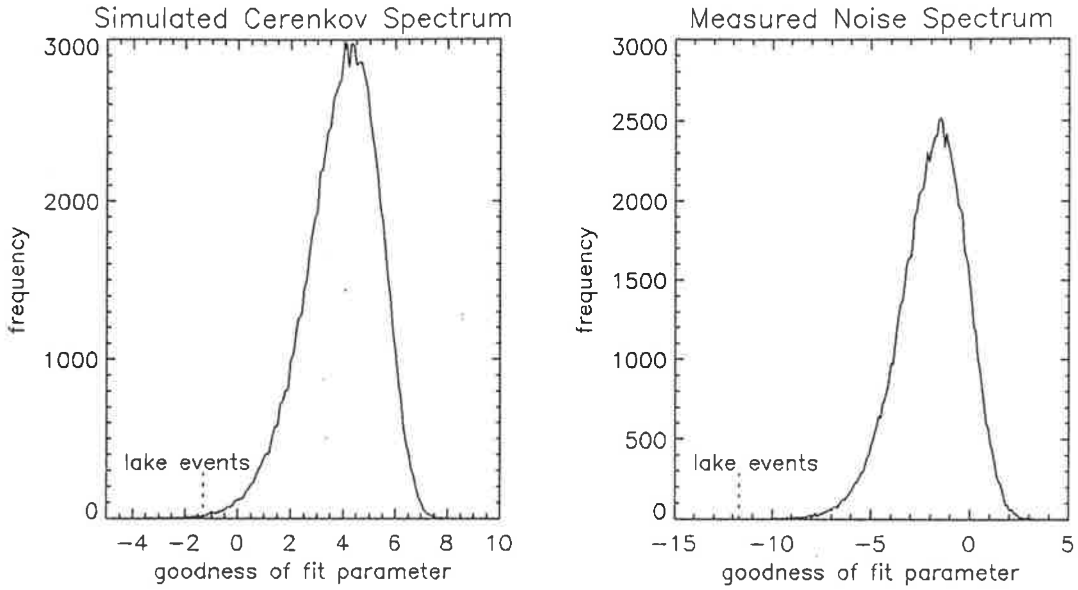

Figure 5.25: Results of calculation of probabilities that measured events are sampled from simulated spectra

measured events does not actually lie on the goodness of fit distribution. Hence, the probability of randomly sampling sets of 17 events from the noise spectrum with lower goodness of fit parameters than the measured events is less than 1 in 100 000. This indicates that the events recorded in the lake are at least 100 times more likely to have been sampled from the simulated spectrum than from the background noise spectrum. Hence we can reject the possibility that the measured events are all noise pulses.

The probability that the measured events are sampled from the simulated spectrum is low but not negligible. This implies that either the assumed model for Cerenkov pulses combined with noise is correct and we have recorded a relatively unlikely set of events, or the model assumed, and hence the simulated spectrum, is incorrect. These hypotheses could be tested by measuring a large number of sets of 17 events in the lake. If the resulting distribution of goodness of fit parameter for the sets of measured events agrees with the simulated distribution shown in figure 5.25 then we can deduce that the assumed model of Cerenkov pulses combined with noise is correct. From the existing data we can say that the measured events are not a random sample from the noise distribution and hence contain information about muon-induced Cerenkov pulses. The probability that the measured events were derived from the predicted spectrum of Cerenkov signals modulated by noise fluctuations is approximately 100 times greater than the probability they were sampled from the noise distribution. Hence, in principle, it would be possible to extract information relating to muon-induced Cerenkov pulses in the lake using the upgraded version of Harvey II, however, significantly more data are required to verify the validity of the assumed model of Cerenkov signals combined with DC noise and to identify any features, such as peak position, in the spectrum of measured events.

5.5.3.3 Further Measurements of the Delta Function Response

In order to further investigate the effect of varying the coincidence time window on the contribution of background noise to the gated spectra the delta function response of the new system was recorded for various delays between the leading edges of the gate pulse and signal pulse. The results for delays of 1,4 and $6\mu s$ are shown in figure 5.26.

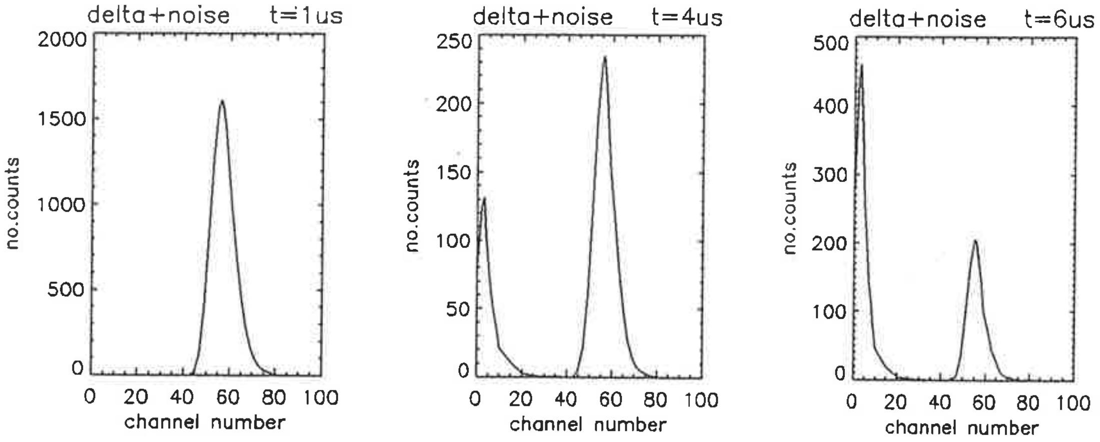

Figure 5.26: Delta function response for various delays

From the results in figure 5.26 it can be seen that for a coincidence time window of $1\mu s$ the resulting spectrum exhibits no low level noise pulses and therefore no complete noise pulses occur before the signal pulse. All the pulses registered are signal pulses fluctuated by noise resulting in a delta function fluctuated by the background noise spectrum. As the coincidence time window increases complete noise pulses can occur before the signal pulse and these appear as a typical noise distribution at the lower end of the spectrum. The number of these noise pulses increases with increasing coincidence time window such that for a coincidence window of $6\mu s$ about two thirds of the total number of pulses recorded are noise pulses and one third are signal pulses modulated by noise. The difference between the delta responses for coincidence time windows of $1\mu s$ and $6\mu s$ are an indication of the improvement in the rejection of noise events obtained by upgrading the electronics.

5.6 Conclusions

In this chapter the measurement of light pulses in the Blue lake using a specifically designed test device, Harvey II, is described. The aim was to determine whether it is possible to observe the Cerenkov light from relativistic muons in the lake using a photomultiplier tube and no light shielding. The results indicate that the background light level is high such that the photomultiplier tube used saturates at depths less than 40 metres when operated looking upwards on moonless nights. The high background light level affects the detection of Cerenkov pulses from muons in two ways. Firstly, the fluctuations in the DC level can affect the amplitudes of Cerenkov pulses or, secondly, noise pulses may be registered in place of Cerenkov signals.

For the results obtained during the field tests in April 1994, the high proportion of noise pulses recorded make it impossible to derive any information about the Cerenkov signals present. The pulse height spectra recorded of light pulses occurring in coincidence with muons triggering the muon telescope are very similar to random samples of events from the corresponding noise spectra. Hence, any Cerenkov signals are indistinguishable from the noise pulses registered.

By reducing the coincidence time window during which light pulses are registered, as in the measurements taken during the field trip in October 1994, the effect of background light can be reduced so that the only effect of noise is to modulate the amplitude of Cerenkov pulses. The Cerenkov signals can then be identified by modelling the amplitude fluctuations due to the background noise. By simulating the expected spectra and comparing these to the measured results and also to random samples of noise events it can be seen that the probability that the measured results are Cerenkov pulses modulated by noise is significantly greater than the probability that the measured results are solely due to noise pulses. Hence it has been shown that it is possible to observe muon-induced Cerenkov pulses in the Blue Lake using Harvey II with the coincidence time window reduced to $1\mu s$ in order to reduce the effects of the high background light level.

Although the effect of noise on the detection of Cerenkov signals has been minimised using the existing electronics to the point where Cerenkov signals can be identified, the amount of noise detected is still relatively high. If desired, this could be reduced by further decreasing the coincidence time window. With the existing system it is not possible to achieve a coincidence window of less than about $1\mu s$. This is ultimately limited by the MCA used to collect the data, as the MCA will not register pulse widths of less than about $1\mu s$. However by using fast electronics incorporating fast analogue to digital conversion and fast amplification techniques, pulses of much shorter duration eg. of the order of 20 ns, can be recorded. This would reduce the rate of noise pulses occurring in coincidence with Cerenkov signals and consequently significantly improve the signal to noise ratio.

Chapter 6

Summary and Future Work

The aim of this work was to develop a design for, and assess the performance characteristics of, a high energy neutrino detector to be located in a natural lake in South Australia. The proposed detector is intended to observe high energy neutrinos from astrophysical point sources such as active galactic nuclei, X-ray binary systems and supernova remnants. The method of detection is via the Cerenkov radiation produced in water by upward travelling muons resulting from interactions between high energy neutrinos and nuclei in the Earth. The detector consists of an array of downward looking photomultiplier tubes submerged in a lake, to register Cerenkov light from upward travelling muons. The direction of the muons, and hence that of the parent neutrinos, can be determined from the relative times at which photomultiplier tubes register signals.

Two natural lakes were considered as possible locations for the proposed detector:- the Blue Lake in Mt.Gambier, S.Australia and Weebubbie Cave at Eucla, W.Australia. The main factors considered in the choice of a detector site were the total available surface area and the transmission of Cerenkov light through the water. Current calculations of the predicted flux of upward neutrino-induced muons from astrophysical sources indicate that the surface area of such a detector must be at least 10^4m^2 to detect events at a rate of few per year. Both the sites considered satisfy this condition, however, the possibility of expanding the detector beyond this minimum size is feasible in the Blue Lake only. The amount of Cerenkov light transmitted through the water determines the amplitude of signals registered by the photomultiplier tubes and hence has a significant effect on the detector's efficiency in observing muons. The optical properties of the water at both sites were investigated using a spectrometer to measure the attenuation length of water samples. The transmission at both sites was found to be very similar with the longest attenuation length of about 5 metres being observed in water collected from a depth of 50 metres in the Blue Lake during February 1992. Spectrometer measurements of Blue Lake water taken over a period of 18 months indicated that the optical properties of the water varied seasonally with the clearest water occurring at depths greater than about 40 metres during the summer months. Considering the similarity in optical properties of the water at both sites and the greater available surface area and accessibility of the Blue Lake, it is proposed that the detector be located in the Blue Lake at a depth of at least 40 metres.

The water in the Blue Lake was also analysed *in situ* using a specifically designed transmissiometer called Harvey I. The aim of this procedure was to eliminate any errors that might occur in the spectrometer results as a result of removing samples of water from the lake. The attenuation length measured using Harvey I was found to be consistently slightly higher than the value obtained using the spectrometer. This was a result of a significant amount of light scattering occurring in Blue Lake water and the fact that Harvey I detected more of this scattered light than the spectrometer. Further, it is expected that the attenuation length corresponding to the detection of Cerenkov light by the proposed detector would be greater still as the amount of scattered light registered would be correspondingly higher due to the absence of any light collimation in the proposed detector.

Having determined the preferred site for the proposed detector, the detector design was then optimised using Monte Carlo techniques to simulate the detector response to muons. The optimisation of the detector design was based on the fact that in order to observe high energy neutrinos from point sources the following conditions must be met. Firstly, the rate of signal events registered should be at least a few events per year from every source. Secondly, the signal to noise ratio should be at least 3 to ensure that genuine signal events can be detected above the high rate of background events. Finally, the angular resolution should be as high as possible (ideally less than about 1°) in order that point sources can be identified. These factors all depend on the geometry of the detector and the triggering conditions which must be satisfied in order that an event is registered. By simulating the detector response as a function of detector geometry and triggering conditions the optimum design was determined.

The proposed detector consists of 3 vertically spaced layers of downward looking photomultiplier tubes, with the tubes in each layer arranged on a square grid. The variable parameters in this design are the surface area of the photomultiplier tubes, the grid spacing between the tubes in a layer and the vertical separation between the layers. The variable parameters in the triggering conditions are the lower level threshold in each photomultiplier tube and the minimum number of photomultiplier tube hits required per layer. Firstly, the expected rate of signal events from a point source was determined as a function of the variable parameters listed. The point source considered was Cygnus X-3, using the predicted neutrino flux as scaled from the apparent gamma-ray fluxes observed by Lloyd-Evans,1983 and Samorski and Stamm,1983. The expected rate of background events was then determined. The main sources of background events are atmospheric neutrinos passing upward through the detector and downward travelling atmospheric muons. The predicted signal to noise ratios for a range of detector geometries and triggering conditions were then determined and the results summarised in table 4.7.

From the simulated results of signal event rate, signal to noise ratio and angular resolution, the optimum design of a detector located in the Blue Lake was selected. The final design is as shown in figure 4.11 and consists of 3 layers of photomultiplier tubes separated vertically by 9 metres, with a grid spacing between tubes in each layer of 4 metres. The photocathode area of the photomultiplier tubes is 0.2 metres and the optimum triggering conditions are a lower level threshold in each tube of 1 photoelectron and a minimum of 4 photomultiplier tube hits per layer. A detector of this design has a predicted angular resolution of 0.47°, a signal event rate due to neutrinos from Cygnus X-3 of 2-3 per year and a signal to noise ratio of 4.8 ± 0.4.

The final chapter of this thesis describes a series of *in situ* meaurements which were taken to assess the feasibility of detecting muons in the lake via the emitted Cerenkov light. A custom built device (Harvey II) was used to track individual muons and record the resulting Cerenkov light. This device was also used to measure the amount of background light in the lake to determine if it would be necessary to surround the proposed detector in a light-tight enclosure. The results obtained indicate that it is possible to observe muons via the emitted Cerenkov light, although the background light level is high enough that the observed Cerenkov signals are significantly modulated by fluctuations in the background light level. However, it is still possible to extract information on the muon-induced Cerenkov signals from these results provided that a sufficiently accurate model for the modulation of Cerenkov signals by background light is available.

The measurements taken using Harvey II show that even when using relatively slow electronics and with no shielding from background light, it is possible to observe the Cerenkov light from individual muons. In the proposed detector, fast electronics would be required in order that timing information from photomultiplier tube signals could be used. Also, the detector would be enclosed in a light-tight container to facilitate continuous operation. Both these factors would significantly reduce the effect of background light and hence improve the signal to noise ratio relative to the results obtained with Harvey II. Hence, it can be inferred that the proposed detector would be capable of detecting the Cerenkov light emitted by relativistic muons.

Future work on this project involves the construction of a small prototype detector with the aim of developing an algorithm for determining muon direction from the relative times at which photomultiplier tubes register Cerenkov signals. A possible design for this prototype consists of 4 photomultiplier tubes located at the corners of a 4 metre square to reproduce the optimum grid spacing in the full-sized detector. The prototype would utilise fast electronics and would be used to observe downward travelling atmospheric muons. Comparison of the reconstructed track directions with the known angular dependence of atmospheric muons would provide a means of assessing and optimising the direction reconstruction algorithm. Also, by operating this prototype in conjunction with a muon telescope, specific muon trajectories could be selected and the reconstructed directions compared with the known trajectories.

References

Aglietta M. et al. (1993) Proc.23rd ICRC, Calgary, vol.1, 216

Alexandreas D.E. et al. (1993) Proc.23rd ICRC, Calgary, vol.1, 373

Allkofer (1975) Introduction to Cosmic Radiation, Verlag Karl Thieneig

Amenomori M. et al. (1993) Proc.23rd ICRC, Calgary, vol.1, 342

Askar'yan G.A. (1962) Sov.Phys. JETP vol.14, 441

Baltrusaitis R.M. et al. (1985) Proc 19th ICRC, La Jolla, vol.1, 111

Barwick S. et al. (1992) J.Phys.Nucl.Part.Phys. vol.18, 225

Battersby S.J.R., Drolias B. and Quenby J.J. (1995) Astroparticle Phys., in press

Bauer D. and Morel A. (1967) Am.Geophys. vol.23, 109-123

Becker-Szendy R. et al. (1995) Ap.J. vol.44, 415B

Belolaptikov et al. (1993) Proc.23rd ICRC, Calgary, vol.4, 573

Belolaptikov et al. (1994a) Nucl.Phys.B (Proc.Suppl.) vol.35, 301

Belolaptikov et al. (1994b) Nucl.Phys.B (Proc.Suppl.) vol.35, 290

Berezinsky V.S. (1977) Proc.Neut.77 vol.1, 177

Berezinsky V.S. et al. (1990) Astrophysics of Cosmic Rays, translated by L.J.Reinders, North-Holland (Amsterdam), 370

Biermann P.L. (1992) High Energy Neutrino Astrophysics, eds V.J.Stenger et al., World Scientific (Singapore), 86

Bionta R.M. et al. (1987) Phys.Rev.Lett. vol.58, 1494

Bobsiut F. et al. (1991) Proc.3rd Int.Workshop on Neutrino Telescopes, Venice, ed M.Baldo Ceolin, 387

Boldyrev I.N. et al. (1991) Proc.3rd Int.Workshop on Neutrino Telescopes, Venice, ed M.Balo Ceolin, 337

Borione et al. (1995) Proc.24th ICRC, Rome, vol 2, 430

Bratton C.B. et al. (1988) Proposal to Construct the GRANDE Facility for the Study of Astrophysical Sources and High Energy Particle Interactions, submitted to NSF

Camerini U. et al. (1993) Proc.23rd ICRC, Calgary, vol.4, 530

Crouch M.F. et al. (1978) Phys.Rev.D vol.18, 2239

Engstrom R. (1980) RCA Photomultiplier Handbook, 82

Fichtel C.E. (1994) Ap.J.Suppl. vol.90, 917

Frank I. and Tamm I. (1937) C.R.Acad.Sci.URSS vol.14, 109

Gaisser T.K. and Stanev T. (1984) Phys.Rev.D vol.30, 985

Gaisser T.K. and Stanev T. (1985) Proc.19th ICRC, La Jolla, vol.7, 156-159

Gaisser T.K. and Grillo A.F. (1987) Phys.Rev.D vol.36, 2752

Gaisser T.K. and Stanev T. (1987) Phys.Rev.Lett. vol.58, 1695

Gaisser T.K. (1990) Cosmic Rays and Particle Physics, Cambridge University Press, 238

Gray L. et al. (1995) Proc.24th ICRC, Rome, vol.1, 816

Halzen F., Zas E. and Stanev T. (1991) Proc.22nd ICRC, Dublin, vol.4, 686

Hill G. PhD thesis, University of Adelaide, to be published

Hillas A.M. (1984) Nature vol.312, 50

Hirata K.S. et al. (1987) Phys.Rev.Lett. vol.38, 1490

Jerlov N.G. (1976) Marine Optics, Elsiver Oceanography Series vol.14, 55-63

Jones L.W. (1985) Proc.19th ICRC, La Jolla, vol.9, 323-326

Karaevsky S. et al. (1993) Proc.23rd ICRC, Calgary, vol.4, 550

Khrenov and Linsley (1981), Proc.17th ICRC, Paris, vol.10, 354

Kirk J.T.O. (1981) Aust.J.Mar Freshwater Res. vol.32, 533

Kolb E.W., Turner M.S. and Walker T.P. (1985) Phys.Rev.D vol.32, 1145

Koshiba M. (1988) Nucl.Phys.A vol.478, 355

Koshiba M. (1992) Physics Reports vol.220, 229-381

Kullenberg G. (1968) Deep-Sea Res. vol.15, 423-432

Learned J.G. (1993) Proc.23rd ICRC, Calgary, vol.4, 515

Learned J.G. (1993a) Proc.23rd ICRC, Calgary, vol.4, 538

Linsley J. (1985) Proc.19th ICRC, La Jolla, vol.7, 359-362

Lloyd-Evans J. et al. (1983) Nature vol.305, 784

Lowder D. et al. (1993) Proc.23rd ICRC, Calgary, vol.4, 569

Merck M. et al. (1993) Proc.23rd ICRC, Calgary, vol.1, 361

Mock P.C. et al. (1995) Proc.24th ICRC, Rome, vol.1, 758

Nishikawa K. et al. (1992) 4th Int.Workshop on Neutrino Telescopes, Venice, ed M.Baldo Ceolin, 337

Oyama Y. (1989) PhD thesis, Institute for Cosmic Ray Research, University of Tokyo

Pennypacker C.R. et al. (1989) Ap.J. vol.340L, 61

Protheroe R.J. et al. (1984) Ap.J.Lett. vol.280, L47

Protheroe R.J. and Patterson J. (1984) J.Phys.G vol.10, 841

Protheroe R.J. and Clay R.W. (1985) Nature vol.315, 205

Protheroe R.J. and Stanev T. (1992) High Energy Neutrino Astrophysics, eds V.J.Stenger et al., World Scientific (Singapore), 40

Punch M. et al. (1992) Nature vol.358, 477

Raubenheimer B.C. et al. (1987) Proc.20th ICRC, Moscow, vol.1, 267 and 303

Rhode W. et al. (1995) Astroparticle Physics, to be published

Reno M.H. and Quigg C. (1988) Phys.Rev.D vol.37, 657

Resvanis L.K. (1992) High Energy Neutrino Astrophysics, eds V.J.Stenger et al., World Scientific (Singapore), 325

Resvanis L.K. (1994) Nucl.Phys.B (Proc.Suppl.) vol.35, 294

Roberts A. (1992) Reviews of Modern Physics vol.64, no.1

Rowan-Robinson M. (1985) The Cosmological Distance Ladder, W.H.Freeman and Company (New York)

Samorski M. and Stamm W. (1983) Ap.J.Lett vol.268, L17

Sikora M. and Begelmann M.C. (1992) High Energy Neutrino Astrophysics, eds V.J.Stenger et al., World Scientific (Singapore), 114

Silberberg R. and Shapiro M.M. (1979) Proc.16th ICRC, Tokyo, vol.10, 357

Sobel H. (1991) Nucl.Phys.B (Proc.Suppl.) vol.19, 444

Sobel H. (1993) 5th Int.Workshop on Neutrino Telescopes, Venice, ed M.Baldo Ceolin, 493

Stanev T. (1990) Nucl.Phys.B (Proc.Suppl.) vol.14a, 17

Stecker F.W. et al. (1991) Phys.Rev.Lett. vol.66, 1697 and (1992) vol.69, 2738E

Stecker F.W., De Jager O.C. and Salamon M.H. (1992) Astrophys.J.Lett. vol.390, L49

Stecker F.W. and Salamon M.H. (1995) Space Science Rev., in press

Stenger V.J. (1993) Proc.23rd ICRC, Calgary, vol.4, 527

Svoboda R. (1990) Nucl.Phys.B(Proc.Suppl.) vol.14A, 97-102

Szabo A.P. (1992) PhD thesis, University of Adelaide

Szabo A.P. and Protheroe R.J. (1994) Astropart.Phys. vol.2, 375

Telfer A. (1993) E&WS, SA, internal report

Tilav S. et al. (1993) Proc.23rd ICRC, Calgary, vol.4, 561

Vestrand W.T. and Eichler D. (1982) Ap.J. vol.261, 251

Volkova L.V. (1980) Sov.J.Nucl.Phys. vol.31(6), 784-789

Wheeler J.C. and Harkness R.P. (1990) Rep.Prog.Phys. vol.53, 1467

Wolfendale A. (1973) Cosmic Rays at Ground Level, Inst.of Physics, 27

Woosley S.E. and Weaver T.A. (1986) Ann.Rev.Astron.Ap. vol.24, 205

Weekes T.C. (1992) Space Science Reviews vol.59, 315-364

White N.E. and Holt S.S. (1982) Ap.J. vol.257, 253

Wilkes R.J. (1994) Proc. SLAC Summer Institute

Yodh G.B. (1992) High Energy Neutrino Astrophysics, eds V.J.Stenger et al., World Scientific (Singapore), 257